KU LEUVEN

ARENBERG DOCTORAL SCHOOL
Faculty of Science

Nano-Engineered Polymer-Steel Hybrids: Chemical and Physical Compatibilization

Ellen Bertels

Supervisor:
Prof. B. Goderis
Prof. M. Smet

Dissertation presented in partial
fulfillment of the requirements for the
degree of Doctor in Sciences

February 2015

Nano-Engineered Polymer-Steel Hybrids: Chemical and Physical Compatibilization

Ellen BERTELS

Examination committee:
Prof. E. Nies, chair
Prof. B. Goderis, supervisor
Prof. M. Smet, supervisor
Prof. P. Van Puyvelde
Prof. I. Verpoest

Prof. B. van Mele
(VUB, Belgium)
dr. B. Verheyde
(VITO, Belgium)

Dissertation presented in partial
fulfillment of the requirements for
the degree of Doctor
in Sciences

February 2015

Uitgegeven in eigen beheer, Ellen Bertels, Celestijnenlaan 200F box 2404, B-3001 Heverlee (Belgium)

ISBN 978-90-8649-794-2

D/2015/10.705/4

Preface

Dit boek zet een punt achter mijn doctoraat en de daarbij horende unieke periode. Een periode van hard werk, maar evenzeer een periode van vriendschap en plezier. Hierbij passeerden vele gezichten de revue, waarvan enkele een speciaal woord van dank verdienen.

Om te beginnen bedankt aan mijn promotoren, Bart Goderis en Mario Smet. Zij boden me de kans mee mijn schouders onder dit project te zetten en mijn steentje bij te dragen aan het grotere SIM geheel. Bovendien kon ik bij hen terecht voor wetenschappelijke hulp en een nalezend oog.

Ook alle andere leden in dit SIM-NanoForce programma mogen niet vergeten worden. Amit, Michaël, Gabriëlla, Klaas en alle anderen, bedankt voor de ettelijke uren die we samen doorbrachten in het labo en op vergaderingen, voor de samenwerking waardoor we elkaar steeds verder konden helpen.

Een woord van dank aan iedereen die me hielp bij het realiseren van experimenten: Marcel Lasker die vooral praktisch met raad en daad klaar stond, Karel Duerinckx die geweldige NMR input leverde (en metingen deed), Danny Winant die hielp met de TGA metingen en Kevin Bruyninckx die steeds paraat stond voor het synthetiseren van surfactanten.

Dank je aan alle collega's die hielpen bij het entertainment buiten de experimenten om. Dorien, Kevin, Lien, Maja, Olivier en Thomas bedankt voor de leuke middagpauzes, maar ook de leuke uitjes en housewarmings na de uren . Jullie zorgden voor de afleiding die werken in dit labo ontzettend aangenaam maakte, en toonden dat collega's geweldige vrienden kunnen zijn!

Bedankt aan alle leden van de jury. Voor jullie tijd die ik kreeg om dit werk te evalueren, alsook voor de nuttige commentaren en suggesties om van dit boek een mooi geheel te maken.

Vrienden en familie, bedankt om keer op keer te luisteren naar de (al dan niet verstaanbare) doctoraats- en werkverhalen.

Als laatste maar zeker niet als minste, wil ik zowel mijn ouders als mijn vriend Robbe bedanken. Bedankt ma en pa voor de steun en de kansen die ik de voorbije jaren kreeg. Bedankt Robbe, ondanks een Pellenberg intermezzo stond je steeds achter en naast me met een luisterend oor, bracht je begrip op voor de lange werkdagen, en kreeg je me steeds weer aan het lachen.

Bedankt...

Abstract

In a variety of applications the combination of metals and polymers can offer advantages, such as a high design freedom, a relatively low mass-to-strength ratio and a high fatigue resistance, resulting in best of both worlds when designed correctly. However, challenges exist in joining dissimilar materials, and the interphasial properties highly influence the mechanical properties of the resulting hybrids. This work aims at improving these interphasial properties, firstly by the application of silane coupling agents to improve adhesion, secondly by adding nanomodifications to the interphasial region. While the former ideally couple the substrate to the matrix by forming a covalent bridge thereby increasing adhesion and forming a first gradient, the latter enable the creation of a gradient interphase, decreasing the mismatch in properties between the constituents and enabling stress transfer from the polymer to the steel.

To start with different substrate cleaning procedures were evaluated, as they define the interactions between the substrate and the silane coupling layer and are a necessary condition to obtain decent bonding. Different processing variables influence the appearance of the coupling layer. A systematic variation of the silane coating parameters enabled determination of the optimized layer, that led to a highly improved mechanical strength of stainless steel-epoxy joints, with inferior interfacial adhesion no longer being an issue. This optimized silane layer also proved to be successful when transferred to a different system, thereby exchanging the plate-like substrate for a fibrous substrate or the epoxy for a polyamide matrix.

After optimization of the silane coupling layer, the epoxy became the weak point in the hybrid. Theoretically addition of nanomodifications may further improve coupling and induce a more efficient stress transfer from the matrix to the substrate, increasing mechanical performance. However, addition of hyperbranched polylysine nanoparticles to the interphase disrupted the optimized silane structure and resulted in a defect interphase, decreasing performance. Application of carbon nanotubes on the interphase starting from an aqueous solution, also deteriorated coupling, probably because they show a limited interaction with the coated substrate and limit the interaction between the polymer matrix and the silane.

Despite the failure of the nanomodifications, a highly efficient triphenylmethyl functionalized hyperbranched polyglycerol surfactant was developed, enabling dispersion of 2.85 mg of multi-walled carbon nanotubes in water with as low as 1 mg of surfactant. This surfactant may be promising in other applications, either when used to deposit tubes from aqueous dispersions for a different purpose or to dissolve carbon nanotubes in a polymer matrix.

Beknopte Samenvatting

Polymeer-staal hybrides bieden voordelen voor tal van toepassingen door bv. een hoge vrijheidsgraad in ontwerp, een relatief lage massa-sterkte verhouding en een verbeterde weerstand tegen vermoeiing. Zo bieden ze het beste van twee werelden als ze op de juiste manier samengebracht zijn, wat bemoeilijkt wordt door de totaal verschillende eigenschappen van de constituenten. Deze verschillende eigenschappen moeten opgevangen worden aan de interfase, die dan ook vaak in grote mate de mechanische eigenschappen en sterkte van de resulterende composieten bepaalt. Dit werk doelt op het manipuleren van de interfase en zijn eigenschappen, allereerst door een aanpassing van de polymeer-staal adhesie met behulp van silanen, ten tweede door het aanbrengen van nanomodificaties aan de interfase. In het ideale geval vormen de silanen een covalente brug tussen het substraat en de matrix, om zo adhesie te verbeteren, terwijl ze, door hun intermediaire eigenschappen, kunnen leiden tot de vorming van een eerste gradiënt. De nanomodificaties doelen op het creëren van een gradiënt interfase om zo het verschil in componenteigenschappen op te vangen en spanning efficiënter over te brengen van polymeer naar staal.

Aangezien het substraat oppervlak de interacties met het silaan bepaalt, werden allereerst verschillende staal reinigingsmethodes geëvalueerd. Dit toonde aan dat de voorbehandeling van het substraat een voorwaarde is om tot een aanzienlijke verbetering in mechanische eigenschappen te komen. Hierna volgde een systematisch onderzoek van de invloed van verschillende parameters tijdens het afzetten van de silaanlaag om een optimale koppeling te bereiken. Dit resulteerde in een superieure adhesie tussen roestvrij stalen substraten en een epoxy matrix, waarbij de matrix en niet de interfaciale adhesie de beperkende factor vormde. Bovendien kon deze optimale silaan depositie procedure

moeiteloos overgedragen worden naar systemen met stalen vezels in plaats van platen of een polyamide in plaats van een epoxy matrix, om ook daar de adhesie te verbeteren.

Na het optimaliseren van deze silaanlaag, vormt de epoxy matrix het zwakke punt in de hybrides. In theorie kan het toevoegen van nanomodificaties aan de interfase de mechanische sterkte dan verder verhogen door het verminderen van spanningsconcentraties. Toevoegen van hypervertakte polylysine nanodeeltjes aan de silaan interfase verstoorde de geoptimaliseerde structuur en resulteerde in een poreuze interfase die opnieuw het zwakke punt in de hybrides vormde. Ook toevoegen van koolstof nanobuisjes aan de interfase, vertrekkend vanuit een waterige oplossing, verslechterde de adhesie tussen polymeer en substraat door de beperkte interactie tussen nanobuisje en substraat en de verstorende werking op de interactie tussen matrix en substraat.

Ondanks het falen van de nanomodificaties is een erg efficiënt triphenylmethyl gefunctionaliseerd hypervertakt polyglycerol surfactant ontwikkeld, dat 2.85 mg koolstof nanobuisjes in waterige oplossing kan brengen met slechts 1 mg surfactant. Dit maakt deze moleculen veelbelovend voor andere toepassingen, waarbij nanobuisjes vanuit waterige oplossing afgezet worden, of waarbij de surfactanten helpen bij de dispersie van nanobuisjes in een polymere matrix.

List of Symbols and Abbreviations

a/b : mg carbon nanotubes (a) per mg of surfactant (b)
$acac$: Acetic acid
AFM : Atomic force microscopy
APS : 3-Aminopropyltriethoxysilane
$BTSE$: 1, 2-Bistriethoxysilylethane
CMC : Critical micelle concentration
CNT : Carbon nanotube(s)
$COOHCNT$: Acid functionalized carbon nanotube(s)
CPS : Counts per second
DAC : 1, 2-Diaminocyclohexane
$DDBS$: Dodecylbenzenesulfonate
DLS : Dynamic light scattering
D_2O : Deuteriumoxide
$DGEBA$: Diglycidyl ether of bisphenol A
DH : Degree of hydrolysis
DLS : Dynamic light scattering
$DMSO - d_6$: Deuterated dimethylsulfoxide
DPD : Dolly-plate-dolly
EDX : Energy dispersive X-ray spectroscopy
EM : Electron microscopy
$EtOH$: Ethanol
FIB : Focussed ion beam
GPS : 3-Glycidoxypropyltrimethoxysilane

$HAADF$: High angle annular dark field
$H-bonding$: Hydrogen bonding
HLB : Hydrophilic-lyophilic balance
HR : High resolution
M : Metal
$MeOH$: Methanol
$MWCNT$: Multi-walled carbon nanotube(s)
NMR : Nuclear magnetic resonance
$PA6$: Polyamide 6
$PDMS$: Polydimethylsiloxane
PEO : Poly(ethylene oxide)
PG : Hyperbranched polyglycerol
PL : Hyperbranched polylysine
PPO : Poly(propylene oxide)
SDS : Sodium dodecylsufate
SE : Spectroscopic ellipsometry
SEM : Scanning electron microscopy
SST : Stainless steel
$SWCNT$: Single-walled carbon nanotubes
$(S)TEM$: (Scanning) Transmission electron microscopy
TGA : Thermogravimetric analysis
$trityl$: Triphenylmethyl
US : Ultrasonic
$UV-Vis$: Ultraviolet-visible spectroscopy
$(N)V$: (No) vacuum
XPS : X-ray photoelectron spectroscopy
$x\ \%\ PGy$: Hyperbranched polyglycerol with a core molar mass of y g/mol and x % of the end groups functionalized
$ZDOI$: Zero depth of immersion

A : Surface area
C_a : Capillary number
d : Diameter
F : Force
F_r : Recorded force

F_{sv} : Solid-vapor force
F_{lv} : liquid-vapor force
F_{sl} : Solid-liquid force
g : Gravitational acceleration
h : Height
l : Length
m : Mass
N : Number of hydroxyl groups available
$2p$: Wetted perimeter
p_i : Probability that a molecule carries i functionalizations
R_a : Roughness arithmetic mean value
R_q : Roughness quadratic mean value
t : time
T : Temperature
W : Work
$v\%$: Percentage by volume
V : Volume
W_{sl} : Free energy of adhesion
$wt\%$: Percentage by weight
x : Distance

γ : Surface energy
γ_{lv} : Liquid-vapor interfacial surface energy
γ_{sl} : Solid-liquid interfacial surface energy
γ_{sv} : Solid-vapor interfacial surface energy
γ^{lw} : Lifshitz-van der Waals component of the surface free energy
γ^{+} : Acid component of the surface free energy
γ^{-} : Basic component of the surface free energy
γ^{d} : Dispersive component of the surface energy
γ^{p} : Polar component of the surface energy
η : Viscosity
θ : Contact angle
θ_{adv} : Advancing contact angle

θ_{eq} : Equilibrium/Young contact angle
θ_{rec} : Receding contact angle
ν : Relative speed
ρ : Density
σ : Stress at break
τ : Time where 62.31 % of hydrolysis is completed
ϕ : Average fraction of functionalizations

Table of Contents

List of Figures

List of Tables

General Introduction

Composite materials become increasingly important in everyday life, as they can offer best of both worlds, making them interesting for different applications. As steel-polymer laminates and sandwich materials or as fiber reinforced composites they can combine the stiffness, toughness and formability of steel with the lightness, damping capacity, insulation,... of polymers. Airplane manufacturers e.g. used composites for decades in secondary structures, and nowadays they also gain importance for more crucial parts, with the Boeing 787 consisting of more than 50% of composites. When joined correctly, polymer-steel hybrids have different advantages compared to mechanically fastened joints, among which their improved fatigue resistance and low weight-to-strength ratio. This makes them extremely interesting for structural materials, thereby leading to energy savings. Whereas traditional carbon and glass but also steel fibers offer the advantage of high stiffness, the steel fibers used in this work combine this high stiffness with a high strain-to-failure, improving composite performance. Although also spider silk and certain carbon nanotube spun fibers can combine a high stiffness with a high strain-to-failure, they are both more rare and harder to produce in large quantities compared to steel fibers. However, interphase failure, due to inferior adhesion and a (stiffness) mismatch between the properties of the constituents, limits the exploitation of those materials in structural applications.

This research is part of the SIBO program Nanoforce of the Strategic Initiative Materials (SIM), involving a collaboration with different Flemish universities, but also two main industrial partners, Bekaert and Recticel. It aims at creating lightweight and multifunctional polymer-steel hybrids with good durability. The guiding hypothesis within this PhD research states that the polymer-steel adhesion as well as the polymer toughness and/or yield stress in the interphasial region need to be improved and that it is necessary to decrease the polymer-steel stiffness mismatch at the interface. The adhesion in the interphasial region between the materials can be increased by applying of suitable coupling agents (sizings), leading to better chemical interactions between the phases which delays the adhesive failure at the interphase. Decreasing the stiffness mismatch can be done in different ways: nanoreinforcements can be included in the interphasial region, as well as in the matrix material. Throughout this project, standard substrates and matrices have been selected, as the general aim is to apply findings on an industrial scale.

This thesis starts with a literature study to get a general framework (Chapter 1), followed by a description of the materials and characterization techniques used (Chapter 2). The next chapter (Chapter 3) describes the optimization of the stainless steel substrate cleaning procedure. This led to an optimal oxide structure, the main requirement to get durable bonding which has a remarkable influence on the coating formation and the resulting hybrid bond strength. After optimizing the cleaning procedure, wet deposition of silane coupling agents was studied (Chapter 4). When correctly deposited, these molecules act as a covalent bridge between the substrate and the matrix, although many parameters profoundly affect the silane layer appearance and its bonding to the substrate surface. In the subsequent stage of the project polylysine nanoparticles (Chapter 5) were added to the interface to increase the number of anchoring points between the matrix and the coupling agent, to obtain a higher density and consequently a higher stiffness at the interphase. Finally the influence of carbon nanotubes (CNT) at the interface was studied (Chapter 6), as they may create gradient properties. This gradient may decrease the stiffness mismatch at the interphase, thereby increasing the mechanical performance of composites. Also matrix modifications may increase the mechanical properties of those hybrids, but this was beyond the time scope of this work. Figure 0.1 schematically represents the modifications possible when working with polymer-steel hybrids.

Insight into these hybrid materials requires a thorough chemical, physical and mechanical characterization. The silane typical sol-gel chemistry was followed by NMR. Next the influence of solution, depo-

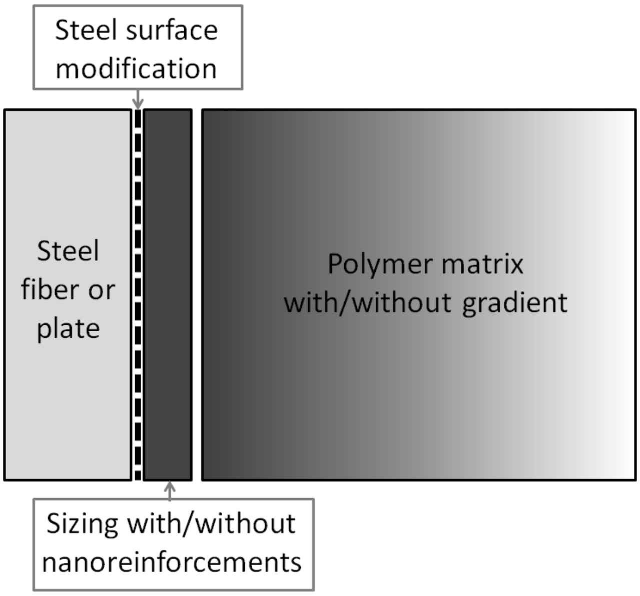

Figure 0.1: Schematic presentation of the possible modifications to polymer-steel systems.

sition and oven treatment conditions on the resulting steel coverage and silane appearance was monitored using e.g. electron and atomic force microscopy, spectroscopic ellipsometry and X-ray photoelectron spectroscopy. Polylysine and CNT depositions were studied again by means of electron microscopy. UV-visible spectroscopy and dynamic light scattering provided insight in CNT solutions and the influence of changing solution parameters. Throughout the work mechanical tests were conducted to support findings, while scanning electron microscopy allowed visualization of the most important fracture surfaces.

Chapter 1

Literature

1.1 Adhesion

1.1.1 Adhesion in General

According to Baldan, one talks of adhesion when a measurable amount of mechanical work is necessary to separate two surfaces of different chemical composition or shape [4]. This definition can be further refined on different levels as suggested by Bateup: macroscopically, adhesion is that state in which an interface is formed between two bodies such that mechanical work is transferred between the two. Microscopically, adhesion is defined as the state in which an interface is formed between two bodies such that the molecular forces resist separation [5]. The typical measure of the strength of an adhesive bond across an interface relates to the amount of energy to separate two surfaces. This involves the breaking of (chemical or physical) bonds, as well as the plastic deformation of one or both of the bulk materials on either side of the interface. In case of good adhesion, the energy necessary to break the bonds at the interface typically represents only a small fraction of the total energy necessary for the separation of the two surfaces, as most of the mechanical work is used to deform, under stress, the material adjacent to the interface. Therefore, the measured energy of adhesion not only depends on the ability of the interfacial bonds to sustain stress, but also on the amount of plastic deformation caused locally by this stress [6, 7].

Adhesives are defined as non-metallic substances capable of joining materials. They interact with the surface of the materials to be joined [8, 9]. Adhesively bonded joints offer many advantages over the more traditional joining techniques such as mechanical fastening and welding. They allow for a more uniform stress distribution and consequently an improved fatigue performance, but also a greater ability to join dissimilar materials. They can bind very thin to heavy sections without distortion and produce bonds with more homogeneous surfaces. Moreover they have the ability to join thin gauge metals and to construct honeycomb structures, which can be used for low-weight-high-strength structures with a cheaper production price, mainly due to reduced hand labor compared to other bonding techniques.

When applying adhesive bonding to join metallic to non-metallic structures, this can result in low-weight-high-strength hybrids with high joint stiffness and superior fatigue performance [4, 6, 9]. Nonetheless the use of adhesives for joining those materials also suffers from problems. Firstly there is a mismatch between the materials, in stiffness as well as in thermal expansion. The second problem concerns the low interfacial adhesion between dissimilar materials. Thirdly the interface may suffer from water sensitivity, illustrated by the fact that many epoxy adhesives loose strength in a humid environment [9].

1.1.2 Adhesion Mechanisms

Literature provides lots of information on adhesion and despite the lack of a universal theory, the complex phenomenon of adhesion generally can be summarized according to four mechanisms occurring at the interface: physical bonding (encompassing adsorption and electrostatic attraction), chemical bonding, (inter)diffusion and mechanical bonding or interlocking [4, 8, 10]. Most authors state that these mechanisms cannot occur isolated one from another, but that they overlap or take place simultaneously depending on the nature of the bodies brought together.

1.1.2.1 Physical Bonding

Physical bonding can be described according to the adsorption or wetting theory and the electrostatic attraction theory. It comprises forces corresponding to lower bond energies of approximately 8-20

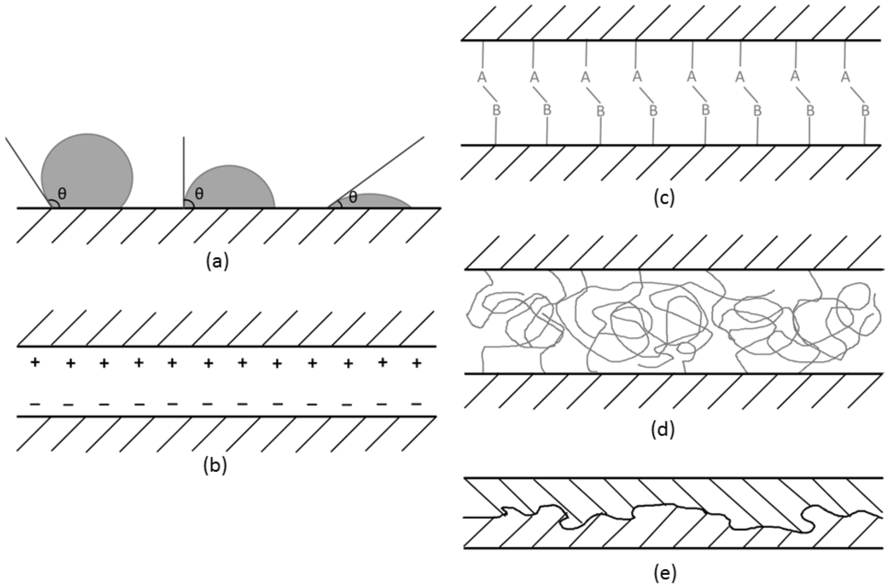

Figure 1.1: Schematic representation of adhesion mechanisms: The concept of wetting (a), electrostatic attraction (b), chemical (covalent) bonding (c), interdiffusion (d) and mechanical interlocking (e).

kJ/mol such as van der Waals and acid-base forces. The adsorption theory (Figure 1.1a) states that an adhesive must wet the surface to be bonded. Next it will adhere to the substrate because of interatomic and intermolecular forces established at the interface, provided that an intimate contact is achieved. This contact requires complete (spontaneous) spreading of the adhesive over the surface of the adherent, which can be fulfilled in the case of a sufficiently high surface energy of the substrate and a rather low surface energy of the liquid applied. This thermodynamic mechanism of adhesion only requires an equilibrium process at the interface, because in neutral environments such as air, thermodynamics will attempt to minimize the surface free energy [8]. In general it is believed that adsorption is the most important among the adhesion mechanisms, as good adhesion first of all requires intimate contact at the interface [4].

The electrostatic interaction theory (Figure 1.1b) postulates that as a result of the interaction between adhesive and adherent (with different band structures and thus sharing of mutual electrons), an electrostatically charged double layer of ions develops at the interface, provoking Coulomb attraction forces between net charges [9]. This theory applies e.g. for sulfonated polystyrene in combination with a glass substrate, but is also mentioned when combining epoxy and aluminum [11].

1.1.2.2 Chemical Bonding

Chemical bonding (Figure 1.1c) involves the formation of a chemical bond between compatible groups of the materials joined together. It concerns primary bonds (ionic, metallic, or covalent) with a strength in the order of 100-1000 kJ/mol, although some authors state that also stronger secondary bonds contribute to chemisorption and chemical bonding [4, 12]. Here the importance of the adsorption theory appears, as bonding energies drastically decrease with increasing intermolecular distance, indicating the importance of intimate contact between the surfaces brought together [4].

1.1.2.3 Interdiffusion

The interdiffusion theory of adhesion (Figure 1.1d) states that adhesion is due to mutual diffusion of (macro)molecules across the interface, leading to their entanglement. This creates an interphase where the clear boundary between the joined phases diffuses and eventually disappears, causing the development of a gradual transition zone from one phase to the other. In the case of two polymer phases brought together, the interdiffusion of adhesive and substrate requires adequate mobility of the chain segments, mutual solubility of the polymers and similar solubility parameters [10, 13].

1.1.2.4 Mechanical Interlocking

The interlocking theory (Figure 1.1e) is based on the mechanical anchorage of the adhesive in pores and irregularities of the adherent [4, 10, 13, 14]. According to this theory, roughening the surface increases the amount of anchoring points thereby increasing adhesion, especially when using a liquid adhesive onto a solid surface. Venables reported that mechanical interlocking is critical for good bond strength and long-term durability for metal-polymer bonds [15]. However, roughening a surface can be counterproductive as it can create defects and cracks, and may trap air bubbles at the bottom of crevices. These bubbles act as stress concentrators and promote failure in rigid adhesives because areas of high stress can lead to fracture propagating into the adhesive [4, 16]. Nonetheless it must be pointed out that some researchers believe roughening just increases the surface area, thereby increasing the opportunity to form adhesive bonds, as well as the energy dissipation after loading [8, 16, 17].

1.1.2.5 Adhesion Mechanisms in Composites

Adhesion and mechanical performance of composites are mainly influenced by three types of interaction: mechanical interlocking and physical and chemical bonding, all influencing each other [18]. Most pretreatments mainly influence the first two mechanisms, while application of adhesives or coupling agents rather induces chemical bonding or alters the critical surface tension, thereby changing the wetting behavior [8, 9].

1.2 Polymer-Steel Hybrids

1.2.1 Steel Surface

1.2.1.1 Stainless Steel in General

Many types of metal and steel can be found in literature, with a wide range of properties and applications. Stainless steel (SST) draws attention because of its excellent corrosion resistance. Combination with an appropriate matrix may lead to composites with excellent mechanical properties such as high strength and toughness combined with a relatively low weight.

In general SST consists of FeCr- and FeCrNi- (and FeCrMn-) based alloys with at least 10.5 wt% of chromium. Excellent corrosion resistance originates from a chromium-rich oxide layer of typically 1-3 nm thickness, which forms spontaneously under oxidizing conditions and is self-repairing in oxygen environments. It acts as a barrier against ion diffusion between the alloy and the ambient phase [19–21]. Theoretically the oxide layer consists of a wide array of chromium and iron oxides, with Cr_2O_3 and Fe_2O_3 being the most common ones. Formation of this passive layer takes place within seconds, and the low mobility of the atoms and ions limits the oxide film growth. The process of long range ordering of this layer lasts longer, typically several hours [19, 22, 23]. Formation of the so-called passive layer can be enhanced by the addition of oxide-forming elements, e.g. aluminum and silicon [19–21]. Oxidation treatments induce the formation of a base oxide layer with oxide islands growing on top, ultimately resulting in a thin, uniform and dense oxide layer [22].

1.2.1.2 Stainless Steel Properties

SST 304 (18/8), the substrate used in this work, is a highly alloyed steel containing 18 wt% of chromium and 8 wt% of nickel in combination with other alloying elements, mainly carbon, nitrogen, manganese, and copper. These elements lead to the formation of an austenitic phase, revealing the type of microstructure consisting of face centered cubic crystals as the primary phase [21]. This results in a material with a high stiffness [24]. Austenitic steel is non-magnetic and suited for cold deformation and welding. Carbon increases hardness, but decreases formability. Chromium induces corrosion resistance, while nickel stabilizes the austenitic structure (during cooling).

Upon annealing stainless steel, the surface becomes enriched in certain alloying elements such as chromium and nitrogen, resulting in a surface composition different from the bulk [19, 20, 25]. This results in the formation of a ductile material, with a high strain-to-failure [24]. Moreover annealing controls the final grain size and appearance of the substrate [21, 26].

In general steel is used to increase stiffness and strength of hybrids or composites. In the fibrous form also carbon and glass fiber offer these properties. However, steel fibers have the advantage of combining this stiffness with a high ductility, resulting in a higher strain-to-failure (20%). Although also spider silk and certain carbon nanotubes spun fibers can combine a high stiffness with a high strain-to-failure, they are both more rare and harder to produce in large quantities compared to steel fibers.

1.2.1.3 Surface Appearance

Every metal surface has its own characteristics, leading to specific behavior. The quality of the passive film depends on the alloying content of the metal, but is also influenced by other factors such as the fabrication process, the surface topography, the morphology and type of mechanical and chemical surface (pre)treatments [4]. Appropriate cleaning leads to experimentally determined concentrations of surface hydroxyl groups of 8, 13 and 9-13 groups per nm^2 for oxide covered silicon, chromium and iron respectively [24, 27].

The passive layer however is a dynamic system with its properties and stability largely influenced by its environment [4]. A metal substrate surface as such does not exist for a long time because of its high surface energy. After exposure to the atmosphere it is covered almost instantly with an oxide layer and a hydroxylated region formed by reaction with water. This layer still can be covered with strongly and weakly adsorbed water, organic carbon and contaminants from the surroundings (Figure 1.2) [21, 24, 28–30]. Moreover, sample transport also induces adsorption of silicon contaminants.

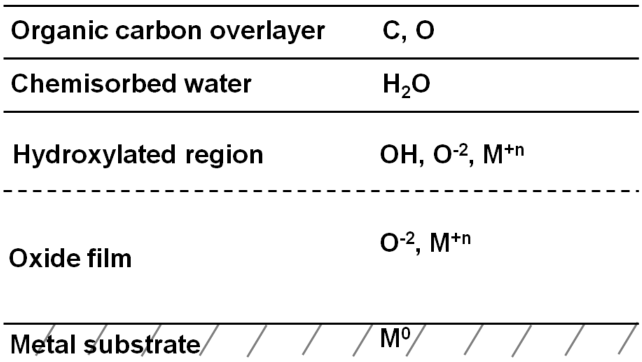

Figure 1.2: Schematic representation of a steel surface. The bulk material mainly comprises metallic elements (M^0). In contact with air these elements oxidize, which leads to (hydr)oxides on the surface, with (chemi)sorbed water and (carbon) contaminants on top of it.

Even freshly prepared surfaces have the above mentioned thin layer of carbon contaminants [31] which impedes the formation of chemical bonds [32]. To avoid this contaminant adsorption as much as possible, substrates should be used or stored in e.g. a desiccator immediately after cleaning [31, 33–35].

1.2.1.4 Substrate Pretreatments

Substrate pretreatment is probably the most important processing step governing the quality of an adhesively bonded joint [4]. The structure and chemical composition of the substrate surface affect the reactivity and adhesion properties of the surface, as well as the corrosion resistance [19]. Due to contaminants originating from substrate processing, application of a protective layer and adsorption from the surroundings, the surface must be cleaned or pretreated before use. A suitable surface pretreatment can produce a contaminant free surface, can roughen this surface macro- or microscopically and can produce a fresh, stable oxide layer. Moreover it can also increase the surface energy (through contaminant removal) and change the chemical composition (of the oxide) or introduce surface functional groups that enable modification in a next stage [4, 8, 14, 16, 20, 28, 35–38].

Selection of an appropriate treatment depends on different factors such as cost, (environmental) safety, effectiveness and stability of the treated surface, but also on speed, simplicity, environmental friendliness and the possibility for easy integration in a manufacturing process. Different types of pretreatment can increase the bond strength: physical, mechanical, (photo/electro)chemical, thermal or plasma treatment. Each of these has its own effect and improves adhesive bond performance by a different degree. This was also demonstrated by Liu et al. (Figure 1.3), who studied the influence of different substrate pretreatments. In most cases, care has to be taken to rinse the substrate after cleaning, to remove cleaning residues and to increase reproducibility.

Physical treatments in general remove species competing for adhesive adsorption later on: impurities (with low cohesive strength), lubricants and contaminants such as oil and grease. In this way the treatment increases the surface energy. However, while providing a clean surface, solvent degreasing may not promote the formation of acceptable surface conditions for longer term bond durability as it does not introduce new or extra coupling chemistry. Care is required to ensure that the solvent does not degrade the substrate surface structure [32].

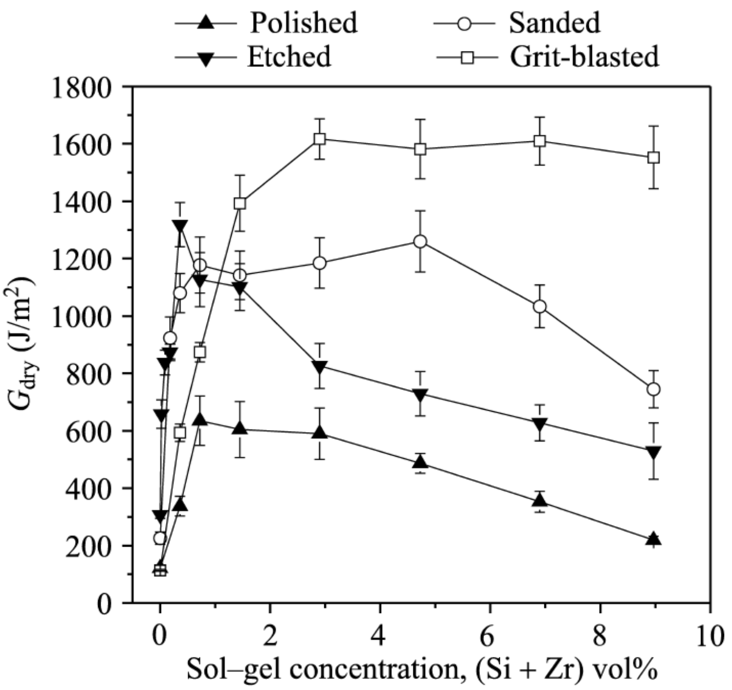

Figure 1.3: Fracture energy as a function of sol-gel precursor concentration and substrate pretreatment for epoxy/aluminium asymmetric double cantilever beam joints reinforced with sol-gel coatings as found by Liu et al. [39].

Mechanical treatments alter the surface roughness thereby increasing mechanical interlocking and resulting in a higher fracture energy due to a change in the stress state at the interface. Grit blasting e.g. removes contaminants such as mold release agents and roughens the surface. However, damage from overly aggressive abrasive blasting may lead to a decreased joint strength [40].

Chemical treatments introduce or increase the number of functional groups and etch away some material and thereby change the surface chemistry and topography. They can also directly influence the (hydr)oxide composition (Cr/Fe) as they produce a fresh stable oxide layer instead of the initial weak oxide layer.

1.2.2 Polymer Matrix

Polymers offer many advantages such as low weight, cost, abrasive, moisture and chemical resistance, toughness, strength, thermal and electrical insulation, formability and machinability. However, when compared to metals, polymeric materials lack stiffness and their physical properties are temperature-dependent.

In general the most used adhesive materials for structural stressed applications are thermosetting polymers [4]. Thermosetting polymers are those with a three-dimensional network structure, having atoms connected by strong covalent bonds. These materials generally result from an irreversible (condensation) polymerization, in which elevated temperatures, pressure, radiation or chemical agents tend to promote an irreversible reaction. Thermoplastic materials become pliable or moldable above a specific temperature and solidify again upon cooling [4, 14, 18, 41].

1.2.3 Hybrids

Polymer-steel hybrids offer unique multifunctionalities, e.g. as polymer-steel laminates and sandwich materials or as fiber-reinforced composites. This leads to a combination of stiffness, toughness and formability (mainly due to the steel) with the lightness, damping capacity, insulation,... of polymers. When using hybrids, optimization of the interactions occurring at the interface leads to an increase in failure resistance by preventing or delaying adhesive failure at the interphase. In practice the substrate as well as the matrix can be pretreated in different ways, all having the common purpose to increase strength and durability by promoting a more intimate bond via an increase of surface tension and roughness of the substrate surface or via a change of its chemistry [4, 8, 14].

1.2.3.1 Polymer-Steel Hybrids in Detail

Polymer-steel hybrids can offer best of both worlds and lead to savings in cost, weight and to improved fatigue resistance and dimensional stability. Moreover, they can sustain higher load levels when developed correctly. Today light weight-high strength and -high performance materials, originally developed for aerospace applications, can be found in different markets: computer and electronics, construction, aircraft and automobile industries [4, 32, 42]. Structural adhesive bonding is used e.g. to stiffen structures against buckling or to bond skin-to-core in metallic honeycomb structures such as elevators, spoilers,... [32]. Steel fibers offer the advantage of high ductility compared to classical carbon and glass fibers, resulting in a higher (composite) strain-to-failure (up to 22%, respectively 10 and 5 times higher compared to carbon and glass fibers) combined with a high stiffness.

However the different characteristics of metals and polymers offering advantages in structural applications, also pose the biggest challenge. The large difference in physical and chemical characteristics leads to a lack of adhesion and failure resistance after joining both [43]. Metal cohesive energies are much higher compared to polymers and also the stiffness of the former exceeds that of the latter (respectively 200 GPa and 1-3 GPa), causing stress concentrations at or near the interphase. Thermal expansion of metals is around 10 times smaller than that of polymers. This enhances the problem of stress concentrations due to the mismatch at the interface, especially after cooling, but also leads to cracks in coating materials resulting in a lower overall performance [29]. This results in an early onset of matrix cracks and substrate matrix debonding.

Optimized interfacial interactions decrease adhesive failure at the interphase [44]. In practice the substrate as well as the matrix can be (pre)treated in many different ways (see Section 1.2.1.4). Addition of tougheners to the matrix or the interphase can result in discouraged crack propagation and better performance [13]. Most pretreatments however, have the common purpose of increasing strength and durability by promoting a more intimate bond via an increase of surface energy and roughness of the substrate surface or via a change of its chemistry [4, 8, 14]. Coupling agents applied during chemical treatments improve adhesion between the constituents, and especially silanes show up when bonding organic materials to metallic substrates, replacing more toxic chromium pretreatments [6].

1.2.3.2 Interphase

When applying a polymer matrix to an inorganic substrate, the substrate-matrix interaction creates an interphase that has different chemical, physical and mechanical properties from the bulk polymer [29, 45]. Sharpe was the first to define the interphase as "A transition zone between the surface of a substrate and the bulk of a polymer that is solidified against the substrate". Unfortunately, the boundaries of the interphase are difficult to define, forming a complex diffusion zone and resulting in a gradient of properties that may extend from a few nm to a few thousand of nm, depending on the system [7]. Despite the limited thickness of the interphasial region, it directly influences the ability of the matrix to transfer load to the steel, and thus its structure and properties are dominant factors governing the overall composite properties and performance [45]. In general the interfacial bonding strength increases with reduced thickness of the adhesive layer as stress is able to be transferred through the interface more easily, although too thin layers may cause stress concentrations [8].

Stiff interphases provide very efficient stress transfer, although they support brittle failure and reduce fracture toughness of the interphase, which results in cracking and consequently limits damage tolerance. Tough interphases slightly reduce the effectiveness of stress transfer, but they can provide a significant enhancement of damage tolerance. Moreover, tough interphases are less sensitive to the direction of external loading compared to stiffer ones [28, 29, 46].

Optimizing the properties of the interphase is a crucial task that influences the overall quality of composites by deviating the major crack path away from the surface, towards the interphase or matrix region. This can be done in two ways; by adding nano-engineered sizings to the steel surface, in this way increasing chemical or physical bonding, or by creating gradient properties in the polymer neighboring the substrate surface, thereby decreasing the stiffness mismatch.

Introduction of a coupling agent, such as a silane, changes the failure mechanism from pure interfacial debonding to cohesive failure within the matrix (or the interphase in case of thicker coupling layers). It may also allow plastic yielding of the matrix to occur [17]. Creation of a gradient interphase can decrease the sudden change in mechanical properties at the interface, thereby decreasing stress concentrations and improving material properties.

1.3 Chemical Bonding: Silane Coupling Agents

1.3.1 Silane Structure and Reactions

The general structure of monosilanes can be depicted as (Y-R)$_{4-n}$-Si-X$_n$, with Y representing an organofunctional group, X a hydrolysable group, mostly alkoxy or chlorine, R a spacer or linker group and Si a silicon atom. The organofunctional group is chosen to improve reactivity or compatibility with the polymer matrix. The hydrolysable groups are merely intermediates in the formation of silanol groups for bonding to inorganic (hydroxylated) surfaces. As can be seen from the structure, both ends of the molecule can undergo chemical reactions, either separately or simultaneously. Under proper control of environmental conditions the hydrolysable groups can be reacted without altering the Y group or vice versa. Bis-silanes have the general formula X_3-Si-$(CH_2)_n$-R-$(CH_2)_n$-Si-X_3, with R in this case an organic linker or an organofunctionality. These molecules clearly have a larger number of hydrolysable groups compared to monosilanes and are mainly used as crosslinkers for other silanes or in corrosion resistance applications [47].

Silanes differ in physical and chemical characteristics, illustrating the importance of choosing appropriately. Nonetheless some silanes repeatedly show up in literature: 3-glycidoxypropyltrimethoxysilane (GPS), 3-aminopropyltriethoxysilane (APS) and 1,2-bis-(triethoxysilyl)-ethane (BTSE) (Figure 1.4). GPS contains an epoxy group that generally has less affinity for the substrate, but ring opening of this group during handling should be taken into account as it lowers reactivity towards the matrix later on. Under standard conditions the ring will still be unopened during hydrolysis, due to its slower kinetics compared to the alkoxy group. However, when curing the silane at an elevated temperature, ring opening may speed up [48, 49]. APS has an aminogroup, able to interact with different matrices. Under inappropriate conditions this group may also interact with the substrate. BTSE contains no organofunctional group and is not chosen for its interaction with a specific matrix.

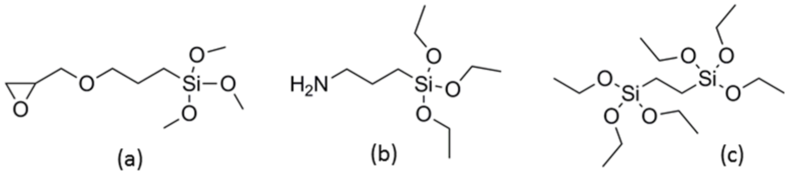

Figure 1.4: Frequently used silanes: GPS (a), APS (b) and BTSE (c).

In order to obtain maximum silane adhesion to an inorganic substrate the silane alkoxy groups first have to hydrolyze before use in order to transform them into hydroxyl groups, thereby releasing an alcohol molecule (Figure 1.5a (left)). After this the silanol (SiOH) groups adsorb to the metal (hydroxide) surface by hydrogen bonds upon contact with the substrate (Figure 1.5b). Condensation can take place during a drying or curing operation, producing a covalent linkage between silane molecules forming a siloxane (Si-O-Si) network (self-condensation) (Figure 1.5a (right)) or between a silane molecule and the inorganic surface, anchoring the silane molecule to the substrate by a metallosiloxane (M-O-Si) bond (Figure 1.5c). Both condensation reactions can occur simultaneously and the water released can participate again in the hydrolysis reaction of other molecules. From Figure 1.5 it is clear that self-condensation should be minimized as it consumes hydroxyl groups necessary to couple to the steel substrate, and leads to the formation of clusters forming weak points in composites. The time span that starts after obtaining sufficient hydrolysis and ends when self-condensation becomes numerous, is called the working window, and is influenced by different parameters (Section 1.3.3.1). Preferably the solution is handled during this time span. Meanwhile the organofunctional group remains available for covalent reaction or physical interaction with the matrix [9, 14, 20].

Despite the existence of 3 hydrolysis steps per trialkoxy species, different molecules undergo different steps at the same time. Already after the first hydrolysis step competition between hydrolysis and self-condensation appears, depending on the conditions used [49–51]. This does not state a problem when choosing appropriate conditions: sufficient bonding to the substrate does not require complete or maximum hydrolysis. Nonetheless a certain amount of active silanol groups should

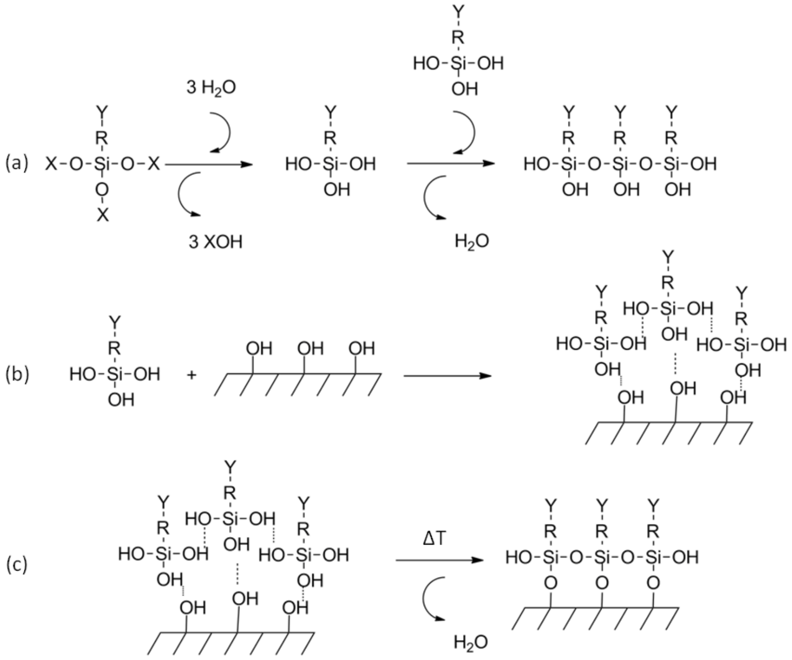

Figure 1.5: Silane reactions: hydrolysis (left), self-condensation (right) (a), adsorption on an inorganic surface by hydrogen bonding (b) and condensation to an inorganic surface (in combination with self-condensation) (c).

be generated in solution in order to obtain sufficient bonding to/wetting of the substrate [49, 52]. The presence of dimers in solution probably is not as detrimental for adhesion properties as the presence of oligomers or entire networks.

Usually only one oxygen atom from each silicon center is bound to the substrate surface, while the other silanol groups condense with other silanol groups or remain in the free form [50, 51, 53, 54]. The degree of order in the silane layer increases with the number of siloxane bonds, although in general complete crosslinking cannot occur due to steric hindrance [55]. In an ideal monolayer about 67% of the hydroxyls are involved in a siloxane bond [56, 57]. Some authors mention that alkoxygroups can condense to the inorganic surface directly, and that alkoxy silane radicals may condense with a silanol group. Nonetheless these reactions are more difficult and slower compared to the condensation reaction between hydrolyzed species [58–60].

Upon handling it should be taken into account that many silanes have hydrophobic characteristics initially, making them insoluble in water unless they possess strongly hydrophilic groups (such as primary or secondary amines). Upon hydrolysis they become more or even highly hydrophilic because of the silanol groups formed. After curing and the formation of a siloxane network, the hydrophobicity of the parent silane is regained.

1.3.2 Silanes in Composites

Silane coupling agents can be used to join polymeric and inorganic materials, in order to obtain composites with enhanced properties including thermal endurance, chemical or moisture resistance, increased mechanical strength, durability and electrical performance [58, 61–63]. According to literature the fracture toughness improves after addition of silanes by changing crack propagation, thereby delaying failure [61, 64]. However, the properties and quality of silane layers depends strongly on the deposition conditions and can vary greatly between applications [20]. In general silane coupling agents result in a chemical bonding interaction, forming a covalent bridge that links together the organic and inorganic components of the joint [9], although according to Mohseni et al. the increase in adhesion can be explained by the relative increase in surface free energy of the substrates compared to the blank sample without silane treatment. For sure different adhesion mechanisms play an important role [65].

It is believed that the higher the density of metallosiloxane (M-O-Si) bonds formed at the interface, the stronger the interfacial adhesion between the silane film and the substrate. Higher hydroxyl densities thus increase adhesion, although maximum one silanol group per silane molecule can attach to the substrate, which occurs in the ideal case. Mostly only occasional bonding to the substrate takes place, resulting in weaker bonding [50, 63]. However, Basin noted that as the density of chemical bonds increases at the contact zone, the adhesion strength may pass through a maximum value because of an increased concentration of mechanical stresses at the interface at a certain amount of bonds [17].

The thickness of the silane layer partially determines the layer properties, as well as the final joint properties. Most authors state that adhesion properties increase with decreasing layer thickness. Also Young's modulus would increase with decreasing thickness, which can be ascribed to the reduction of the molecular mobility of chains near a solid surface [2, 46, 66].

1.3.2.1 Silane-Metal Interaction

Silane coupling agents modify the substrate surface in order to change the nature of interfacial interactions and thus adhesion via a complex set of factors. When studying silane-substrate interactions, the chemical bonding theory shows up most frequently, as silanes primarily promote covalent bonding [6, 61, 65]. This assumes the formation of a (reversible) covalent (or ionic) metallosiloxane bond by condensation between the hydroxyl groups of the substrate surface and the silanol groups of the hydrolyzed silane. This has indeed been proven for iron and different types of steel. The chemical stability of those bonds largely depends on the substrate and its pretreatment [52, 63, 67].

The adsorption theory also plays an important role in explaining silane-metal adhesion. Different types of molecular interactions (van der Waals forces and acid-base interactions with the oxides on the metal surface) require wetting and intimate contact at the interface. A freshly cleaned metal surface should be wetted sufficiently by the silane solution. Especially alcoholic solutions have good wetting characteristics, due to their lower surface tension compared to purely aqueous solutions [68, 69].

Incompletely coordinated metal cations can act as electron-accepting Lewis sites, e.g. towards amine groups of an APS molecule [25, 67]. In case of a porous substrate structure, mechanical interlocking can also take place [16, 39, 69].

Care has to be taken when using silanes with a heteroatom as this atom may also be able to interact with the substrate surface. The aminosilane nitrogen atom can act as a base towards the hydroxyl surface [65, 70]. The pH of the silane solution determines the charge of the substrate surface as well as of the silane and thus the affinity and orientation of the silane after application. Upside-down orientation not only reduces the amount of available functional groups to interact with the matrix, it also may lower the surface energy [33, 71]. Obviously this orientation decreases hybrid performance after joining the silane coated substrate with a polymer matrix. Second, care has to be taken to work within the stability regime of both the substrate and the silane. From this it is clear that a non-matching choice of the pH would lead to inferior or even no adhesion between the silane and the substrate.

1.3.2.2 Silane-Polymer Interaction

Silane coupling agents not only interact with the steel substrate, but also with the polymer matrix, making it act as a (covalent) bridge between both [14, 41, 72, 73]. Originally silane coupling agents were designed for thermoset matrices, thereby selecting the organofunctional group of the silane for optimal chemical reactivity with the resin during curing [47, 67]. The effectiveness as a coupling agent parallels this reactivity [61, 63, 74]. The several 100-fold difference in the performance of different silanes with given polymers demonstrates the need for a proper match [41, 75]. Acid-base interactions also play an important role during coupling, e.g. between acid epoxy and alkaline APS [57]. Moreover reactions between the matrix and the (non-ideal layer of) silane probably can create a crosslinked interpenetrating network linking the substrate to the matrix [9, 41, 76, 77]. This requires sufficiently high compatibility in terms of reactivity, solubility and surface energies and wettability, which are influenced by the type of the functional groups [6, 78], especially when working with thermoplastics.

In contrast to the limited improvement in the mechanical properties of composites with just good physical compatibility (molecular entanglement, acid-base interactions), chemical bonding substantially improves the interfacial adhesion of silanes and matrices. Nonetheless it should be noted that a strong coupling between a reinforcing constituent and the matrix can result in a brittle composite, especially with thermoset matrices [41, 64, 79].

1.3.2.3 Wet Chemical Application of Silanes

The exact appearance and properties of the silane film formed on the steel substrate do not only depend on the silane used, but also on its deposition method and the conditions during and after deposition. Most of the time silane coating takes place by wet chemical methods because of their handling speed, lack of necessity for specific equipment and thus low cost [63]. The method used in this work (Figure 1.6) consists of the preparation of a silane solution which has to be used within its working window (Section 1.3.1). After dipping a cleaned substrate in this solution, excess can be rinsed off in water and/or alcohol, blown away or gently wiped off. Finally a condensation step follows (Section 1.3.1), most often at an elevated temperature (before application of the matrix). From this description the largest drawbacks of wet chemical application become clear. It is a multistage process requiring control of many parameters, and involving the use of solvents and the creation of waste flows.

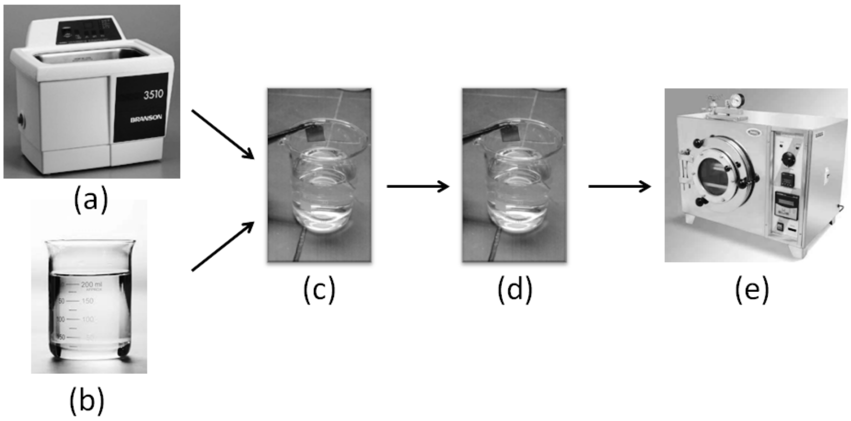

Figure 1.6: Schematic representation of wet chemical silane coating, starting with cleaning of the substrate (a) and silane solution preparation (b), followed by dipping the substrate in the solution (c) and optional rinsing (in ethanol) (d). Next this ensemble is oven treated to complete condensation reactions (e).

1.3.3 Silane Coating Parameters

1.3.3.1 Solution Parameters

Application of a silane layer starts with the preparation of a solution with different tunable parameters: the type and concentration of the silane, the pH and the solvent and ratios thereof when using a binary mixture. The polymer matrix used determines the silane chosen, as interaction between both is necessary to obtain sufficient coupling. A catalyst or change in pH can improve solution stability or change hydrolysis and condensation kinetics, thereby influencing the working window [80]. Hydrolysis should generate sufficient silanol groups to couple to the substrate. Meanwhile self-condensation and precipitation should be avoided as they decrease the number of silanol groups able to react with and adsorb on the substrate during dipping (Figure 1.5).

The pH influences kinetics as shown in Figure 1.7. Despite the unclear underlying mechanisms, it is generally accepted that hydrolysis rates increase in a more alkaline or more acid environment. Intuitively this increase in silanol entities should speed up self-condensation and most authors do mention an increase in condensation kinetics at a more alkaline pH. Nonetheless self-condensation kinetics slow down in acid environments, due to more stable silanol entities [81, 82]. Silanes bearing amino functionalities display autocatalytic behavior, especially regarding hydrolysis. Moreover the kinetics of other silane systems can increase by the addition of aminosilanes [47, 81, 83]. Despite the relative stability of silanol groups under acid conditions, amines lose their autocatalytic activity in acid media. This leads to slower and incomplete hydrolysis [84].

The solvent influences hydrolysis and condensation kinetics. Different types of solvent can be found, e.g. toluene, dichlorobenzene, dioxane, water, alcohols or a mixture thereof in varying ratios. Alcoholic solvents may give rise to transetherification reactions, counteracting hydrolysis by the exchange of an alkoxy or silanol group for the alkoxygroup of the solvent [1, 85]. Water may be preferred from an environmental and health point of view, and according to Vandenberg et al. APS deposition from an aqueous solution leads to thinner and more homogeneous films compared to deposition from e.g. toluene, acetone, chloroform,... [86]

Reactions in Figure 1.5 demonstrate the need for water during hydrolysis. Abel et al. already stated that a critical quantity of water has to be present to allow hydrolysis to take place [87]. However when using APS (or other hydrophilic silanes), traces of water in the solvent as well as environmental and substrate adsorbed water can assist hydrolysis to proceed [58, 60, 88]. Aminosilanes in general can reach

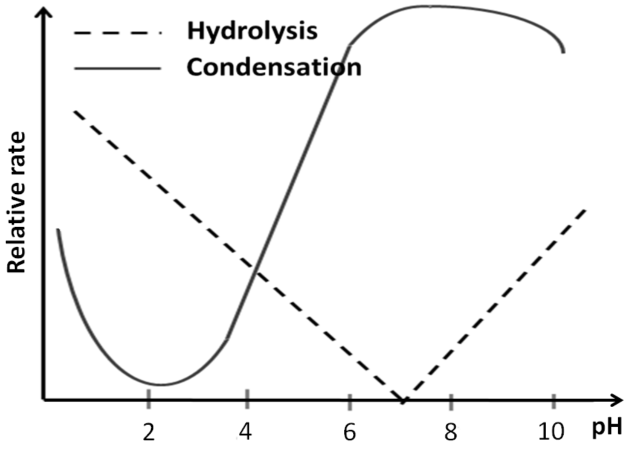

Figure 1.7: Hydrolysis and condensation rates of silanes as a function of the solution pH as found by Pan [1].

full hydrolysis when deposited from an alcoholic solution, without the addition of water, not only because of their hydrophilicity, but also because of their autocatalytic nature [47, 59, 89–91]. Abel et al. showed that for organofunctional silanes without an amine group, e.g. GPS, no significant hydrolysis occurs if the solvent mixture used contains a major proportion of alcohol (90%) because of alcoholysis/transetherification. Also in aqueous solutions hydrolysis rates can be very slow, decreasing self-condensation as well as silane uptake on the substrate upon dipping [54, 58, 60, 87]. The exact amount of water needed to obtain sufficient hydrolysis in combination with a minimum of self-condensation depends on the silane and conditions used [81, 92]. Note here that the epoxy group is not necessarily inert in aqueous solutions, but may undergo hydrolysis resulting in a diol. However, epoxy group hydrolysis proceeds at much lower rates than methoxy hydrolysis, so in general ring opening can be ignored [93].

In solutions of (aqueous) alcohols alkoxy exchange with the solvent may accompany hydrolysis, but only after far advanced hydrolysis [47]. Probably this reaction takes place within the entire pH window, but it would become faster than hydrolysis and condensation only at low pH, as was shown for APS [47]. According to Roche et al. the extent of transetherification remains low under all circumstances, having ignorable influence on the final silane film properties [84, 94].

Usually silane concentrations range from 0.5 up to 4% by weight when used as a coupling agent. This range leads to good solubilization and control over the final film. The concentration largely influences hydrolysis and even more self-condensation rates, and controls the final film thickness on the substrate. Together with crosslink density and molecular orientation this determines the quality and mechanical properties of the film [20, 51, 75, 95]. Low concentrations cause incomplete coverage of the substrate. High concentrations and the concomitantly increased amount of oligomers and physisorbed molecules lead to thicker films and create porous, non-uniform films and clusters as the high number of molecules may impede correct accommodation on the substrate surface (Figure 1.8) [96–98]. Moreover microscopic cracks can arise upon drying because of the fixed and less mobile clusters on the substrate, reducing the ability for stress relaxation [56, 65]. These phenomena deteriorate mechanical properties by promoting defect formation at the silane interface [83, 99]. Lower concentrations and lower hydrolysis rates cause thinner and more uniform films. Those are crosslinked to a higher extent, which should result in higher adhesion strengths [1, 39]. However, full crosslinking of the silane layer can decrease interfacial adhesion, probably because it impedes interpenetration with the matrix.

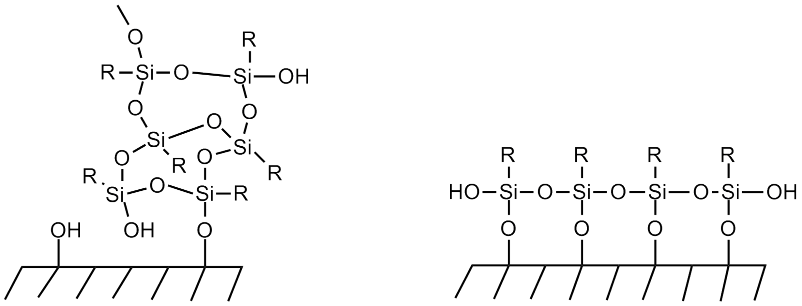

Figure 1.8: Incorrect accommodation of a silane cluster on a steel substrate after self-condensation in solution (left). Formation of an ideal silane monolayer on a steel substrate in the absence of self-condensation in solution (right).

For aminosilanes in dilute solutions more open silanol structures dominate, while in concentrated solutions low molar mass cage structures are favored. This leads to an increased probability for the formation of an oriented monolayer when depositing from a dilute solution [47]. Moreover, at higher concentrations the silanol groups of the low molecular mass siloxanols are stabilized by hydrogen bonding to amine groups, decreasing condensation [85].

According to Tsai et al. a linear relationship exists between the degree of hydrolysis (and subsequent condensation) and the time after preparation, although the exact working window depends on the structure of the silane used as well as on pH, solvent,... [1, 100] Silanization requires good stability of the solution as condensation reactions and resulting precipitation of insoluble (polymeric) siloxane gel and oligomeric structures are detrimental for the silane adsorption on the substrate. Upon ageing self-condensation in unstable solutions decreases the foreseen silane and silanol concentration, leading to underperforming films [14, 50, 57, 81].

Literature mentions largely deviating values concerning silane solution kinetics. However, (hydrolysis) rates strongly depend on impurities in the system, and characterization of each individual system is mandatory [54, 83, 101].

1.3.3.2 Deposition Parameters

After steel cleaning and preparation of the silane solution, silane layer deposition takes place followed by an oven treatment. It is generally accepted that the hydrolyzed silane molecules physically adsorb onto the hydroxyl covered inorganic surface forming hydrogen bonds, as shown in Figure 1.5. Maximum one single silanol group per molecule binds to the substrate surface, while the remaining silanol groups condense with each other or remain in the free form [51, 54, 88, 91]. For wet chemical silane deposition, the silane solution can be brushed or spin coated on the substrate, but for ease of handling dipping with slightly agitated move was preferred during this work. For this type of deposition both dipping and rinsing parameters can be varied.

The substrate is dipped in the silane solution, where the exact handling maneuver and dipping time can be varied as desired. The coupling agent does not necessarily adsorb as a monolayer. First of all this is often inhibited by the formation of dimers and oligomers in solution, depending on the solution parameters. Second, different layers can be adsorbed, depending on the dipping time and maneuver. Most authors assume no immediate formation of covalent bonds to the substrate (except for BTSE) during dipping, although some authors do assume immediate covalent bond formation [102, 103]. According to the prevailing assumption an interphase with stronger chemisorbed and weaker physisorbed layers is formed instead of a single layer [104].

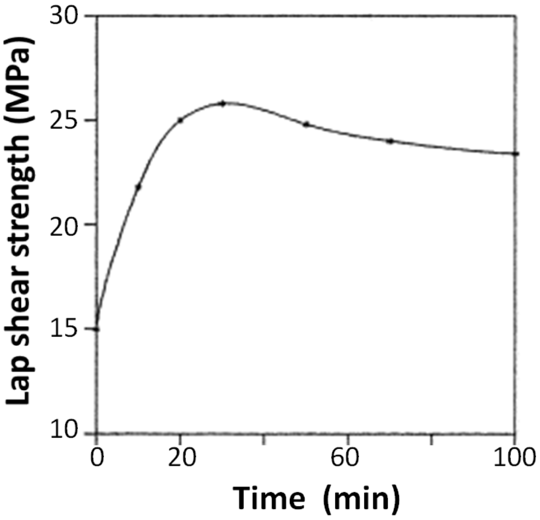

Figure 1.9: Effect of the dipping time in an APS solution on the adhesion strength of copper-epoxy joints as found by Gu et al. [2].

The longer the dipping time, the thicker the physisorbed layer on top of the more strongly anchored chemisorbed layer [52]. This leads to a thicker silane layer after curing and a decreased mechanical strength of resulting composites [2, 65, 86]. However, some authors assume that the dipping time has no influence on the silane adsorption and on the resulting composite performance for intermediate dipping times up to 30 min. They state that silane adsorption onto the metal surface is instantaneous via the formation of hydrogen bonds [97, 105]. Gu et al. on the contrary found that the dipping time does have an influence on the film thickness and resulting adhesion (although in the absence of rinsing) (Figure 1.9). They obtained highest shear strength for an immersion time of 3 min of a copper sample in an APS solution before application of an epoxy matrix. Their evidence indicates that the substrates tend to be etched during immersion, forming copper ions that influence adhesion [2]. Witucki et al. stated that 1 to 2 min of dipping should be taken into account to allow sufficient silane accumulation at the surface [78].

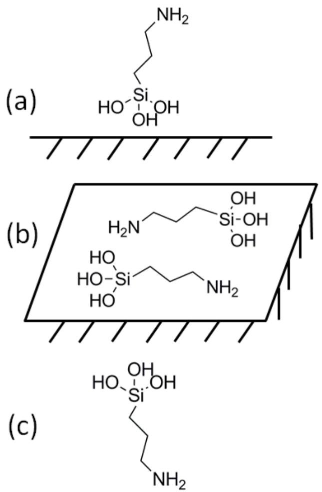

Figure 1.10: Possible molecular orientations of a single hydrolyzed APS molecule after absorption on the SST substrate: H-bonding between the silanol groups and the substrate surface (a), H-bonding of both a silanol group and the amine group to the substrate surface, with the silane lying parallel to the surface (b) and H-bonding between the amine group and the substrate surface (c). For clarity no charges are displayed.

Care has to be taken as literature also mentions 'upside-down' (Figure 1.10) (organofunctional) silanol adsorption at shorter dipping times as well as insufficient adsorption to cover the entire substrate surface, causing inferior adhesion strength [2, 33, 71, 106]. The exact orientation of the silane on the SST substrate may also be influenced by other parameters, mainly the solution pH. Figure 1.10 shows the different orientation options for a single APS molecule adsorbed on an inorganic surface.

After dipping the substrate in the silane solution, excess silane can be rinsed off by dipping the substrate again in e.g. pure water, alcohol or in a mixture of both. This mainly removes the physisorbed silane and the amount remaining is affected by the solvent, the pH and the duration of the rinsing process. Removing weakly bound molecules leads to less vertical self-condensation and a relatively higher degree of interaction with the substrate during oven treatment. Authors believing in covalent bond formation during dipping, state that the non-adherent, hydrogen bonded silane is removed, whereas the covalently bonded molecules remain attached [13, 102, 103]. However, both adsorption theories (covalent and hydrogen bonding) give the same result after oven treatment. They agree about the difference between the layer closest to the substrate with a stronger and more chemical adsorption, and the layer on top being less ordered and only weakly bound.

Abel et al. compared the absence of rinsing with water and methanol rinsing for 30 s after APS deposition from a 6% solution and found very different adsorption behavior, film thickness and film chemistry for every protocol. Water rinsing of deposited APS films would induce a chemical reaction at the outer surface, leading to the formation of a polysiloxane-like layer as a result of the rapid hydrolysis and subsequent polymerization, forming a film of 3 nm thickness. Methanol rinsed films have a thickness of only 2.1 nm, while unrinsed films obviously have the highest thickness (> 4 nm) [87]. Also Puomi et al. acknowledged the influence of the rinsing solvent. They stated that large amounts of APS films can be rinsed off by water, especially at a more alkaline (natural) pH, leaving behind only a fraction of the initial silane [85]. Cave and Kinloch obtained improved adhesive strength and durability with organofunctional silanes when using rinsed samples, in contrast to findings of Gu et al.. Nonetheless in the work of Gu et al. the adhesive strength without rinsing still was markedly higher compared to untreated joints. Disagreements may be due to different starting solutions, ageing times, heating temperatures or different substrate treatments [2, 107].

Regarding the influence of rinsing BTSE forms an exception, as it seems that no BTSE can be removed. This probably relates to the

BTSE structure with 6 silanol groups per molecule, resulting in increased bonding with the substrate and other silane molecules after dipping [57, 61, 85, 108]. When ageing those samples after deposition (before oven treatment) less silane can be rinsed off due to self-condensation reactions taking place between (chemi- and) physisorbed silane molecules [2, 107].

1.3.3.3 Oven Conditions

Most literature agrees that silane adsorption initially occurs through hydrogen bonding and that after the rinsing step a condensation/curing step should take place, linking the substrate and silane covalently (Figure 1.5). Moreover this treatment also increases the degree of self-condensation and can be performed by leaving the deposited film to air, by blow drying, by spin coating or by using plasma, infrared or (vacuum)oven curing. The nature of the drying process has a large influence on the thickness and appearance of the silane layer, and high pressure air blow drying with compressed air e.g. leads to much thinner films compared to low (nitrogen) pressure drying. The rotating spinning method gives rise to very homogeneous silane films [85, 105, 109]. During this and most experimental wet coating work, an oven treatment takes care of the condensation step due to its ease of accessability. However, this also means that many parameters can influence the resulting layer, such as the presence or absence of a vacuum, the residence time and the oven temperature.

A vacuum increases the solvent evacuation and the removal of the molecules released during condensation. Treatment at elevated temperatures speeds up reaction kinetics. Moreover it not only converts physical bonds into covalent metallosiloxane linkages, it also further densifies the partially crosslinked silane network [85, 98, 110]. Concomitant reorganization of the adsorbed layers leads to a more efficient chemical condensation either with the surface or between the (physisorbed) silane layers, and can change the overall adhesion performance [39, 53]. In the meantime solvents, water and reaction byproducts can be driven out of the film faster [31, 89, 99, 105, 111]. In general it is assumed that longer curing times have a similar effect as a further increase of the condensation temperature [112]. In the presence of a vacuum the oven temperature or the residence time can be lowered.

The formation of metallosiloxane bonds and consequential strong adhesive bonding requires heating or further treatment, whereas self-condensation occurs already at room temperature. However, elevated temperatures do speed up self-condensation and increase the degree of crosslinking [20, 48, 113]. Riegel et al. stated that also hydrolysis rates increase with temperature. This would be even more temperature dependent than condensation processes, although in the work done maximum hydrolysis was already obtained before deposition [114]. The increased amount of self-condensation thins down the film in the first stage of heating because of network formation, after which more crosslinking takes place. Probably the loss of volatile components, or even evaporation of the silane molecules themselves (e.g. for GPS) also partially contribute to this film thinning. The increased film density leads to a more uniform, harder, and less porous film [89, 97, 109, 115, 116]. In case of over-crosslinking however, films show too brittle behavior and a lower interpenetration with the matrix later on. This decreases the adhesive strength [98, 109].

According to Le Pen et al. resulting films are not homogeneous because of a different degree of reticulation at the interfacial layer close to the substrate surface compared to the bulk of the film [113]. Confinement, frustration or more rapid crosslinking at the interface causes a lower extent of crosslinking [14, 46, 91, 117].

When curing the silane layer, care has to be taken not do degrade the film because of the higher temperatures reached [1, 98, 118]. Gamma-substituted silanes, the coupling agents mostly used, have sufficient thermal stability to withstand short term process conditions of 350°C and long term continuous exposure to at least 160°C in ambient atmosphere (or to higher temperatures for an inert atmosphere). Also the specific substitution plays a significant role in thermal stability. Electron withdrawing substituents reduce thermal stability, while electropositive groups have an enhancing effect [1, 111, 119].

APS binds to a substrate surface by (weaker) hydrogen bonds which have to be treated at at least 50°C to increase the bond stability [85, 89, 99]. Because of their hydrophilic character the resulting films contain more entrapped water, but probably also adsorbed CO_2 which can be desorbed by heating above 100°C [58, 89]. Most literature mentions minimum oven temperatures between 100 and 120°C to obtain full crosslinking and maximum adhesion and durability [53, 58, 62, 80, 120]. Some researchers state that longer curing times (of about 3 h) are needed to reach less porous and more stable aminosilane films. In this way upside down adsorbed molecules (Section 1.3.3.2) have the possibility to flip their position [58, 68, 99]. Pena-Alonso mentioned that although densification increases during curing, no highly crosslinked APS structures can be formed because of steric hindrance caused by the non-hydrolysable aminopropyl group [59]. Aminosilanes are mentioned to remain stable up to 370°C [30, 112], but oxidation of the amine group above 160-180°C should be taken into account as it reduces silane-matrix interactions and thus adhesion strength [1, 2, 84].

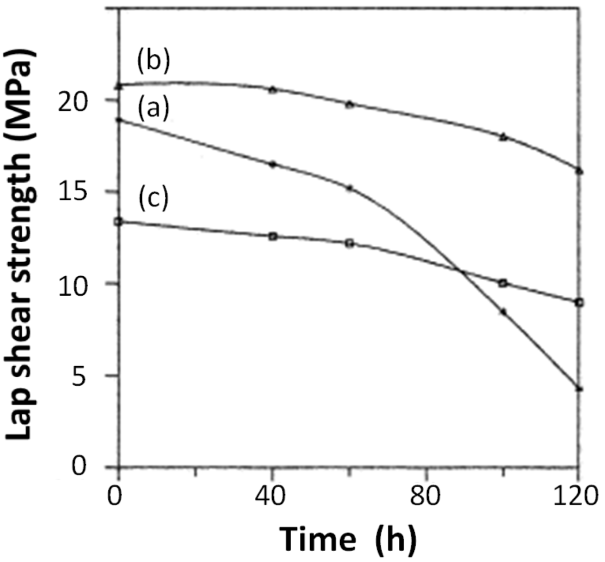

Figure 1.11: Durability dependence of APS bonded copper-epoxy joints in boiling water on the temperature of the oven treatment as found by Gu et al.: 25°C for 7 days (a), 110°C for 1 h (b) and 170°C for 1 h (c) [2].

Najari et al. tested zinc coated with an APS layer, with both the adherence and coverage increasing steadily with the oven temperature ranging from room temperature to about 160°C. The presence of several non-cohesive silane layers on the zinc surface at room temperature probably results in low adherence [53]. Also Gu et al. observed higher mechanical strength (of the bulk APS) and increased bond durability after heating APS coated substrates. This is shown in Figure 1.11, with the horizontal axis denoting the dipping time in boiling water after silane coating (and not the oven residence time) [2].

As stated before, Puomi et al. claimed that BTSE instantaneously forms covalent, hydrolysis-resistant bonds to both aluminum and iron, while others state that crosslinking of a bulk BTSE film cannot be completed at 100°C, even after long curing times [85, 97, 105, 121]. For GPS the amount of siloxane bonds and crosslinks also should increase with temperature, while at room temperature the drying process cannot be completed [58, 73]. Literature enumerates different curing temperatures for GPS, generally varying from 90 up to 180°C. Nonetheless some researchers report treatment at 80°C, although reactions would proceed 4 times slower when reducing the temperature from 100°C to 100°C [31, 58, 122]. Deflorian et al. found that GPS films deposited on aluminum or zinc substrates and reacted at 100°C do not result in a uniform layer, while samples treated at 200°C do show a uniform distribution. The faster curing process at 200°C seems to cause an immediate increase in viscosity (because of increased average molecular weight) that dominates the capillary forces tending to form silane drops. This leads to a surface (entirely) covered with the silane, as is the case immediately after immersion [123]. When using GPS, care has to be taken again not to oxidize the functional group. Most authors agree that oxidation of the epoxy group only occurs above 250°C [98, 109, 124]. Gledhill et al. studied GPS on a mild steel alloy and strongly suggested that room temperature drying conditions promoted greater durability enhancing effects than elevated temperature drying, while Rider et al.suggested the need for temperatures above 80-100°C to obtain good adhesion and optimum joint durability [16, 122, 125].

1.4 Tensiometry

Improving hybrid performance starts with improving adhesion between the constituents. Interaction between the substrate and matrix increases the stress transfer between both. The adsorption theory (Section 1.1.2.1) is of major importance as wetting of the adherent by the adhesive is critical, although it is not sufficient for strong bonding.

Chemical bonding works over very small distances and requires close contact. To obtain mechanical interlocking the silane/matrix must spread on the surface sufficiently to penetrate into the surface irregularities. The primary objective of a surface pretreatment is to facilitate these phenomena as much as possible [4].

The importance of wetting again becomes clear when taking a closer look on the stages of matrix application. In a first stage the matrix should spread on the substrate surface and wet it, in the next step shrinking and retraction of the matrix should be avoided prior to drying or curing to avoid e.g. surface defects [126]. This spreading strongly depends on the surface free energy of both the substrate and the spreading liquid, and a critical surface tension of wetting exists, which is needed to ensure spontaneous spreading of the liquid [4]. Following sections will explain those concepts more into detail.

1.4.1 Surface Tension and Surface Free Energy

Molecules in a pure substance interact and forces cancel each other. However, surface molecules are surrounded and attracted by fewer molecules compared to those in the bulk, creating an imbalance at the surface. Surface tension represents the force (F) needed to hold a surface together due to this imbalance. It can be defined as a tensor that acts perpendicularly to a line on a surface, as shown in Figure 1.12, and has units of N/m as it equals force per unit length [127].

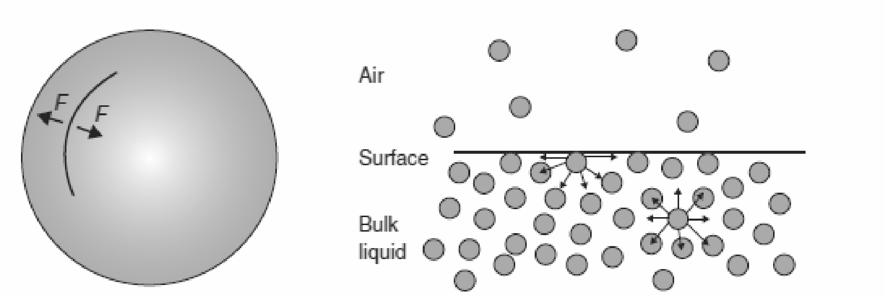

Figure 1.12: Schematic representation of the surface tension acting on a line at the surface (left). Forces acting on molecules in the bulk and near a surface (right) [127, 128].

If the material is in equilibrium this unbalanced force results in a higher energy of the surface molecules compared to the bulk molecules. Surface energy (γ) can be defined as the energy difference between molecules in the bulk and at the surface. This scalar non-directional property of an area has units of $\mathrm{J/m^2}$ [4, 129].

In general for liquids the surface tension is equivalent to the surface energy per unit area. This can be attributed to the high mobility of the molecules, and the surface will reach equilibrium as soon as it is formed as a liquid can spontaneously contract to minimize its surface area [127, 128]. The limited mobility of molecules at a solid surface impedes minimization of the surface area and reaching of the equilibrium configuration. When stretching a solid surface, the bulk molecules do not increase the surface molecular density, but the distance between the molecules increases. This produces a change in the molecular interaction forces and therefore the surface energy, leading to a non-equilibrium state. Because of this the surface energy of a solid does not necessarily equal the surface tension, and the surface energy values obtained from contact angles are only an approximation [130].

1.4.2 Young Contact Angle

A drop of liquid put in contact with a planar and ideal solid surface in the presence of its own vapor typically reaches an equilibrium condition. Along the contact line of three phases the liquid-vapor interface forms a characteristic angle (θ) with the liquid-solid interface [131]. Figure 1.13 represents the contact zone between a solid (s), a liquid (l) and a vapor (v) phase. It depicts the characteristic angle formed between the liquid and the solid at the circular solid-liquid-vapor three phase contact line, also called the Young contact angle [131]. The interactions between the liquid and the solid at the three phase line determine the contact angle behavior, whereas events at the interface away from the contact line will not affect it directly [132].

Thomas Young described the balance of forces at the contact line as

$$F_{sv} = F_{lv} \cos\theta + F_{sl} \tag{1.1}$$

with F_{sv}, F_{lv} and F_{sl} the solid-vapor, liquid-vapor and solid-liquid force. Young described this phenomenon as the result of the cohesion

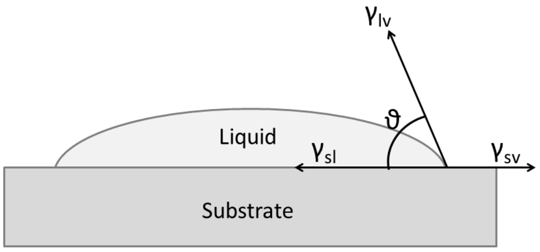

Figure 1.13: Graphical representation of the Young contact angle and the liquid-vapor (γ_{lv}), solid-vapor (γ_{sv}) and solid-liquid (γ_{sl}) interfacial energy.

of superficial particles at the surfaces of the solid and liquid, and the common surface of the solid and liquid [132, 133]. This expresses the concept of surface tension as a force per unit length acting perpendicularly to a line on a surface.

When forming a fresh surface and doing work against the liquid surface, the molecules will easily adapt to their equilibrium state due to the high mobility of the liquid molecules. In other words, the work done to form a new surface is equal to the change in surface free energy. Here a new equation can be derived using thermodynamic arguments

$$\gamma_{lv} \cos\theta = \gamma_{sv} - \gamma_{sl} \tag{1.2}$$

Here the contact angle relates with three interfacial energies: the liquid-vapor (γ_{lv}), solid-vapor (γ_{sv}) and solid-liquid (γ_{sl}) interfacial energy [127, 134]. According to this equation the contact angle can be interpreted in a thermodynamic way as $\cos\theta$ is a ratio of energies.

Spreading relates to the ability of a liquid to spread over a surface and strongly depends on the surface free energy of both the substrate and the spreading liquid. A liquid spreads along a solid surface when the net free energy is lowered by replacing a solid-vapor surface by a solid-liquid and a liquid-vapor surface together [4]. Total wetting takes place if

$$\gamma_{sv} > \gamma_{sl} + \gamma_{lv} \tag{1.3}$$

Low equilibrium contact angles indicate strong solid-liquid interaction and a high γ_{sl} causing easy spreading of the liquid on the solid. High angles generally mean less spreading and poor wetting. A zero contact angle typifies complete wetting, an angle between 0° and 90° points at (partial) wetting, while higher angle values indicate non-wetting. From this it is clear that the contact angle can give a quantitative measure of solid-liquid molecular interactions (Section 1.4.5) [127].

A final note has to be made that the Young equation starts with some basic assumptions

- Use of an ideal solid surface that is assumed to be perfectly isotropic, smooth and homogeneous.
- Use of a system always being in an equilibrium state (no fluid motion) [135] and the solid not perturbed by chemical interaction or by adsorption due to the liquid phase or its vapor [136]. Interaction or dissolution of the substrate in the probe liquid may alter the liquid surface tension and thus change the resulting contact angles.

Fulfilling these conditions results in a single and unique contact angle. Such ideal surfaces are almost impossible to achieve, and a real interface is rarely in its lowest energy state for most of the time, but rather in a metastable equilibrium. During experiments liquid drops on a solid surface can have many different stable angles, continuously varying between two extremes: the maximum angle called the advancing angle and the minimum one referred to as the receding angle. The difference between those extremes is called hysteresis, a quantity that can provide information about surface characteristics (Section 1.4.4).

1.4.3 Contact Angle Measurement

The surface energy of the solid cannot be determined as such, but can be calculated when monitoring the wetting of the solid substrate by a liquid, resulting in the contact angle. Wetting phenomena relate to molecular interactions and are a consequence of chemical attractions. Consequently, the contact angle and thus wettability directly or indirectly provide information on adhesion [43]. Contact angles are very sensitive to the upper 0.5-1 nm of a surface, making tensiometry the most surface sensitive analysis technique.

Different methods can be used to measure the contact angle, either static or dynamic. The latter comprises two major methods both having their own advantages and specifications: the goniometer method (visual and direct) and the dynamic Wilhelmy method (indirect). The goniometer technique can place drops on different positions on the solid surface, enabling characterization of heterogeneous surfaces. This work however, focuses on the Wilhelmy technique, where the substrate is dipped automatically in a liquid, measuring the total force on the wetted part of the sample. This allows analysis of a large area of material, and small imperfections do not unduly affect the measured contact angle. This decreases statistical errors and avoids operating errors and inaccuracies. Moreover the Wilhelmy technique allows low contact angles to be measured much easier as it measures force, which increases with decreasing contact angle.

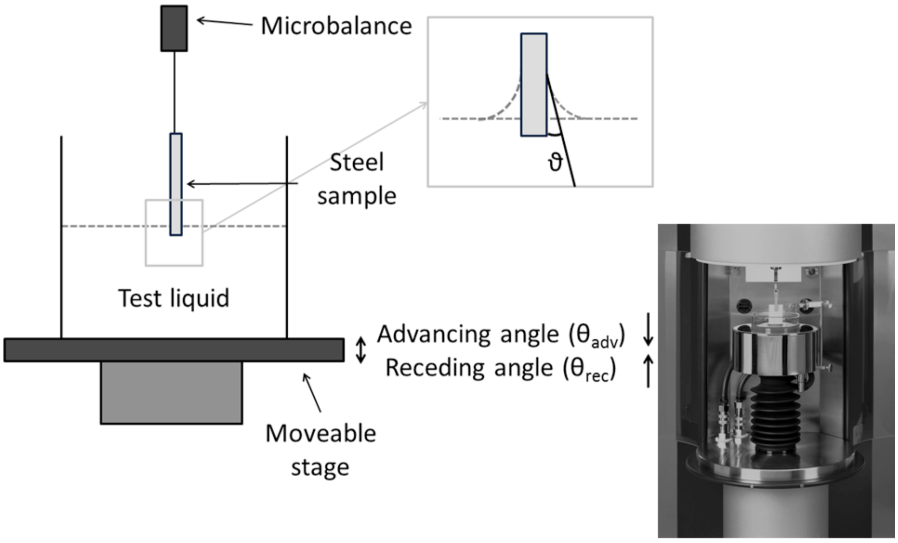

Figure 1.14: Schematic representation of the Wilhelmy technique resulting in an advancing and a receding angle (left). Picture of the equipment used (Kruss force tensiometer) (right).

Figure 1.14 depicts the experimental setup of the Wilhelmy technique, with the sample suspended from the hook of the microbalance and put in contact with the test liquid in an appropriate vessel. The vessel can move down and up, resulting in respectively the advancing (θ_{adv}) and receding (θ_{rec}) angle. The very precise and sensitive microbalance measures the total force acting (F) on a sample partially immersed in a liquid. This force consists of different forces: the weight of the plate, the buoyancy force and the wetting force due to the liquid surface tension. Combining this with the Young-Laplace equation results in (full derivation can be found in the work of Fuentes [127])

$$F = mg - \rho g A h + 2p\gamma_{lv}\cos\theta \tag{1.4}$$

with mg, A and h respectively the sample weight, cross-sectional area and depth of immersion and $2p$ the wetted perimeter, defined as the long horizontal edge of the sample, equaling twice the sample width. ρ denotes the liquid density, γ_{lv} points at the liquid surface tension and θ represents the contact angle.

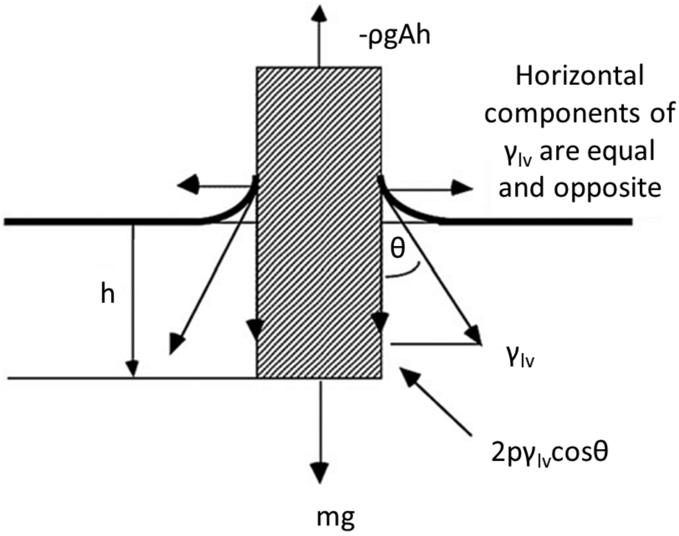

Figure 1.15: Forces acting on a substrate suspended on a microbalance: the sample weight, the buoyancy force and the wetting force (side view with the thickness exaggerated for clarity) [131].

Figure 1.15 represents the forces acting on an immersed substrate. The microbalance measures a null force when only gravitational force acts on the sample, meaning the recorded force F_r upon moving the vessel, can be presented as

$$\begin{aligned} F_r &= F - mg \\ &= -\rho g A h + 2p\gamma_{lv}\cos(\theta) \end{aligned} \tag{1.5}$$

with F_r assumed positive when directed downwards .

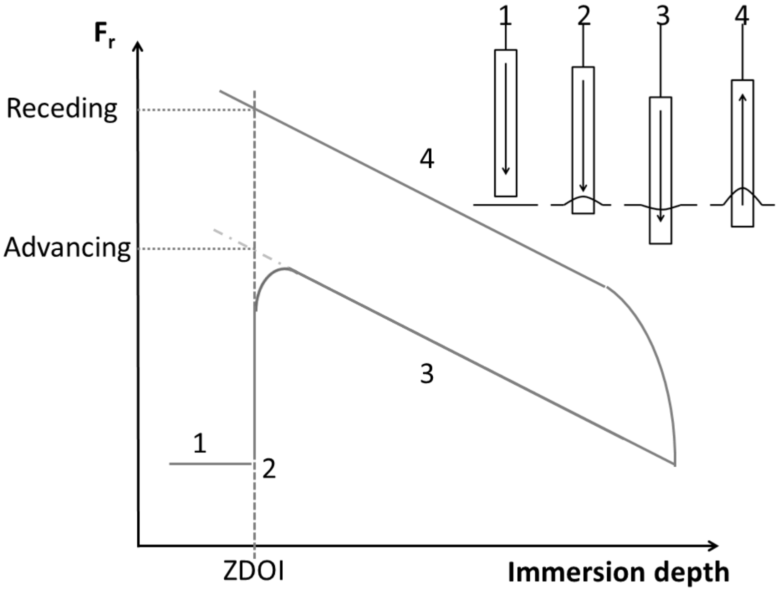

Figure 1.16: Graph representing the recorded force as a function of the immersion depth as obtained after measurement using the Wilhelmy technique. Force recorded upon approaching the liquid surface (1), when touching the surface (2), upon further immersion (3) and when retracting the sample again (4).

First the vessel moves towards the substrate until the desired immersion depth is reached, meanwhile recording the advancing angle. Next substrate withdrawal takes place while continuously measuring the receding angle. This results in a graph of force vs. depth of immersion, as shown in Figure 1.16. The sudden increase in recorded force (step 2) is due to the surface tension contribution at the position where the sample touches the liquid, also called the zero depth of immersion (ZDOI). Pushing the sample further into the liquid (step 3) causes a decrease in net force due to the buoyancy with the slope of the curve approximately equaling $-\rho g A$. Gradually withdrawing the sample in the next step (step 4) leads to an increase of the recorded force. The final detachment of the sample occurs at an immersion depth smaller than zero as the liquid typically sticks to the sample requiring further displacement. This knowledge combined with the position of the sample, the wetted length and the liquid surface tension, leads to calculation of the contact angle from equation 1.5, resulting in an advancing (θ_{adv}) and a receding (θ_{rec}) angle.

None of the existing theories directly relates the advancing and receding events with the equilibrium angle (θ_{eq}). Equation 1.6 is an empirical method to convert the advancing and receding angle in an equilibrium contact angle θ_{eq} (called θ in further Chapters) (Section 1.4.4) [137]

$$\cos\theta_{eq} = 0.5\cos\theta_{adv} + 0.5\cos\theta_{rec} \tag{1.6}$$

In general measurements take place at room temperature, but as mentioned by Bernadin et al. small variations in temperature hardly influence the resulting angle. Only at temperatures (T) above 120°C a fairly linear water contact angle decrease with temperature can be found [138]. Some authors mention dθ/dT to approximate -0.1°/K, while others find values ranging from -0.03 to -0.18 °/K over a temperature range of 5°C up to 1000°C [138].

Note that receding contact angles determined by the Wilhelmy plate method represent values of ′washed′ surfaces, resulting in a lower influence of contaminants. Because of this, no difference in the receding angle for unwashed and washed samples can be detected [139]. The relatively large volume of liquid used within this method ensures that small amounts of material that might dissolve from a polymer surface do not overly affect the surface tension of the probe liquid [140].

1.4.4 Advancing and Receding Angle, Hysteresis

On an ideal surface, the advancing and receding angles will be identical, resulting in the equilibrium Young contact angle. In practice few, if any, surfaces are ideal. Advancing and receding events can be very different processes (not the reverse of one another) with very different activation energies, and the former may influence the latter.

This implies that there could be multiple different activation energies for synchronous or sequential events that occur around the perimeter of the contact line by various mechanisms [132, 141]. The difference between those angles is referred to as hysteresis.

Two types of hysteresis can be distinguished: kinetic and thermodynamic hysteresis. The first and least frequently found type can be distinguished easily from its thermodynamic counterpart due to the time or cycle dependency of the contact angle. Changes in the liquid-solid system occur on a time scale comparable to the time of measurement, thus angles appear to change with time. Solvent penetration, swelling and rapid reorientation or dissolution of surface groups affect the dynamic contact angle hysteresis resulting in temporal dependency [131, 139]. This type of hysteresis should be avoided by picking a different measuring liquid, as the resulting angles are not useful.

Contact angle hysteresis may be related to the pinning of the contact line at heterogeneities at the substrate surface [142]. These kinetic barriers produce a variation of the local contact angle around the contact line and explain why advancing angles are mostly representative of the portion of the surface which interacts unfavorably with the liquid [127, 142]. According to Gao and McCarthy [141], the contact line cannot advance across this region until the advancing contact angle is reached (locally). This local contact angle will be high due to poor interaction between this portion of the solid and the liquid. On the other hand, the contact line will easily overcome the portion of the surface with high interaction due to the high interaction with the liquid. Following the same analysis, receding contact angles are more influenced by portions of the surface with high interaction with the liquid. The contact line of the liquid receding front will easily overcome the portion with poor interaction with the surface [127, 141, 142].

The second type of hysteresis is the thermodynamic or ′true′ contact angle hysteresis, an invariant and characteristic property of the surface [139]. Measurements result in both a stable advancing and receding angle, reproducible regardless time. Moreover, the number of immersion cycles performed on the sample has no influence on this type of hysteresis. Both surface roughness and (chemical or morphological) heterogeneity of the solid surface cause this phenomenon commonly found for real samples, although the former is believed to have a larger influence on apparent contact angles and resulting hysteresis [143]. Surface roughness means non smooth at the level of 0.1 up to 0.5 µm and an increase in roughness increases hysteresis by influencing both the advancing and receding angle. Surface heterogeneity means non homogeneous at the level of 0.1 µm or above. Some research even showed that roughness on the nanometer scale can contribute to this type of hysteresis, while only compositional variability smaller than 6-12 nm would lead to the disappearance of this phenomenon [140, 144]. Too high roughness and interpretation of resulting angles may lead to erroneous results as they will reflect surface topography rather than exclusively the surface energetics [144].

It is believed that thermodynamic hysteresis can be explained by the existence of a large number of metastable systems due to thermodynamic reasons, which can be omitted by applying the ′shaking technique′, resulting in the equilibrium contact angle. This technique supplies mechanical energy to the system, inducing relaxation to a state close to the thermodynamic equilibrium in a very short time span as resonant formation of capillary waves slowly reduces the amplitude to zero, putting the system in its lowest energy minimum. In this way the system can lose memory of its past state [140, 145].

Some researchers expressed their concerns about this shaking approach as it may encourage others to ignore the practical effects of contact angle hysteresis. The causes of contact angle hysteresis do not only affect the contact angle measurements themselves, but also the other practical interactions of liquids with solid surfaces, including adhesion, coatability and dewetting. Thus, any effort to characterize a non-uniform surface by a single contact angle value will miss significant characteristics of the wetting behavior of that surface [140]. Good et al. mentioned that tapping the solid also introduces oscillations in the liquid surface, making it an unacceptable method of decreasing hysteresis [136]. Care has to be taken to avoid environmental noise, having a similar influence as it typically results in a diminished hysteresis [131, 139]. In the absence of shaking (as in this work) the equilibrium angle often is calculated according to Equation 1.6.

Considering the theory of pinning of the contact line using water as the measuring liquid, makes clear that the advancing and receding angle relate more to respectively the low and high energy component of the surface because of the water polarity (with the polar and disperse component $\gamma_p = 52.2\,\mathrm{mN/m}$, $\gamma_d = 19.9\,\mathrm{mN/m}$). Higher advancing contact angles suggest a more non-polar surface (and relate to the low energy component of the surface along the contact line), whereas lower receding angles point at a more polar surface (and relate to the high energy component). This was experimentally demonstrated by different authors [139, 140, 142, 146, 147]. Neumann et al. set up a basic wetting model to study the effect of surface heterogeneity on the contact angle. By considering the capillary rise of a liquid at a vertical solid surface in a gravitational field, they found that the advancing contact angle can be expected to be a measure of the wettability of the low energy portions of the solid surface and the receding angle of the portions of higher energy. A full mathematical derivation can be found in Neumann et al [147]. When using a non-polar measuring liquid, the advancing angle will decrease upon increasing the apolar content of the surface [148].

This clearly shows the importance of taking into account both the advancing and receding angle, and not only the advancing angle, which in the case of static measurements is the only angle obtained. This leads to an overestimation of the true angle and after data processing to an underestimation of the surface free energy. Additionally, using both angles offers a big advantage as knowledge of hysteresis can be a useful tool for surface characterization [149]. Adhesion and ease of coating generally better correlate with the receding angle as it may tell if a liquid forced to wet a substrate will remain intact (and not recede) prior to drying or curing. Hence a lower receding angle of the coating liquid prevents dewetting and other coating defects [139, 150].

The force required for a drop to start moving on a surface relates to the difference between the advancing and receding contact angle. This implies that in the absence of hysteresis, a water droplet on a surface will not be stable and will easily slide or roll, regardless of the magnitude of the contact angle. Because of this a surface with water advancing and receding contact angles of respectively 99° and 99° should be considered more hydrophobic than a surface exhibiting angles of respectively 170° and 100°[151]. Hysteresis of 1-2° may be within the uncertainty of experimental measurement, but real surfaces often exhibit hysteresis in the range of 10° or more, with even 50° commonly seen [136, 140].

Care has to be taken as hysteresis increases at too high measuring speeds as fluid dynamics come into play. At sufficiently slow speed on the contrary, a minor change of the obtained angles will occur, so it is important to calculate the capillary number C_a, a dimensionless number that relates inertial forces to surface tension forces

$$C_a = \frac{\eta v}{\gamma_{lv}} \tag{1.7}$$

with η the dynamic viscosity coefficient of the liquid and v the speed of the liquid relative to the sample. C_a specifies the maximum moving speed of the sample: if it is smaller than 10^{-4} speed usually is regarded as appropriate [140, 152] and the dynamic contact angles are largely independent of the rate of contact line motion [140].

1.4.5 Surface Free Energy Calculations

From the contact angles obtained by e.g. the Wilhelmy technique, the surface free energy of the substrate can be calculated, but it must be noted that the equilibrium contact angle (Eq. 1.6) should be used when applying surface energy theories. Use of metastable advancing and receding angles would lead to wrong calculations. Also γ_{lv} can be measured easily, and values for different solvents can be found in literature. The Young contact angle is a quantitative measure of solid-liquid molecular interactions and thus provides information on the generally non-equilibrium surface energy of solids. However in order to solve the Young equation (Eq. 1.2) some assumptions concerning relations between the specific energies have to be made, and two major schools of thought evolved in the development of the surface free energy approach: the equation of state approach and the surface tension component approach [144]. More detailed information and theoretical derivations are beyond the scope of this work and can be found in [127, 131, 153].

While approaches for surface energetics calculations are logically and conceptually, mutually exclusive, they share some basic assumptions [144]

- All approaches rely on the validity and applicability of the Young equation (Eq. 1.2) for surface energetics from experimental contact angles.
- Pure liquids are always used; surfactant solutions or mixtures of liquids should not be used, since they would introduce complications due to preferential adsorption.
- The values of γ_{lv} and γ_{sv} (and γ_{sl}) are assumed to be constant during the experiment, i.e. there should be no physical or chemical reaction between the solid and the liquid.
- The liquid surface tensions of the testing liquids should be higher than the anticipated solid surface tension.
- The values of γ_{sv} going from liquid to liquid are also assumed to be constant, i.e. independent of the liquids used.

1.4.5.1 One-liquid method - Equation of state approach

Neumann [154, 155] postulated that an equation-of-state type of relation exists between the solid-vapor, the solid-liquid and the liquid-vapor surface free energies. The solid is assumed to be ideal in the following sense

- The solid surface is smooth and chemically homogeneous.
- There is no solid dissolution nor is there any absorption of any of the components from the liquid or gaseous phase by the solid.
- The solid is sufficiently rigid so that any movement of the three phase line does not change its state of strain.

Different equations of state can be found, such as Antonow's rule stating there is a relation between the surface energies. After derivation of the Berthelot combining rule [156] the work of adhesion (W_{sl}) can be approximated in terms of surface free energy (Eq. 1.8). In the Dupre equation the work of adhesion equals the work required to separate a unit area of the interface of a solid-liquid pair (Eq. 1.9)

$$W_{sl} = 2\sqrt{\gamma_{lv}\gamma_{sv}} \tag{1.8}$$

$$W_{sl} = \gamma_{lv} + \gamma_{sv} - \gamma_{sl} \tag{1.9}$$

Combining equation 1.8 and 1.9 with the Young equation 1.2 yields

$$\cos\theta_{eq} = -1 + 2\sqrt{\frac{\gamma_{sv}}{\gamma_{lv}}} \tag{1.10}$$

This relation states that the solid-vapor surface free energy can be determined when the contact angle and liquid surface tension are known. However, as this is only an approximation and less accurate for interactions between two very dissimilar types of materials, it generally overestimates the strength of the interaction.

1.4.5.2 Surface tension component approach

Fowkes [153] launched the idea of dividing the surface free energy into individual components that each have their origin in a specific type of intermolecular forces. He stated that the dispersion component connects with the London interactions, that act independently of other types of interactions, hence the possibility to create a separate surface energy component. The London dispersion force, together with the Debye and Keesom forces are part of the van der Waals interactions. The latter 2 forces have been considered as part of the inductive interactions. However, Fowkes' research was mainly focused on systems in which only dispersion forces take place. Owens and Wendt extended Fowkes' concept to a more general approach for cases where both dispersion (d) and polar (p) forces may operate [144, 157]

$$\gamma_{sl} = \gamma_{sv} + \gamma_{lv} - 2\sqrt{\gamma_{sv}^{d}\gamma_{lv}^{d}} - 2\sqrt{\gamma_{sv}^{p}\gamma_{lv}^{p}} \tag{1.11}$$

Combination of equation 1.11 with the Young equation (Eq. 1.2) results in

$$0.5\gamma_{lv}\left(1+\cos\theta\right) = \sqrt{\gamma_{sv}^{d}\gamma_{lv}^{d}} + \sqrt{\gamma_{sv}^{p}\gamma_{lv}^{p}} \tag{1.12}$$

From this the surface free energy can be determined from the experimental contact angle when using at least two measuring liquids (with known surface tension components) in order to quantify both the polar and dispersive component of the solid. In practice this means use of a liquid with a dominant polar character on one hand and a liquid with a dominant dispersive character on the other hand.

Van Oss, Chaudhury and Good [158] developed another approach (although claimed to be a generalization of the Fowkes' approach), dividing the surface energy into two other, different components: long-range and short-range interactions. The former contain the Lifshitz-van der Waals component (γ^{lw}), including London dispersion, Keesom and Debye forces. The latter include the acid-base component (γ^{ab}), which can be divided in an acid (γ^+) and a basic (γ^-) constituent [144, 158], both leading to hydrophilic behavior [136].

$$\gamma_{lv} = \left(\sqrt{\gamma_{sv}^{lw}} - \sqrt{\gamma_{lv}^{lw}}\right) + 2\left(\sqrt{\gamma_{sv}^{+}} - \sqrt{\gamma_{lv}^{+}}\right)\left(\sqrt{\gamma_{sv}^{-}} - \sqrt{\gamma_{lv}^{-}}\right) \quad (1.13)$$

combination with the Young equation (Eq. 1.2) results in

$$0.5\gamma_{lv}\left(1+\cos\theta\right) = \sqrt{\gamma_{sv}^{lw}\gamma_{lv}^{lw}} + \sqrt{\gamma_{sv}^{+}\gamma_{lv}^{-}} + \sqrt{\gamma_{sv}^{-}\gamma_{lv}^{+}} \quad (1.14)$$

As this equation contains three unknowns, three different measuring liquids, preferentially one non-polar and two polar ones, have to be used. However, in apolar systems some researchers ignore the acid and base component because London dispersion is the most important force component of molecular interaction in these systems. For polar systems some researchers drop the Lifshitz-van der Waals term, simplifying calculations.

1.4.5.3 Use of Surface Free Energy Calculations

Researchers often lose sight of the constraints and limitations of the contact angle measurements themselves. It is far more important to focus on collecting high quality contact angle measurements than on trying to analyze the contact angle data with one of the various surface energy theories. The majority of the information about a surface that can be revealed by wettability data will be revealed through careful consideration of the contact angle measurements alone [140]. Here it is important not to characterize a non-uniform surface by a single equilibrium contact angle as it will miss significant characteristics and wetting behavior of the surface [140].

The one-liquid method is just an approximation, where small measuring errors or uncertainties can result in large surface energy deviations, especially when working with very dissimilar types of materials [140, 144]. Surface free energy calculations according to the surface tension component approach are time-consuming as at least 2 measuring liquids should be used. Moreover these calculations assume that an equilibrium state can be reached, and well described contact angles must be obtained in order to correctly evaluate surface energy components. Theoretical models describing the wetting kinetics of synthetic materials show a dependency of the contact angle on the wetting velocity. The results depend on the number and the choice of liquids since small variations in experimental measurements can induce very large differences in the numerical results [127].

In the present research an attempt was made to use 3 different measuring liquids (water, ethylene glycol and 1-bromonapthalene; diiodomethane resulted in kinetic hysteresis), but results were highly inaccurate. As small measuring errors or uncertainties may result in deviations in the surface free energy, it was decided to just work with contact angles, in this way not introducing additional errors [140, 144].

1.5 Interphasial Gradient

Laminated steel plate-polymer hybrids reduce weight by creating sandwich structures with a light core and strong skin. In this way these materials may benefit optimally from desirable features of each of its constituting components [159]. However, as noted before 2 problems arise: a lack of adhesion between the constituents, as well as a mismatch between their (mechanical) properties, decreasing hybrid performance. The first problem might be solved using (APS) coupling agents, the second by introducing a gradient interphase.

Inhomogeneous interphases with a gradual or monotonic change in properties along the thickness direction of the materials are called gradient interphases. The change may concern a variation in composition, density, structure, nanoreinforcement dimension,... generally leading to a change in the overall mechanical properties as it improves the efficiency of (mechanical) stress transfer from matrix to reinforcement and decreases (thermo)mechanical stresses, leading to superior mechanical properties [160, 161]. Certain authors mention the gradient increases adhesive properties [162], and also an APS coupling layer would contribute to the gradient character of the interphasial region as it has a modulus intermediate between the substrate and the matrix [160, 161, 163].

The interphase can concern e.g. a mixture of thermoplastic materials [159], but also fiber-reinforced materials [160, 162] using e.g. a thermoset (epoxy) matrix [160, 162]. In nature different biomaterials have chemical and morphological interface gradients between hard an soft tissues, leading to excellent mechanical properties. It is suggested that these gradient structures not only decrease interfacial stresses, but also increase toughness, reduce fracture and enhance energy dissipation between both constituents [164, 165].

Nanomodifications at the interphasial area creating gradient structures may not only decrease the interfacial stiffness mismatch at the benefit of mechanical properties. Their advantage merely lies in the lower overall concentration of generally expensive modifying agent and thus cost. Moreover it is also anticipated that gradient structures with less stiff polymeric cores may lead to better damping and isolation properties compared to high stiffness materials used throughout the entire polymer layer in steel-polymer laminates.

1.6 Hyperbranched Polylysine

Silane coupling agents improve the bonding between the substrate and the matrix, acting as a bridge between both constituents. However, it is suggested that the addition of an appropriate functionalized hyperbranched polymer at the interphase may increase this coupling, by adding a higher amount of functionalities and thus creating more coupling opportunities. In other words the adhesion strength would be associated with the bonding number [166]. Dendrimers and hyperbranched polymers possess tens to hundreds of functional groups at the periphery. Moreover different types of terminal groups can be anchored, depending on their purpose. In this way these molecules can e.g. take part in the curing reaction of a polymer composite. Lower generation dendrimers and hyperbranched systems have a more open structure so the polymer matrix can interpenetrate, establishing more interactions [166]. These species do not suffer (as much) from thermal shrinkage, in this way decreasing expansion mismatches [167].

In dentistry literature reports on the use of dendritic species in combination with a silane coupling agent applied on titanium surfaces. These species react in the matrix, improving mechanical properties [167]. Mei et al. tried to enhance the interfacial adhesion in epoxy-metal laminated composites by adding a dendrimer onto the interface. They assumed a more effective load transfer between constituents after adsorbing the dendrimer on an alumina surface using acid-base interactions [166].

Figure 1.17 depicts polylysine, a hyperbranched molecule used during this work. This polymer contains amino end-groups and amide bonds in the core of the molecule. It can be obtained by polycondensation of lysine [168]. This work aims at an increase of the number of bonds to increase adhesion. After application of a GPS layer on the substrate, the epoxy groups of this silane may react with the amine functionalities of the polylysine, anchoring it on the substrate. Next remaining polylysine functional (end-)groups can react with the epoxy functional groups of the matrix, in this way establishing a higher number of covalent bonds.

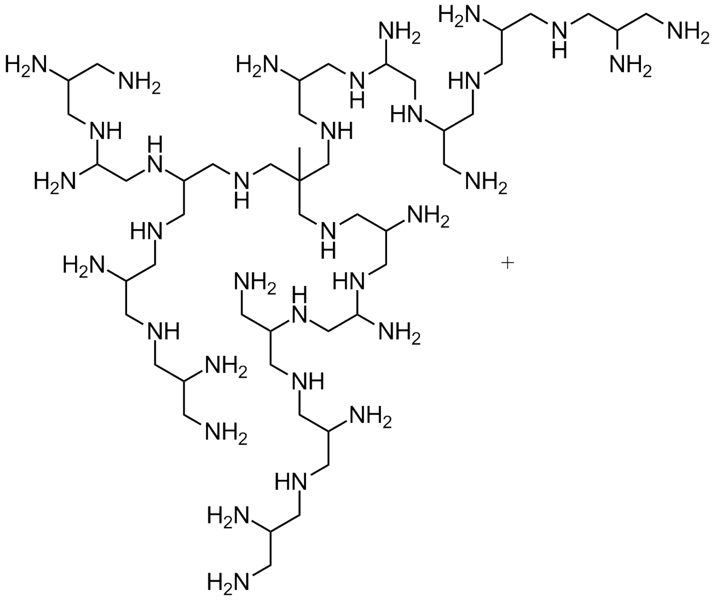

Figure 1.17: Schematic representation of a hyperbranched polylysine molecule containing amino end-groups and amide bonds in the core.

1.7 Carbon Nanotubes

Whereas silane coupling agents directly influence the bonding between the substrate and matrix, the introduction of carbon nanotubes at the interphase or in the polymer matrix may decrease the so-called stiffness mismatch.

1.7.1 Carbon Nanotubes in General

In 1991 Iijima et al. discovered carbon nanotubes (CNTs), cylindrical structures resembling rolled-up graphite sheets ideally being defect free with sp^2 hybridized carbon-carbon bonds and extended conjugation [169, 170]. Due to this structure these one-dimensional nanofibers possess unique mechanical, optical, electronic and thermal (conductivity) properties [169, 171, 172]. They are used for e.g. biosensors and molecular scale wires because of their electronic and thermal properties, whereas their mechanical properties make them interesting candidates as polymer or composite reinforcements. Literature also mentions combinations of both when e.g. used as nanofiller in polymeric composites with improved mechanical performance and possessing electrical conductivity [173–175]. Nonetheless CNTs tend to entangle and to aggregate due to their structure, which results in the formation of nanoropes and bundles, structures with inferior properties compared to isolated tubes [172, 176].

1.7.2 Processing in General

The main route available to engineering nanotubes for electronic applications as well as nanocomposites and multifunctional devices is solution based processing [177–179], which requires tubes to be dispersed in liquids such as organic solvents or surfactant solutions [176, 180, 181]. Preferentially this results in the formation of a stable dispersion or solution, thereby overcoming the strong intertube π-π-stacking responsible for bundle formation [182]. Nanotube exfoliation requires mechanical methods such as ultrasonication (US) or high shear mixing to break bundles apart, but nonetheless (most frequently) additional substances have to be added to keep the individualized tubes stable [183]. Different solvents, often consisting of molecules having π-electrons, can overcome this issue e.g. dimethylformamide, N-methylpyrrolidone, but also 1,2-dichlorobenzene, chloroform and tetrahydrofuran [174, 181, 184, 185]. However most of the previously mentioned solvents are toxic, and e.g. alcoholic systems, important in sol-gel chemistry and condensation polymerization can be an alternative, although currently especially aqueous solutions draw attention because of environmental and safety reasons [171, 180, 186].

When using aqueous solutions, bundles are generally broken apart by ultrasonication, while a physical or chemical treatment renders the individualized tubes or small bundles soluble. Whereas attaching chemical groups changes sp^2 into sp^3 hybridization thereby altering properties, physical methods preserve the intrinsic CNT structure and thus e.g. electronic performance [171, 187, 188]. The latter methods usually consist in the use of surfactants, synthetic polymers or even natural macromolecules acting as a dispersing agent, diffusing (ii) and adsorbing (iii) along the tube in spaces or gaps created by US (i), thereby stabilizing the individual tube (iv), a shown in Figure 1.18 [180, 181, 189, 190]. It is believed that longer sonication times and increased sonication strength favor the breaking up of the bundles, exposing additional surface area for the adsorption of surfactant molecules [183, 190].

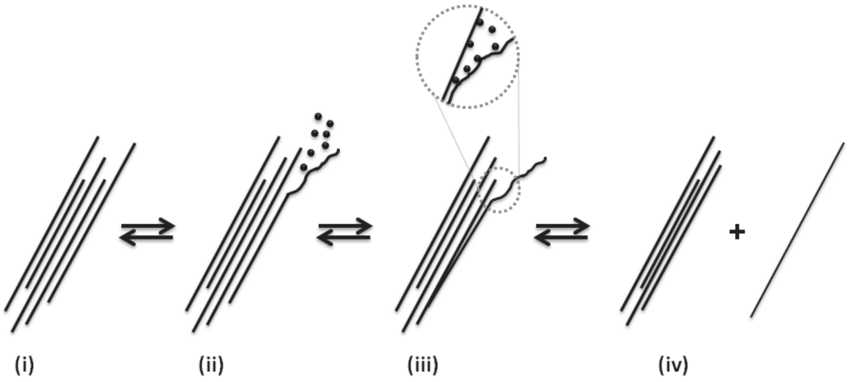

Figure 1.18: US and surfactant assisted nanotube exfoliation: dispersing agents diffusing (ii) and adsorbing (iii) along nanotubes in spaces or gaps created by ultrasonics (iv), thereby stabilizing the individual tube (iv).

1.7.3 Processing: Dispersing Agents

Dispersing agents consist of a part interacting with the nanotube and a (hydrophilic) group for interaction with the solvent. They counteract attractive potentials between tubes by decreasing π-π-interactions [171, 178, 179], while electrostatic or steric repulsion prevents nanotubes from approaching and reagglomerating and reaggregating [180, 185, 188, 191]. Care has to be taken to control the surfactant concentration, as depletion interaction may come into play above the surfactant critical micelle concentration (CMC). Micelles do not fit in between nanotubes, creating lower micelle concentrations at these locations. This leads to a concentration and consequential osmotic pressure difference in the solution, pushing nanotubes together and causing reagglomeration [192, 193]. Depletion interaction received quite some attention in research, but disagreement among authors exists as whether to work above [171, 182, 191] or below [194, 195] the CMC of surfactants. In any case, even in the absence of depletion interaction needlessly high surfactant amounts should be avoided for economic reasons and to avoid performance losses when used at a later stage in e.g. composites.

Literature often mentions molecules with basic nitrogen atoms possessing high affinity towards carbon nanotubes [184, 196, 197], and also compounds having π-electrons (π-aromatic compounds) are suitable to be used as a surfactant [184, 189, 198–200]. Sodium dodecyl sulfate (SDS) is one of the most popular stabilizing agents for nanotube dispersion in aqueous media [178, 181, 193], as well as its derivative (sodium)dodecylbenzenesulfonate ((Na)DDBS) [171, 201, 202]. For the latter π-π-stacking interactions between a phenyl group and the CNT surface increase the binding and efficiency of the surfactant [203, 204]. Among polymer stabilizers especially poly(ethylene oxide) derivatives such as the block copolymers Brij [205], Tween [205] and Pluronic [189] are frequently used, as well as natural macromolecules such as DNA [187]. Adsorption of those polymeric species takes place along the nanotube sidewalls, mostly driven by hydrophobic effects and charge transfer interactions with the surfactant lone electron pairs [187, 206].

Zhang mentioned amphiphilic block copolymers with dendritic structures to be more efficient oil emulsifiers compared to their linear counterparts because of increased penetrability and good absorption and displacement behavior [207]. Xin compared Pluronic, a block copolymer of poly(ethylene oxide) (PEO) and poly(propylene oxide) (PPO) with its five-branched starlike counterpart, having a similar hydrophilic PEO fraction. He found out that the latter had a more pronounced surface activity leading to a higher efficiency, even at lower concentrations of the branched molecule [206]. These branched species improve steric repulsions as confirmed by simulations, and have a higher number of hydrophilic groups extending into water per unit of nanotubes [183]. More hyperbranched and dendrimeric surfactants can be found in literature [183, 208], generally having a hydrophobic core or possessing block-like arms. The review by Sun lists some examples of hyperbranched polymers of which the main chain contains aromatic moieties, thereby aiming at π-π-stacking interactions [209].

1.7.4 Deposition and Applications

Literature mentions nanotube deposition on a substrate for multiple purposes, mainly advanced device applications including nanoelectronics and chemical or biological sensors, but also for biomaterial modification and corrosion protection [178, 210]. Usrey et al. report on the adsorption of CNTs on APS coated substrates, with experiments indicating that single-walled CNT (SWCNT) adsorption strongly depends on the APS concentration on the substrate, the concentration and the type of functional groups, with acidified tubes adsorbing to the greatest extent [178]. Moreover the amount of nanotubes deposited depends on the dipping time, although saturation would take place after about 45 min [178].

Chapter 2

Materials and Methods

This chapter describes materials and methods used throughout this work. The first section describes the materials used. Following Sections describe the methods, which are arranged per Chapter.

2.1 Materials

OCAS, Zwijnaarde, Belgium provided stainless steel plates of type 304 with a thickness of 0.80 mm. Ultrathin stainless steel fibers (316L) with a thickness of 30 µm were kindly provided by Bekaert, Zwevegem, Belgium. Ethanol (Disinfectol, ether denaturate) (EtOH) was provided by Chem Lab, Zedelgem, Belgium, Ridoline C72 and Gardoclean S5080 by respectively Henkel, Tilleur, Belgium and Chemetall, Kontich, Belgium. MilliQ water for tensiometric measurements as well as deionized water used in other experiments was prepared at KU Leuven, Leuven, Belgium.

3-Aminopropyltriethoxysilane (APS), 3-glycidoxypropyltrimethoxysilane (GPS) and acetone were purchased from Acros Organics, Geel, Belgium, 1, 2-bis(triethoxysilyl)ethane (BTSE), methanol (MeOH) and deuterated solvents (methanol-d_4 (MeOD), ethanol-d_6 (EtOD), DMSO-d_6 and acetic acid-d_4 from Sigma Aldrich, Diegem, Belgium and acetic acid from VWR, Haasrode, Belgium. Chemetall, Kontich, Belgium kindly provided Oxsilan.

The epoxy resin formulation used for mechanical testing was a stoichiometric combination of a diglycidyl ether of bisphenol A (DGEBA) based epoxy (EPIKOTE 828 LVEL) with an equivalent weight of 185 g/mol, supplied by Momentive Specialty Chemicals, Bergen op Zoom, The Netherlands, and 1,2-diaminocyclohexane (DAC) with an equivalent weight of 28.5 g/mol, supplied by Sigma-Aldrich, Diegem, Belgium. The combination of the epoxy with the hardener is further referred to as ′epoxy′.

2.2 Steel Surface Characterization

2.2.1 Substrate Cleaning

Different cleaning methods were applied on stainless steel type 304 plates in order to study their influence.

- Uncleaned samples were briefly wiped with a dry tissue to remove (most of the) dust and fingerprints.
- To obtain ′wiped′ samples soft tissues were wetted with acetone or ethanol before gently wiping the substrate for a few seconds.
- Ultrasonically (US) cleaned substrates were first gently wiped with ethanol moisturized tissue to remove fingerprints and most visible contaminants, followed by indirect ultrasonic cleaning (Branson 3210) in ethanol, starting with 5 min of degassing and ending with 10 min of actual cleaning. Indirect cleaning was done by placing the substrates in a perforated SST sample holder in a beaker filled with ethanol. This ensemble was placed in an ultrasonic (US) bath filled with water.
- Chemical cleaning, was done with commercial alkaline cleaners, mainly used for galvanized steel and aluzinc. Again samples were first gently wiped with ethanol moisturized tissue, followed by immersion in the alkaline solution. For Ridoline C72 (pH 12-13) a 10 g/L solution at 60°C was stirred until complete dissolution followed by dipping the substrate for 3 s. For Gardoclean S5080 samples were dipped for 10 s in a 15 g/L solution (pH 9-10) at 60°C.

After cleaning the substrates were briefly water rinsed to remove cleaning residues, but also blow drying with cleaned pressurized air was applied [31]. Especially in the case of alkaline cleaning the removal of cleaning remainders (e.g. Gardoclean or Ridoline) is necessary.

2.2.2 Atomic Force Microscopy

Atomic force microscopy (AFM) measurements can provide information on the appearance of the steel substrates. They were performed on 1 x 1 cm^2 samples with a Multimode Scanning Probe Microscope (Nanoscope) from Digital Instruments with a Nanoscope controller in combination with Nanoscope software V6.13. Veeco RTESPA fosfor (n) doped Si tips (with a backside aluminum coating of 50 ± 10 nm thickness) were used, with the cantilever values being 3.5-4.5 µm, 115-135 µm and 30-40 µm for respectively the thickness, length and width. The resonance frequency and force constant equaled respectively 278-353 kHz and 20-80 N/m. All substrates were mapped as soon as possible after cleaning.

2.2.3 Electron Microscopy

Scanning Electron Microscopy (SEM) analysis revealed information on the SST surface, whereas Energy Dispersive X-ray spectroscopy (EDX) measurements provided information on the chemical composition.

Analysis of blanc SST was done on 1 x 1 cm^2 samples, mounted on a steel sample holder, with an XL FEG SEM (Philips, Eindhoven, The Netherlands), with spot 3 and diaphragm 2 using secondary electrons, an electron beam voltage of 10-20 keV and a secondary electron detector. For EDX measurements using an EDAX detector, a beam voltage of 20 keV and working distance of 10 mm were applied. Data processing took place with EDAX Genesis software.

2.2.4 Tensiometry

Tensiometry reveals information on the upper 0.5-1 nm of the steel substrate. A study of the advancing and receding angle can provide information on the low and high energy component of the surface, as described in the Chapter Literature, Section 1.4.4.

Tensiometry on cleaned SST substrates of 2 x 1 x 0.80 cm^3 was done as quickly as possible after cleaning, water rinsing and blow drying (cleaned pressurized air) of the desired samples, with a maximum time span of 4 min in between cleaning and the start of the measurement (unless mentioned otherwise).

Dynamic contact angle measurements using the Wilhelmy technique were performed with a Kruss K100 tensiometer, with a built-in ionizer to eliminate electrostatic charges (prior to putting the liquid and solid in contact). Accurate substrate dimensions were verified with a caliper for every sample. Water, the measuring liquid, was placed in a 70 mm diameter glass vessel, with water characteristics defined according to Table 2.1.

Table 2.1: Water characteristics used for calculations with tensiometric data.

Property		**unit**
Density	0.998	g/cm^3
Viscosity	1.002	mPa.s
Polar component	52.2	mN/m
Dispersive component	19.9	mN/m
Surface tension	72.1	mN/m

The procedure followed had a detection speed and sensitivity of respectively 3 mm/min and 0.001 g, a measuring speed of 1.5 mm/min, position difference of 0.1 mm and maximum and minimum immersion depth of respectively 7 and 0 mm with a respective delay of 1 and 0 s. The advancing position went from 0 mm to 7 mm, the receding from 7 mm to 0 mm, resulting in about 140 measuring points. At least 3 samples per condition were measured to assure repeatability and to decrease errors.

Samples of about 2 x 1 x 0.8 cm^3 are sufficiently large to neglect boundary effects [140]. To avoid fluid dynamics influencing the contact angle value, the so-called capillary number C_a was calculated and kept below 10^{-4}, so measuring speed can be regarded as appropriate [152](Section 1.4)

$$\begin{aligned} C_a &= \frac{\eta v}{\gamma_{lv}} \\ &= \frac{1.00210^{-3} Pa \cdot s \times 0.02510^{-3} m \cdot s^{-1}}{7210^{-3} N \cdot m^{-1}} \\ &= 3.4810^{-7} \end{aligned} \tag{2.1}$$

2.2.5 X-Ray Photoelectron Spectroscopy

X-ray Photoelectron Spectroscopy (XPS) was used to determine the chemical composition of the top layer of the substrate (nm-range). It enables determination of the chemical requirements resulting in best polymer-steel hybrid performance.

Measurements on a 1 x 1 cm^2 sample were conducted using a S-Probe Monochromatized XPS spectrometer from Surface Science Instruments (VG) with a monochromatic $AlK\alpha$ X-ray source, with a voltage and power of respectively 10 kV and 200 W a 35° take off angle (angle between the surface plane and the axis of the analyzer lens), and a base pressure of 1 x 10^{-9} mbar in the measurement chamber. Survey and low resolution spectra were taken with a pass energy of 157.7 eV and resolution of 0.100 eV) per step. High resolution spectra were taken at a pass energy of 55.8 eV and a resolution of 0.100 eV per step. A flood gun neutralizer with a filament bias of 0.7 V was used to reduce charging of the samples while scanning. Ion gun sputtering was done at 4 kV, with a spot size of 4x4 mm^2 and a sputter pressure of 1.5 x 10^{-7} mbar.

Data processing to obtain chemical states was done using Casa XPS software. Quantification was done by least-squares fitting of Gaussian-Lorentzian line shapes and subtracting a Shirley-type background (for the elemental peaks) and subsequently integrating the area under the remaining peak and dividing by the relative sensitivity. Resulting graphs have units of CPSeV (counts per second x eV), calculated as the measured area divided by the transmission curve of the equipment and the mean free path. This results in the corrected peak surface used for further comparison. As not all elements were monitored, atomic percentages in the sample could not be calculated, although the ratio of 2 corrected peak areas equals the ratio of their atomic abundance.

Peaks are referenced according to the aliphatic carbon peak at 285 eV.

Specifications used for peak calculations concerning blanc surfaces can be found in Table 2.2, while peak decomposition was done according to specifications found in Table 2.3. For the latter an interval close to 2 eV was allowed, although all peaks positions are about the value indicated in the Table.

Table 2.2: Specifications used during peak assignments in XPS spectra of samples prepared using different cleaning procedures.

Element	**Peak End** $[eV]$	**Peak Start** $[eV]$
C	292	279.3
O (Low resolution)	536.6	524.7
O (High resolution)	536	526.6
Fe	716.8	704
N	403.5	399.5
Si	106.5	97.6

Table 2.3: Specifications used for peak decomposition in XPS spectra of samples prepared using different cleaning procedures.

Element	**Subpeak**	**Position** $[eV]$	**FWHM** $[eV]$
C	C-C, C-H	285	2
	C-O	286.5	2
	C-O	288.6	2
O (HR)	O^{2-}	530.4	1.8
	-OH	532.4	1.8
	H_2O	534.3	2
Fe	Fe^0	707.3	4
	FeO	709.4	2.5
	Fe_3O_4	711	2.5
	$FeOOH/Fe_2O_3$	713	2.5

2.2.6 Mechanical Characterization

Mechanical testing reveals information on the mechanical strength of SST-epoxy joints. Combining those results with chemical (and physical) information enables determination of optimal conditions.

Mechanical testing was done in collaboration with the Materials and Chemistry Department (MACH), Vrije Universiteit Brussel, Brussels, Belgium. The combination of epoxy with hardener is further referred to as ′epoxy′. For the standard steel plate testing method a modified butt joint (aluminum) dolly test was developed experimental by the people of MACH as depicted in Figure 2.1.

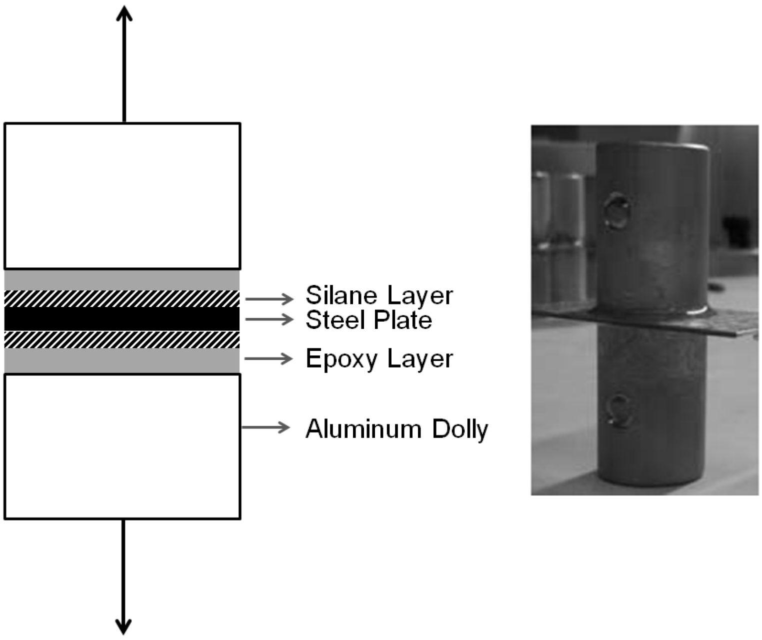

Figure 2.1: Schematic representation of a dolly sample (left) and image of a dolly sample (right) after preparation.

Testing was done at room temperature in accordance with ISO 4624 : 2003 with a dolly-plate-dolly (DPD) symmetric sample configuration with an Instron test bench (Instron 5885H, capacity 250 kN) in which the DPD samples were mounted by means of threaded steel screws. The dollies were pulled away from the stainless steel substrate with an upper jaw speed of 0.5 mm/min against a fixed lower jaw. The load at break for each DPD sample was recorded in five independent measurements and averaged. The stress at break (σ, MPa) was calculated by using Equation 2.2, where l is the load at break (in N) and d is the diameter of the dolly (in mm)

$$\sigma = \frac{l4}{\pi d^2} \tag{2.2}$$

Steel plates were treated as mentioned in the text, followed by application of epoxy on the dolly surfaces. This epoxy formulation was prepared by mixing the epoxy resin and amine hardener by a mechanical mixer (Heidolph RZR 2041) at 2400 rpm for 5 min followed by a degassing step in a vacuum oven for 15 min at ambient temperature before using it for the dolly sample preparation. After application of this epoxy, the surface treated plates were placed in between, with glass beads inserted into the epoxy layer to control its thickness. Joints were held together with an in-house made set-up with a dead weight of 500 g to maintain uniform thickness during the first step of the resin curing at room temperature for 12 h. Final curing of the epoxy was done in two stages in a heated oven, first at 80°C for 2 h, next at 180° for 1 h, leading to an epoxy thickness of about 0.2 mm after curing.

The blanc reference samples was only US cleaned before epoxy application and testing and has no silane layer. The US cleaned and Ridoline cleaned sample were coated with a standard APS layer (Section 2.3) before application of the epoxy matrix. An APS layer was deposited from a 2/90/10 water-ethanol solution, with 30 s of dipping and 15 s of ethanol rinsing, followed by oven treatment for 1.5 h at 70°C under vacuum.

2.3 Silane Coating Application

Silane solution names throughout this work are indicated as $x/y/z$ with y and z representing the volumetric percentage of respectively water and alcohol in the solvent. The volumetric percentage of silane in the binary water/alcohol solvent is represented by x. E.g. a 2/90/10 mixture means mixing 90 v% of water with 10 v% of alcohol, followed by the addition of 2 v% of silane (with respect to the 90/10 binary solvent), in other words 100 mL of this solution contains 2 mL of silane, 88.2 mL of water and 9.8 mL of alcohol.

2.3.1 Application of the Silane Coating in Practice

Silane coating took place according to the following procedure

- (US) cleaning of the substrate (as in Section 2.2.1).
- Silane solution preparation (using micropipets) in a beaker sealed with parafilm or in a 20 mL vial with lid.
- Dipping of the cleaned substrate in the solution while gently agitating.
- Rinsing using the same handling maneuver as during dipping.
- Optionally blow drying using pressurized cleaned air.
- Removing excess solution by a gentle tissue touch at the bottom of the substrate after hanging it vertically.
- Oven treatment of the samples (keeping them in the vertical position to avoid water and silane accumulation in the middle of the sample.

Those steps are applied unless mentioned otherwise. Applying a silane layer always took place according to the in this work called ′standard coating procedure′, unless mentioned otherwise. This procedure consists in

- US cleaning of the substrate (as in Section 2.2.1).
- Meanwhile preparing a 2/90/10 APS/H_2O/EtOH solution, aged appropriately (see Section 4.1).
- 30 s of dipping the cleaned substrate in this solution.
- EtOH rinsing for 60 s.
- Applying an oven treatment at 70°C for 1.5 h under vacuum.

2.3.2 Kinetic Study: Nuclear Magnetic Resonance Spectroscopy

2.3.2.1 NMR in General

Nuclear magnetic resonance spectroscopy (NMR) enables study of the silane solution kinetics and determination of the working window (Chapter Literature, Section 1.3.1).

Proton NMR (^{1}H NMR) measurements to monitor hydrolysis were performed on a Bruker 400 Advance (Bruker, Billerci, MA) (400 MHz) at room temperature, averaging 8 scans with a spectral width of 20.62 ppm and an acquisition time of 1.99 s. Chemical shifts were referenced to the water-hydrogen peak at 4.79 ppm and the time between sample preparation and the first measurement was kept as low as possible: i.e. between 165 s and 180 s. ^{13}C NMR measurements to monitor GPS ring opening were done using a Bruker 400 Advance at room temperature, averaging 502 scans with a spectral width of 238.90 ppm and an acquisition time of 1.36 s. Times mentioned represent the time between solution preparation and the start of the measurement. ^{29}Si NMR measurements to study self-condensation behavior were done using a Bruker 600 Advance (Bruker, Billerci, MA) (600 MHz) at room temperature, averaging at least 256 scans with a spectral width of 5031.70 ppm and an acquisition time of 0.55 s, taking into account that the relaxation time was more than sufficient for silicon to relax (5 x T_1). Recording a single ^{29}Si spectrum takes at least 2 h, and when discussing results, the time associated with a given measurement refers to the time lapse between the preparation of a given solution and the start of the measurement. All measurements used 5 mm diameter XR-5 precision tubes from Norell.

Silane solution preparation took place by adding the desired amount of deuterated water to a 5 mm tube with a micropipet and adding deuterated methanol or ethanol in the same way (if needed). Next the desired volume of the appropriate silane (and acetic acid if needed) was added with a micropipet after which the ensemble was gently shaken for a few seconds and placed into the NMR equipment. During this work it was decided to focus on water/ethanol mixtures with varying ratios, as from an economical and environmental point of view this is a more attractive combination compared to e.g. water/methanol. However, as ethanol-d6 prices largely exceed those of methanol-d4, first optimization work used methanol-d4, followed by repetition of promising ratios with ethanol replacing methanol.

2.3.2.1.1 ^{1}H NMR APS ^{1}H NMR peak assignment can be found in Figure 2.2, with peak 2 that represents 2 β-protons taken as the reference peak. The left ethanol peak (due to the α-protons of the ethanol released after hydrolysis)can be integrated and used to calculate the degree of ethanol release and thus of hydrolysis.

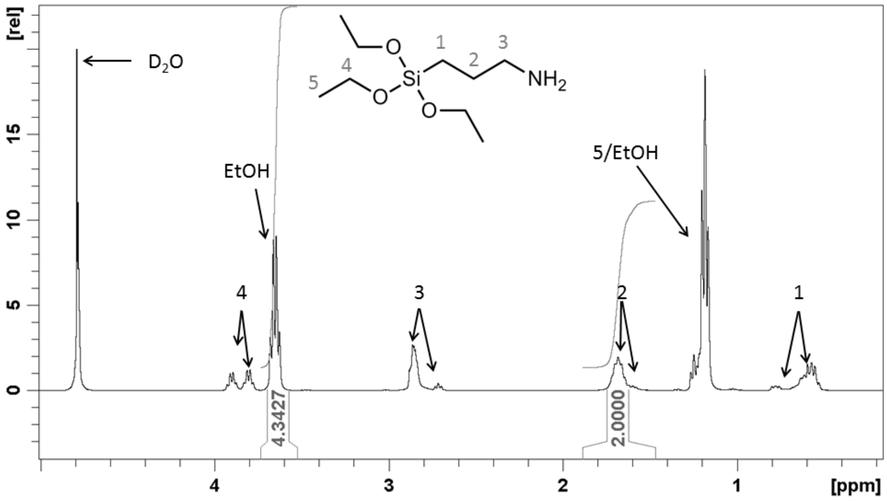

Figure 2.2: ^{1}H NMR spectrum of an APS/water/methanol solution and concomitant peak assignments.

Analogous GPS ^{1}H NMR peaks can be assigned (Figure 2.3), with peak 2 taken as the reference peak representing 2 protons. The peak belonging to the released methanol was used to calculate the degree of hydrolysis . Care has to be taken here as there is still a peak underneath the methanol peak, due to the 2 γ-protons.

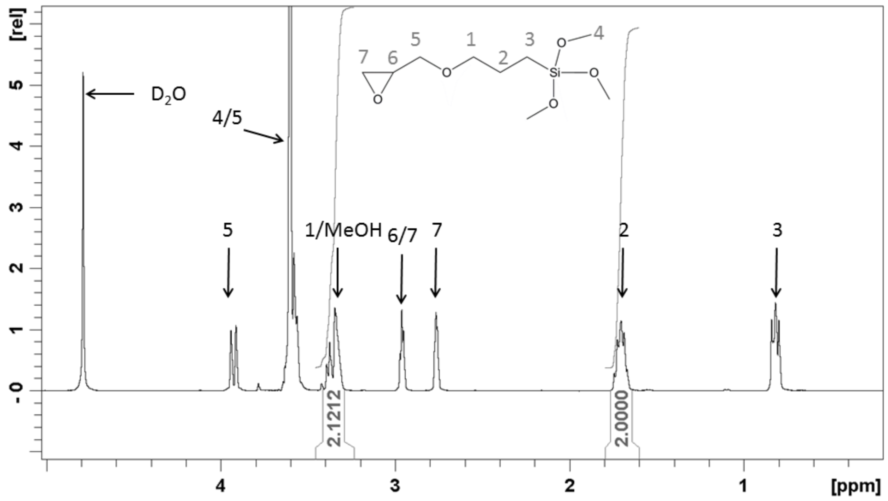

Figure 2.3: ^{1}H NMR spectrum of a GPS/water/methanol solution and concomitant peak assignments.

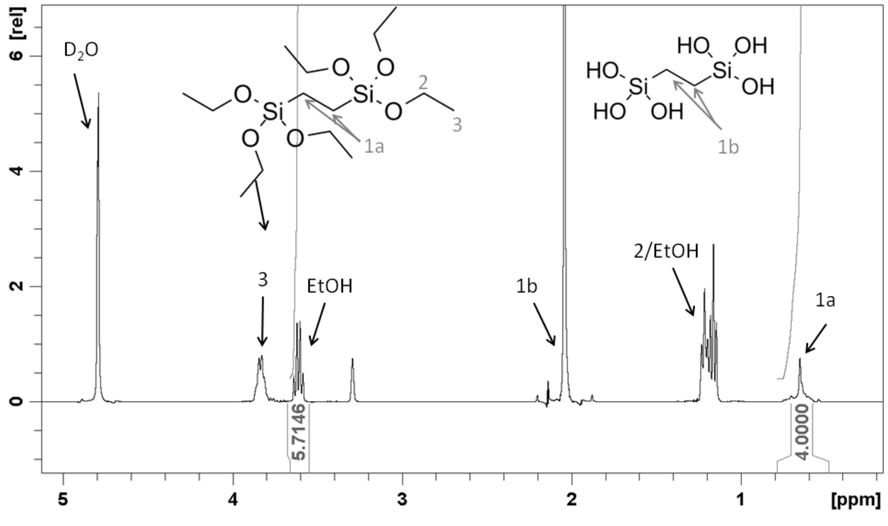

Figure 2.4: ^{1}H NMR spectrum of a BTSE/water/methanol solution and concomitant peak assignments.

Figure 2.4 depicts an ^{1}H NMR spectrum for BTSE and the concomitant peak assignments and integrations. Peak 1 is considered as the reference peak, representing 4 protons, while the left ethanol peak is used again to calculate the degree of ethanol release.

The fraction of ethanol (for APS and BTSE) and methanol (for GPS) released equals the fraction of species hydrolyzed, which can be found by monitoring solutions in time. After setting a reference peak (with a value of 2 for APS and GPS, of 4 for BTSE), the surface beneath the released alcohol peak can be found. For GPS this peak was first corrected for the peak below by subtracting a value of 2, corresponding with the amount of protons it belongs to. In case of ethanol release the peak due to the α-hydrogens should saturate at a value of 6 protons due to the 3 molecules of ethanol released per silane molecule, each having 2 α-protons. In case of methanol release the peak should saturate at a maximum of 9, due to the 3 methanol molecules released per GPS molecule, each having 3 protons. The fraction of alcohol released at a certain moment in time equals the fraction of molecules already hydrolyzed at that time. From the (subpeak corrected) surface beneath the methanol (S_m) and ethanol (S_e) peak the alcohol release for APS (Eq. 2.3), GPS (Eq. 2.4) and BTSE (Eq. 2.3) and thus the degree of hydrolysis DH (in %) at a time t can be calculated as

$$DH_t = \frac{S_{e,t}}{6} \times 100 \tag{2.3}$$

$$DH_t = \frac{S_{m,t}}{9} \times 100 \tag{2.4}$$

In practice, the surface beneath the alcohol peak is integrated and the area normalized to one of the methyl peaks. A capacitor curve fits accurately the evolution of this normalized integral value with time, where the fraction of alcohol release and thus the degree of hydrolysis (DH) equals

$$DH = A\left(1 - exp\left(\frac{-t}{\tau}\right)\right) \tag{2.5}$$

With A the maximum degree of hydrolysis and τ the time where 62.31% of the hydrolysis is completed. This fit enables determination of the time until maximum hydrolysis, that equals the time where the extent of alcohol release has saturated. When studying hydrolysis kinetics, the fitted data were used, as in this way trends can be seen more clearly.

2.3.2.1.2 ^{29}Si NMR Figure 2.5 assigns the peaks found after ^{29}Si NMR measurements of a silane solution. Peak *a*, *b*, *c* and *d* can be attributed to respectively unhydrolyzed species, to silanol monomers, to dimers and to trimers (and larger condensed species). Broader peaks point at less uniformity and larger networks.

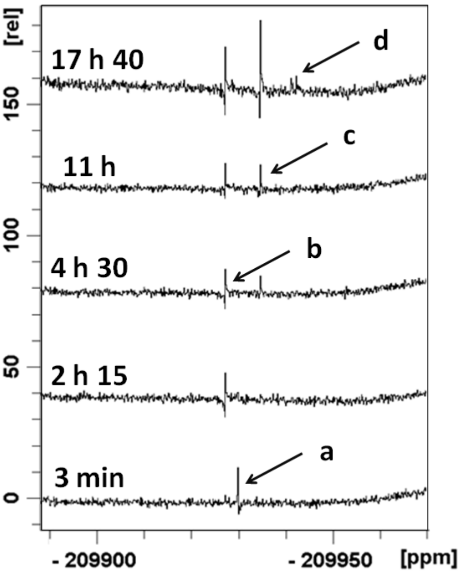

Figure 2.5: ^{29}Si NMR spectra monitoring self-condensation for a 2/90/10 APS/D_2O/MeOD solution. Peak *a*, *b*, *c* and *d* can be attributed to respectively unhydrolyzed species, to silanol monomers, to dimers and to trimers (and larger condensed species).

2.3.2.2 Measuring Details

Table 2.4 gives details on the solution composition of samples used to determine the influence of the type of silane and of the pH on hydrolysis and self-condensation kinetics. Table 2.5 provides sample information on ^{13}C NMR measurements monitoring GPS ring opening.

Table 2.4: Samples prepared to study the influence of the type of silane and of acid on silane solution kinetics. The table consists of the compositional name used throughout this work (Name), the amount of silane, acetic acid, water (D_2O) and methanol (MeOD).

Silane	**Name**	**Silane** [µL]	**Acetic Acid** [µL]	**D_2O** [µL]	**MeOD** [µL]
APS	2/90/10	15		670	67.5
	2/1.3/90/10	15	10	650	72.8
GPS	2/90/10	15		670	67.5
	2/1.3/90/10	15	10	660	73.4
BTSE	2/1.3/50/50	15	10	370	370
	2.1/2.3/50/50	15	17	360	360
APS-BTSE	2/1/90/10	20	10	870	97.1

Table 2.5: Samples prepared to study GPS ring opening in solution. The table consists of the compositional name used throughout this work (Name), the amount of silane, acetic acid, water (D_2O) and methanol (MeOD).

Name	**Silane** [µL]	**Acetic Acid** [µL]	**D_2O** [µL]	**MeOD** [µL]
2/90/10	15		670	67.5
2/1.3/90/10	15	9.75	660	73.4

Table 2.6 and 2.7 depict respectively APS and GPS samples and BTSE samples prepared to study the influence of the solvent ratio and the type of alcohol used. Table 2.8 represents samples used to study the influence of the alcohol used on the self-condensation behavior of solutions.

Table 2.9 and 2.10 give details on the sample preparation applied when monitoring the influence of the silane concentration on the hydrolysis and self-condensation kinetics.

Table 2.6: Samples prepared to study the influence of the solvent ratio and the type of alcohol on APS and GPS solution hydrolysis kinetics. The table consists of the compositional name used throughout this work (Name), the amount of silane, water (D_2O) and alcohol: methanol (MeOD) or ethanol (EtOD).

Name	**Alcohol**	**Silane** [µL]	**D_2O** [µL]	**Alcohol** [µL]
2/100/0	-	15	740	0
2/90/10	MeOD	15	670	67.5
2/90/10	MeOD	15	670	67.5
2/70/30	EtOD	15	520	220
	MeOD	15	520	220
2/50/50	MeOD	15	367.5	367.5

Table 2.7: Samples prepared to study the influence of the type of alcohol on BTSE solution hydrolysis kinetics. The table consists of the compositional name used throughout this work (Name), the amount of silane, water (D_2O) and alcohol: methanol (MeOD) or ethanol (EtOD).

Name	**Alcohol**	**BTSE** [µL]	**Acetic Acid** [µL]	**D_2O** [µL]	**Alcohol** [µL]
2/1.3/50/50	MeOD	20	15	480	480
	EtOD	20	15	480	480

Table 2.9: Samples prepared to study the influence of the silane concentration on self-condensation kinetics in solution. The table consists of the type of silane and alcohol used, the compositional name used throughout this work (Name), the amount of silane, acetic acid, water (D_2O) and alcohol: methanol (MeOD) or ethanol (EtOD).

Silane + Alcohol	**Name**	**Silane** [µL]	**Acetic acid** [µL]	**D_2O** [µL]	**Alcohol** [µL]
APS (EtOD)	2/90/10	20		880	98
	5/90/10	50		860	95
GPS (MeOD)	2/1.3/90/10	20	15	870	96
	5/1.3/90/10	50	15	840	94

Table 2.8: Samples prepared to study the influence of the type of alcohol used on self-condensation kinetics in solution. The table consists of the type of silane, the compositional name used throughout this work (Name), the amount of silane, water (D_2O), acetic acid and alcohol: methanol (MeOD) or ethanol (EtOD).

Silane	**Name**	**Alcohol**	**silane** [µL]	**Acetic Acid** [µL]	**D_2O** [µL]	**Alcohol** [µL]
APS	2/90/10	MeOD	20		880	98
		EtOD	20		880	98
GPS	2/1.3/90/10	MeOD	20	15	870	96
		EtOD	20	15	880	98
BTSE	2/1.3/50/50	MeOD	20	15	480	480
		EtOD	20	15	480	480

Table 2.10: Samples prepared to study the influence of the silane concentration on hydrolysis kinetics. The table consists of the type of silane and alcohol used, the compositional name used throughout this work (Name), the amount of silane, water (D_2O) and alcohol: methanol (MeOD) or ethanol (EtOD).

Silane + Alcohol	**Name**	**Silane** [µL]	**D_2O** [µL]	**Alcohol** [µL]
APS (EtOD)	2/90/10	20	880	98
	5/90/10	50	860	95
GPS (MeOD)	2/90/10	15	670	68
	4/90/10	40	860	96
	8/90/10	80	830	92

2.3.3 Spectroscopic Ellipsometry

Spectroscopic Ellipsometry (SE) measurements help in determining the thickness of thin layers.

These measurements were performed by the Materials and Chemistry Department (MACH), Vrije Universiteit Brussel, Brussels, Belgium, using a M2000X VIS-VASE of J. A. Woollam Co. Inc. working in the UV-visible-NIR (250-1700 nm) spectral range with a 10 nm wavelength resolution to determine the thickness of the deposited silane coatings. The spectra of different samples were acquired at three different incident angles (70°, 75° and 80°), within the range of 245-800 nm. CompleteEASE version 5.04 software was used to fit the calculated response δ (λ) (phase difference) and Ψ (λ) (amplitude component) of the model to the experimental data, where the blanc, uncoated SST plates were used as a reference. As the SST plates were mirror polished, the surface roughness at the interface was not taken into account [120]. For the purpose of comparison, a constant refractive index of 1.4 was assumed for the silane layer [86].

2.3.4 Electron Microscopy

Scanning electron microscopy (SEM) measurements on coated substrates help to visualize the consequences of self-condensation in solution. Transmission EM (TEM) and variations thereof enable determination of the silane layer thicknesses and help in allocating certain elements.

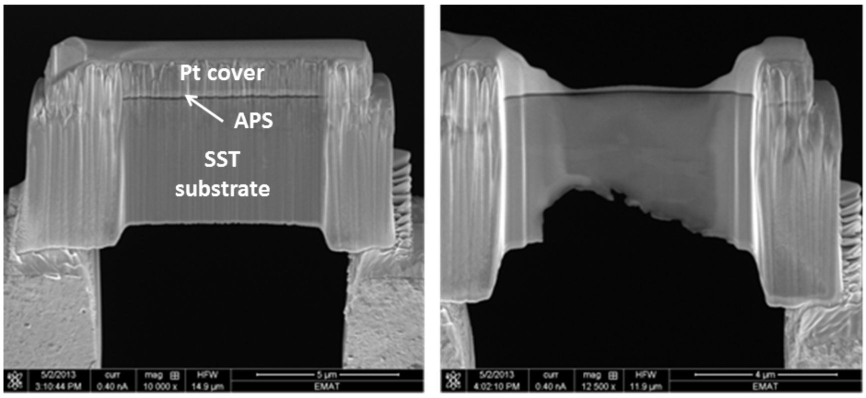

Figure 2.6: FIB-SEM images of a TEM sample, before and after thinning of the sample, that was platinum coated before turning on the focused ion beam.

SEM measurements were done as described in Section 2.2.3. EMAT (Electron Microscopy for Materials Science), University of Antwerp, Antwerp, Belgium provided (Scanning) Transmission Electron Microscopy ((S)TEM)micrographs. TEM, high resolution TEM (HR-TEM) and High Angle Annular Dark Field Scanning TEM (HAADF-STEM) micrographs were collected from a FEI Tecnai F20 operated at 200 kV. In order to visualize the silane layer more clearly, samples were protected with a platinum covering layer and thinned down to electron transparency by a focused ion beam (FIB) treatment, resulting in samples as shown in Figure 2.6.

2.3.5 Atomic Force Microscopy

Atomic force microscopy (AFM) measurements can provide information on the appearance of the coated steel substrates, and were performed as in Section 2.2.2. Measurements were performed as soon as possible after silane coating.

2.3.6 Tensiometry

Tensiometry reveals information on the upper 0.5-1 nm of the substrate. As the substrate is coated with a thin layer of silane, it also provides information on the silane layer. A study of the advancing and receding angle can provide information on the low and high energy component of the surface, as described in the Chapter Literature, Section 1.4.4.

Coated samples were measured as soon as possible after taking them out of the oven, with the time between the oven treatment and the start of the measurement about 4 min, unless mentioned otherwise. Measurements were performed as described in Section 2.2.4.

2.3.7 Mechanical Characterization

Mechanical testing reveals information on the mechanical strength of silane coupled SST-epoxy joints. Combining those results with chemical (and physical) information enables determination of optimal silane coating conditions.

Mechanical testing was done in collaboration with the Materials and Chemistry Department (MACH), Vrije Universiteit Brussel, Brussels, Belgium. The blanc reference sample was only US cleaned before epoxy application and testing, other samples were silane coated. When studying the influence of solution ageing, a 2/90/10 APS/H_2O/EtOH solution was left for 16 days before deposition. Meanwhile other details were kept the same as in Section 2.5.7.

2.3.7.1 Mechanical Characterization: Stainless Steel Dollies

After simulations done by the University of Gent, Gent, Belgium, the mechanical testing setup was slightly changed using SST dollies instead of aluminum dollies. If these dollies were used, it is explicitly mentioned (in the respective Figure caption). The testing methodology and data processing when using this type of dollies is identical to the methodology and processing when using aluminum dollies.

2.3.7.2 Stainless Steel Fibers

Stainless steel fiber (type 316) samples were silane coated as described before (Section 2.3.1). When using an epoxy matrix the composite plates were prepared using a vacuum assisted resin infusion technique, whereas in case of a polyamide matrix the samples were prepared by compression molding [211]. Those samples required a different testing setup to determine the mechanical strength, and 3-point bending tests were used to characterize those samples. Measurements and processing were done by Michaël Callens, Department of Materials Engineering, KU Leuven, Leuven, Belgium.

2.3.8 X-Ray Photoelectron Spectroscopy

X-ray Photoelectron Spectroscopy (XPS) is used to determine the chemical composition of the silane layer on the SST substrate. It enables determination of the chemical requirements resulting in best polymer-steel hybrid performance.

Measurements were performed as in Section 2.2.5. Specifications used for calculations concerning the influence of the rinsing procedure and oven conditions on the appearance of coated stainless steel surfaces can be found in Table 2.11. Specifications used when assigning oxygen subpeaks can be found in Table 2.12. An uncoated sample was included as a reference. When comparing data, high and low resolution data were converted appropriately to obtain reliable comparison.

Table 2.11: Specifications used during peak assignments after XPS measurements for coated samples with different rinsing procedures.

Element	**Peak End** *eV*	**Peak Start** *eV*
C (Low resolution)	292	279.3
C (High resolution)	290.25	281.05
O (Low resolution)	536.6	524.7
O (High resolution)	536	526.6
Fe	716.8	704
N	403.5	395
Si	105.4	98.4

Table 2.12: Specifications used for decomposition of the oxygen peak in XPS spectra for samples using different rinsing procedures (high resolution peak) [67].

Element	**Peak** *eV*
O^{2-}	530.0
OH	531.6
(Si-)OSi	532.7
H_2O	533.6

2.3.9 ThermoGravimetric Analysis

Measuring the weight loss of a sample as a function of time (and temperature) by ThermoGravimetric Analysis (TGA) can give information of the behavior of silane solutions under different oven conditions. Measurements can was performed at the department of Materials Engineering, KU Leuven, Leuven, Belgium on an instrument of TA instruments under constant nitrogen flow. A 2/90/10 APS/H_2O/EtOH sample was heated up as quickly as possible to respectively 50, 70, 90, 110 or 130°C, and kept there for 4 h. The theoretical silane mass remaining after condensation assumes no measuring errors, no evaporation of the solvent during handling prior to the measurements and perfect self-condensation of the silane, forming 3 siloxane bonds per molecule.

2.4 Interphase Adaptations: Polylysine

2.4.1 Sample Preparation

As polylysine is a solid powder, the desired mass was determined using a balance, assuming 0.01 mol of amine groups for every g of polylysine. Next other components were added, and deposition was done analogous to what was described in Section 2.3.1.

2.4.2 Kinetic Study: Nuclear Magnetic Resonance Spectroscopy

Hydrolysis kinetics were determined as described in Section 2.3.2. Polylysine was added to a test tube containing the appropriate (amount of) solvent and GPS.

2.4.3 Mechanical Characterization and Electron Microscopy

Mechanical characterization (using stainless steel dollies) was performed with the help from the Materials and Chemistry Department (MACH), Vrije Universiteit Brussel, Brussels, Belgium as described in Section 2.3.7.1, SEM on tested samples was done by EMAT, University of Antwerp, Antwerp, Belgium, according to the procedure in Section 2.3.4.

2.5 Interphase Adaptations: Carbon Nanotubes

Surfactants synthesized in this work starting from polyglycerol (PG) with molar mass y and with x% of the hydroxyl end-groups functionalized with triphenylmethyl groups are further referred to as x%PG y. Solutions involving carbon nanotubes are named according to the amount of surfactant (b mg) and the amount of CNTs (a mg) added to 20 mL of solvent, resulting in an a/b ratio. All samples throughout this work contained 20 mL of solvent, unless mentioned otherwise. As a standard solutions were ultrasonically treated for 60 min before characterization, unless mentioned otherwise.

Silane solution names are again indicated as $x/y/z$ with y and z representing the volumetric percentage of respectively water and alcohol in the solvent.

2.5.1 Coating Handlings

Carbon nanotubes can be deposited at the SST (silane coated) substrate. For the standard layer deposition started with SST substrates coated according to the optimized APS deposition process (2/90/10 APS/H_2O/EtOH, 30 s of dipping, 60 s of EtOH rinsing). However, before oven treatment for 1.5 h at 70°C under vacuum, CNT deposition took place from a sonicated 90/10 H_2O/EtOH solution. The standard CNT deposition procedure started from a CNT solution (20 mL, 90/10 H_2O/EtOH), in which the (APS coated) substrate was dipped for 1 h. Next the edges of the sample were gently touched with tissue to remove excess solution, followed by an oven treatment for 1.5 h at 70° under vacuum.

2.5.2 Surfactant Characterization: Dynamic Light Scattering

Dynamic Light Scattering (DLS) enables study of the the critical micelle concentration in a solution. When reaching the CMC, the intensity of the scattered light is expected to suddenly increase [212].

Measurements were done with a 3D LS spectrometer (LS instruments) with 3D LS spectrometer V6.2 software. The scattered light was detected at an angle of 90° at room temperature. By adding an extra dimension, multiple scattering could be eliminated, although to the price of higher noise. A series of aqueous solutions with different concentrations was prepared from a stock solution.

2.5.3 Surfactant Solution Characterization: Nuclear Magnetic Resonance Spectroscopy

The degree of functionalization of the trityl functionalized PG was determined by nuclear magnetic resonance (^{1}H NMR) (Bruker Avance 300, Bruker, Billerci, MA) (300 MHz) at room temperature in DMSO-d_6 with $\delta = 7.5\text{-}6.8$ (m, -C_6H_5 from trityl), 4.9-4.3 (m, -OH) and 3.8-3.2 (m, CH and CH_2 from the PG). ^{13}C NMR measurements were done with the same equipment. ^{13}C NMR spectra of purified material in dmso-d_6 proved successful functionalization, with the quaternary carbon adjacent to the trityl phenyl groups giving rise to a signal at 85.7 ppm. The peak at 143.9 ppm originates from the quaternary carbon from the phenyl groups, whereas the other 5 phenyl carbons produce peaks at 128.3 ppm, 127.8 ppm and 126.9 ppm. The signals from the hyperbranched PG structure can be found between 81 and 60 ppm. DEPT-135 spectra confirm this analysis. Further specifications used were analogous to Section 2.3.2.

2.5.4 CNT Solution Characterization: UltraViolet-Visible Spectroscopy

UltraViolet-Visible Spectroscopy (UV-Vis) can be used to determine the amount of dispersed carbon nanotubes in solution if the absorbance per mg of dispersed carbon nanotubes is known. The amount of dispersed multi-walled CNTs (MWCNTs) is proportional to the absorbance of the solution [184]. To determine the absorbance per mg of dispersed CNTs a low amount of nanotubes was dispersed, and TEM confirmed full dispersion of the nanotubes.

While sonicating the CNT solution (UP200S US processor, Hielscher Technology) for 60 min with a cycle of 0.65 and an amplitude of 70%, samples were taken and analyzed at regular time intervals. These intervals are referred to as ultrasonication time (US time). The analysis by UV-vis (Lambda 900, Perkin Elmer) happened in a 1.00 mm cuvette (QS high precision cell, Helma Analytics) to evaluate solubility and surfactant efficiency. The absorbance at wavelengths from 700 nm down to 200 nm was measured and corrected by subtracting a surfactant solution baseline. To further avoid interference from the surfactants displaying varying absorption between 200 nm and 400 nm, the absorbance at a wavelength of 500 nm was chosen for further analysis (after the mentioned baseline correction). An absorbance of 0.244 and 0.238 for respectively the pristine and the acid functionalized CNTs was found for every mg of nanotubes dispersed (in 20 mL of water) by combining TEM (displaying full dispersion) with UV-Vis. Sigmoidal fits added to the resulting data only serve as a guide to the eye.

2.5.5 Solution Characterization: Transmission Electron Microscopy

TEM reveals information about the dispersion quality of a carbon nanotube solution.

Measurements were done by EMAT (Electron Microscopy for Materials Science), University of Antwerp, Antwerp, Belgium. Samples were prepared by suspending a CNT/surfactant solution in ethanol, followed by deposition of a drop of this suspension on a carbon coated TEM grid. TEM and HR-TEM micrographs were collected from a FEI Tecnai F20 operated at 200 kV.

2.5.6 Deposition Characterization: Scanning Electron Microscopy

SEM analysis of CNT coated SST samples (1 x 1 cm^2) (mounted on a steel sample holder) was done with an XL FEG SEM (Philips, Eindhoven, The Netherlands), with spot 3 and diaphragm 2 using secondary electrons, an electron beam voltage of 10 keV and a secondary electron detector. Samples were carbon sputtered before analysis, ensuring conductivity. Data processing took place with EDAX Genesis software. EMAT, University of Antwerp, Antwerp, Belgium, also provided SEM images of samples, taken with a FEI Quanta Microscope operated at 10 keV.

2.5.7 Mechanical Characterization

Mechanical testing was done in collaboration with the Materials and Chemistry Department (MACH), Vrije Universiteit Brussel, Brussels, Belgium, as described in Section 2.3.7.1, thereby using stainless steel dollies.

Chapter 3

Steel Surface Characterization

Many research reports on hybrid and composite failure associated with the substrate-adhesive interphase, the primary zone of weakness [9, 80]. This highlights the importance of appropriate interface and surface control. Surface conditioning/pretreatment seems the key to adhesive bonding and long-term service capability due to various reasons [38, 213]. Silane application improves bond durability, but the importance of substrate treatments prior to silane coating cannot be underestimated.

A successful joint requires intimate contact between the adhesive and the substrate surface. This means adequate wetting of the substrate, which requires at least a clean surface. It has been theoretically described that increasing the surface energy of adherent and lowering the surface energy of the adhesive enhances wetting (Section 1.4). Therefore, the primary objective of a surface pretreatment is to increase the surface energy of the adherent [214]. Moreover pretreatments should increase the availability of reactive groups for interaction with the silane in a next stage, resulting in more and stronger bonds and thus improved composite performance after application of the appropriate matrix. This becomes clear from the silane reaction scheme in the Literature Chapter (Figure 1.5). This scheme points at the need for a controlled oxide layer in addition to a clean and smooth surface to achieve good bonding between silane and steel (Section 1.3.2.1) [42]. Franquet et al. mentioned that silane film uniformity and thickness strongly depend on the substrate pretreatment [35].

During this work, protocols are optimized using stainless steel 304 steel plates (SST) as the substrate. Experimental details can be found in the Chapter Materials and Methods, Section 2.2.

3.1 Results and Discussion

3.1.1 Morphological Characterization: AFM and SEM

Figure 3.1 depicts an AFM height (left) and phase (right) micrograph of an uncleaned SST substrate, both demonstrating the presence of nanometer sized features. After ultrasonic (US) cleaning their presence decreases, resulting in a surface as shown in Figure 3.2 (different scale!). The production processing of the steel substrate causes the vertical lines clearly seen. The last figure provides information on the roughness of a US cleaned SST substrate, with R_a (arithmetic mean value) and R_q (quadratic mean) respectively 11.0 and 14.4 nm. Honkanen et al. did similar experiments, thereby noting similar roughness [22]. Boulange et al. on the contrary found a higher roughness, with a R_a value of 50 nm [215], probably due to differences during substrate production.

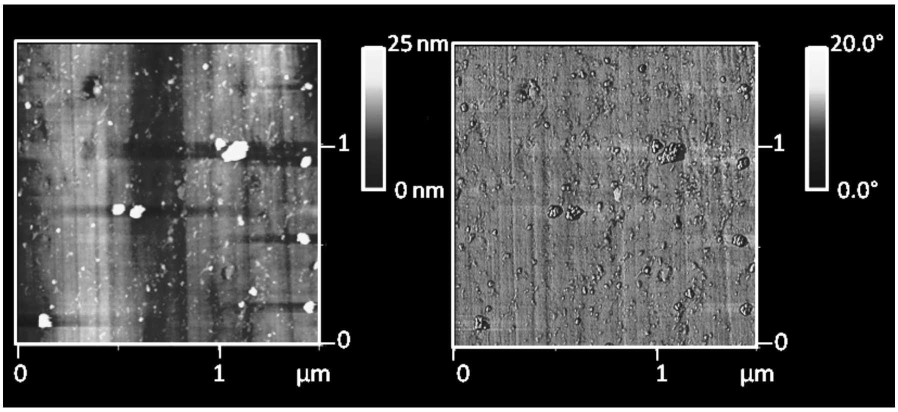

Figure 3.1: AFM micrographs of an uncleaned SST surface demonstrating nanometer sized features: height (left) and phase (right) image.

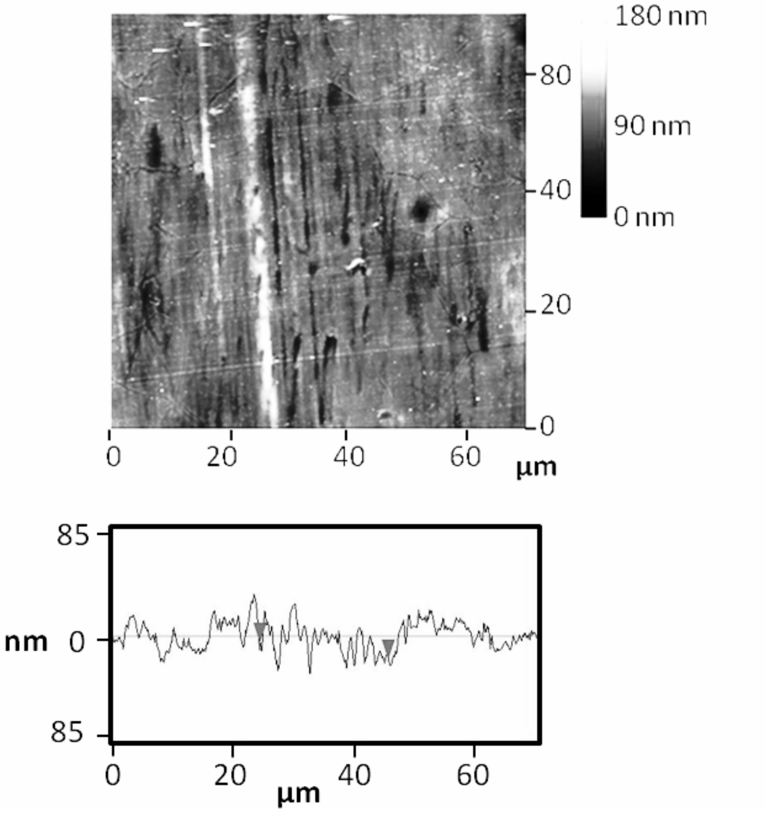

Figure 3.2: AFM height micrograph and roughness profile of a US cleaned SST surface.

SEM micrography (Figure 3.3) confirms the topography found by AFM measurements, again demonstrating the processing artifacts (upper and left image), as well as the presence of scratches and damage due to sample handling (right image). At the upper image features with a diameter of about 10 µm appear, which might be grain boundaries, typical for this type of materials.

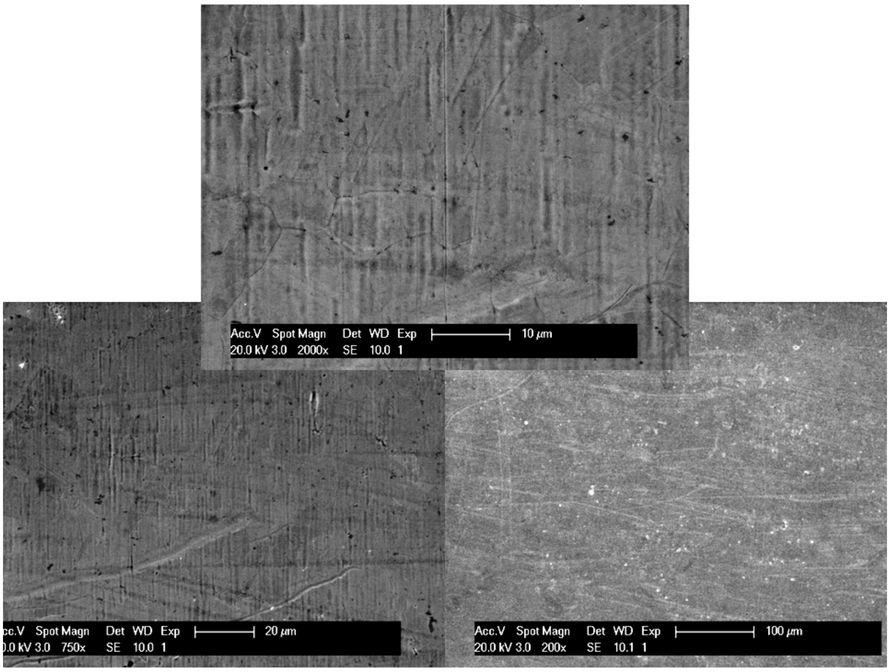

Figure 3.3: SEM micrographs of a US cleaned SST sample, demonstrating handling damage.

3.1.2 Chemical Characterization: EDX, Tensiometry and XPS

EDX spectra (Table 3.1) confirm the 18/8 composition of the SST 304 substrate used, although this technique is not as accurate as e.g. XPS (a deviation of 2% of is possible). Moreover it only provides information on the upper layer as it has a measuring depth of ± 2 µm. The detected intensity is proportional to the elemental molar mass, which causes high(er) detection limits for lighter elements, including carbon and nitrogen. Because of this higher detection limit, no carbon signal shows up, although the surface should contain at least some carbon contaminants. EDX clearly demonstrates the presence of silicon, due to compositional silicon in the substrate and contaminant adsorption on the surface.

Table 3.1: Composition of a US cleaned SST substrate surface as obtained by EDX. Because of the higher detection limit, no carbon signal can be seen.

Element	**Wt** %
O	3.16
Si	0.47
Cr	18.36
Fe	69.66
Ni	8.35

Both carbon and silicon signals in Figure 3.4 mainly originate from contaminants such as aliphatic carbon and polydimethylsiloxane. The impurity layer as well as the oxygen layer of the steel surface are very thin as concluded from XPS measurements and sputtering of uncleaned samples (Figure 3.4) (See also Section 1.2.1.3). 90 s of sputtering removes about 10 Å of the upper surface and removes a large portion of the carbon, most of the oxygen and almost all silicon. The reduction in the amount of silicon and carbon points at the removal of contaminants. Reduction of the oxygen peak proves (partial) removal of the oxide layer. Removal of these contaminants and the oxide layer, causes higher exposure of the bulk material and an increased iron signal, mainly due to metallic iron. These results confirm findings of Vittoz, who found that iron is mainly located in the bulk, below the passive, oxidized layer and below a contaminant film [216]. The small nitrogen peak can be caused by contaminants or compositional nitrogen. Literature already mentioned enrichment of this element at the surface after annealing [25]. However, the signal is very low as the abundance of this element is $< 0.1\ wt\%$.

The carbon signal after sputtering is probably mainly caused by recontamination, illustrating the speed of carbon contaminant adsorption, even in a vacuum chamber. Underhill et al. already noted the appearance of a thin layer of carbon contaminants on freshly prepared surfaces, even in the cleanest atmosphere [31]. The absence of silicon after sputtering points at the fact that these impurities absorb much more slowly or that they are due to handling rather than to environmental exposure. Even after sputtering a fraction of oxygen can be seen (Section 1.2.1).

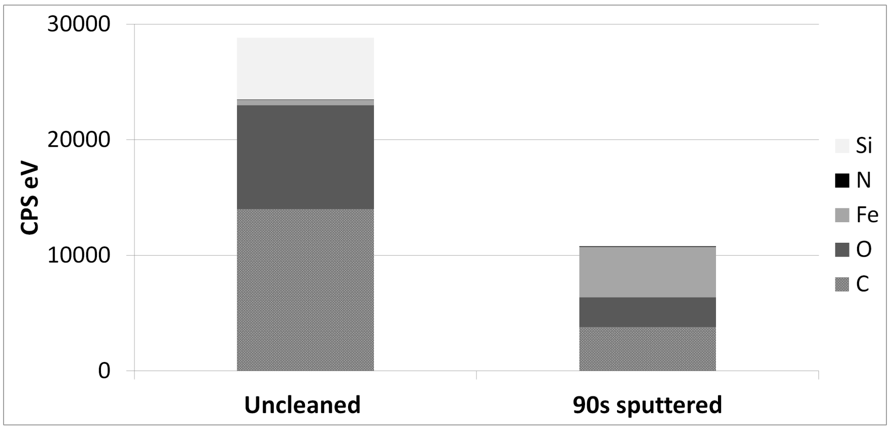

Figure 3.4: Elemental abundance before and after 90 s of sputtering of an uncleaned SST substrate as calculated from XPS measurements. The amount of contaminants clearly decreases after sputtering, while the iron signal becomes more visible due to exposure of the bulk material.

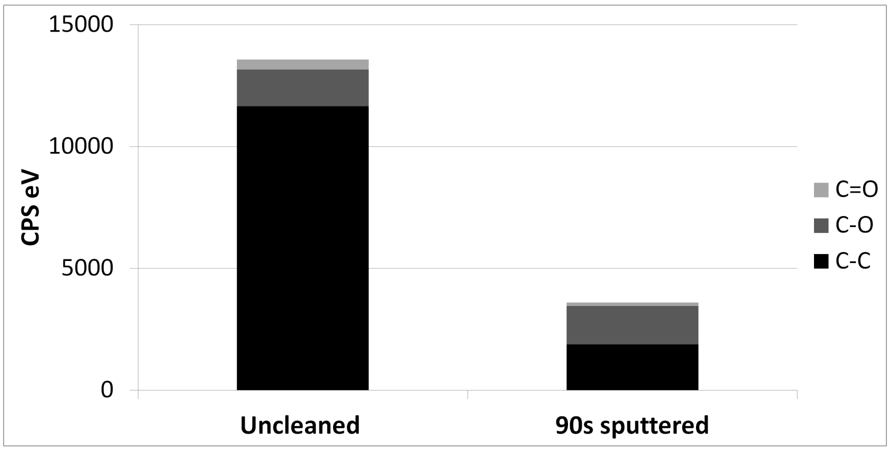

Figure 3.5: Relative abundance of carbon subpeaks before and after sputtering of an uncleaned SST substrate as calculated from XPS measurements. Cleaning mainly removes aliphatic carbon.

Figure 3.5 depicts the carbon subpeaks of an uncleaned sample and their abundance before and after sputtering. It confirms the presence of a carbon layer before sputtering of an uncleaned SST substrate, mainly consisting of aliphatic carbon. Sputtering removes most of those aliphatic species, while most of the oxidized species remain after sputtering. This probably can be ascribed to compositional oxidized carbon, fast reoxidation or preferential readsorption of the more polar carbon species.

3.1.2.1 Influence of Cleaning Method

As stated before an increase of the surface energy can enhance wetting and adhesion. During this work it was decided to work with water contact angles that reveal information of a surface. As described in Section 1.4.4 a lower contact angle corresponds to a higher surface energy. The advancing angle relates more to the dispersive part of the substrate surface, while the receding angle relates more to the non-dispersive part.

Figure 3.6 depicts the water contact angles as obtained by the Wilhelmy technique (Section 1.4.3) for different cleaning methods: (acetone and ethanol) wiping, alkaline cleaning with Gardoclean or Ridoline and ultrasonic cleaning in ethanol. Uncleaned samples do have the highest contact angles, both advancing and receding, due to contaminants, while cleaning lowers these angles. Softer physical cleaning methods (wiping), alter those angles only to a limited extend. Chemical alkaline cleaning however, does lower both the advancing and receding angle, but the latter only to a rather limited extend. Ultrasonic cleaning results in the same equilibrium angle compared to alkaline cleaning, but in a significantly lower receding angle, which mainly relates to the polar interactions and (potential) matrix retraction after application of e.g. an epoxy matrix. These polar interactions are related to the (hydr)oxide groups, necessary to bind to the silane later on. Although the equilibrium contact angle after US and alkaline cleaning is not that different, the former method results in a higher contact angle hysteresis, pointing at higher hydrophilicity (Section 1.4) [151]. As both acetone and ethanol wiping result in the same values, only aceton wiping was evaluated during further testing. As Ridoline seems slightly more efficient than Gardoclean as an alkaline cleaning agent the former was used for further testing.

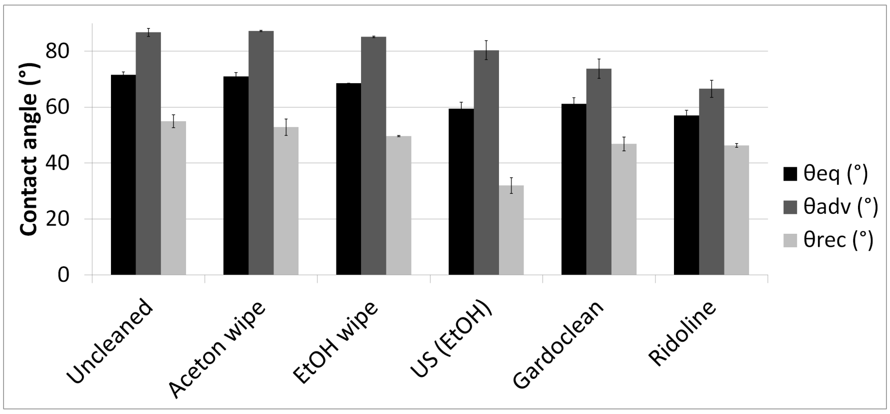

Figure 3.6: Influence of the cleaning method on the equilibrium, advancing and receding contact angle of a SST substrate. Although US and alkaline cleaning result in similar equilibrium angles, US cleaned substrates have higher hydrophilicity.

Honkanen et al. found similar (equilibrium) contact angles for as-received steel. However they observed a contact angle of 57° ± 10° and 78° ± 2° after ethanol wiping and ultrasonic cleaning respectively, which is exactly the opposite of the results found in this work: 67.5° ± 0.6° and 59.5° ± 2.3° for ethanol wiping and ultrasonic cleaning respectively. Their contact angle after wiping has a rather large standard deviation, and methods can slightly differ, e.g. in the duration of the treatment and strength of the ultrasonics, explaining the differences and pointing at the importance of optimizing cleaning procedures case by case [6].

Figure 3.7 depicts the abundance of different elements after the application of different cleaning methods on SST substrates as calculated from the corrected peak area after XPS measurements. All cleaning methods remove part of the carbon and most of the silicon species. Due to the thinner covering contaminant layer after cleaning, X-rays can penetrate deeper into the steel (surface) itself, exposing a higher amount of oxygen (due to the passive oxide layer) and iron (this last one to an even higher extent). Study of the relative abundance of the elements (Figure 3.8) reveals the same trends. Ultrasonic cleaning removes most silicon and exposes most oxygen explaining the lower receding contact angles found during tensiometry. Alkaline cleaning causes lower advancing and higher receding angles compared to US cleaning, probably due to excessive oxygen removal. Note the lack of nitrogen in these samples (the number of counts can be neglected, as they are around the processing error), although literature mentions nitrogen enrichment at the surface after annealing [25].

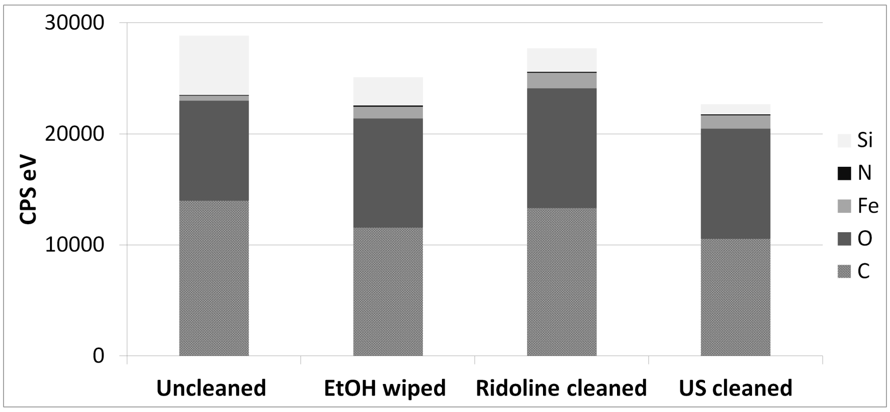

Figure 3.7: Influence of the cleaning method of a SST substrate on the abundance of different elements as calculated from XPS measurements. US cleaning clearly results in the lowest Si and C signal.

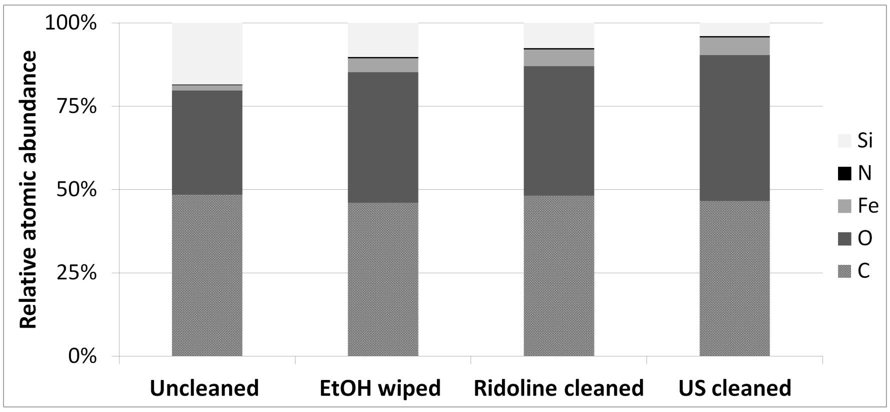

Figure 3.8: Influence of the cleaning method of a SST substrate on the relative abundance of different elements as calculated from XPS measurements.

Figures 3.9 shows the abundance of the XPS carbon subpeaks due to C-C , C-O and C=O species. Cleaning obviously removes carbon components, although to a different extent depending on the cleaning method. The aliphatic carbon peak decreases for all cleaning techniques used, but most drastically in the case of ultrasonic cleaning, while only to a relatively low and intermediate extent for alkaline cleaning and ethanol wiping respectively. Ultrasonic cleaning leads to highest abundance of oxidized carbon species, especially on a relative scale. Also alkaline cleaning leads to a slightly increased amount of oxidized carbon species, probably due to oxidation of carbonaceous remainders during cleaning or readsorption of those species. Ethanol wiping only lowers the absolute amount of all carbonaceous species.

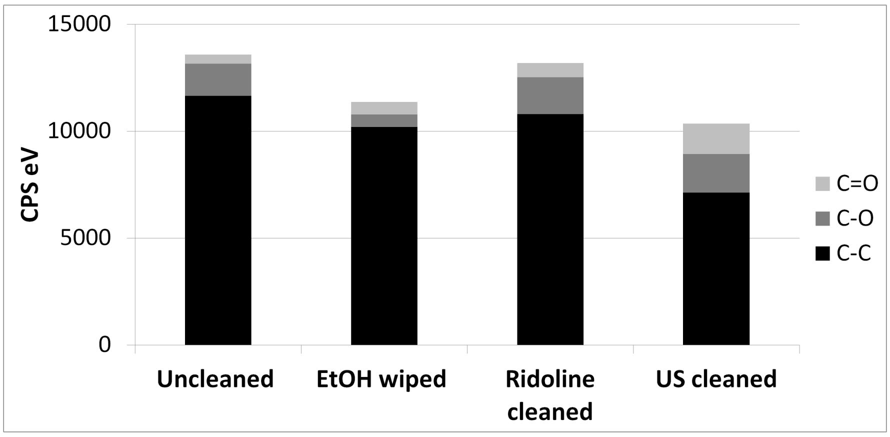

Figure 3.9: Abundance of carbon subpeaks as a function of the cleaning method of a SST substrate as calculated from XPS measurements. US cleaning obviously removes the largest amount of (aliphatic) carbon.

As stated before, chemical treatments can generate a new oxide layer as they remove the initial oxide layer or even etch deeper metallic interfaces, resulting in high substrate porosity. In the meantime chemically active sites can be created on the surface [28]. Figure 3.10 depicts the oxygen peak (as found by XPS) before and after cleaning and reveals that cleaning mainly influences higher reduced oxygen (species) with lower binding energies. Cleaning especially increases the O^{2-} peak and changes the -OH peak only to a rather limited extent. In all cases, water seems barely present, pointing at removal of the chemisorbed water, mentioned in Section 1.2.1.3.

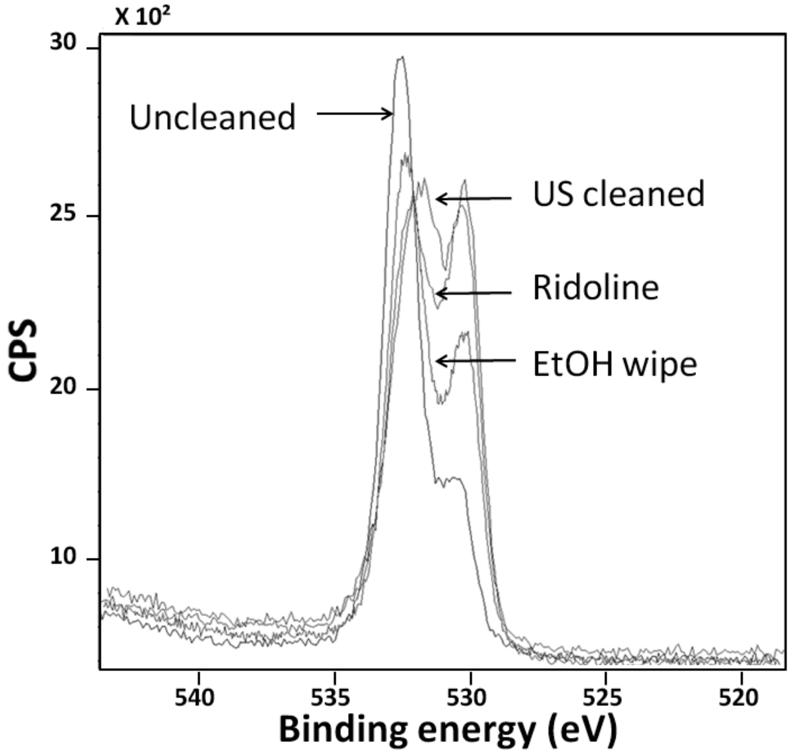

Figure 3.10: Oxygen peak as found by XPS for SST substrates cleaned in different ways. The x-axis displays the binding energy, the y-axis the counts per second (CPS).

Figure 3.11 depicts the exact abundance of the oxygen subpeaks (H_2O, -OH and O^{2-}) and confirms the increased signal of oxidized species after cleaning. This can be ascribed to the exposure of the oxide layer as well as to the generation of (hydr)oxides after cleaning, especially of O^{2-}. The Literature Chapter (Section 1.2.1.3) described the structure of metal oxide layer, with hydroxides on top of oxides. It is conceivable that cleaning removes the upper hydroxide layer to a large extent. Alkaline and US cleaning result in the highest amounts of oxidized species, although alkaline cleaning results in a higher abundance of O^{2-}, probably due to the removal of the upper oxide layer, but possibly also due to the alkaline activity of the cleaning agent. Ultrasonic cleaning especially generates and exposes hydroxyl groups, and exposes oxides, but only to a lesser extent compared to hydroxides. This seems to be in line with the theory of Strobel et al., stating that (chemical) treatments can remove the initial oxide layer (or even etch deeper metallic interfaces), meanwhile creating chemically active sites [28, 140]. Here it has to be taken into account that Strobel reported that overoxidation can lead to a brittle oxide layer, with a detrimental influence on mechanical performance later on [42, 139].

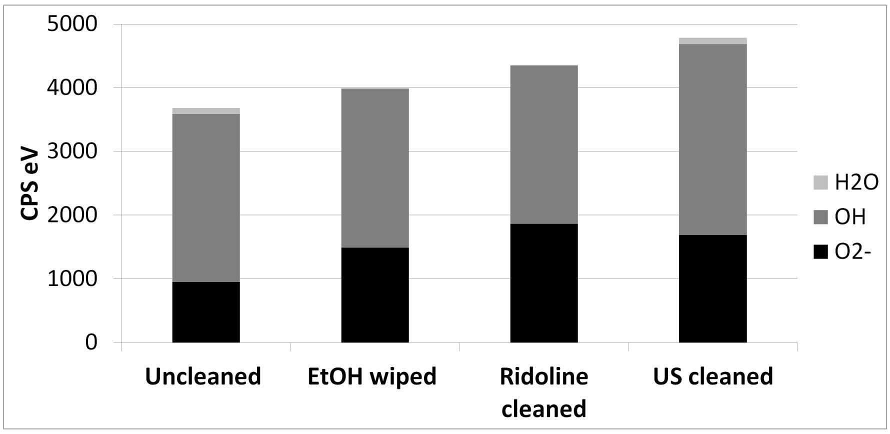

Figure 3.11: Abundance of oxygen subpeaks as a function of the cleaning method of a SST substrate as calculated from XPS measurements. The highest oxygen abundance can be found after US cleaning.

An increase in the oxide concentration will increase the Lewis acid and Lewis base character of the surface [136], thus lowering the receding contact angle and increasing bonding performance towards silanes. According to Strobel et al. adhesion correlates with the electron donating character of the surface [139]. From this point of view ethanol wiping does not perform sufficiently, as it does not create/expose sufficient (hydr)oxides to bind with the silane in the next stage, as confirmed by tensiometry displaying higher advancing and receding angles for these species. This may be due to insufficient carbon removal as well as (consequential) incomplete exposure of the passive oxide layer. Sinmazcelik already noted that solvent degreasing does not promote the formation of acceptable surface conditions for longer term bond durability [32].

Figure 3.12 shows that cleaning increases the iron peak in general, with large variations in the oxidation state, depending on the cleaning technique applied. This can be attributed to the removal of contaminants (and the oxide layer in some cases), increasing exposure of the bulk material. The apparently smaller peak after ethanol wiping is (mainly) due to the use of a different resolution and not to a lower iron signal. Use of correction factors enables comparison of those data in further work.

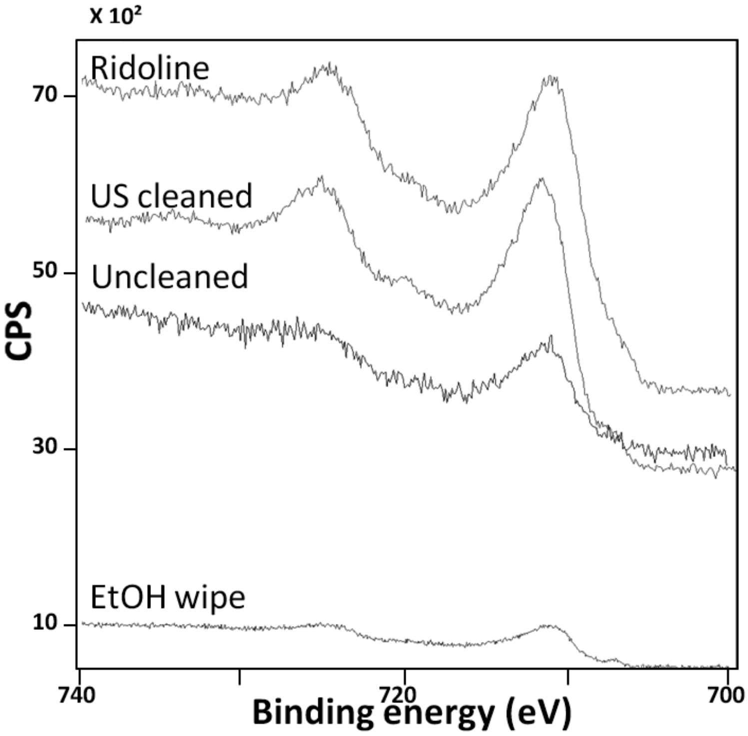

Figure 3.12: Iron peak as found by XPS for SST substrates cleaned in different ways. The x-axis displays the binding energy, the y-axis the counts per second (CPS). The smaller peak after ethanol wiping is due to the use of a different resolution, but correction factors were applied to compare data in further work.

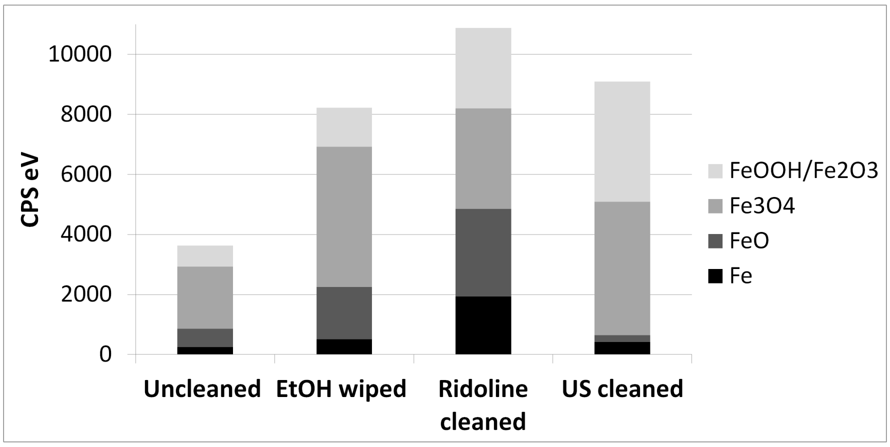

Figure 3.13: Abundance of iron subpeaks of a SST substrate as a function of the cleaning method as calculated from XPS measurements. Especially alkaline cleaning exposes a large amount of (metallic) iron.

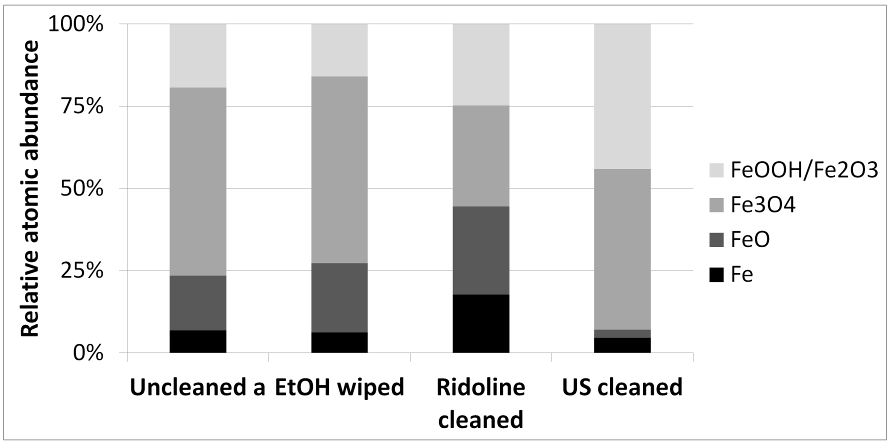

Figure 3.14: Relative abundance of iron subpeaks of a SST substrate as a function of the cleaning method as calculated from XPS measurements.

Figures 3.13 and 3.14 confirm that cleaning decreases the thickness of the contaminant layer as the iron signal increases. However, the type of iron differs widely. Alkaline cleaning increases the absolute amount of iron to the largest extent, with the highest increase in the metallic iron (Fe^0) and the FeO iron peak. The reason for this higher intensity can be twofold: removal of a higher amount of carbon and silicon contaminants (or less readsorption) or an increased removal of the oxide layer resulting in a higher exposure of the bulk. The slightly lower oxygen signal after alkaline cleaning and the higher relative abundance of the metallic iron point at increased removal of the oxide layer. The Fe-peak of a US cleaned sample clearly contains a higher amount of oxidized species compared to alkaline cleaning. This points again at higher removal of the oxide layer. The higher amount of (polar) oxidized species after US cleaning explains the low(er) receding angle for US cleaning compared to a Ridoline treatment. Ethanol wiping clearly exposes a higher amount of iron species compared to the as-received substrate (Figure 3.7), although to a smaller extent compared to other cleaning methods. Study of the relative abundance of the subpeaks demonstrates that the ratios of different iron components remain the same before and after ethanol wiping, indicating that soft physical cleaning has no oxidizing potential regarding the metal nor does it change the composition of the passive layer.

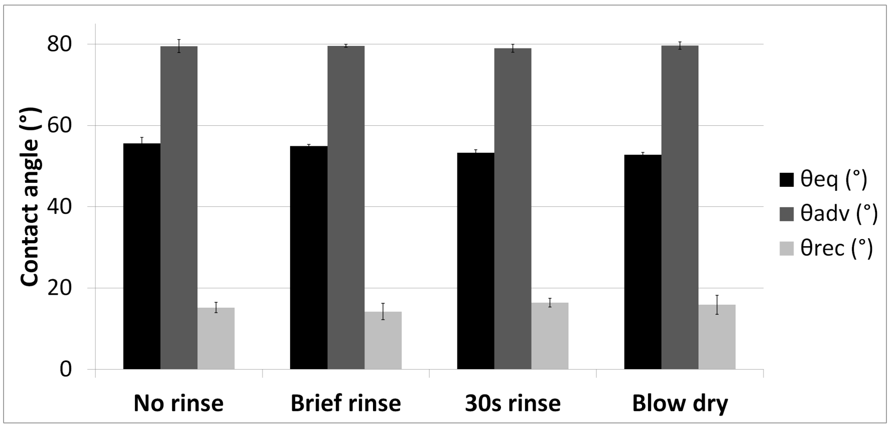

Figure 3.15: Influence of a treatment after US cleaning on the equilibrium, advancing and receding contact angle of a silane coated and oven treated SST substrate. All post treatments result in similar contact angles.

Figure 3.15 depicts the water equilibrium, advancing and receding contact angle of APS coated (standard procedure) samples for different procedures applied after US cleaning. Four treatments are applied, respectively no rinsing after cleaning, a brief and a 30 s water rinse after cleaning and blow drying of the cleaned substrate. All 4 treatments result in similar contact angles after silane deposition and oven treatment, indicating that the same type of layer is formed, with the same silane orientation, density and degree of condensation. The identical curves obtained by tensiometry (on top of the identical angle values, curves not shown) seem to confirm this.

3.1.2.2 Influence of Ageing after Cleaning

Figure 3.16 demonstrates that trends in water contact angles remain the same upon exposure of the cleaned samples for 1.5 h to air before measurement, but angle values increase. For alkaline cleaning, standard deviations of contact angles increase, pointing at less homogeneity. The higher angles confirm the rather ′fast′ adsorption of contaminants, creating a more hydrophobic surface and increasing both the advancing and receding angle and thus also the equilibrium contact angle [126]. Cleaning methods resulting in lower contact angles (alkaline and US cleaning) have a higher increase in (relative and absolute) contact angle values compared to the wiping methods. This probably relates to the higher surface energy of the better cleaned samples, resulting in faster and higher amounts of recontamination. When remeasuring contact angles after 6 h no additional change in contact angle is observed. This does not mean that no additional contaminant adsorption takes place, but it does confirm the fast coverage of the entire substrate with a contaminant layer of at least 1-2 nm thickness, the measuring depth reached with tensiometry.

Literature already mentioned carbon contamination takes place quickly after cleaning, requiring only a few minutes to absorb at least 2-3 monolayers of carbon contaminants [216]. Even freshly prepared surfaces possess the before mentioned thin layer of carbon contaminants which inhibit the formation of chemical bonds [31, 32]. To avoid this contamination adsorption as much as possible, substrates should be used (almost) immediately or be stored in e.g. a desiccator after cleaning [31, 33–35].

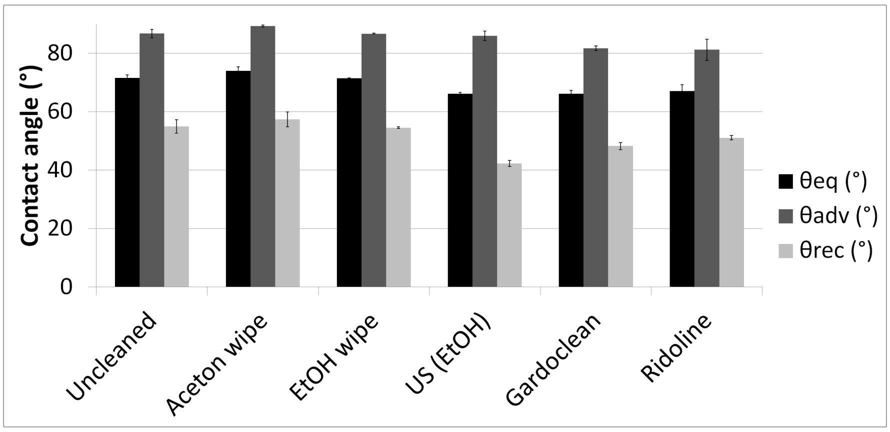

Figure 3.16: Influence of 1.5 h of ageing after cleaning of a SST substrate on the equilibrium, advancing and receding contact angle. All angles clearly increase after ageing (compare with figure 3.6).

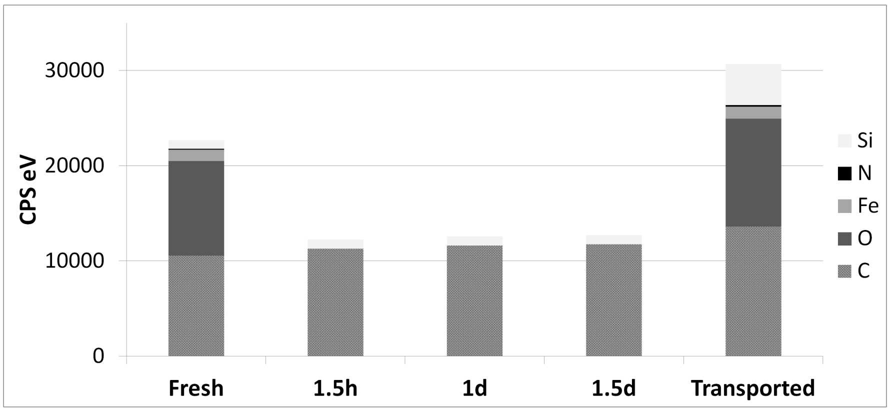

Figure 3.17: Influence of ageing after US cleaning of a SST substrate on contaminant readsorption as shown by the abundance of different elements as calculated from XPS measurements. For samples aged in the vacuum chamber only the silicon and carbon peak were measured. Transported means the sample was not cleaned on place but transported in between cleaning and measuring in a closed container.

Figure 3.17 shows the influence of ageing (in the XPS vacuum chamber) on the adsorption of carbon and silicon contaminants as found by XPS (other elements were not measured). It also illustrates the influence of sample transport on the absolute abundance of different elements. It can be clearly seen that most reabsorption of carbon contaminants occurs in the time span immediately after cleaning. Longer ageing induces some extra contaminant adsorption, although in a relative way. Most recontamination takes place immediately after cleaning. Cleaning the sample in one place and transporting it to another (within a day) clearly leads to excessive contaminant adsorption, especially of the silicon contaminants. This probably can be due to its enclosure in and thus contact with a small plastic container during transport, as well as to ′air′ pollutants.

Figure 3.18 reveals that during ageing especially aliphatic carbon contamination takes place, as was also found in literature [32]. Transporting cleaned samples increases not only the C-C but also the C-O peak, confirming a considerable difference between ′air′ ageing and ′transport′ ageing, although both clearly should be avoided.

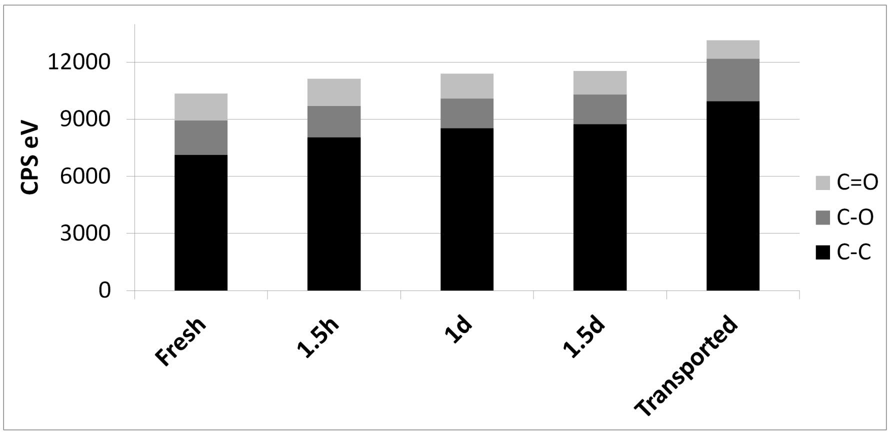

Figure 3.18: Abundance of carbon subpeaks as a function of ageing time of a SST substrate after US cleaning as calculated from XPS measurements. Especially the aliphatic carbon peak increases upon ageing.

3.1.3 Mechanical Characterization

Liu et al. already studied the fracture energy of metal-epoxy joints as a function of the metal pretreatment, and found that this energy at least doubles when using the appropriate treatment [39]. Del Real et al. confirm this trend and report different failure modes for different treatments [80]. Also this work demonstrates an influence of the substrate pretreatment on the joint strength of silane coated metal-epoxy joints as tested with a dolly setup. Figure 3.19 depicts the influence of 2 substrate cleaning methods on the mechanical strength of APS coupled SST-epoxy joints. The strength of a blanc, US cleaned but uncoated substrate is added for comparison. The type of substrate pretreatment clearly has an influence on the quality of the silane layer deposited. As ethanol wiping clearly led to inferior properties regarding wetting properties and the presence of polar groups and contaminants (Section 3.1.2.1), only ultrasonic and alkaline (Ridoline) substrate cleaning before silane application were tested.

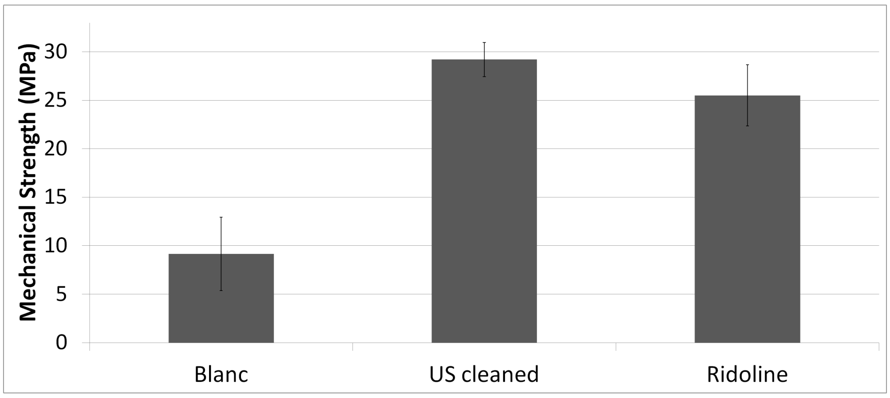

Figure 3.19: Influence of the cleaning procedure of a SST substrate on the mechanical strength obtained from dolly testing of a blanc and silane coated SST-epoxy samples. A silane coating improves the mechanical strength and also appropriate cleaning improves results.

When comparing joints starting from APS coated steel cleaned in different ways, but silane coated in the same way, alkaline cleaning leads to a significant lower strength compared to US cleaning (respectively 25.5 ± 3.2 and 29.2 ± 1.8 MPa). The higher strength for the latter can be attributed to the presence of more oxidized species to react with the silane after its application. Ochoa already claimed that the surface energy and interfacial adhesion possess a direct relationship with the amount of polar groups on the surface [43]. Susac et al. found that an oxide layer improved silane bonding to an aluminum surface [217], and our results (as well as work of Honkanen) indicate that this is also valid for stainless steel [6]. Honkanen mentioned improved silane bonding to a steel surface when using a clean Fe_2O_3-type surface oxide. This work also confirms this trend with the best performance and highest Fe_2O_3 content after ultrasonic cleaning (Figure 3.13) [42].

APS can form only occasional (weaker) bonds with the surface for low hydroxyl concentrations, resulting in more random molecular orientation and a higher amount of self-condensation. This type of bonding favors to the formation of thick silane clusters [20, 45] and explains the more uniform film formation on surfaces with a high hydroxyl concentration.

3.2 Conclusion

Experiments reveal cleaning of as-received stainless steel substrates is necessary to remove carbon and silicon type contaminants and to improve bonding to the silane in a next stage. This increases performance of SST-epoxy joints, coupled by a silane coupling agent. Tensiometry and XPS reveal highest hydrophilicity for ultrasonically cleaned samples, due to the highest amount of (hydr)oxides exposed during this treatment. Alkaline cleaning also leads to rather clean surfaces with a similar equilibrium Young contact angle. However, resulting cleaned surfaces are not as hydrophilic compared to the US cleaned ones, and show a lower amount of (iron)oxides and a higher amount of metallic iron, pointing at excessive removal of the oxide layer. The alkaline cleaning agent may aggressively remove the oxide layer, and generate porosity and a brittle oxide layer that acts as the weak point in the joint and decreases the overall strength. The need for contaminant removal and a high amount of hydroxyl groups to improve joint performance was confirmed by mechanical testing. It leads to a higher sample strength for US cleaning compared to alkaline cleaning before silane application. From this, it was decided to proceed with US cleaned samples during next steps of treatment optimization, as US cleaning obviously leads to the best coupling conditions in the next step of silane application.

Tensiometry revealed that there is no influence of a treatment immediately after cleaning. Nonetheless it was decided to water rinse the substrate, in order to be sure that remainders of the cleaning medium do not influence the silane application in a next step. This application has to take place as soon as possible after cleaning of the substrate, as XPS and tensiometry confirm fast recontamination. This should be avoided as it buries the oxide layer under a layer of carbon and silicon species that inhibit or complicate coupling to the silane.

Chapter 4

Silane Coating Application

Maximal composite performance requires optimization of the adhesion at the interface. Many authors report on optimization of this interfacial strength, and use silanes to construct metal-polymer joints. Covalent attachment of monofunctional organosilanes has been proven to be a simple and versatile method for tuning the properties of solid surfaces such as wettability, surface activity and adhesion [218]. However, this only holds for optimal silane coating conditions, that depend on different parameters in the case of wet chemical application. This type of application offers flexibility during handling, is accessible at a low cost, and is investigated to the fullest during this work.

In order to get maximum silane adhesion to the substrate, silane reactions during the coating process should be kept in mind (Figure 1.5). The working window, the time span starting after obtaining sufficient hydrolysis and ending when self-condensation becomes important is of major importance, and preferably the solution is handled during this time span. Meanwhile the organofunctional group should remain available for covalent reaction or physical interaction with the matrix [9, 14, 20].

The global silane coating process concerns several steps (Figure 1.6), starting with the preparation of an appropriate silane solution. Next the cleaned substrate is dipped in this solution for a certain time, allowing silane adsorption, followed by an optional rinsing step in ethanol to remove excess (physically bound) silane. The combination of this dipping and rinsing is called 'the deposition process' in next sections.

Condensation of the ensemble takes place in a vacuum enabled oven. The process from solution preparation up to oven treatment will be further referred to as the coating process. Literature does not always agree on the influence of different parameters on the resulting hybrid performance, due to the sensitivity of the system to small changes and impurities in the system. This work aims at parameters optimized for the highest mechanical strength for commercially available systems, and tries to explain trends observed during testing. A note has to be made that optimization of the coating process mainly focuses on the steel-silane interaction, the most crucial point in these hybrids. Silane-matrix interaction in general is not taken into consideration, as up to now this does not form the weak point in this type of polymer-steel joints.

Coated samples can be characterized physically/visually and chemically to study the silane layer further into detail. Application of an epoxy matrix on a silane coated substrate results in samples for mechanical testing. More experimental details can be found in the Materials and Methods Chapter (Section 2.3).

4.1 Silane Solution

The solution working window should be respected for optimal adhesion and reproducibility and different parameters influence this working window. The type of silane, the solvent and its composition as well as the silane solution concentration and pH (catalytic effect) all have their own influence. The parameter of temperature, speeding up reaction rates, was not studied during this work, in order to keep the system as simple as possible [219].

Despite the fact that from an economical and environmental point of view water/ethanol solvents offer a more attractive combination compared to e.g. water/methanol, first optimization work uses methanol-d_4 (MeOD), as ethanol-d_6 (EtOD) prices largely exceed those of the methanol. After this, promising ratios are again characterized with ethanol replacing methanol, and also further work starts from ethanol containing solutions.

4.1.1 Solution Characterization: NMR

Hydrolysis determines the reactivity of a silane solution, while condensation determines its stability. In other words hydrolysis determines the start of the working window, whereas the onset of considerable self-condensation (mostly) marks the end. The extent of hydrolysis can be monitored by ^{1}H NMR, while that of condensation can be monitored by ^{29}Si NMR, as described in the Materials and Methods Chapter, Section 2.3.2 [51].

Because of the relative insensitivity of ^{29}Si NMR, these measurements are used merely qualitatively. It is possible to distinguish peaks due to monomers, dimers and trimers or networks, and thus to estimate the time at which self-condensation sets in or becomes considerable [220, 221]. Due to the ^{2}H substituents of D_2O, it has (slightly) slower kinetics compared to H_2O [222]. This means that the minimum ageing time of solutions using distilled water (for larger scale lab work and practical applications) still can be (slightly) lower compared to that of NMR samples.

4.1.1.1 Influence of the Type of Silane and pH

Hydrolysis as well as condensation kinetics depend on the molecule used, and in general hydrophilic silanes are known to hydrolyze very fast, whereas (more) hydrophobic silanes need at least a few hours to hydrolyze completely [63]. Despite the water insolubility of more hydrophobic species, they become hydrophilic upon hydrolysis, rendering them more water soluble. Molecules regain the hydrophobicity of the parent silane after the formation of a siloxane network. Hydrophobicity decreases the solution stability, which can be observed visually. Haziness points at loss of the solution stability or phase separation, due to either a lack of hydrolysis or the presence of condensation reactions [41, 47, 223]. In general the addition of acid increases solubility and speeds up reaction rates [80].

4.1.1.1.1 ^{1}H NMR Table 4.1 displays the time to maximum hydrolysis for different silanes solutions with and without the addition of acetic acid, as well as for an APS-BTSE mixture (in a 2/1 ratio). APS solutions in general display high hydrolysis rates, due to the autocatalytic effect of the amino group, resulting in sufficiently high rates under standard conditions to be used without further additives [47, 81, 83]. An aqueous solution of APS with a natural pH of 10.4 has a hydrolysis rate comparable to that of non-amino silanes in a strongly acidic medium. Addition of acid inhibits (at least partially) this autocatalytic effect, causing a strong increase of the time to maximum hydrolysis. The loss of the amine activity in acid media was already noted before [224, 225]. Given their fast kinetics, all APS mixtures are rather swiftly ready for use from a hydrolysis point of view.

Table 4.1: Time to maximum hydrolysis as determined after fitting ^{1}H NMR data by a capacitor curve for different silanes with and without addition of acetic acid (1.3 *v*%).

Silane	**Name**	**Time without acid**	**Time with acid**
BTSE	2/50/50	demixing	23 min
APS	2/90/10	22 min	21 h
APS-BTSE	2/1/90/10	35 min	-
GPS	2/90/10	> 10 d	4 min

Aqueous GPS solutions on the contrary have a low hydrolysis speed, requiring more than 10 days for maximum hydrolysis. Addition of acetic acid speeds up kinetics, leading to maximum hydrolysis in at most 4 min. Literature already recommended the use of acid conditions (pH in the range from 3.5-5) to speed up hydrolysis of those species. When not doing so, considerable self-condensation would be observed prior to sufficient hydrolysis [102, 124, 226, 227].

When using BTSE in a water/alcohol mixture, visible demixing takes place, which can only be avoided by using at least 50 *v*% of alcohol and adding a sufficiently high amount of acid. Puomi et al. confirmed this instability at higher water contents [85]. Increasing the amount of acid increases hydrolysis rates, as seen by the time to maximum hydrolysis for BTSE that decreases from 23 min down to 11 min after doubling the amount of acetic acid (Figure 4.1). This figure also illustrates the accuracy when fitting data points by the so-called capacitor curve.

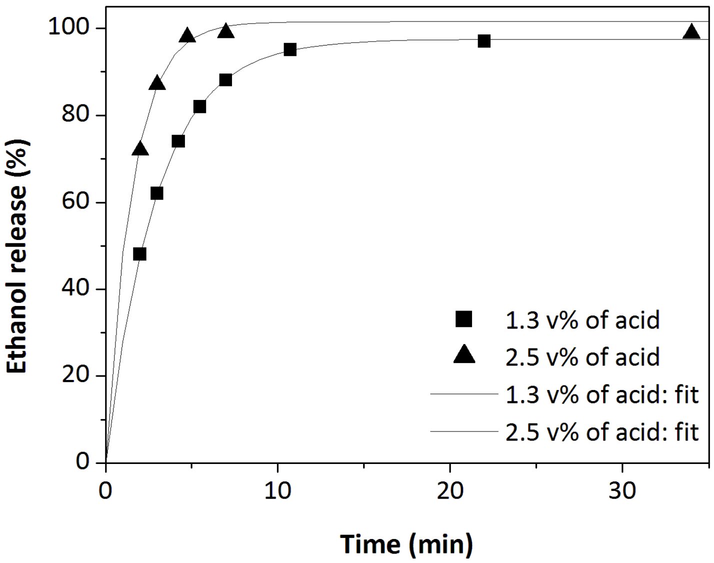

Figure 4.1: Degree of hydrolysis (ethanol release) as calculated from ^{1}H NMR spectra for BTSE/D_2O/MeOD 2/50/50 solutions with a different amount of acetic acid added. A higher amount of acid speeds up hydrolysis. The full line represents a capacitor curve fit, which accurately fits the data points.

Except for BTSE none of the silanes suffers from instability. However, when preparing a 2 *v*% APS-1 *v*% BTSE mixed solution (90/10 water/methanol), dissolution issues seem to disappear. This probably can be attributed to the catalytic effect of the alkaline APS, speeding up BTSE hydrolysis [47, 81, 83]. The hydrolyzed species, being more hydrophilic compared to the native ones, have a higher solubility in the water/methanol binary solvent. Note that the maximum degree of hydrolysis of this mixture (75%) is significantly lower compared to that of single silane solutions (> 90%). This points at incomplete hydrolysis or is possibly caused by unseen phase separation.

4.1.1.1.2 ^{13}C NMR: GPS Ring Opening During handling GPS ring opening can take place, an irreversible reaction decreasing the silane reactivity towards the polymer matrix in the next stage of hybrid preparation [89]. ^{13}C NMR enables monitoring of this reaction by following the disappearance of the epoxy peak, although not in a quantitative way with the settings used in this work. Figure 4.2 and 4.3 demonstrate that in the absence of acid in a 2/90/10 GPS/D_2O/MeOD solution, the ring remains intact for at least a few days, although some opening takes place before the completion of hydrolysis, which takes more than 10 days. The appearance of extra peaks above 70 ppm confirms ring opening after 5 days, while remainders of the alkoxy peak point at incomplete hydrolysis at 'short' times, as found by ^{1}H NMR. When adding acid (1.3 *v*%) the peak caused by the epoxy ring has decreased after 2 days. However, after one day the ring still appears to be intact. Maximum hydrolysis takes place sufficiently fast in this case (less than 4 min), and the solutions should be used within 1 day to avoid considerable ring opening.

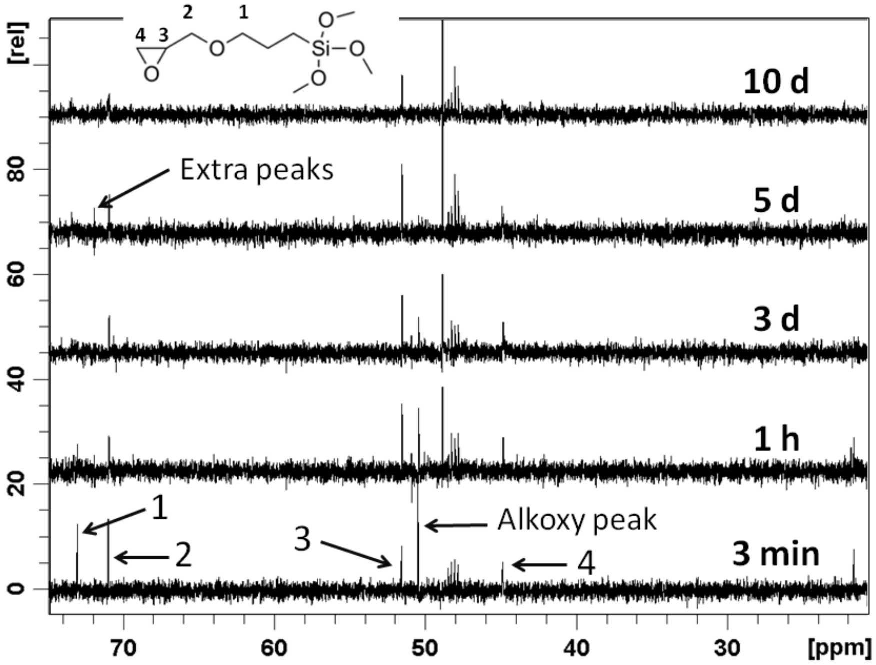

Figure 4.2: ^{13}C NMR spectra for a 2/90/10 GPS/D_2O/MeOD solution as a function of time. Epoxy ring opening takes place before hydrolysis is completed.

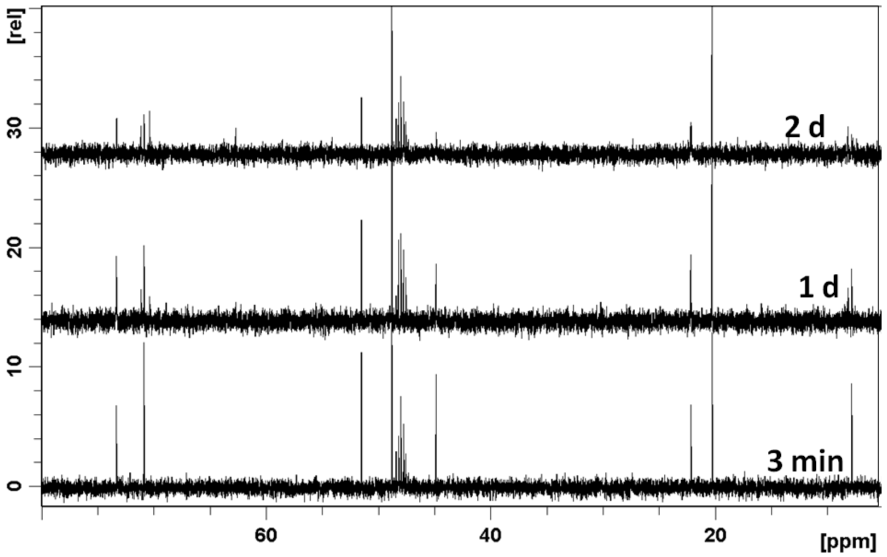

Figure 4.3: ^{13}C NMR spectra for a 2/1.3/90/10 GPS/acac/D_2O/MeOD solution as a function of time. The epoxy ring is still intact after full hydrolysis.

4.1.1.1.3 ^{29}Si NMR Due to the longer duration times of ^{29}Si NMR measurements (2-4 h), they result in an average spectrum covering a larger time span. Times noted in concomitant figures are the times between the solution preparation and the start of the respective measurement. Figure 4.4 depicts the ^{29}Si NMR spectra of a 2/1.5/90/10 APS/acac/D_2O/MeOD solution, together with peak assignments. Peak *a*, due to unhydrolyzed species, converts into peak *b* upon hydrolysis, representing silanol monomers. Limited self-condensation gives rise to peak *c*, caused by dimers, while more extensive self-condensation leads to the appearance of peak *d*, due to trimers and larger condensed species [54, 81, 221]. Broader peaks point at less uniformity and larger networks. Dimers, only showing up after self-condensation do not suffer from orientation and bonding issues after adsorption. Larger self-condensed species on the contrary, lead to adsorption of silane islands and clusters with orientation problems, forming the weak point in the polymer-steel joint later on (Section 2.3.2) [22].

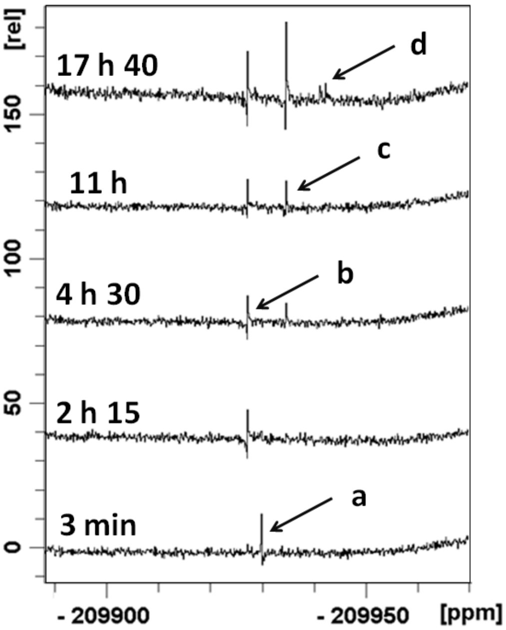

Figure 4.4: ^{29}Si NMR spectra monitoring self-condensation for a 2/90/10 APS/D_2O/MeOD solution. Peak *a*, *b*, *c* and *d* can be attributed to respectively unhydrolyzed species, to silanol monomers, to dimers and to trimers (and larger condensed species).

For an acidified APS solution (Figure 4.4) the dimer peak shows up after 4.5 h and becomes approximately equal to the silanol peak after 11 h. After less than 18 h a third peak clearly becomes visible. As the time to full hydrolysis amounts 21 h, a working window does not exist here; a considerable amount of self-condensation has taken place before hydrolysis is completed. In the absence of acid, this solution is already fully hydrolyzed after 22 min. Monitoring of the concomitant self-condensation (Figure 4.5) shows that a dimer peak appears almost immediately, but remains smaller compared to the silanol peak for a relatively long time. The 3 min spectrum is not depicted as it looks exactly like the 2 h 20 spectrum. The third peak (due to i.a. trimers) seems to slightly arise after 13 h 20. Nonetheless, its small size points at a limited amount of higher self-condensed species, that becomes numerous after 17 h40. For these APS solutions the working window covers a reasonable time span, and the solution preferably has to be used in between about 20 min and 13 h after preparation.

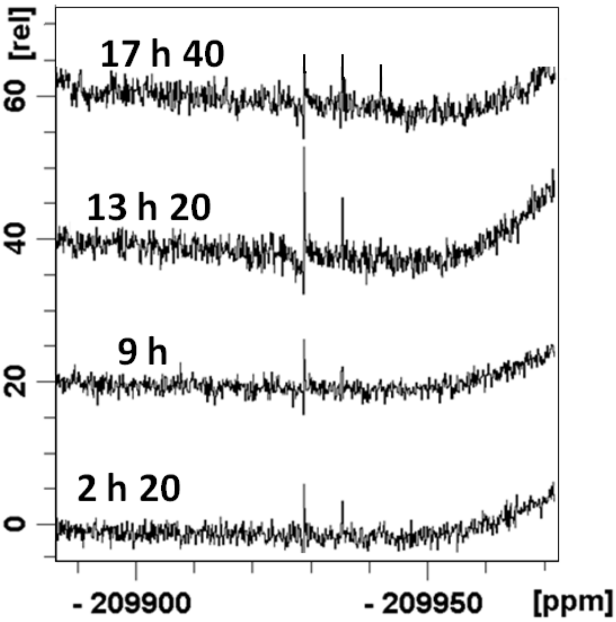

Figure 4.5: ^{29}Si NMR spectra monitoring self-condensation for a 2/90/10 APS/D_2O/MeOD solution, demonstrating the presence of larger condensed species only after more than 17 h.

For acidified GPS solutions (2/1.3/90/10) (Figure 4.6) the dimer peak shows up almost immediately, and becomes more pronounced (and larger compared to the silanol peak) after 11 h. Noticeable appearance of a third peak can be observed after a time span of about 18 h. As maximum hydrolysis of these solutions requires less than 4 min, these mixtures also seem to posses a reasonable working window. Signs of ring opening become visible after about 1 day (See Paragraph ^{13}C NMR), so self-condensation rather than ring opening would limit the working window. Solution deposition best takes place in between 4 min and 11 h after solution preparation. Without the addition of acid, hydrolysis requires 10 days, meaning that these solutions lack a working window as seen from Figure 4.7. As was the case for non-acidified APS, dimer-

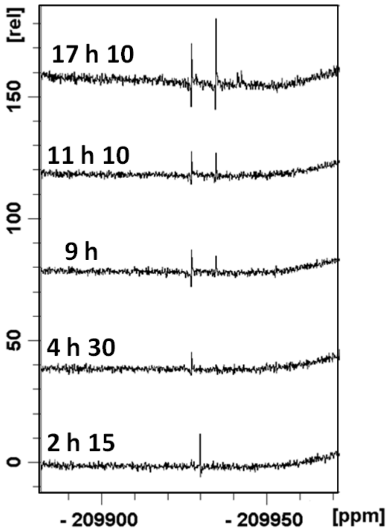

Figure 4.6: ^{29}Si NMR spectra monitoring self-condensation for a 2/1.3/90/10 GPS/acac/D_2O/MeOD solution. After 17 h a trimer peak shows up.

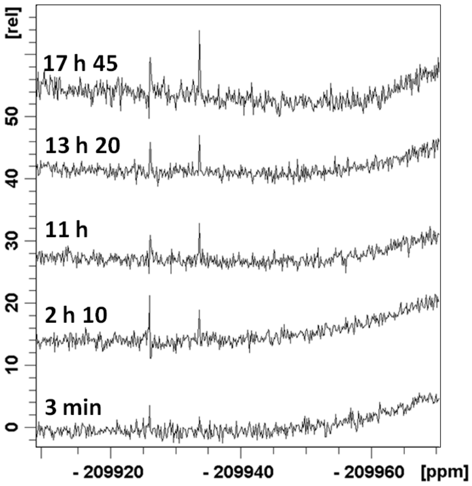

Figure 4.7: ^{29}Si NMR spectra monitoring self-condensation for a 2/90/10 GPS/D_2O/MeOD solution. Until more than 17 h after solution preparation only a monomer and dimer peak can be seen.

ization can be seen rather early, and the concomitant peak overwhelms the monomer peak after at most 11 h. The trimer peak shows up after about 17 h, long before completion of hydrolysis.

For a 2/1.5/50/50 BTSE/acac/D_2O/MeOD solution (Figure 4.8) noticeable traces of self-condensation become visible after 9 h, and considerably only after more than 13.5 h. The spectrum recorded after 11 h looks identical to the spectrum after 9 h. As the time until full hydrolysis amounts to 23 min, a sufficiently broad working window exists for these solutions.

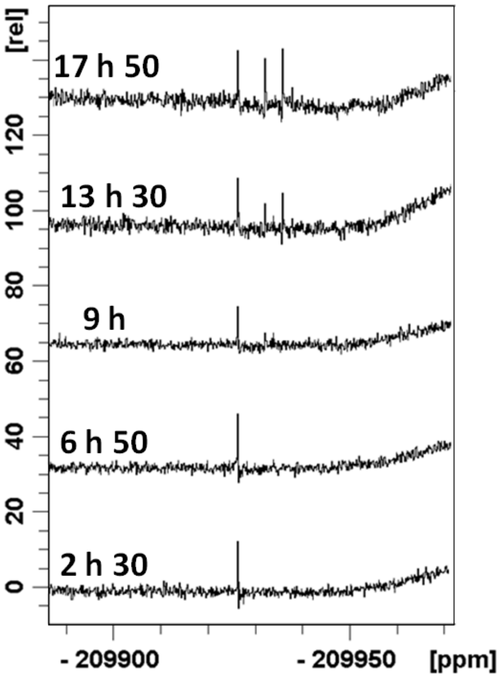

Figure 4.8: ^{29}Si NMR spectra monitoring self-condensation for a 2/1.5/50/50 BTSE/acac/D_2O/MeOD solution. Only after more than 13 h a trimer peak shows up.

In conclusion the addition of acid is strongly recommended when using GPS and BTSE as it speeds up hydrolysis and increases solution stability in the case of BTSE, in contrary to APS where it counteracts the autocatalytic effect. Moreover it delays the onset of self-condensation, which is useful in the case of GPS and BTSE, whereas for APS a broader working window was established for the non-acidified solution, due to its faster hydrolysis rates [49, 92].

4.1.1.2 Influence of the Solvent (Water-Alcohol Ratio)

It is obvious that the solvent composition influences the hydrolysis and subsequent condensation kinetics as hydrolysis requires water. In principle, besides the two reactions mentioned, transetherification with the alcoholic part of the solvent may compete with hydrolysis (Section 1.3.3.1). During this work, the peak due to unhydrolyzed species (or transetherification) vanished after maximum hydrolysis, and also ^{1}H NMR does not reveal any such reactions, so this reaction can be ignored.

4.1.1.2.1 ^{1}H NMR Figure 4.9 depicts the capacitor curve fitted data for APS solutions. It shows that when using a binary solvent, decreasing the water/methanol ratio (for a 2 $v\%$ solution) has a negative influence on the APS hydrolysis kinetics, with the time needed for (complete) hydrolysis increasing from 12 min to 22 min, 44 min and 75 min for respectively a 100/0, 90/10, 70/30 and 50/50 water/methanol ratio. This trend of higher hydrolysis rates at higher water contents was already observed before [51, 81, 92]. Replacing methanol by ethanol shortens the hydrolysis times to 18 min and 21 min for the 90/10 and 70/30 sample respectively. As methanol has a higher polarity compared to ethanol, it probably interacts stronger with the amino functionality, in this way decreasing the autocatalytic effect and thus the hydrolysis rate. For all cases studied APS again hydrolyzes rather fast compared to silanes with other functional groups due to this autocatalytic effect [50]. The effect of the solvent (ratio) on acidified APS solutions was not studied as it was decided to go on with mixtures at their natural pH because of the absence of a working window for the former.

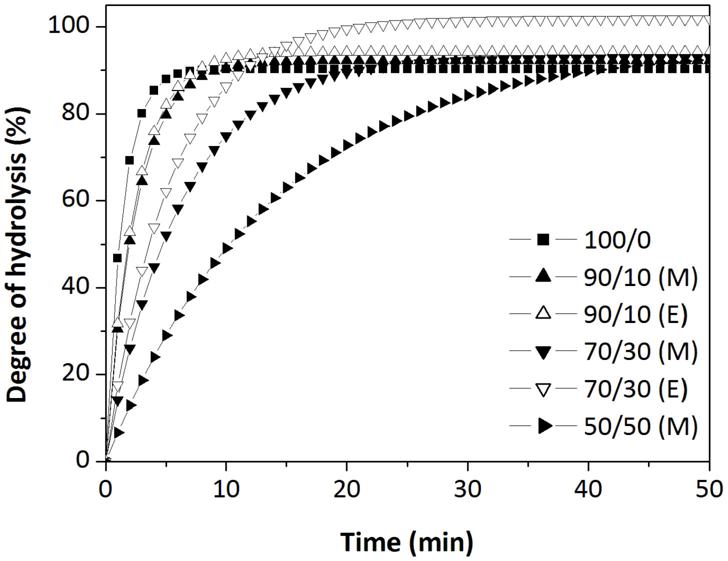

Figure 4.9: Hydrolysis kinetics shown by a capacitor fit of data obtained by ^{1}H NMR on 2 v% APS water/alcohol solutions. Full symbols represent y/z water/methanol solvent ratios (M), open symbols represent y/z water/ethanol ratios (E).

For acidified GPS hydrolysis kinetics were too fast to study solvent effects with ^{1}H NMR. Figure 4.10 depicts hydrolysis kinetics as a function of the solvent (ratio) for a 2 v% GPS solution without acid (after fitting by a capacitor curve), again demonstrating a decrease in rates with increasing alcohol content. In literature the same phenomenon was observed for water/ethanol GPS solutions, where the reduced polarity of ethanol compared to water explained the slower kinetics of alcohol rich solvents [92]. This leads to less species in solution that can act as a catalyst, thereby decreasing the hydrolysis efficiency. The favoring of hydrolysis with increasing water content can also be observed for other silanes, whatever the nature of the pristine silane, but it would be more pronounced for triethoxy silanes compared to their trimethoxy counterpart [81]. From Figure 4.10 it also appears that for GPS hydrolysis kinetics slow down when replacing methanol by ethanol. This can be explained analogously to the change in the water/alcohol ratio, as methanol has a slightly higher polarity compared to ethanol, leading to a higher amount of catalytic species. Note here that acidified GPS solutions probably demonstrate the same trends, although fast kinetics impede hydrolysis studies by NMR.

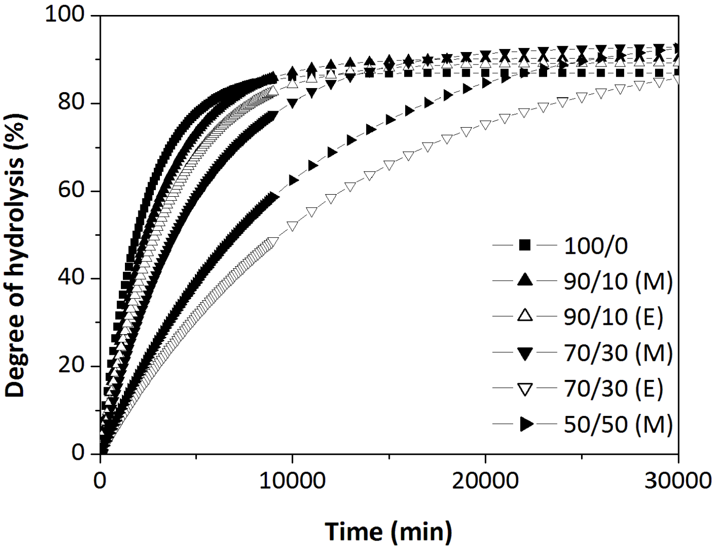

Figure 4.10: Hydrolysis kinetics shown by a capacitor fit of data obtained by ^{1}H NMR on 2 v% GPS water/alcohol solutions. Full symbols represent y/z water/methanol solvent ratios (M), open symbols represent y/z water/ethanol ratios (E).

For acidified BTSE solutions (Figure 4.11) kinetics slow down slightly when replacing methanol by ethanol, probably for the same reason as in non-acidified GPS solutions: the slightly lower polarity of ethanol, decreasing catalytic species in solution. As sufficient stability of BTSE solutions requires at least 50 v% of alcohol, the influence of the solvent ratio on these solutions was not studied.

This work uses a substantial amount of water, as most researchers do [51]. Keeping in mind environmental safety and health as well as speed and ease of handling, for APS and GPS the 90/10 solvent ratio was selected for further systematic work, assuming that the small amount of alcohol would enhance wetting of the substrate surface in

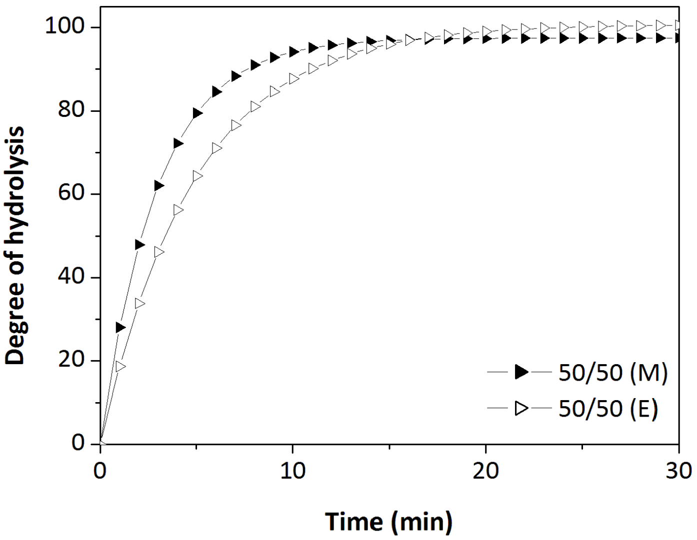

Figure 4.11: Hydrolysis kinetics shown by a capacitor fit of data obtained by ^{1}H NMR on 2 v% BTSE water/alcohol solutions. Full symbols represent y/z water/methanol solvent ratios (M), open symbols represent y/z water/ethanol ratios (E).

a next step by decreasing the surface tension of the solvent [126, 228]. Because of health and safety issues, ethanol is chosen over methanol for further sample preparation.

4.1.1.2.2 ^{29}Si NMR Figure 4.12 demonstrates the effect of replacing methanol by ethanol on the self-condensation behavior of a 2/90/10 APS/D_2O/alcohol solution (compare with Figure 4.5). Arguable, slight humps due to dimerization may be visible but to a very limited extent. Ethanol thus decreases self-condensation kinetics compared to methanol, although in the case of APS the former results in faster hydrolysis. The combination of both increases the time span covered by the working window when replacing methanol by ethanol.

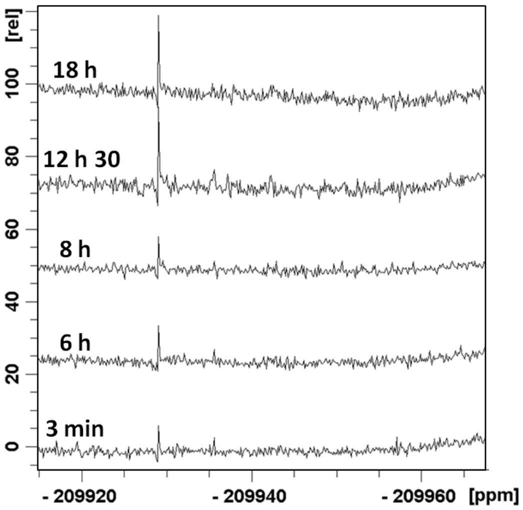

Figure 4.12: ^{29}Si NMR spectra monitoring self-condensation for a 2/90/10 APS/D_2O/EtOD solution. No signs of self-condensation can be seen.

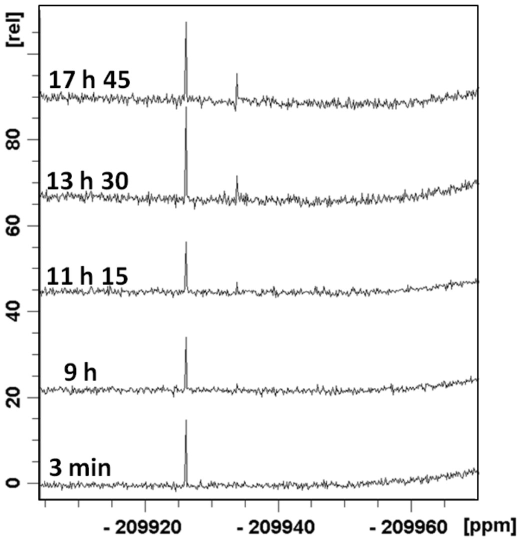

Figure 4.13: ^{29}Si NMR spectra monitoring self-condensation for a 2/1.5/90/10 GPS/acac/D_2O/EtOD solution. The trimer peak remains absent.

Also for GPS condensation kinetics slow down when replacing methanol (Figure 4.7) by ethanol in an acidified solution (Figure 4.13), with slight dimer formation after about 11 h. The trimer peak remains absent up to at least 18 h after solution preparation, again resulting in a sufficiently broad working window.

Whereas changing the alcohol in the solvent from methanol to ethanol only slightly influences the time until maximum hydrolysis for BTSE, it clearly has an influence on the condensation kinetics (Figure 4.8 and 4.14). When using methanol, signs of dimer formation showed up after about 9 h, for ethanol no clear peaks due to self-condensation can be seen until at least 18 h after solution preparation, again broadening the working window, a trend already seen by Chovelon et al. [229].

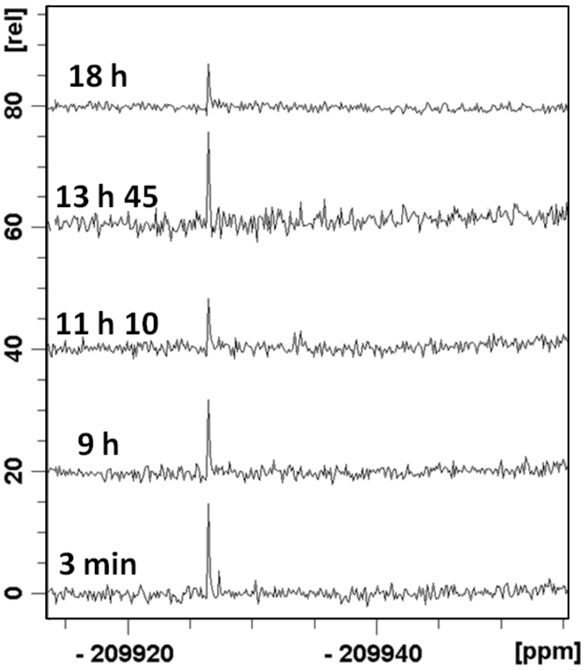

Figure 4.14: ^{29}Si NMR spectra monitoring self-condensation for a 2/1.5/50/50 BTSE/acac/D_2O/EtOD solution. Only a monomer peak can be seen.

For BTSE and GPS replacing methanol by ethanol slows down hydrolysis rates. Some may argue that the decreased amount of silanol species also slows down self-condensation. However, the completely different timescale that the delay covers for both reactions contradicts this. Hydrolysis is only slowed down to a rather small extent (in the range of minutes for BTSE), whereas the onset of self-condensation slows down in the range of a few hours.

Despite the fact that replacement of methanol by ethanol in the binary solvent mixture decreases hydrolysis rates in the case of GPS and BTSE, but not for APS systems, it slows down self-condensation for all systems tested. Resulting NMR spectra in the time interval monitored (about 18 h) reveal at most a limited amount of dimer formation. When using ethanol the monomer peak largely exceeds the dimer peak, and after 18 h no noticeable trimer or network species can be found for any of the ethanol samples. In other words, the working window extends when replacing methanol by ethanol for the systems studied. No (small upfield) peak due to unhydrolyzed species can be found in any of the cases, corroborating the ^{1}H NMR measurements and indicating that no transetherification takes place in this time span [230].

4.1.1.3 Silane Concentration

Also the silane concentration influences reaction kinetics, although literature does not always agree on the mechanism behind this. Most authors report an increase of reaction rates for higher concentrations and Beari e.g. mentioned faster hydrolysis kinetics with increased concentration [50]. Abel et al. showed that the hydrolysis of a concentrated solution (8%) takes place faster compared to a less concentrated one (1%), which is contrary to the hypothesis of Bertelsen et al. [58, 75, 124]. Shaw et al. reported on the effect of an increased concentration, not only causing a thicker silane layer after deposition, but also more cluster formation on the substrate due to increased self-condensation [99].

4.1.1.3.1 ^{1}H NMR Increasing the concentration speeds up the hydrolysis rates, as was shown for APS solutions in Figure 4.15. Obtaining a maximum degree of hydrolysis requires less than 10 min for a non-acidified 5 *v*% solution instead of 18 min for a 2 *v*% solution (90/10 water/ethanol).

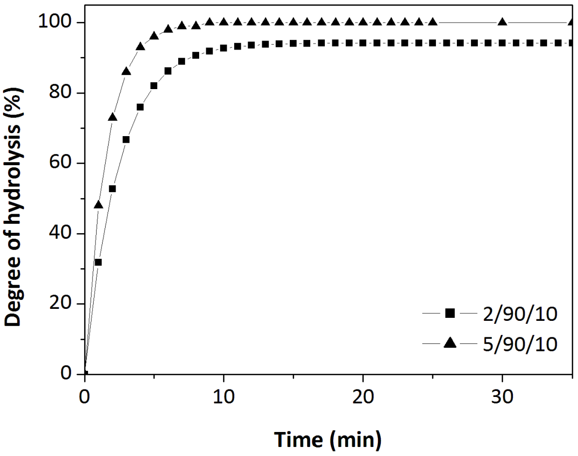

Figure 4.15: Hydrolysis kinetics as determined from ^{1}H NMR spectra for 90/10 water/ethanol APS solutions with a 2 *v*% and 5 *v*% APS concentration. Hydrolysis speeds up when increasing the concentration.

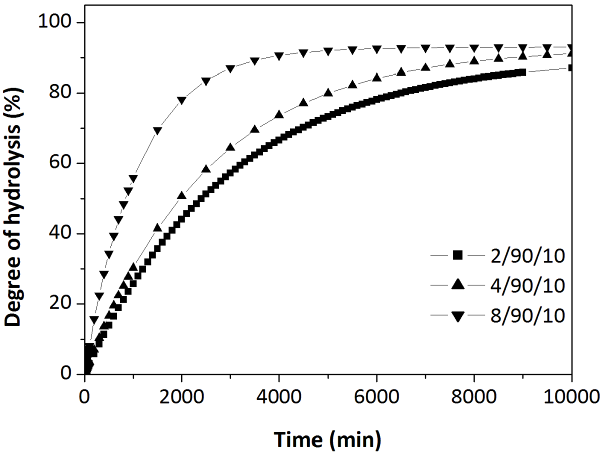

Figure 4.16: Hydrolysis kinetics as determined from ^{1}H NMR spectra for 90/10 water/methanol GPS solutions with a 2 *v*%, 4 *v*% and 8 *v*% GPS concentration. Hydrolysis speeds up when increasing the concentration.

Due to fast hydrolysis kinetics in acidified GPS solutions, neutral solutions were monitored to study the influence of the concentration for those species. Figure 4.16 demonstrates that the same trend holds for APS and GPS solutions (even more clearly). Full hydrolysis of a 2 *v*% GPS solution takes 14.5 days, while the 4 *v*% needs 10 days and the 8 *v*% requires ′only′ 4 days.

4.1.1.3.2 ^{29}Si NMR Comparing Figure 4.5 (2 *v*%) and 4.17 (5 *v*%) reveals the influence of the APS silane concentration on the self-condensation kinetics of a 90/10 D_2O/MeOD binary solvent.

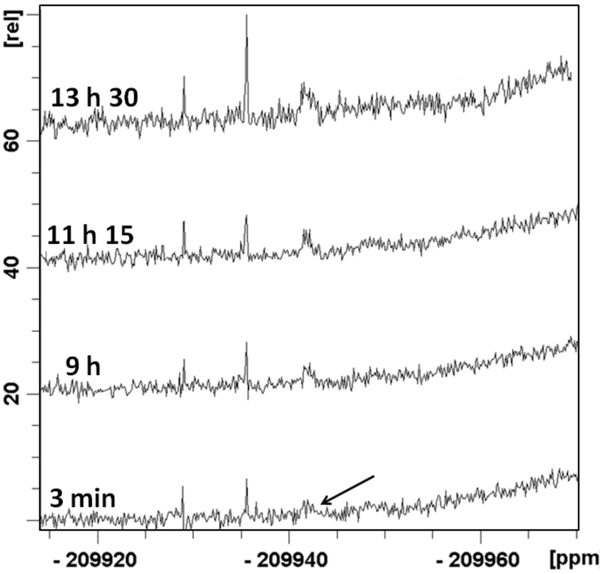

Figure 4.17: ^{29}Si NMR spectra monitoring self-condensation for a 5/90/10 APS/D_2O/EtOD solution. A network peak shows up immediately, as indicated by the arrow.

As was expected, increasing the silane concentration drastically speeds up self-condensation rates. For the higher concentration already during the first measurement a trimer/network peak becomes visible (indicated by the arrow), and the monomer and dimer peak have comparable dimensions. Moreover the peaks due to higher self-condensed species grow considerably with time, and after 13.5 h the monomer peak becomes of minor importance. This trend corroborates earlier literature [1, 221] and has at least two reasons. First of all hydrolysis kinetics speed up with increasing concentration, as seen from ^{1}H NMR measurements, resulting in a higher fraction of the silane being in its silanol form after a shorter time. This increases the chance for silanol condensation and thus for the formation of dimers, trimers or larger networks. Second the increase of the start concentration reinforces this effect as it not only increases kinetics but also causes a larger absolute amount of silane and thus silanol species. This again leads to an increased probability for molecules to meet, and explains why the self-condensation reaction rates increase.

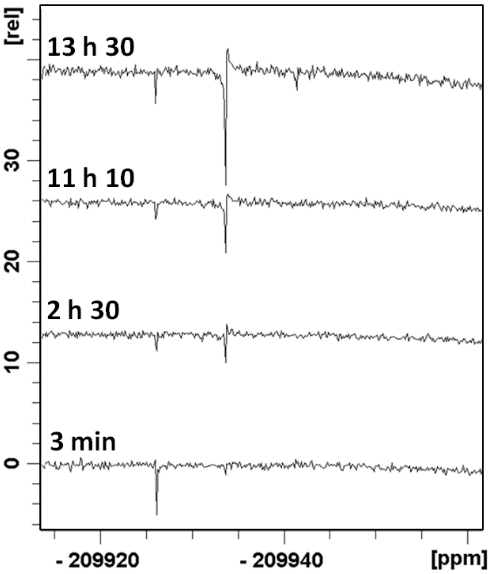

Figure 4.18: ^{29}Si NMR spectra monitoring self-condensation for a 5/1.5/90/10 GPS/acac/D_2O/MeOD solution. The dimer peak overwhelms the monomer peak rather soon.

The same phenomenon can be found for acidified GPS solutions (5/1.5/90/10) (Figure 4.18). As in practice acidified solutions will be used for further work, and their self-condensation takes place at longer time scales compared to hydrolysis, acidified solutions were monitored. Self-condensation for these higher concentrated species speeds up compared to a 2 *v*% sample (Figure 4.6), with the dimer peak overwhelming the monomer peak already after 2.5 h and the third peak appearing after 13.5 h. Again the higher concentration gives rise to faster hydrolysis kinetics, increasing the self-condensation probability and thus the self-condensation rate. Note that the third peak often has a broader appearance compared to monomer and dimer peaks, due to the large variety of oligomers or networks possible [221].

These experiments demonstrate that a lower silane concentration gives rise to less self-condensation, increasing solution stability [54, 85]. Nonetheless extremely low concentrations do not guarantee monolayer adsorption after deposition [47], while dimer formation does not necessarily have a negative influence on composite performance later on [219]. This illustrates the importance of using the appropriate concentration.

4.1.1.4 NMR Summary

Table 4.2: Time span covered by the working window of various 2 *v*% silane solutions. APS solutions are handled at their natural pH (APS/D_2O/alcohol), GPS and BTSE are acidified with acetic acid (GPS/acac/D_2O/alcohol and BTSE/acac/D_2O/alcohol).

Silane	**Alcohol used**	**Start**	**End**
APS (2/90/10)	MeOD	22 min	13 h
	EtOD	18 min	> 18 h
GPS (2/1.3/90/10)	MeOD	< 4 min	11 h
	EtOD	< 4 min	> 18 h
BTSE (2/1.3/50/50)	MeOD	23 min	11 h
	EtOD	30 min	> 18 h

Table 4.2 summarizes the working window of different 2 *v*% silane solutions. From the NMR measurements performed, first decisions can be taken about optimal conditions, keeping in mind the environmental point of view as well as the ease of handling. This means using a maximum amount of water, with a minimum of (acid) additions, and a small amount of alcohol [231]. Ethanol is the preferred alcohol, as it enlarges the working window compared to methanol, and has an advantage from a health point of view. Easily handled APS mixtures are used at their natural pH given their fast kinetics and broader working window. Subsequent APS experiments use a water/ethanol solvent ratio of 90/10. For GPS the same solvent ratio is chosen, but

to enable handling speed and obtain a useful working window, acetic acid is added up to a pH of 4.5. Note here that neither extensive self-condensation, nor epoxy ring opening takes place within 18 h after solution preparation. Further BTSE work uses a 50/50 water/ethanol ratio, acidified with 1.5 $v\%$ of acetic acid to ensure solution stability. The optimal concentration will be determined in next Sections.

4.1.2 Morphological Characterization: SE and SEM

NMR studies enabled determination of the optimal solvent composition and components, and revealed the working window for different conditions. However, the optimal silane solution conditions cannot be determined by solely performing NMR experiments. Spectroscopic Ellipsometry (SE) (Materials and Chemistry Department, Vrije Universiteit Brussel, Brussels, Belgium) and Electron Microscopy reveal the influence of the silane concentration and of ageing the solution beyond the working window.

Table 4.3 depicts the layer thickness of an oven treated APS layer after deposition (including rinsing) from solutions with varying concentrations, as obtained by SE. Even after rinsing, a higher silane concentration clearly increases the layer thickness. This points at an increased amount of strongly (chemi)sorbed silane species when depositing from more concentrated solutions. On one hand this can be caused by the higher amount of species adsorbing as such, on the other hand by a higher amount of self-condensed species that can adsorb as a cluster, also resulting in a thicker layer (on average). Note here that literature mentions a value of 0.7 nm for monolayer coverage [86, 219]. This means that for a 1 $v\%$ APS concentration less than monolayer coverage was observed (implying an inhomogeneous, incomplete coverage), while layers deposited from a 2 $v\%$ solution have a slightly higher thickness than a monolayer. In the absence of rinsing higher silane concentrations also lead to thicker films after deposition, again due to increased self-condensation in solution. Note that the final thickness depends on the final deposition conditions. Vandenberg e.g. found a thickness of 0.7 nm after deposition from a 0.4 $v\%$ solution [86], demonstrating the sensitivity of the system to (slight) changes of parameters in the coating process.

Table 4.3: Thickness of the resulting silane layer after oven treatment as a function of the APS concentration in a 90/10 water/ethanol binary solvent. Note the substrate was rinsed after dipping, leading to very thin silane layers.

1 v%	2 v%	5 v%
< 0.10 ± 0.05 nm	0.83 ± 0.03 nm	4.10 ± 0.04 nm

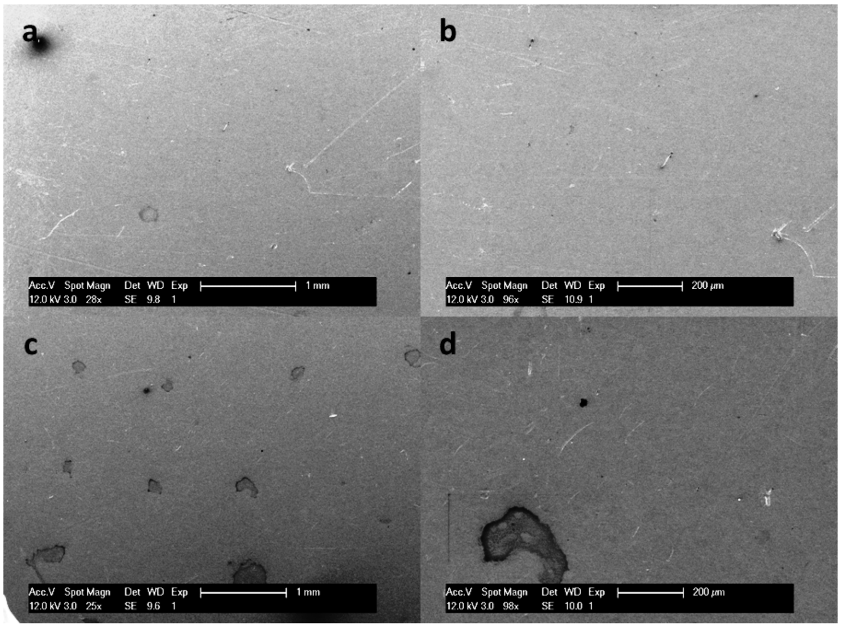

Figure 4.19: SEM micrograph from an oven treated APS layer on a SST substrate deposited from a 2 v% (a and b) and a 5 v% (c and d) APS solution in a 90/10 H_2O/EtOH solvent (rinsed after application). A higher silane concentration gives rise to a higher amount of patches.

SEM visually reveals the difference between oven treated APS layers deposited from respectively a 2 v% (Figure 4.19 a & b) and a 5 v% (Figure 4.19 c & d) solution and oven treated under standard conditions (30 s of dipping, 60 s of ethanol rinsing). Deposition from the higher concentrated solution gives rise to more patches after deposition, mainly due to deposition of clusters and inhomogeneous adsorption. However the substrate structure remains visible, which may be explained taking into account the average layer thicknesses found in Table 4.3. A layer with a thickness of less than 1 nm is hardly able to cover up relief and defects in the range of a few nm. Also Simpson et al. studied APS deposition (on Al surfaces) from different concentrations (followed by rinsing), and concluded that 3 *v*% solutions lead to homogeneous films, whereas deposition from a 6 *v*% solutions creates a less uniform layer containing patches, despite the higher total amount of APS remaining on the surface [232]. This is in line with findings of this work.

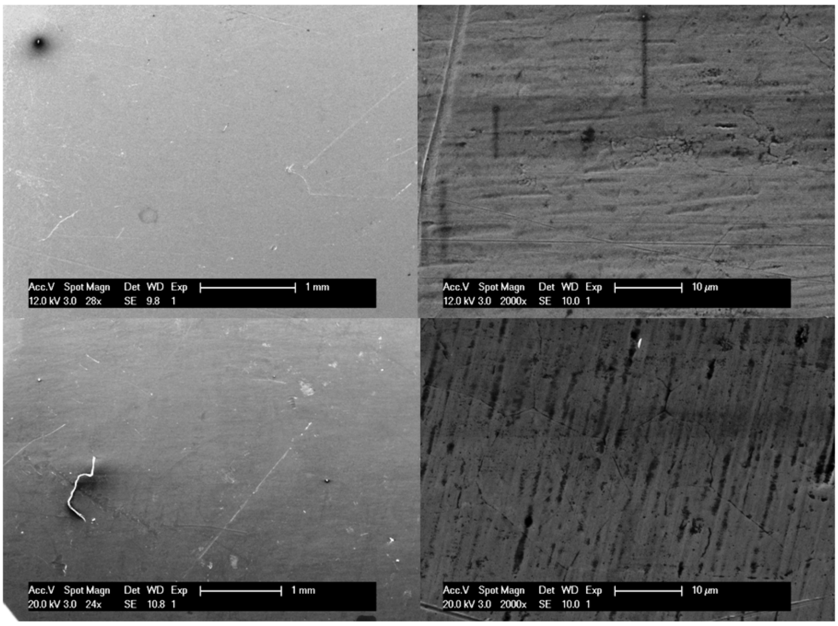

Figure 4.20: SEM micrograph from an oven treated APS (top) and GPS (bottom) layer on a SST substrate deposited from respectively a 2/90/10 APS/H_2O/EtOH and a 2/1.5/90/10 GPS/acac/H_2O/EtOH solution. Both samples are water rinsed after deposition.

Figure 4.20 demonstrates that visually no difference can be seen between an APS layer and a GPS layer deposited from a 2 *v*% solution (acidified for GPS), deposited and oven treated under the same standard conditions . This indicates differences in mechanical performance

(Section 4.1.4) should not be ascribed to the morphology of the silane layer itself but rather to the silane interface(s).

4.1.3 Chemical Characterization: Tensiometry

Tensiometric measurements reveal information on the chemical appearance of a surface (Section 1.4). For thicker APS coatings contact angles hardly reveal anything about the bulk of this layer, whereas for thinner or incomplete layers the influence of the substrate may ′shine through′.

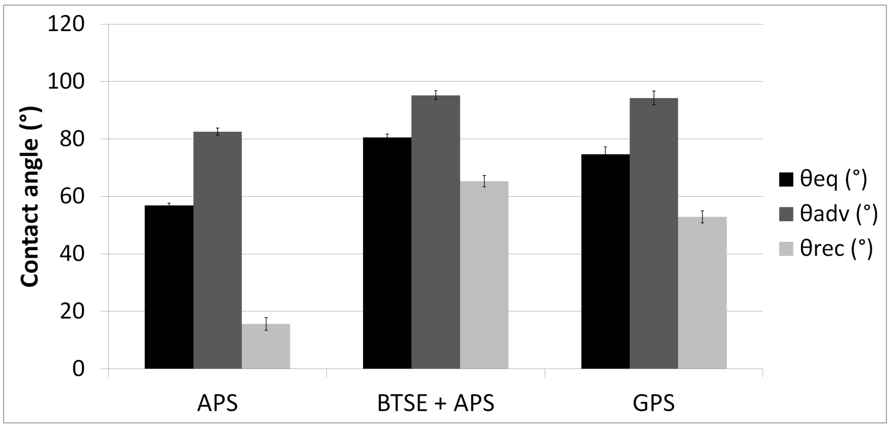

Figure 4.21: Influence of the type of silane deposited on the equilibrium, advancing and receding contact angle of a SST substrate after deposition and oven treatment. APS layers clearly results in lowest contact angles.

Figure 4.21 reveals the influence of the type of silane on the contact angles. It is clear that APS causes lowest advancing, receding and thus also equilibrium angles. In literature, BTSE is added to obtain more extensive crosslinking, improving layer and corrosion properties [233]. Deposition of a mixed layer (from a 2/1/90/10 APS/BTSE/H_2O/EtOH solution) leads to highest angles, due to less polar groups on the upper surface, caused by the BTSE in the solution. GPS causes intermediate angles. Probably the functional epoxy groups partially disappear during oven treatment, and resulting diol groups may participate in the crosslinking process. However, these layers still have some polarity in their structure, leading to intermediate contact angles. APS has a lower apolar contribution.

Figure 4.22 (left bars) shows the influence of ageing of the silane solution on the contact angles. Not aged in this case means solution deposition within the silane solution working window, whereas aged means deposition from the same 2 *v*% solution after ageing it for 11 days, far beyond the working window. Other deposition and oven conditions were kept constant during sample preparation according to the standard coating procedure (Section 2.3.1).

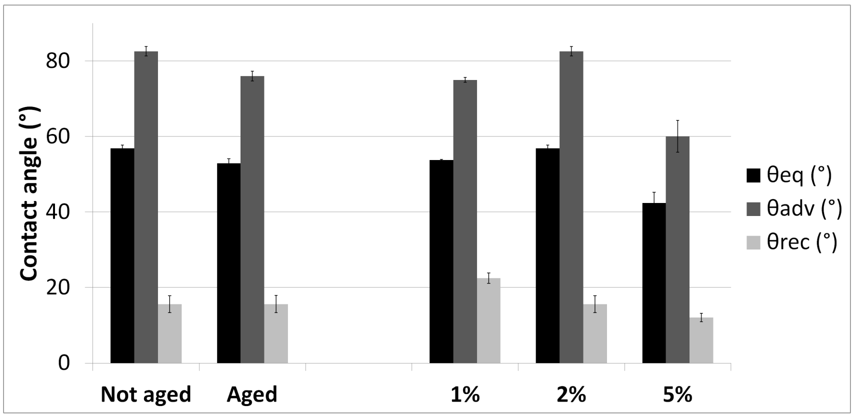

Figure 4.22: Influence of no ageing (not aged) and ageing (11 days) of the silane solution before deposition (aged) and of the APS concentration in a 90/10 H_2O/EtOH solvent on the equilibrium, advancing and receding contact angle of a SST substrate after APS deposition and oven treatment.

All samples have a lower equilibrium contact angle compared to the cleaned, uncoated sample, mainly due to a decrease of the receding angle, caused by the increase in polarity after APS deposition. The equilibrium and receding angle decrease from respectively 59.5 ± 2.3 ° and 32.0 ± 2.8 ° for the uncoated sample down to 56.9 ± 0.8 ° and 15.6 ± 2.2 ° for the not aged sample. The reason for this polarity can be twofold: the presence of polar aminegroups or incomplete self-condensation, leaving hydroxyl groups [234].

Ageing mainly decreases the advancing angle, and thus the low energy part of the surface. This can be explained by the higher amount of self-condensation in solution, increasing the amount of disorder and thus of steric constraints and dispersive forces in the layer after deposition. The APS layer deposited in the absence of excessive ageing is ordered to a higher extent, and thus has a higher degree of crosslinking and improved orientation and stacking after oven treatment, resulting in a higher advancing angle. The fact that both samples have similar receding angles and were deposited from equally concentrated solutions, does not mean that the polar part of the surface looks identical, as both samples just have the same average high energy part. Due to the lower extent of crosslinking (due to steric constraints) of the aged samples, probably a larger fraction of hydroxyl groups remains after oven treatment. The disorder leads to less amine groups at the surface (and more of those groups buried away in the thicker layer), and a combination of both phenomena causes the same average polarity and thus a similar receding angle.

Also the silane concentration influences the contact angles, as seen after deposition, keeping all conditions constant (Figure 4.22, right bars). Again coating lowers the equilibrium contact angle compared to a cleaned uncoated sample and, as in the case of the aged samples, this angle again follows the same trend as the advancing angle. The advancing angle increases for a 2 $v\%$ sample (compared to a 1 $v\%$ sample), but decreases again for the 5 $v\%$ sample. This last decrease follows straightforwardly out of the higher concentration of species. Higher degrees of self-condensation in solution and more adsorption during dipping. Again this puts (steric) constraints on the degree of crosslinking of the APS layer, causing a lower advancing (and receding) angle. The 1 $v\%$ sample also has a lower advancing angle, but for a different reason that probably can be found in the incomplete coverage of the substrate with silane, as demonstrated by SE (Table 4.3). Incomplete coverage and thus insufficient contact between silanol groups lowers the degree of (self)-condensation and causes ′shining through′ of the substrate. The former gives rise to the lower advancing contact angle, while the latter increases the receding contact angle compared to the 2 $v\%$ sample. Moreover, the molecules deposited from this 1 $v\%$ solution may be oriented inappropriately (See Literature, Figure 1.10) or suffer from less efficient packing, changing the contact angles. The receding angle decreases with increasing concentration. For the 5 *v*% sample the lower receding angle can be explained by the higher absolute amount of polar groups; more free hydroxyl groups due to less complete crosslinking, and probably also a higher amount of amine functionalities because of the increased concentration. The higher receding angle for the 1 *v*% sample can be explained by the lower amount of APS deposition in combination with a higher influence of the underlying substrate. However, all receding angles are far below the receding angle of a freshly US cleaned surface (about 32 °), proving the presence of silane.

For the 5 *v*% sample, a larger standard deviation and higher waviness during measurements can be seen, caused by a more inhomogeneous, rougher and thicker APS layer. Contact angles of other samples are rather constant during measurement, pointing at less roughness (effects). Moreover the thicker and probably more porous structures of these high concentration samples cause small kinetic effects, due to solvent penetration and reorientation of functional groups. Literature already reported that higher APS concentrations lead to excessively thick and weakly polymerized silane films [232].

Equilibrium contact angles are in line with literature, and e.g. Kim found equilibrium angles of about 58° for an APS coated glass surface, whereas Howarter reported on advancing and receding angles with extrema from respectively 20° and 80°, and an equilibrium contact angle of about 60° under optimal deposition conditions [219, 235].

4.1.4 Mechanical Characterization

This section investigates the influence of the solution parameters on the mechanical performance of (cleaned) SST-epoxy joints, coupled by a silane layer. The solvent composition was already fixed after NMR measurements, by which only the influence of the silane type, and its concentration remain to be explored.

Figure 4.23 depicts the influence of the type of silane used on the mechanical strength, determined by dolly testing of SST-epoxy samples after deposition and oven treated according to the same procedure. All coatings perform at least more than 3 times better compared to the uncoated substrate (9.2 ± 3.8 MPa), although APS coupling performance clearly exceeds that of GPS and of a APS-BTSE mixture, with the latter 2 coatings having similar performance. Hayes expected the surface-silane interaction to be identical for APS and GPS when deposited under the same conditions, so the difference probably locates in the silane layer itself or at the silane-matrix interface [27]. Lower GPS performance probably can be attributed to a loss of the epoxy functionality during oven treatment (at an elevated temperature, also suggested by tensiometry), while the BTSE in the BTSE-APS mixture gives rise to less efficient matrix coupling, attributed to a less ordered and probably more brittle layer with less amine functionalities available for coupling. Pure BTSE as such was not tested because of the lack of functional groups for proper interaction with the matrix. From this it was decided to go on with APS species for further testing.

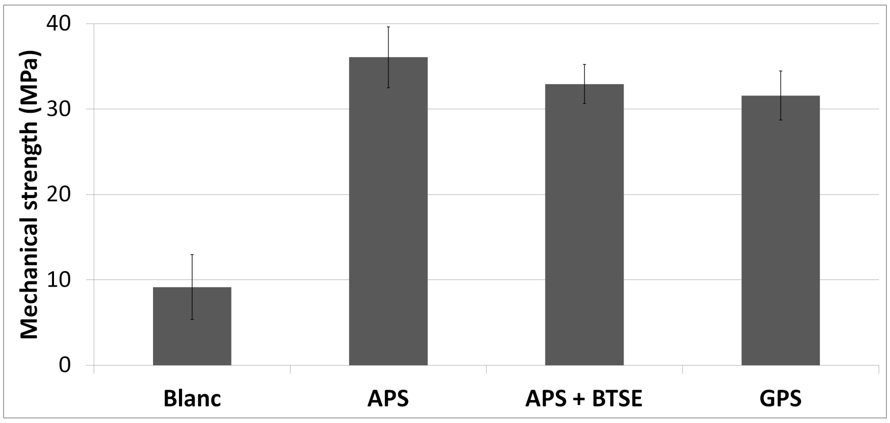

Figure 4.23: Mechanical strength as determined from dolly testing of SST-epoxy samples coated with different types of silanes following the same coating procedures. The blanc sample is not APS coated before epoxy application.

Da Silva and Del Real et al. reported a reduction in adhesive joint strength with decreasing bondline thickness increasing silane concentration and longer ageing times [8, 80, 229, 236]. Adams and Peppiatt attribute this to the fact that thicker bond lines contain more defects such as voids and microcracks [237]. Moreover interface stresses were shown to be higher for thicker bondlines [238, 239]. The thickness of the interphasial region directly influences the ability of the matrix to transfer load to the steel and its structure and properties are dominant factors governing the overall composite properties and performance [45].

Ageing of the APS silane solution beyond the span of the working window (16 days) has a detrimental influence on the mechanical strength as determined by dolly testing (Figure 4.24, left bars). This can be attributed to the formation of clusters in solution, as found by ^{29}Si NMR. Although NMR measurements did not cover such a large time span, they already revealed the influence of time on self-condensation. Longer ageing times cause adsorption into brittle islands on the SST surface (as shown by SEM) with less anchoring possibilities to both the substrate and matrix [42, 85, 232]. Ageing not only decreases the resulting strength by about 50%, but also increases the standard deviation. This points at less reproducibility and inhomogeneous deposition. Literature already mentioned that the adherence as a function of the silane solution ageing time passes through a maximum at full hydrolysis and decreases again after leaving the working window. Moreover also substrate coverage would follow this trend [53, 219, 235, 240].

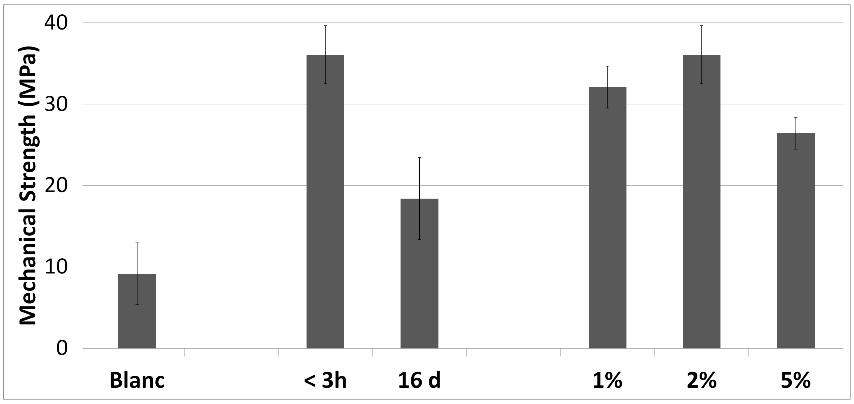

Figure 4.24: Mechanical strength as determined from dolly testing of SST-epoxy samples coated with a freshly prepared and an aged APS solution (left bars) and coated from solutions with a different APS concentration (right bars).

When changing the APS concentration the mechanical strength passes through a maximum (Figure 4.24, right bars). Deposition from the most concentrated solution results in lowest strengths, again due to increased self-condensation, but especially due to an increased amount of adsorption [1, 230, 241]. This results in a thicker, non-uniform APS layer consisting of less organized multilayers with weaker coherence and decreased coupling performance [53, 81, 242]. Deposition from a 1 $v\%$ solution results in intermediate strength, pointing at incomplete coverage [47], as already suggested by SE results, with the average silane layer thickness below the thickness of a monolayer. Incomplete coverage in combination with the possibility for less favorable silane orientation and thus less anchoring points between the silane and the substrate on one hand, but also less anchoring between the silane and the matrix on the other hand, causes this decreased mechanical performance. Nonetheless, this still results in higher performance compared to non-silane treated samples, a trend also found by Najari et al. [53].

The influence of long-time ageing seems to exceed the influence of increasing concentration. Whereas an increased concentration (slightly) increases self-condensation, but mainly causes the adsorption of more species on the substrate, ageing beyond the working window gives rise to larger self-condensed clusters, clearly having a more detrimental result. Literature noted that adsorption of dimers and small oligomers (as in the case of slightly higher concentrations) may increase the amount of accessible amine groups, whereas oligomer formation at longer times lowers the concentration of available silanol groups, necessary for correct interaction with the substrate [53, 240].

4.1.5 Summary

From previous experiments it is clear that silane solution parameters largely influence the appearance of the silane layer after deposition as well as the mechanical performance of SST-epoxy joints coupled by a silane layer. NMR measurements on methanol containing solutions point out that in order to obtain a useful working window for GPS, acid has to be added to the water/alcohol solution. In this way hydrolysis becomes rather fast (completed in less than 4 min), while considerable self-condensation (the dimer peak overwhelming the monomer peak) requires about 11 h. ^{13}C NMR reveals that self-condensation and not the opening of the epoxy ring limits the GPS working window to about 11 h.

APS can be used at its natural pH as hydrolysis kinetics are sufficiently fast. However, when using methanol as a solvent, dimer formation sets in rather quickly. Larger oligomeric species only appear after more than 13 h, resulting in a more than acceptable working window.

For BTSE a 50/50 water/alcohol mixture and the addition of (acetic) acid are required to keep the solution stable. Due to the acid, hydrolysis kinetics become fast, while dimer formation only shows up after 9 h, higher self-condensed species only set in after more than 17 h, again resulting in a sufficiently broad working window.

Also the solvent and its composition play an important role. For BTSE the solvent composition was not varied as it requires at least 50 v% of alcohol to keep these solutions stable. ^{1}H NMR reveals that an increase of the alcohol fraction (compared to the water fraction) has a negative influence on the hydrolysis kinetics of APS and GPS. Hydrolysis requires water, which can explain the increased kinetics with increasing water content. Moreover water has slightly higher polar characteristics compared to the alcohols used, leading to a small increase in catalytic species present. For sure this would increase hydrolysis rates in GPS and BTSE solutions, whereas for APS this would probably counteract this rate as it interacts stronger with the amino group, decreasing its autocatalytic effect. Nonetheless, in this last case the need for water during reactions seems to predominate as seen by the higher hydrolysis rates.

It was decided to work with a high water content for further experiments. Because the silane solution should wet the SST substrate sufficiently, a small amount of alcohol was added, leading to a water/alcohol ratio of 90/10 to be used in further work [85]. For BTSE and GPS the addition of ethanol as the alcoholic part of the solvent slows down hydrolysis kinetics, which is explained by the lower polarity of ethanol compared to methanol, leading to less catalytic species in solution and decreasing kinetics. A small note has to be made here that non-acidified GPS solutions were monitored to check the solvent effects on hydrolysis, as in the presence of acid hydrolysis becomes too fast to be monitored accurately. For APS solutions, hydrolysis rates increase when replacing methanol by ethanol, again explained by the lower polarity of ethanol. Methanol probably has stronger interactions with the amine functionality, decreasing its autocatalytic activity and thus causing slower hydrolysis kinetics. For the 3 types of silane ethanol slows down self-condensation kinetics, broadening the working window, with trimer (and larger oligomer) formation not observed up to at least 18 h after solution preparation.

Mechanical testing clearly indicates that APS induces higher mechanical strength compared to GPS and a BTSE-APS mixture when coupling a SST substrate to an epoxy matrix. The lower performance probably can be attributed to the loss of the GPS epoxy functionality after oven treatment, while the BTSE in the BTSE-APS mixture results in less amino functionalities available for coupling and a less polar network, as indicated by tensiometric measurements. From this it was decided to go on with APS species for further testing.

The influence of the silane concentration in the solution was checked. NMR reveals increasing hydrolysis rates with increasing APS concentration. However more importantly, due to the higher concentration and higher hydrolysis kinetics, also self-condensation speeds up with increasing concentration, leading to the onset of trimer and cluster formation already after a few minutes when using a 5/90/10 APS/H_2O/EtOH solution. This trend of increased self-condensation kinetics was also found for GPS, but not investigated any further. The increased self-condensation rate at a silane concentration of 5 *v*% leads to adsorption into larger, brittle patches (as seen by SEM) or as less organized multilayers with weak cohesion to the steel surface. The resulting non-uniform layer causes a lower degree of self-condensation as well as less anchoring points to (both the matrix and) the substrate. Here the APS layer becomes the weak point after hybrid formation and decreases mechanical performance, as shown by dolly testing. Lower concentrations (1 *v*%) rather cause incomplete covering of the surface, as was shown by ellipsometry, with the average layer thickness below the monolayer dimensions, causing insufficient anchoring points to couple the steel to the matrix. Moreover silane molecules may have an unfavorable orientation.

Tensiometry clarifies the trends seen, with the receding angle decreasing with increasing concentration, while the advancing angles goes through a maximum. Mechanical trends confirm highest strengths for 'intermediate' APS concentrations, and seem to relate to the equilibrium (and advancing) angle of the samples, but opposite to what was expected: higher angles result in a higher strength. This illustrates that it is not only about increasing the surface energy, but also about controlling the APS layer.

Finally a quick check on the influence of long-time ageing (beyond the working window) confirms that deposition from an aged solution results in performance even poorer than that of non-treated samples, pointing at the really detrimental influence of cluster formation in solution. In the case of higher concentrations a thicker layer forms because of an increased amount of adsorbed species, that mainly in the dimeric form. Formation of dimers and small oligomers do not state the biggest problem as they adsorb on the SST surface as easily as the monomer, with acceptable orientation, ordering and anchoring to the substrate. Oligomer formation at longer ageing times induces disorder and leads to less anchoring points with the substrate, but also with the matrix [53, 240].

4.2 Deposition Conditions

Starting from a 2/90/10 APS/H_2O/EtOH solution (unless mentioned otherwise), aged for a minimum of 25 min and a maximum of 4 h, silane deposition on the substrate can take place. It is generally accepted that the hydrolyzed silane can physically adsorb to the hydroxyl groups of an inorganic surface as shown in Figure 1.5. During the deposition step the solution dipping time is important, with the layer thickness depending on the dipping time. Short times lead to insufficient silane adsorption, while long(er) times can cause excessive adsorption and a chemisorbed layer near the substrate surface with a weaker and less ordered physisorbed layer on top. Rinsing immediately after this deposition step should remove this physisorbed excess, with the degree of removal depending on the rinsing time as well as the rinsing solvent. In the absence of rinsing, a thicker and less uniform layer appears [6, 229]. Most silanes are easily removed when exposed to water or organic solvents [57]. During this work, it was decided to (mainly) work with ethanol as the rinsing solvent, as water has a higher contact angle (poorer wetting) and may lead to silane accumulation and the formation of patches on the SST substrate after rinsing, becoming weak points in the silane layer.

Preparation and experimental details again can be found in the Chapter Materials and Methods, Section 2.3.

4.2.1 Morphological Characterization: AFM, SEM and TEM

Figure 4.25 and 4.26 depict AFM micrographs of respectively a rinsed and an unrinsed APS layer on an SST substrate after oven treatment of the sample (take into account the different scale and slight recontamination of the rinsed sample!). For the rinsed sample no clear larger images could be made, and this smaller scale has some clarity issues. However it can be seen that in case of rinsing the structure seen resembles the SST surface structure. Also for the unrinsed sample most of the SST structure remains visible, despite the thicker coating (see Section 4.2.2), which points at a still relatively thin APS layer (in the nm range), following the morphology of the substrate surface or pointing at the deposition of a rather soft layer, with the AFM tip mapping the steel surface as it taps through the APS layer. The latter is unlikely as literature often mentions silane layers to be hard and brittle. For the unrinsed sample granules with a diameter between 150 and 800 nm seem to appear, as well as brighter patches with less fine structure, probably caused by clusters.

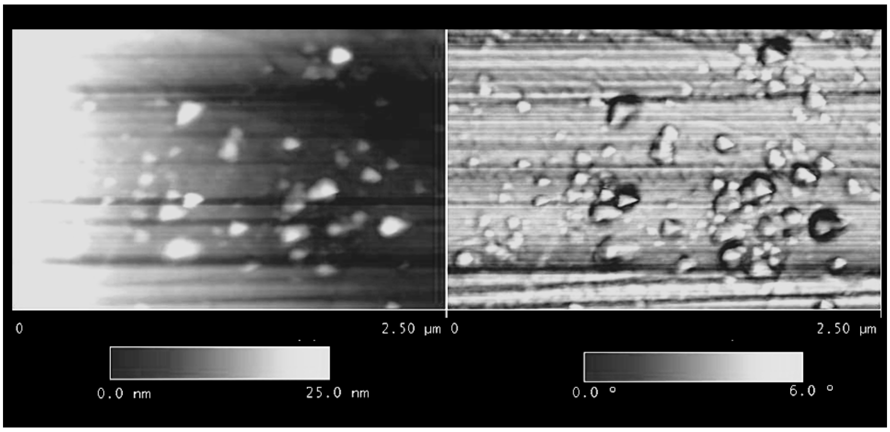

Figure 4.25: AFM height (left) and phase (right) micrograph of an oven treated APS layer on a SST substrate, ethanol rinsed after deposition from a 2/90/10 APS/H_2O/EtOH solution.

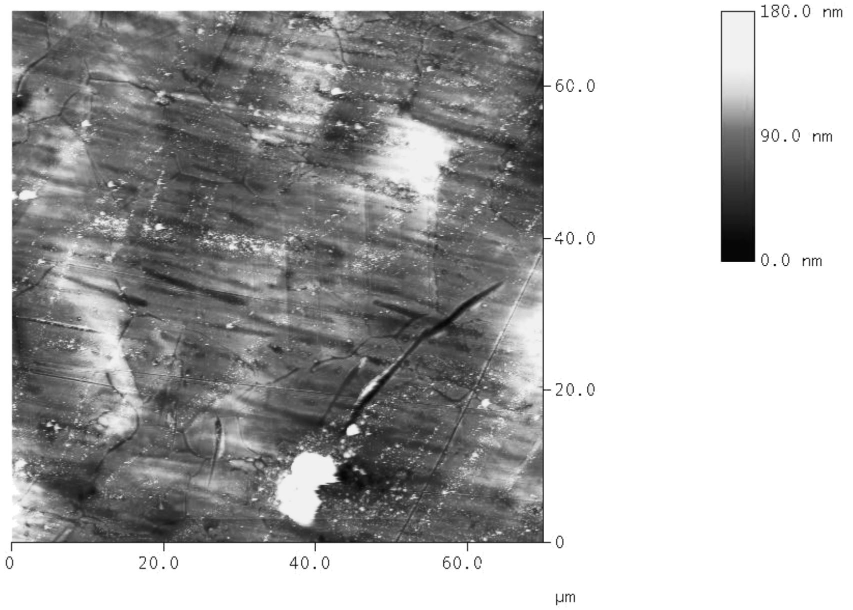

Figure 4.26: AFM height micrograph of an oven treated APS layer on a SST substrate, not rinsed after deposition from a 2/90/10 APS/H_2O/EtOH solution.

Comparing the roughness of these coated samples with the roughness of cleaned steel substrates (Table 4.4), reveals that silane deposition hardly influences the roughness, either in the absence or the presence of rinsing. In other words, the silane layer hardly fills the holes due to the substrate roughness, but rather follows the SST surface morphol-

Table 4.4: AFM determined arithmetic (R_a) and quadratic mean (R_q) roughness of SST substrates coated with APS from a 2/90/10 APS/H_2O/EtOH after oven treatment. Data for a blanc, uncoated sample (no APS) were added for reason of comparison.

Protocol	$\mathbf{R}_a$ [nm]	$\mathbf{R}_q$ [nm]
No APS	11.0	14.4
APS EtOH rinsed	11.3	14.2
APS not rinsed	11.01	14.06

ogy (and probably covers the surface entirely), while patches still have relatively small roughness, as seen from the roughness profile (data not shown) [33]. For all those silane layers the SST surface structure remains visible, pointing at the inability to accurately visualize these thin layers by AFM.

SEM clearly reveals that (ethanol) rinsing does have an influence on the APS layer deposited. At a larger scale (Figure 4.27, left images) the unrinsed sample (bottom) clearly shows (more) patches due to silane clustering. Rinsing probably removes the excess silane, and decreases the amount of clusters [47].

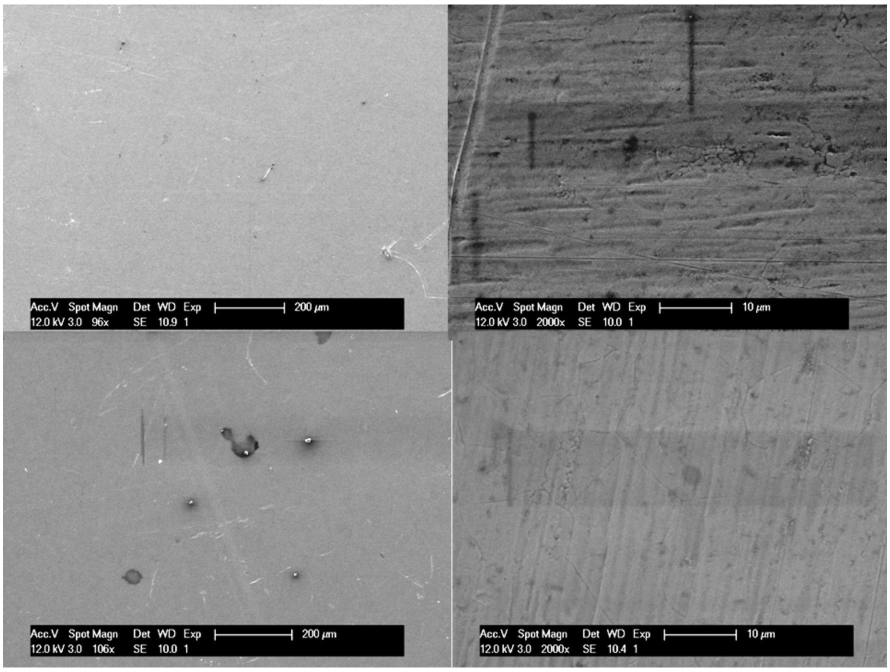

Figure 4.27: SEM micrograph of an oven treated APS layer deposited on a SST substrate, respectively EtOH rinsed (top) and not rinsed (bottom) after dipping in a 2/90/10 APS/H_2O/EtOH solution.

Depositing a mixed BTSE-APS layer in the absence of rinsing leads to an even more inhomogeneous deposition, probably due to a higher amount of clusters formed in solution. Bottom images in Figure 4.28

clearly depict the formation of silane rich islands, surrounded by a thinner silane layer covering the entire substrate. Rinsing on the contrary (Figure 4.28, top) again reveals the structure of the underlying substrate, pointing at a thin and more homogeneous deposition.

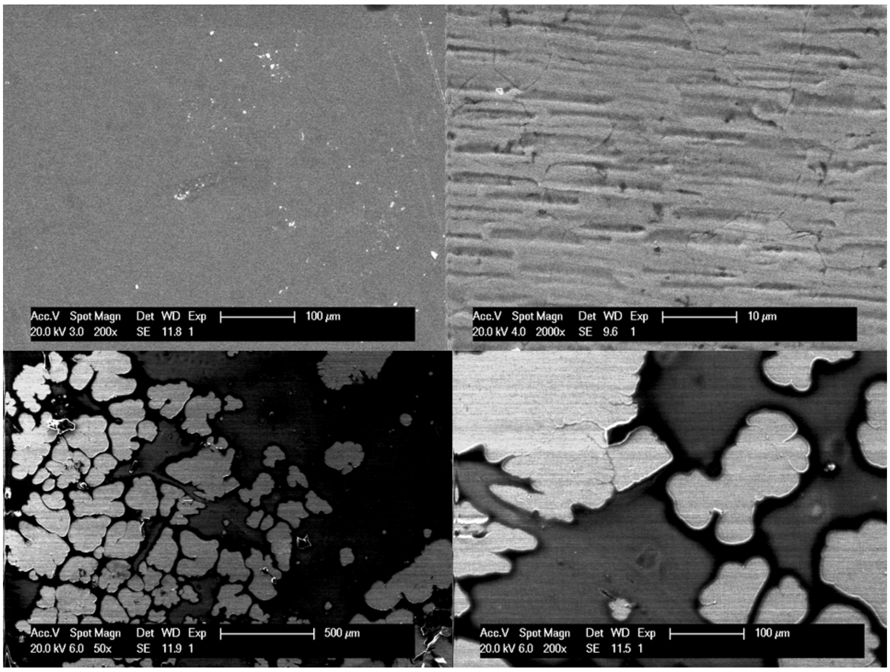

Figure 4.28: SEM micrograph of an oven treated mixed BTSE-APS layer deposited on a SST substrate respectively EtOH rinsed (top) and not rinsed (bottom) after deposition, the latter clearly demonstrating more patches.

Deposition from a more concentrated solution in the absence of rinsing obviously leads to a relatively thick silane layer after oven treatment, as shown in Figure 4.29. In the presence of rinsing both low and higher APS concentrations give rise to limited layer thicknesses as seen by Table 4.3. Obviously skipping the rinsing step has a larger influence on the layer thickness than the use of increased concentrations (Section 4.2.2), due to a lack of removal of the excess physically bound species causing formation of a thick APS layer.

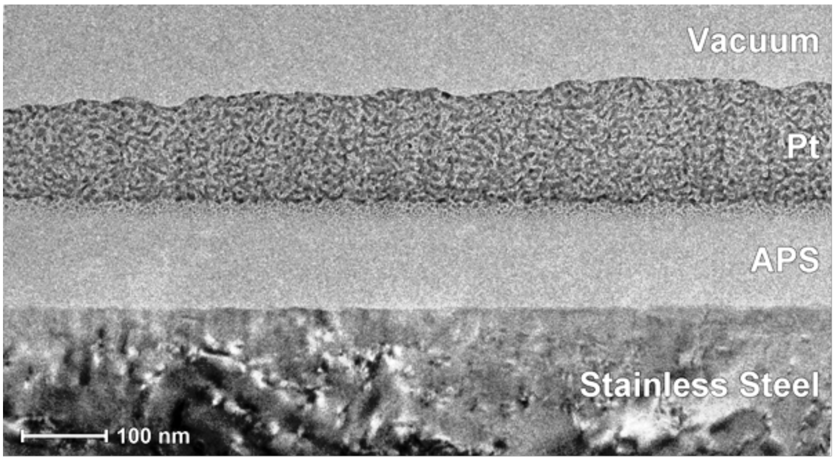

Figure 4.29: Oven treated silane layer deposited from a 10/90/10 APS/H_2O/EtOH solution on a SST substrate, in the absence of a rinsing step. The TEM overview micrograph displays (bottom to top): SST substrate - APS silane layer - covering Pt layer - background.

Figure 4.29. represents a TEM overview image of a silane layer deposited from a 10/90/10 APS/H_2O/EtOH solution after oven treatment, clearly showing the existence of a thick but -at this scale- rather uniform APS layer with a cross section of about 125 nm, in line with thicknesses of unrinsed layers found in literature [22]. The covering platinum was deposited during sample preparation (See Section 2.3.4) to protect the APS layer when thinning down the sample with a Focused Ion Beam (FIB). Imaging of the interfacial region with HR-TEM (Figure 4.30) not only clearly reveals the silane and substrate, but also the oxide layer covering the steel surface, which remains intact during and after APS deposition. At this scale interfaces are not perfectly flat and smooth because of the relief and roughness of the steel substrate itself. Honkanen mentioned that the surface topography influences the silane layer arrangement as a rough surface may disrupt the order of the first silane layer preventing the formation of the second. No visual disruptions can be seen here, probably due to the small dimensions of the silane molecules. Despite the limited roughness of the SST substrate, this issue often has to be taken into account [6]. However, as noted before an increase in surface roughness can increase mechanical interlocking and thus adhesion performance later on.

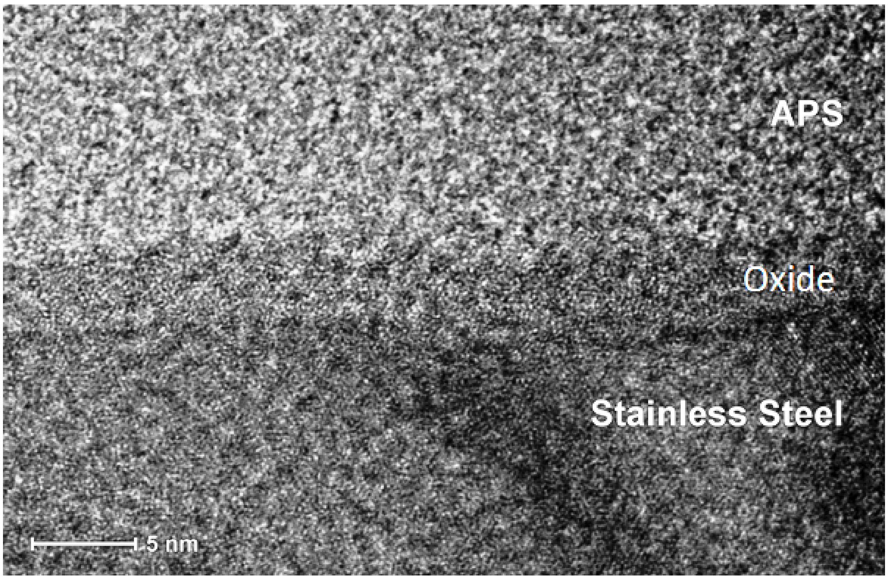

Figure 4.30: Oven treated silane layer deposited from a 10/90/10 APS/H_2O/EtOH solution on a SST substrate, in the absence of a rinsing step. The HR-TEM micrograph displays the interfacial region, not only depicting the substrate and APS layer, but also the oxide layer covering the steel substrate.

Figure 4.31 depicts the High Angle Annular Dark Field-Scanning Transmission Electron Microscopy (HAADF-STEM) image of the layer stack presented in Figure 4.29, as well as several EDX maps taken from the region indicated on the HAADF-STEM image. The EDX maps show the whereabouts of the different atomic species in the sample area indicated by the square. Carbon and silicon enrichment above the oxide layer confirm the presence of the silane. A closer look at the platinum signal reveals interpenetration of the covering layer with the APS layer, probably due to incorporation of the platinum in the softer APS stack during sample preparation. The APS-SST interface on the contrary is relatively sharp and flat. Oxygen EDX mapping results in a higher signal of the substrate in comparison to the silane layer, although the latter also contains a considerable amount of this element. The high intensity line in this map nicely illustrates the preservation of the so-called passive (oxide) layer.

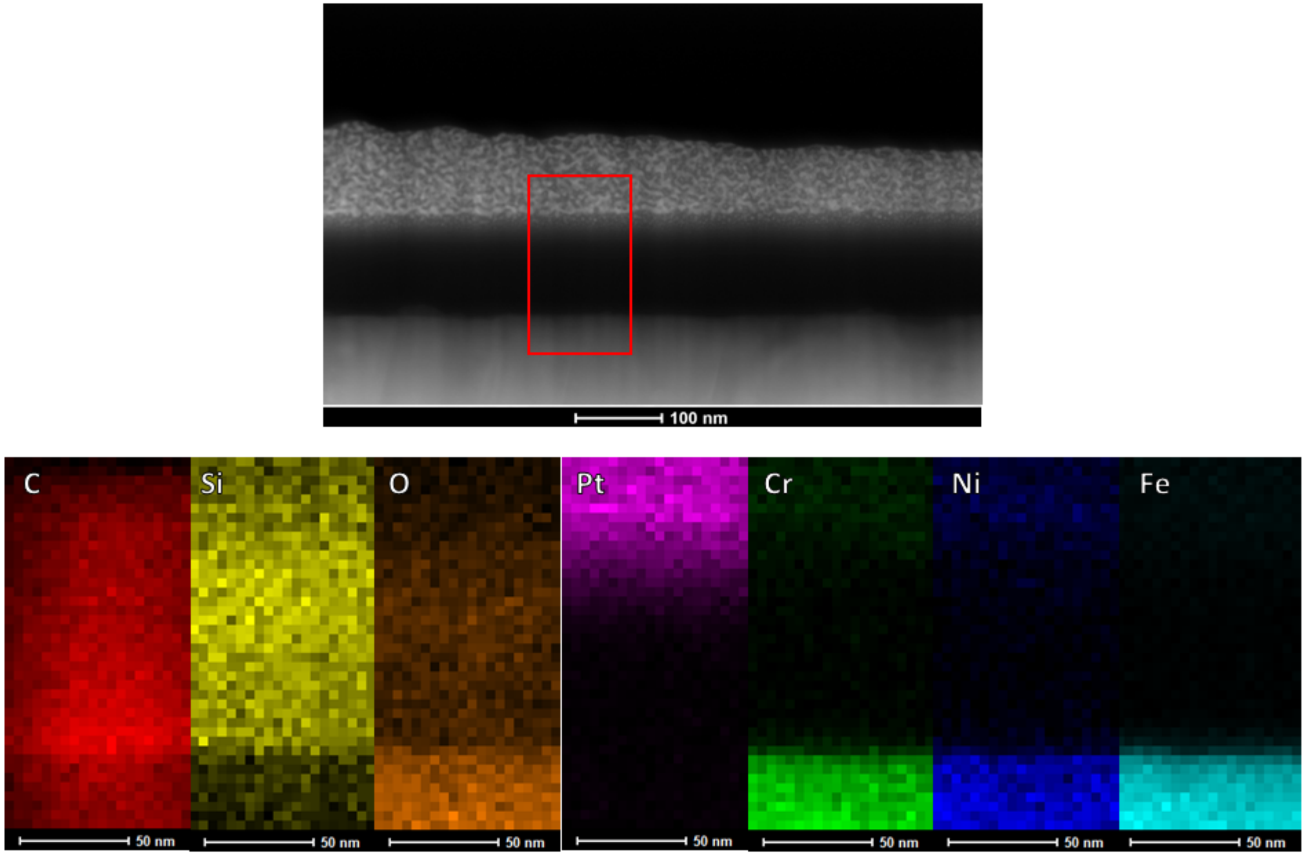

Figure 4.31: Oven treated silane layer deposited from a 10/90/10 APS/H_2O/EtOH solution on a SST substrate in the absence of a rinsing step. HAADF-STEM image of the layer stack (top) and concomitant EDX mapping for different elements (bottom).

4.2.2 Chemical Characterization: EDX, Tensiometry and XPS

EDX spectra resulting in average elemental abundances (Table 4.5) confirm the higher thickness of the unrinsed samples compared to the rinsed ones, as less of the substrate elements remain visible (mainly Fe, Cr and Ni), while the amount of Si, but also of C and O increases substantially. EDX also confirms that the absence of rinsing has a larger influence on the silane thickness compared to an increase in the concentration.

Table 4.5: Elemental abundance (*at*%) as determined by EDX measurements on an oven treated APS layer deposited on a SST substrate, respectively EtOH rinsed and not rinsed after deposition from a 2/90/10 APS/H_2O/EtOH solution. The 5 *v*% samples were also EtOH rinsed and added for reason of comparison.

	EtOH rinsed	**Not rinsed**	**5 v%**
C	1.60	18.15	8.88
O	3.40	18.23	7.68
Ni	4.16	1.51	3.30
Si	1.09	23.44	6.14
Cr	18.19	8.84	15.78
Fe	70.23	28.21	55.85

Zeng resumed tensiometric work of different authors, showing large differences among contact angles obtained, not only depending on the technique used, but also on the deposition conditions, as confirmed during this work. Most advancing angles in literature vary in between 45° and 93°, whereas receding angles vary from 0° up to 33° [243]. Different reasons are suggested for those differences, among which a different degree of crosslinking as well as the absence of highly ordered packing, arising from weak van der Waals interactions between the short APS propyl chains [55, 243]. Also the substrate roughness influences contact angles, but as this work uses identical substrates for all experiments, this can be ignored.

Figure 4.32 shows the influence of the dipping time on the water contact angles of coated SST substrates (all 1 min ethanol rinsed before oven treatment). Compared to the cleaned, uncoated substrates (θ_{eq}, θ_{adv} and θ_{rec} resp. 59.5±2.3, 80.4±3.5 and 32.0±2.8), all samples again have lower contact angles, indicating an improvement of the wettability. Despite the fact that Section 4.1.4 revealed highest bond strength for the 2 *v*% sample, different concentrations are tested. Previously, poorer performance of the 1 *v*% sample was caused by insufficient substrate coverage after deposition, while the 5 *v*% gave rise to a slightly thicker and less ordered silane layer. Changing the dipping time may change the amount of silane adsorbed and thus the resulting properties.

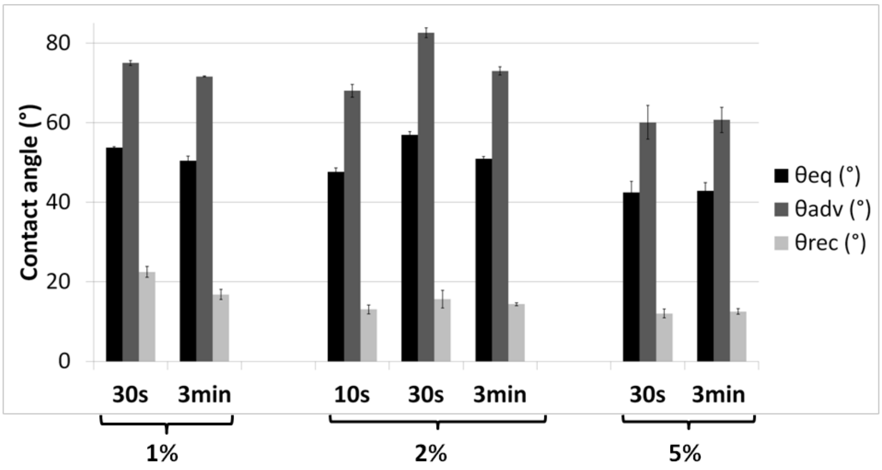

Figure 4.32: Influence of the dipping time of the substrate in the silane solution (different concentrations of APS in a 90/10 H_2O/EtOH solvent) on the equilibrium, advancing and receding contact angle of a SST substrate after deposition and oven treatment.

Study of the 1 *v*% sample reveals that dipping 3 min instead of 30 s decreases both the advancing and the receding angle, the latter pointing at a higher degree of silane adsorption or a decrease in the degree of self-condensation. Probably a combination of both takes place. The lower advancing angle indicates a lower degree of self-condensation, due to less ordering and packing and more steric constraints in the deposited layer [139]. Harun et al. found upside-down adsorption of APS on mild steel under incorrect deposition conditions, and also Quinton and Dastoor mention upside down orientation for shorter dipping times [67, 106], although these species would be able to flip their position upon oven treatment [229].

Study of the 2 *v*% solution shows that the advancing and equilibrium contact angles pass through a maximum with increasing dipping time. The receding angle can be considered constant, pointing at the same amount of high energy interactions for all dipping times. However, again this not necessarily means the polar part of the surface remains identical. Quinton and Dastoor found reversible and upside down APS adsorption at shorter dipping times [106], meaning that polar silanol groups point upward from the surface instead of the polar amine groups. The lower advancing angle after 3 min (compared to 1 min) of dipping probably is induced by a higher number of species remaining at the surface after rinsing, pointing at more and strong (chemi)sorption at longer dipping times. This increased amount of less ordered silane gives rise to a lower degree of crosslinking. 10 s of dipping probably does not allow for complete surface coverage, neither for appropriate orientation. These phenomena again hinder the degree of crosslinking, decreasing the advancing contact angle in comparison with the 30 s dipped sample.

The contact angles of the rinsed 5 *v*% species remain about the same after 30 s and 3 min of dipping, pointing at similar layer properties in both cases. It is likely that at this higher concentration maximum chemisorption takes place in a rather short time span, although an increased dipping time may cause more physisorption. The next step rinses away this weakly bound excess, leaving behind a similar layer for both rinsing times. Measurements for these 5 *v*% samples result in wavy (contact angle vs. immersion depth) spectra compared to the other samples, pointing at more inhomogeneity. In comparison to other concentrations, the 5 *v*% series suffers from a very low degree of crosslinking, as seen by the lower contact angles again pointing at a high degree of steric constraints.

Figure 4.33 demonstrates the influence of the ethanol rinsing time on the contact angles after deposition from APS solutions with different concentrations (30 s dipped). For the 1 *v*% sample rinsing hardly influences the contact angle, and measurements result in straight, text-book like tensiometric profiles. As stated before, these solutions result in incomplete coverage of the substrate, due to insufficient silane adsorption during dipping [55]. However, this gives rise to strongly anchored chemisorbed molecules, that cannot be rinsed away.

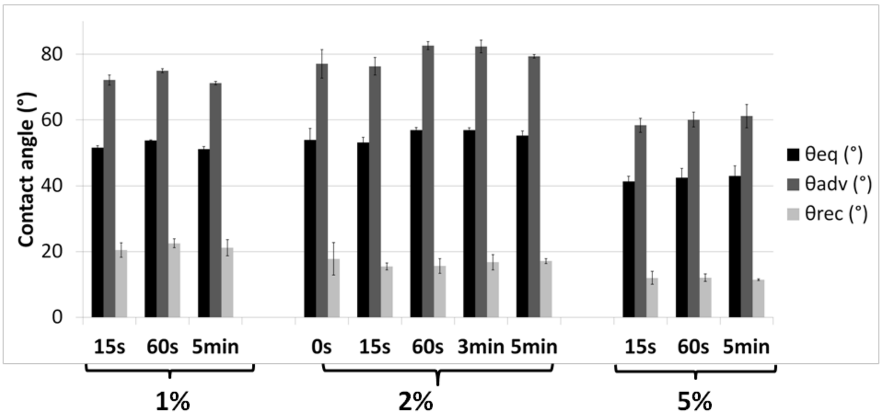

Figure 4.33: Influence of the rinsing time (in EtOH) of the substrate after APS solution deposition (different concentrations in a 90/10 H_2O/EtOH solvent) on the equilibrium, advancing and receding contact angle of a SST substrate after deposition and oven treatment.

Rinsing does have an influence on the 2 *v*% samples. Absence of rinsing (0 s) or short rinsing (15 s) gives rise to inhomogeneous coverage of the substrate, due to incomplete removal of the highly unordered physisorbed layer, as seen by the waviness of the tensiometric profile recorded during measurement (not shown), as well as by the higher standard deviations found. Both rinsing times cause similar contact angles, and the lower advancing angle again can be explained by less ordering of the (physisorbed) layer, inhibiting proper self-condensation. Rinsing for 60 s (and 3 min) results in highest advancing contact angles, probably due to the fact that this results in the best (ordered) layer conditions and the highest degree of self-condensation. These rinsing conditions remove the physisorbed layer and possibly also allow reorientation of the silane remaining. Longer rinsing times (5 min) cause a slight decrease of this angle and an increase of the receding angle. It seems that under these conditions of longer rinsing times, also the stronger (chemi)sorbed layer is partially removed, again resulting in a lower degree of self-condensation due to less complete coverage.

The samples in the 5 *v*% series have similar receding contact angles for all rinsing times, due to a similar high energy part of the coated surface. The advancing angle seems to increase slightly with increased rinsing times, probably due to more removal of physisorbed species and more time for the silane molecules to reorient. However, note that standard deviations are rather large compared to angle differences, so results should be interpreted with care.

Also XPS reveals the influence of rinsing (Figure 4.34). For all samples it is clear that silane sticks to the substrate after deposition as the iron signal decreases while the Si and N signal increase due to silane coverage [42]. The higher carbon signal after deposition does not concern contaminant adsorption (it is far too high), but can be ascribed to propyl carbon from the silane itself [67]. In the absence of rinsing, the iron signal disappears completely because of the thicker silane layer. Comparing different rinsing methods reveals that ethanol rinsing removes less silane compared to water rinsing when using APS deposited

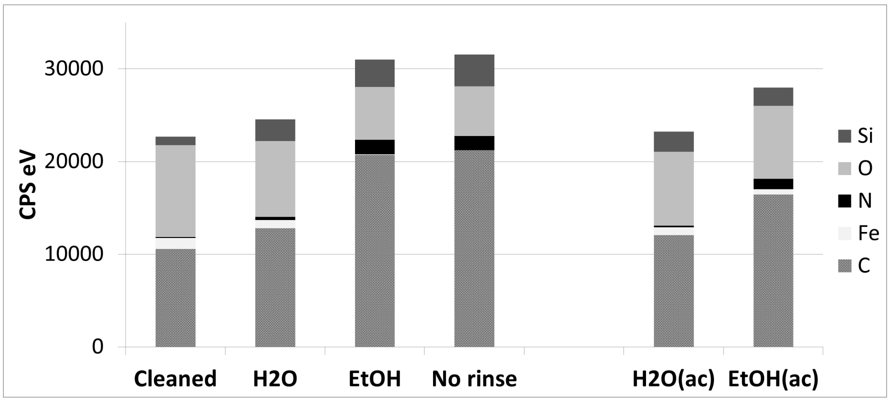

Figure 4.34: Influence of the rinsing method on the abundance of different elements as calculated from XPS measurements after oven treatment of coated samples. Data of an uncoated, cleaned sample are added for comparison. Data on a silane layer deposited from a neutral standard solution are compared with a layer deposited from an acidified APS solution (ac).

from a neutral as well as from an acidified solution (ac), contrary to what was found in certain literature (Chapter 1, Section 1.3.3.2). Note that in the case of acidic deposition, a thinner layer remains for both rinsing solvents, due to less initial deposition or due to more efficient silane removal during rinsing because of weaker interactions.

Although in general a thicker layer causes premature failure in composites, an additional feature has to be taken into account: the C/Si and the N/Si ratio, both taking into account a contaminant correction factor (Table 4.6). Both ratios give an indication of silane orientation. A higher value points at a higher amount of N and C detected in comparison to Si and thus indicates an improved orientation of the amino functionalities. A lower value points at molecules lying down or at upside down adsorption, burying amine groups. Water rinsing results in very low values, whereas ethanol rinsing causes much higher values. This can have a twofold explanation: initial adsorption is upside down, and molecules flip in the correct position upon rinsing in ethanol, or molecules adsorb the right way and flip upside down upon water rinsing. Puomi et al. noted improved and faster rearrangement after rinsing [85]. An increased availability of the nitrogen group leads to an improved adhesion performance as the nitrogen is part of the amine group, necessary to couple to the matrix in the next stage.

Table 4.6: The N/C and N/Si ratio after different rinsing procedures calculated from XPS measurements, corrected for silicon and carbon contaminants. Higher values point at an improved silane orientation.

	C/Si	**N/Si**
H_2O rinsed	1.5	0.24
EtOH rinsed	4.9	0.75
Not rinsed	4.2	0.61
H_2O rinsed (ac)	1.2	0.13
EtOH rinsed (ac)	5.5	1.05

Figure 4.35 demonstrates the peak decomposition for an unrinsed sample, Figure 4.36 depicts the oxygen peak (high resolution) of APS coated samples. The bare uncoated but US cleaned sample added for comparison, clearly contains a large portion of oxides and hydroxides. Also the water rinsed sample clearly contains a rather large oxide (O^{2-})

peak, which can be attributed to the thinner APS layer remaining after rinsing. Possibly water rinsing leads to incomplete coverage, and the (incompletely) buried substrate surface below still can be ′seen′ by the XPS equipment, explaining the large oxide peak seen. Of all samples the ethanol rinsed species clearly has the largest contribution of high energy oxygen bonds. Si-O-Si bonds give rise to this high energy peak, confirming the higher degree of self-condensation compared to the unrinsed sample [67]. Compared to the ethanol rinsed sample, the unrinsed sample has a larger contribution at a slightly lower binding energy, caused by the O-H bonds. This confirms the presence of more ′dangling′ silanol ends, and a smaller degree of self-condensation, also previously observed by other researchers [67].

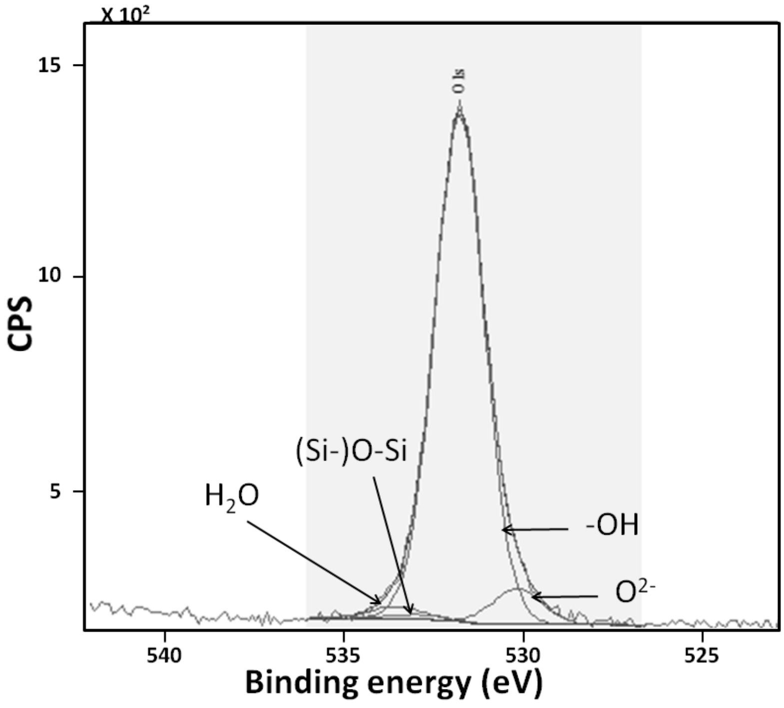

Figure 4.35: Oxygen peak decomposition of an APS coated (unrinsed) and oven treated SST substrate.

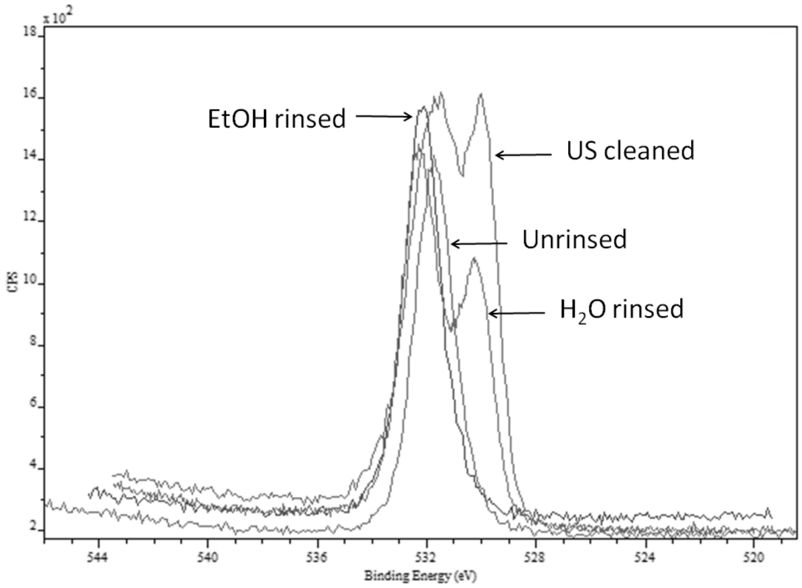

Figure 4.36: Oxygen peak as found by XPS for APS coated and oven treated SST substrates using different ways of rinsing. The x-axis displays the binding energy, the y-axis the counts per second (CPS).

Note that both the unrinsed and ethanol rinsed sample only have a very small oxide (O^{2-}) contribution. The reason for this can be twofold: firstly the oxides can disappear by reaction with the silane, secondly the silane layer burying the steel surface can become thicker, hiding the oxide signal. Probably a combination of both should be taken into account, as the silane layer is anchored to the steel surface and the iron peak (found by XPS) for those samples has only low intensity, pointing at coverage with a layer of a few nm thickness. Also Harun et al. noted that the oxide peak virtually disappears after appropriate silane coverage [67]. The high energy part of the water rinsed sample completely overlaps with that of the ethanol rinsed sample, indicating a high degree of self-condensation of the silane that is left behind.

Figure 4.37 compares the extent of self-condensation of an APS layer for different rinsing procedures. The y-axis represents the ratio of the Si-O-Si peak (calculated from the high resolution oxygen peak) divided by the total silicon signal (calculated from a low resolution

Si peak) [42]. This seems the most straightforward way to compare the degree of self-condensation. The Si-OH (oxygen sub)peak is not appropriate to do so as it also can have a contribution of the surface hydroxyl groups, while the resolution of the silicon peak itself is too low for exact decomposition. By no means this image can be interpreted as the degree of self-condensation because of the different resolutions used. Nonetheless it provides a clear image of differences between samples, and confirms the lower degree of self-condensation for the unrinsed samples.

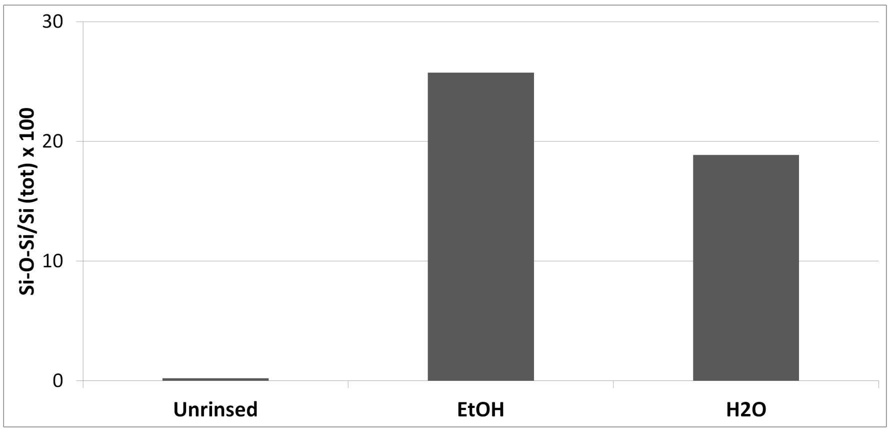

Figure 4.37: Influence of the rinsing procedure on self-condensation, as calculated from the ratio of the Si-O-Si signal to the total Si signal (determined by XPS). Note the y-axis does not represent the total degree of self-condensation.

Figure 4.38 displays the abundance of the oxygen subpeaks as a function of the rinsing procedure. In case of water rinsing, a large part of the underlying (hydr)oxides still appears after coating, increasing the total oxygen signal, while in the absence of rinsing or after ethanol rinsing this subpeak decreases, due to shielding of this oxide layer or reaction of these species with the silane. It is clear however that the unrinsed sample has a lot of hydroxyl groups remaining after oven treatment, while for the rinsed samples a lot more self-condensation took place, especially after ethanol rinsing.

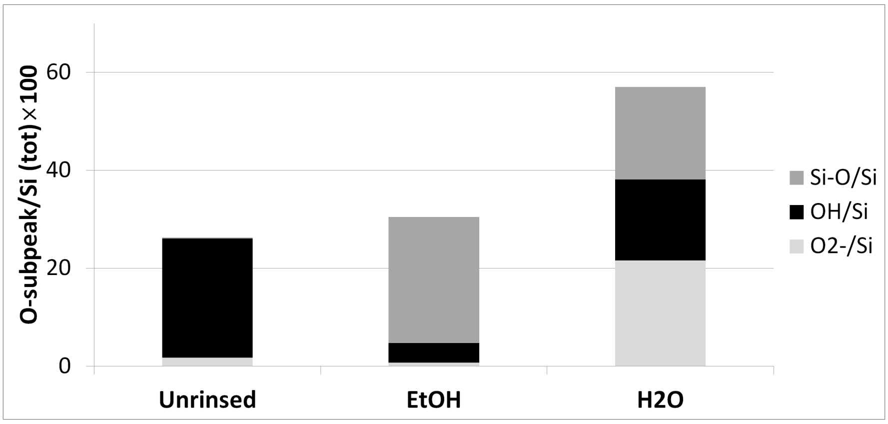

Figure 4.38: Abundance of oxygen subpeaks as a function of the rinsing procedure of a coated SST substrate as calculated from XPS measurements.

4.2.3 Mechanical Characterization

Dolly testing results of samples prepared from the same APS solution, with identical rinsing conditions and oven treatment but with a different dipping time are presented in Figure 4.39. Irrespective of

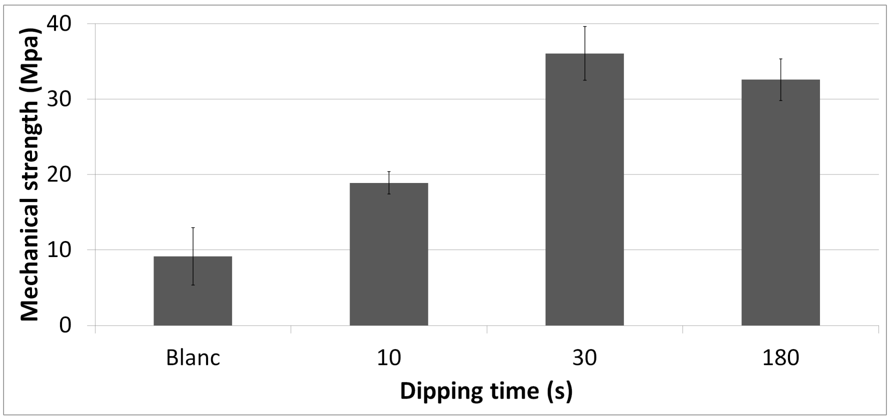

Figure 4.39: Mechanical strength as determined from dolly testing of SST-epoxy joints coupled by an (oven treated) APS layer deposited from a 2/90/10 APS/H_2O/EtOH solution with varying dipping times and a constant rinsing time.

dipping time, the mechanical strength always exceeds that of the blanc sample (9.2 ± 3.8 MPa). The sample strength passes through a maximum with increasing dipping time, and follows the same trend as the advancing and equilibrium contact angle. The shortly dipped samples (10 s) suffer from inferior strength due to incomplete coverage, as indicated in previously. However, also the sample dipped for 3 min has a lower mechanical strength compared to the 30 s dipped sample. Earlier characterization pointed at the accumulation of silanol groups which impedes efficient accommodation on the substrate as well as sufficient self-condensation. This clearly contradicts the statement that in the case of rinsing after dipping of the samples, the amount of silane left never depends on the dipping time, but only on concentration [105, 244]. A similar effect has been observed in the case of copper/epoxy hybrids with APS treated copper surfaces [2], and it is generally accepted that thicker and brittle layers then cause inferior interfacial strength [2, 245].

The rinsing time influences the mechanical strength to the same extent as the dipping time, as seen in Figure 4.40. Various APS concentrations were checked as higher concentrations may require longer rinsing times to remove the thicker physisorbed layer. Again all resulting strengths exceed that of the uncoated sample and vary parallel to

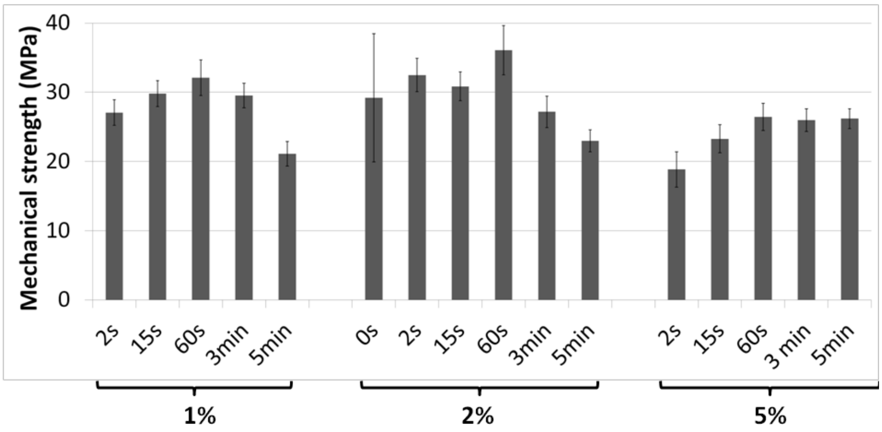

Figure 4.40: Mechanical strength as determined from dolly testing of SST-epoxy samples coated with an (oven treated) APS layer deposited with a constant dipping time and varying rinsing times.

the trends seen during tensiometry. The 1 $v\%$ sample displays a rather small variation in the strength with increasing rinsing time for moderate durations, probably due to the low amount of initially adsorbed silane. Nonetheless shorter rinsing times decrease mechanical performance. Probably even this concentration leads to some physically adsorbed species after dipping, that require a certain removal time. A reason for the increased strength for intermediate times can be the flipping or removal of wrongly oriented molecules upon rinsing. At longer times the strength again slightly decreases, due to the removal of stronger chemisorbed APS molecules, even more decreasing coverage.

For the 2 $v\%$ series also the unrinsed sample (0 s) was tested, demonstrating a large standard deviation of the mechanical strength. As the mechanical trends in general again follow the advancing and equilibrium angle, explanations can mainly be found in the degree of crosslinking of the silane layer, although probably also the layer thickness plays an important role. For rinsing times below 60 s insufficient removal of the APS excess takes place, leading to a weaker, less homogeneous and to a different degree crosslinked silane layer. Rinsing for longer times ($>$ 60 s), removes silane excessively, and probably also removes part of the more tightly bound, ordered silane, causing incomplete substrate coverage [47].

The mechanical strength of the 5 $v\%$ series displays a more or less similar trend. Higher concentrations lead to more physisorbed molecules, but also a higher amount of stronger adsorbed species, and this series as a whole suffers from a lower strength. Shorter rinsing times again result in a lack of removal of the excess silane. Longer rinsing times on the contrary seems to result in similar strengths compared to the 60 s rinsed sample. Despite the removal of the physisorbed layer, the silane layer left behind is still too thick, forming the weak point in the hybrids. These trends again are in line with tensiometric results.

4.2.4 Summary

The interfacial strength of silane coupled SST-epoxy joints using different dipping times and keeping other conditions constant, increases with dipping time and goes through a maximum around 30 s of dipping for a 2 $v\%$ solution. Combining these results with tensiometric results points at an increased amount of stronger adsorbed species with time. Literature mentions 'upside-down' silanol adsorption (and 'lying' molecules) at shorter dipping times [106] as well as insufficient adsorption and thus poor surface coverage and self-condensation as a possible cause of the lower average interfacial strength. Longer dipping times cause excessive adsorption of stronger bound molecules and steric constraints, again causing less self-condensation. In other words short dipping times result in insufficient anchoring in combination with a weaker coupling layer, while for longer dipping times the problem lies in the thicker and weaker coupling layer.

The optimal rinsing time for different APS solution concentrations in a 90/10 water/ethanol solvent was checked. The absence of rinsing leads to a thick silane layer because of the large amount of physically adsorbed species, and patches can be observed both visually and by XPS. However, for all samples visually studied the substrate morphology 'shines through' the silane layer, pointing at relatively thin layers for all conditions checked, although in the absence of rinsing this morphology is less defined. Brief rinsing times lead to insufficient removal of the physisorbed layer, resulting in a thicker, poorly ordered and less self-condensed silane layer that decreases mechanical performance. Longer rinsing times on the contrary excessively remove APS, including the chemisorbed molecules, which also destroys the interfacial strength due to the creation of a defective coating.

4.3 Oven Conditions

As silane adsorption initially only occurs through hydrogen bonding, a condensation/curing step should take place after deposition. During this and most experimental work an oven treatment takes care of the condensation step.

During the oven treatment again different parameters come into play. Firstly there is the use of a vacuum, that may enable solvent and by-product evacuation during the drying operation. Secondly, variation of the oven temperature changes the degree of silane crosslinking and can assist again in evacuation of solvents and by-products. Finally also the oven residence time determines the degree of crosslinking, although a time-temperature equivalency is expected, where higher oven temperatures require shorter residence times to obtain similar properties.

Sample preparation again starts from a US cleaned SST substrate and preparation of a 2/90/10 APS/H_2O/EtOH solution, followed by a dipping (30 s) and rinsing (1 min in EtOH) procedure. Next, samples are oven treated, thereby varying conditions of time, temperature and vacuum. Full details on experimental procedures can be found in the Materials and Methods Chapter, Section 2.3.1.

4.3.1 Morphological Characterization: SEM and TEM

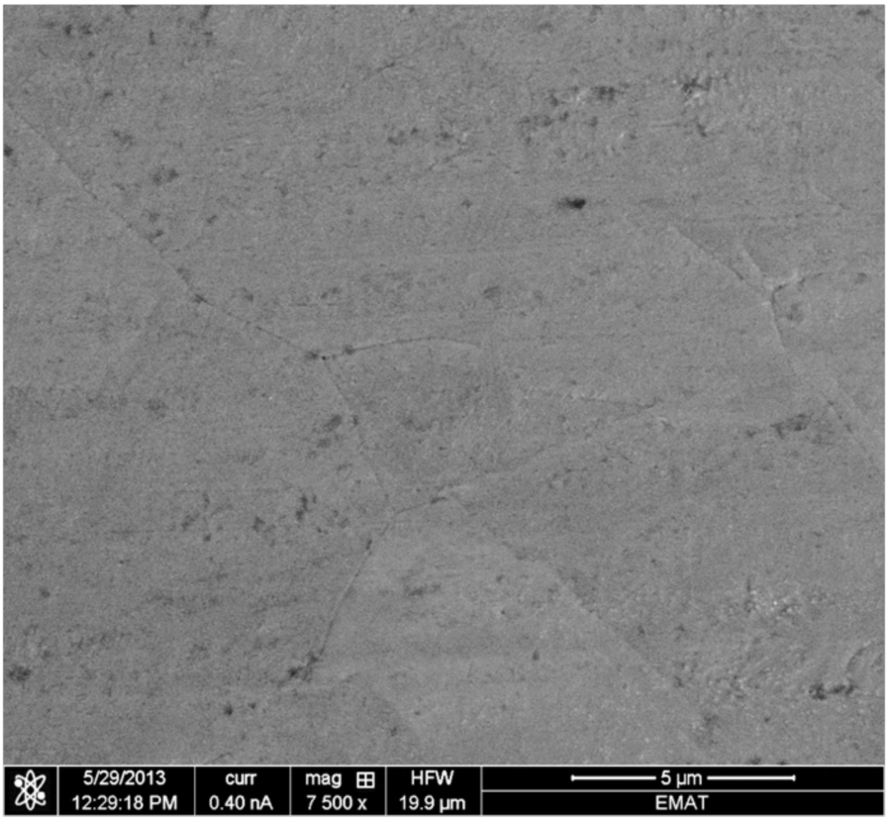

Figure 4.41: SEM micrograph of a SST substrate coated with APS according to standard deposition conditions, and oven treated at 70°C for 1.5 h without vacuum. No clear signs of APS can be seen.

Electron microscopy observation of a silane layer (oven treated in the absence of vacuum) suggests that the resulting layer is very thin. From this it becomes clear that one cannot expect to see changes due to different oven conditions. Nonetheless, those micrographs will shortly be discussed.

SEM micrography shows that under standard conditions the SST grain structure remains visible (Figure 4.41) and a homogeneous very thin silane layers seems to be deposited, as Honkanen et al. already noticed [22]. In order to visualize the silane layer more clearly, a sample was thinned down to electron transparency by a FIB treatment after platinum coverage.

Figure 4.42 displays a scanning TEM (STEM) micrograph of the thus obtained sample, that again reveals the extremely thin dimension of the APS layer (the lighter layer on top of the ′black′ layer), about 9 nm in diameter (on average). Combination of this image with the super-X elemental mapping images, provides more information and proves the presence of a silane layer. The signal in the Fe, Cr and Ni map can be attributed to the steel substrate. The oxygen layer on top of these elements, confirms the existence of a thin oxide layer covering the surface, having a thickness of about 4.5 nm, consistent with literature (See Section 1.2.1.3). The thin higher intensity lines in the Si and N spectrum, just above the high intensity O band, can be attributed to the silane. The contours of this silane layer gently follow the substrate surface morphology. The low intensity part of the C spectrum seems to overlap with the substrate, while the ′line′ with higher intensity is exactly where the silane layer appears. Nonetheless the Si and N spectra are more clear to prove the presence of the silane layer. The platinum spectrum reveals the Pt used to protect the APS layer during FIB treatment. It clearly penetrates into the silane layer which not necessarily points at a porous or weak and brittle layer, but rather can be due to the FIB treatment that was complicated by the difference in properties between the silane layer and the SST substrate. However, this confirms that electron microscopy cannot reveal more information about the influence of different oven parameters.

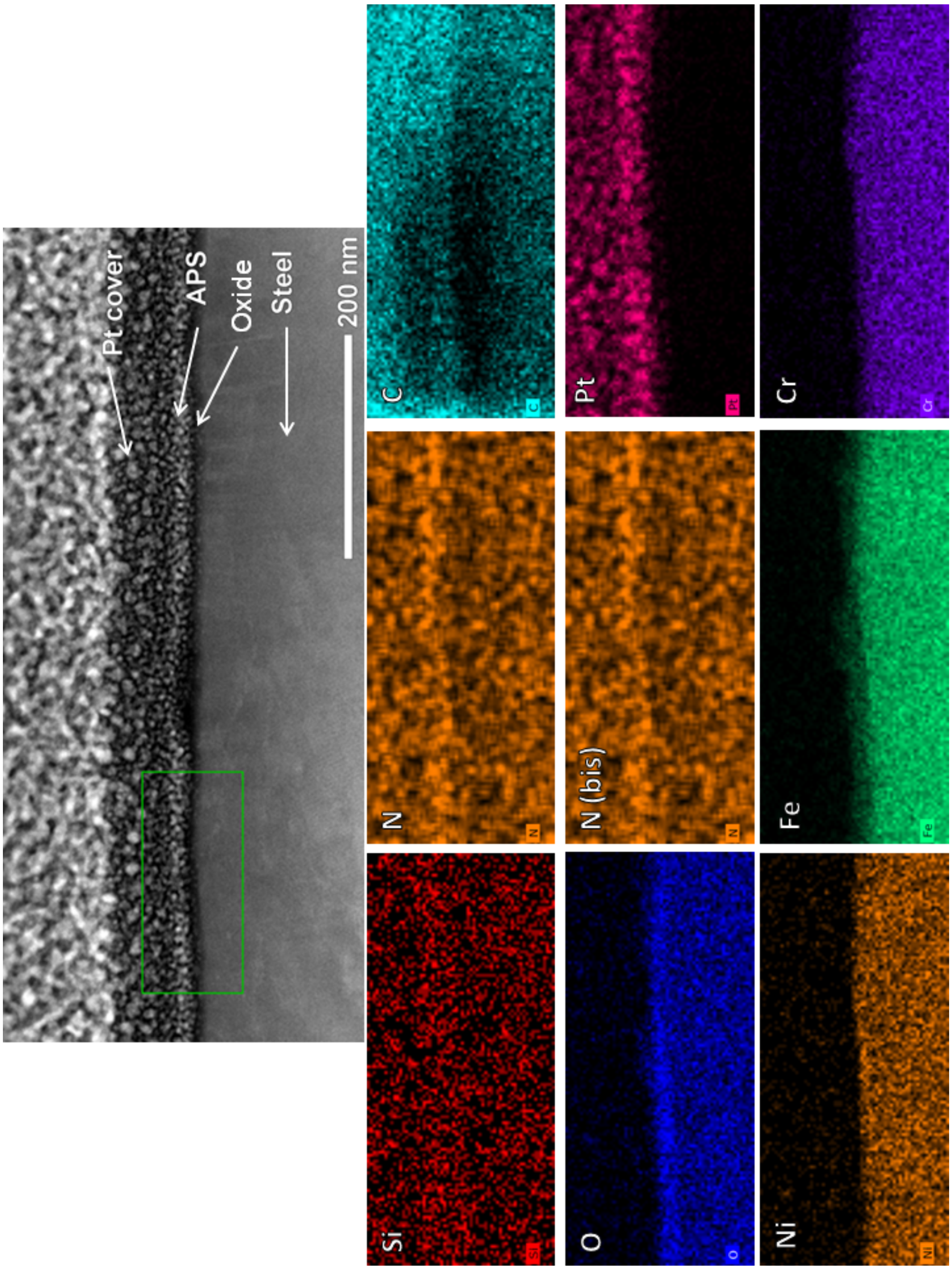

Figure 4.42: STEM micrograph of a SST substrate coated with APS according to standard deposition conditions, and oven treated at 70°C for 1.5 h without vacuum (top). Super-X EDX elemental mapping (bottom) of the rectangular part indicated at the STEM micrograph. Note the N-map was added twice to facilitate comparison of the position of different elements.

4.3.2 Chemical Characterization: TGA, Tensiometry and XPS

Tensiometric measurements (Figure 4.44) demonstrate the influence of variations in the presence of a vacuum, temperature and oven residence time on the contact angle of samples prepared from a 2 *v*% APS solution, with 30 s of dipping and 1 min of rinsing. Clearly all oven parameters do have their influence, as described further below.

Thermogravimetric analysis (TGA) measurements for 4 h at a constant temperature and solution composition (2/90/10 APS/H_2O/EtOH) under nitrogen atmosphere reveal different processes at different temperatures the lowest 50°C, a temperature often claimed to be necessary to reach a considerable degree of condensation [85, 89, 99]. In the ideal case 0.94 *m*% of the starting solution remains behind after full self-condensation and complete evaporation of the solvent and reaction by-products. In practice (Figure 4.43) it can be seen that at least 0.99 *m*% remains after reaching equilibrium, while no trend can be seen in the exact mass left behind. Handling inaccuracies determine at least partially these phenomena, as e.g. already part of the solvent may evaporate before the start of the measurement resulting in a relatively higher left-over mass. Also tightly bound water may remain in the layer after thermal treatment at these temperatures, increasing the mass. Finally it is conceivable that part of the higher mass left at equilibrium can be attributed to the nonexistence of an ideal, fully self-condensed silane layer due to steric constraints and insufficient mobility of the molecules. In this way they can reorient themselves completely during condensation. Figure 4.43 demonstrates that for higher temperatures the equilibrium mass sets in earlier (also shown in Table 4.7), as expected.

A non-isothermal measurement of a predried APS film by VUB researchers on exactly the same system showed three distinct weight loss peaks. The first occurs around 64°C, due to the evaporation of water released during condensation reactions. Evaporation of strongly adsorbed water or decomposition causes a peak at 275°C while that at 437°C can be due the decomposition of the silane film [246].

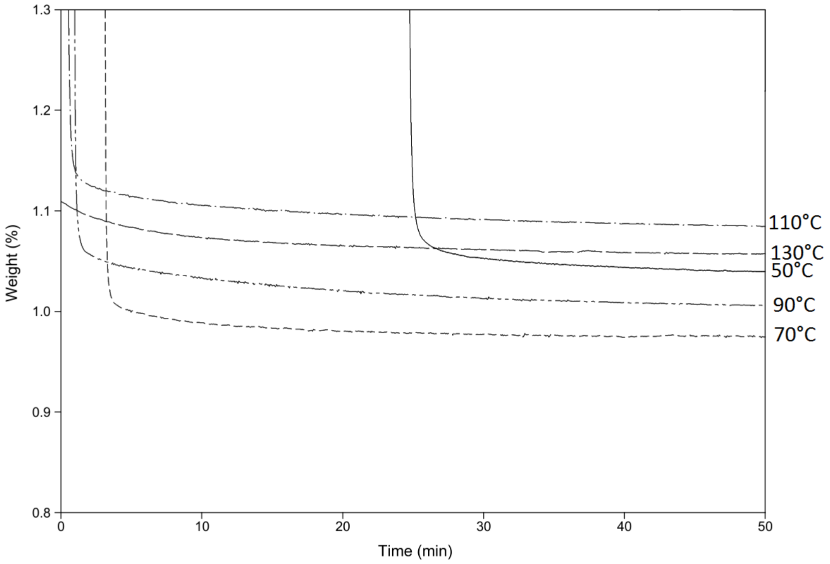

Figure 4.43: TGA spectrum as obtained after an isothermal measurement of a 2/90/10 APS/H_2O/EtOH solution at different temperatures.

Table 4.7: Estimation of the time (t) until maximum self-condensation as determined from isothermal TGA measurements at different temperatures (T).

T [°]	**t** [min]
50	180
70	165
90	135
110	110
130	75

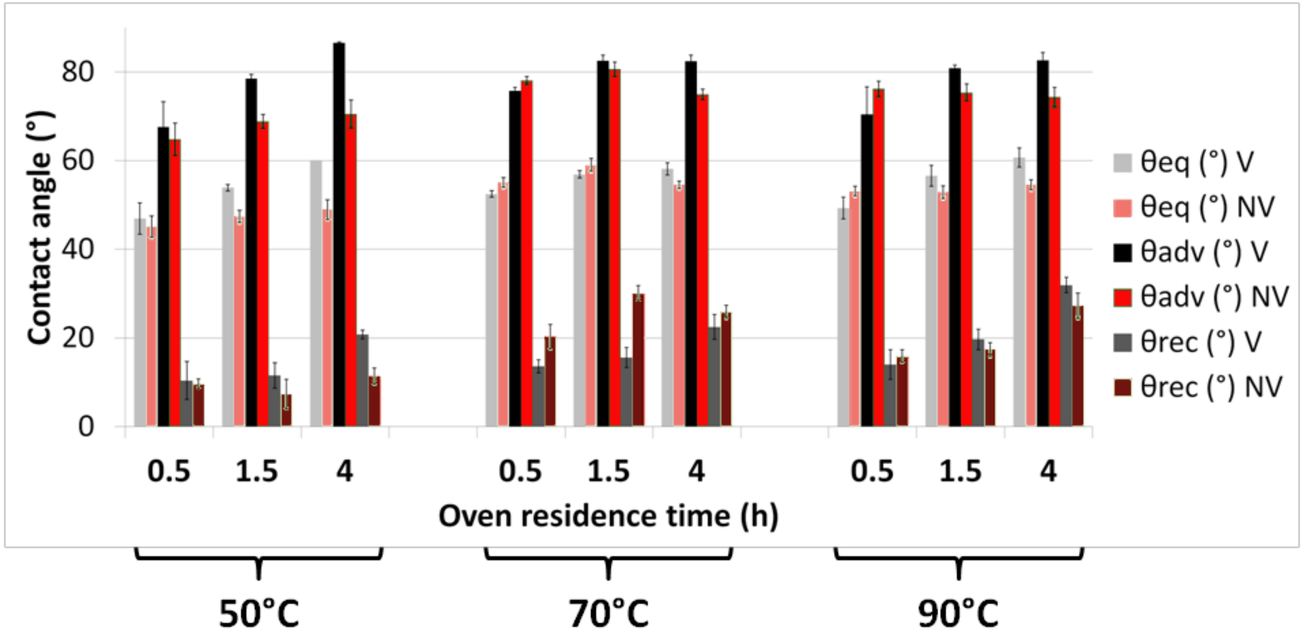

Figure 4.44: Influence of the oven conditions on the equilibrium, advancing and receding contact angle of a stainless steel substrate after deposition (from a 2/90/10 APS/H_2O/EtOH solution). The greenish samples represent data of samples treated in the absence of vacuum (NV), greytones represent samples treated in the presence of a vacuum (V).

Combination of these results with tensiometric data enables explanation of the phenomena taking place. As all samples initially contain an identical amount of APS, the lower contact angles at shorter residence at 50°C probably can be attributed to lower degrees of self-condensation, as reactions are not completed to their maximum yet. Abel et al. observed that most crosslinking only occurs above 50°C [89], and in the absence of vacuum, these reactions even take longer, while applying a vacuum increases reaction rates. Moreover water is not evacuated to the fullest at shorter times and especially the absence of vacuum, causing still lower contact angles. Underhill et al. expect water to disrupt hydrogen-bonded silanol linkages and to stimulate self-condensation instead of condensation to the surface [31]. Moreover, an increased amount of water adsorbed to the surface may impede displacement with silane molecules. This confirms and explains the improved self-condensation when applying a vacuum [31]. The degree of self-condensation at 50°C reaches a maximum at longer times, explaining higher angles after 4 h. The rather high advancing angle (in the presence of vacuum) also partially relates to the possibility for molecular rearrangement and thus more efficient stacking at this low temperature.

Oven treatment at 70°C leads to higher receding angles. However the increasing trend with oven residence time remains. Treatment at 90°C reveals the same trend, but slightly increases angle values. This probably can be attributed to complete removal of water, as well as an increased amount of self-condensation with residence time [139, 234**?**].

Longer oven residence times clearly decrease the XPS intensity of most signals, as shown in Figure 4.45. Increasing the residence time at 70°C from 1.5 h up to 4 h leads to a decrease in the intensity of the silicon and nitrogen signal, while the iron signal appears again and the oxygen signal increases because of a higher (substrate)oxide contribution. This points at a thinning down of the APS layer, which first of all can be attributed to the disappearance or evaporation of some of the APS. However, for sure also a (slightly) higher amount of crosslinking at longer residence times causes this thinning down, as was already found by tensiometric measurements, and confirmed by Bimin et al. [234].

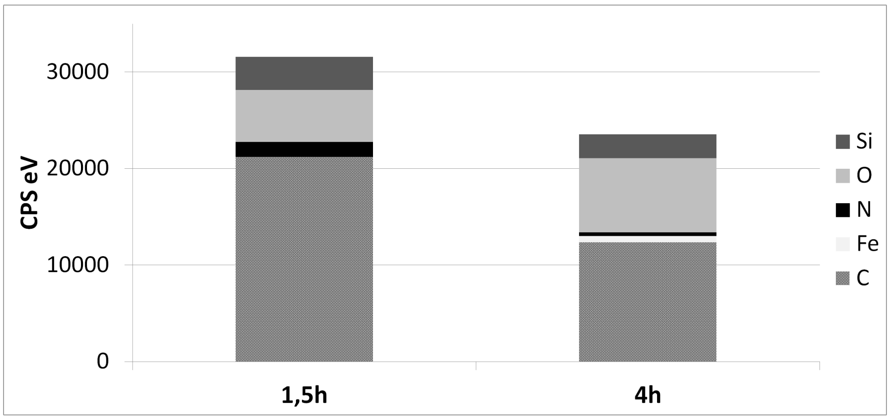

Figure 4.45: Influence of the oven residence time at 70°C on the abundance of different elements (in an unrinsed sample) as calculated from XPS measurements after oven treatment of coated samples.

Thinning down, especially with time, but also with temperature was already noted before [86, 89, 116, 219]. Table 4.8 confirms the theory of increased crosslinking with increased oven residence times. It displays the Si-O-Si/Si ratio, with the Si-O-Si signal determined from the oxygen peak. The Si signal represents the surface beneath the (low resolution) silicon peak. Note that again this ratio cannot be interpreted as the absolute degree of self-condensation. Also the Si peak confirms the increased self-condensation with time as it slightly shifts to a lower binding energy. The XPS data in Figure 4.45 concern an unrinsed sample, but concepts probably also apply to the rinsed samples (although not measured), as they corroborate tensiometric measurements, causing higher angles for longer oven treatment at 50°C, 70°C and 90°C.

Table 4.8: Ratio Si-O-Si/(Si-O-Si + OH) and Si-O-Si/Si ratio as a function of the oven residence time at 70°C for unrinsed samples.

residence time [h]	**Si-O-Si/Si** -
1.5	0.01
4	60.02

Figure 4.46 depicts the influence of vacuum on the presence of different elements for different deposition conditions, followed by an oven treatment of 1.5 h at 70°C. The sample labelled as Rinsed (ac) concerns an APS coated sample, starting from an acidified APS solution, followed by a standard deposition (including rinsing) procedure. It is clear that the presence of a vacuum decreases the total signal intensity detected. A more detailed view reveals that especially the oxygen signal increases in the absence of a vacuum, due to a lower degree of self-condensation and less water removal. The slight decrease of the carbon, nitrogen and silicon signal points at some APS removal in the presence of a vacuum. The decrease in the carbon signal probably also partially can be attributed to a slightly lower amount of contaminant absorption in the presence of a vacuum, due to less impurities remaining in the oven during treatment. The lower iron signal when applying a vacuum points at densification in case of a vacuum oven treatment, shielding the Fe signal. However, in the absence of rinsing no iron signal can be detected, irrespective of whether or not vacuum is applied.

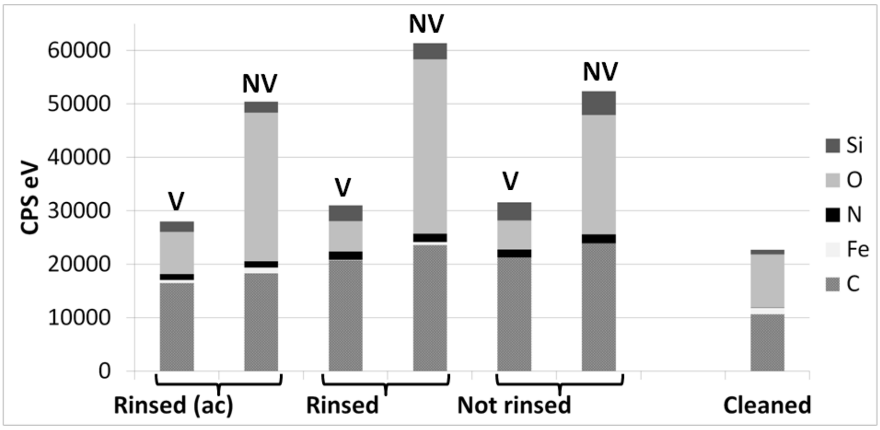

Figure 4.46: Influence of the presence(V) or absence (NV) of a vacuum during oven treatment at 70°C on the abundance of different elements as calculated from XPS measurements.

Figure 4.47 and Table 4.9 also demonstrate the positive influence of using a vacuum. It increases the degree of self-condensation, as illustrated by the lower fraction of hydroxyl groups and by the higher Si-O-Si fraction. Moreover applying a vacuum removes a higher fraction of water, that deteriorates the mechanical properties of resulting hybrids as they weaken the epoxy matrix. The benefit of water removal upon drying was already noted by Puomi et al. [85], whereas Underhill et al. found inhibition of extended self-condensation under humid conditions (for GPS), with an increased humidity sensitivity with increasing temperature [31]. Note that the signal due to siloxane linkages in the absence of rinsing is extremely low, pointing at the high amount of physisorbed species putting steric constraints on the degree of self-condensation.

Table 4.9: Influence of the presence of a vacuum on the Si-O-Si/Si ratio (x 100). Use of a vacuum increases the degree of crosslinking.

Sample	**Vacuum?**	**Si-O-Si/(Si)**
Rinsed (ac)	yes	0.50
	no	0.14
Rinsed	yes	0.64
	no	0.15
Unrinsed	yes	0.005
	no	0.003

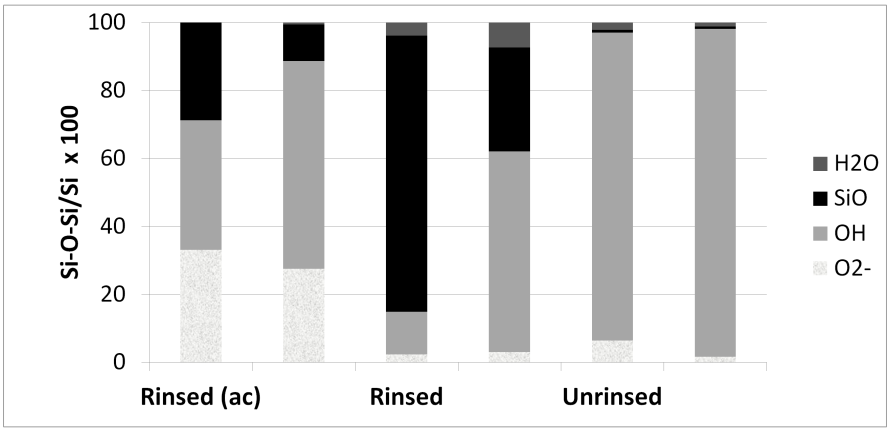

Figure 4.47: Influence of the presence of a vacuum during oven treatment at 70°C on the relative abundance of different oxygen subpeaks as calculated from XPS measurements after oven treatment of coated samples.

4.3.3 Mechanical Characterization

From Figure 4.48 it is clear that oven treatment parameters also have their influence on the mechanical strength of APS coated SST-epoxy joints, as found by dolly testing. Again all samples have a higher strength compared to the uncoated sample, which has a strength of 9.2 ± 3.8 MPa. Lower temperatures and shorter times (at 50°C and 70°) cause insufficient crosslinking and thus more limited performance. Moreover, during subsequent treatment of these samples (curing the applied epoxy), water released during condensation reactions may interfere with the epoxy matrix curing reaction, lowering its crosslink density and mechanical performance [247, 248]. A higher oven temperature and longer oven residence times lead to evaporation of silanes and over-crosslinking, increasing brittleness and hampering interpenetration with the polymer matrix, decreasing interfacial strength [20, 20, 42, 75, 75, 97, 249]. Also literature reports on the appearance of microcracks and the decrease of uniformity at higher oven temperatures or residence times [109].

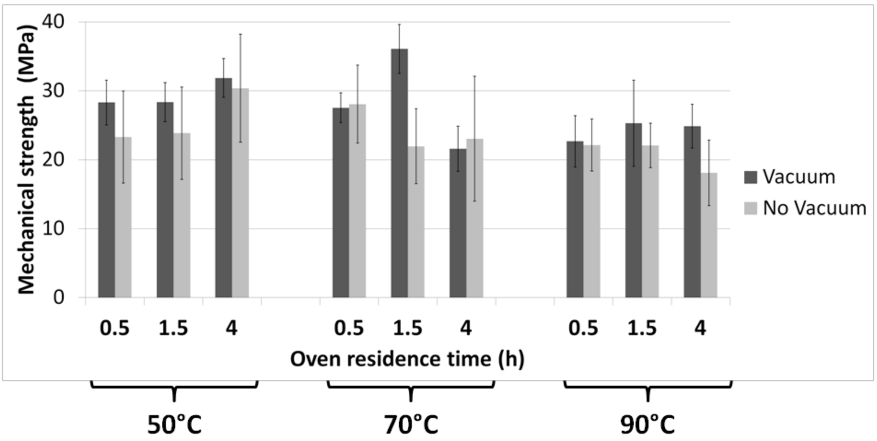

Figure 4.48: Mechanical strength as determined from dolly testing of SST-epoxy samples coated with an oven treated APS layer deposited under the same conditions but with a different oven treatment.

After applying the optimized deposition conditions, the mechanically tested substrate can be imaged by SEM (Figure 4.49), and elemental mapping (Figure 4.50). Figure 4.49 B focuses on a defect in Figure 4.49

A. Epoxy covers the substrate, as confirmed by the carbon signal found throughout the entire image, pointing at the epoxy and not the silane interphase being the weak point in the hybrid. Nonetheless one small spot displays an iron signal, pointing at a gap in the epoxy coverage. This looks like a bubble formed in the epoxy, so probably an epoxy defect rather than a failing silane coupling causes this phenomenon. This spot does not reveal any silicon signal, probably rather due to the very thin (and hardly traceable) APS layer than to its absence. Parts of the other defects demonstrate an increased silicon and oxygen signal, probably due to some silane clustering forming a weak point in the hybrid.

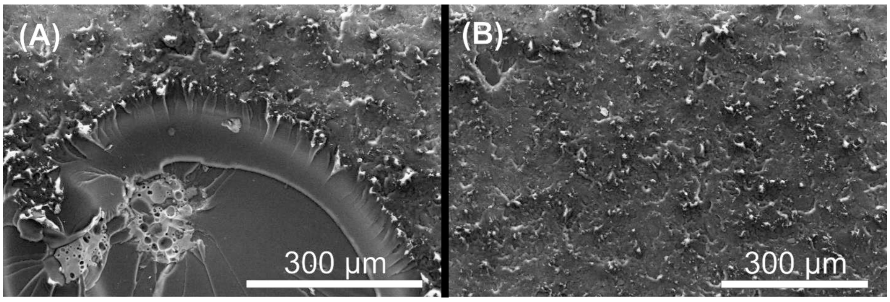

Figure 4.49: SEM image of the substrate after mechanical testing using optimized deposition conditions. The substrate is covered in epoxy, with exception of the round bubble defects.

Figure 4.51 displays an image of another substrate prepared according to the optimized procedure, clearly showing some failure at the epoxy-substrate interface. Figure 4.52 and 4.53 display this mechanically tested substrate and concomitant elemental mapping and clearly reveal more bubbles and extended defects. The presence and removal of epoxy causes the contrast variation in Figure 4.52, as confirmed by the carbon signal in Figure 4.53 that complements the iron signal. Again hardly any silicon signal can be detected, indicating the absence of extended clusters and the presence of an optimized silane layer, no longer being the weak point in the hybrid.

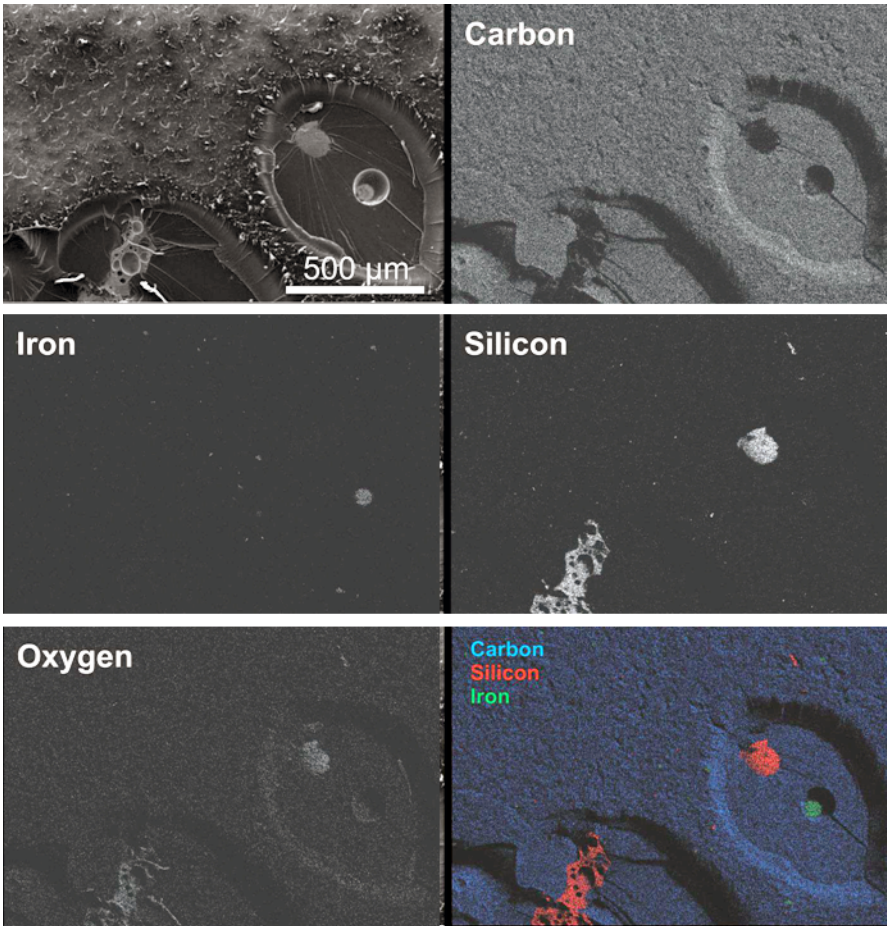

Figure 4.50: SEM image and elemental maps of a defect in Figure 4.49 that represents a substrate after mechanical testing of a sample coated according to the optimized process.

Figure 4.51: Image of the a (second) substrate after mechanical testing of a sample coated according to the optimized process.

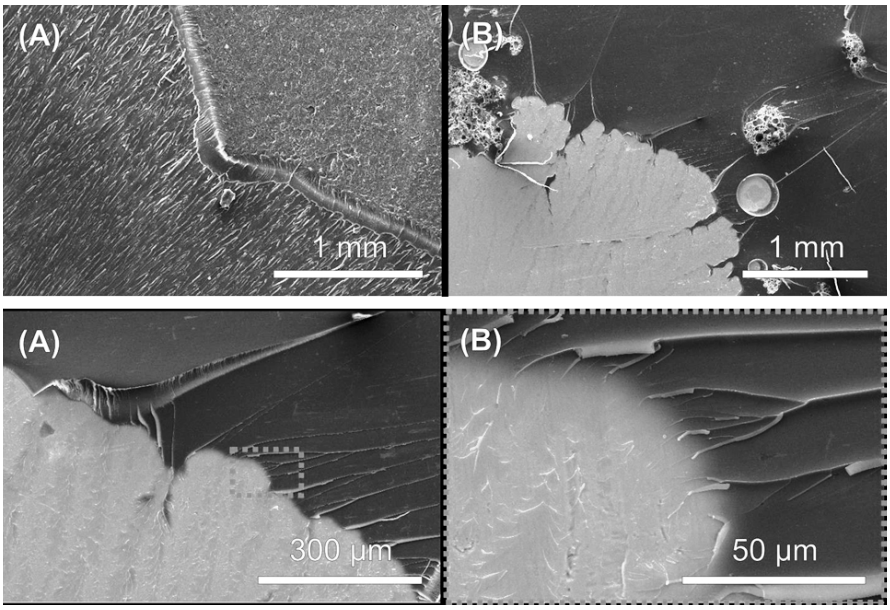

Figure 4.52: SEM image of the substrate after mechanical testing of a sample coated according to the optimized process.

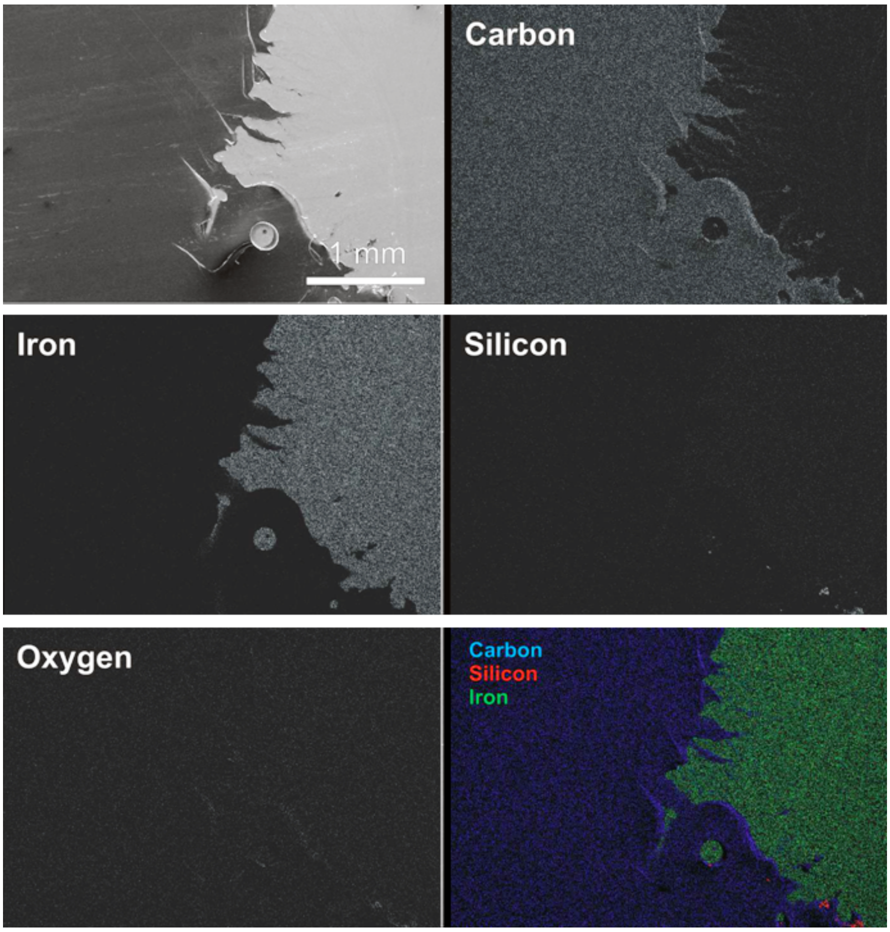

Figure 4.53: SEM image and elemental maps of a defect in Figure 4.52 that represents a second substrate after mechanical testing using optimized deposition conditions.

4.3.4 Summary

The oven conditions used for APS condensation influence the layer appearance and the interfacial strength of SST-epoxy. All samples are prepared from a 2 *v*% solution, with 30 s of dipping and 60 s of ethanol rinsing. Variation of different oven parameters results in highest strength for an oven treatment of 1.5 h at 70°C under vacuum. For sure the presence of a vacuum enhances the adhesion strength of coupled SST-epoxy joints. It increases the degree of self-condensation and removes water and reaction by-products that may interfere with the matrix, thereby reducing its properties. Increasing the oven temperature speeds up self-condensation reactions, but can cause over-crosslinking. In combination with longer residence times, higher temperatures lead to evaporation of APS and the formation of a brittle layer due to over-crosslinking. Lower temperatures on the contrary do not result in sufficient self-condensation, or may require longer residence times to obtain similar crosslinking degrees. Moreover, they do not allow full water removal. In general over-crosslinking appears more detrimental compared to insufficient crosslinking.

4.4 Influence of Ageing of Coated Substrates

Chapter 3 already revealed the influence of ageing on cleaned substrates. Also coated samples suffer from contaminant adsorption during ageing after oven treatment, influencing bonding to the matrix in the next stage. Figure 4.54 clearly demonstrates that storing samples after coating is detrimental for the wetting properties, with both the advancing and receding angle increasing drastically, due to adsorption of (most likely aliphatic carbon) contaminants. These species impede bonding to the silane in a next step.

Ageing of the APS coated substrate before epoxy application decreases the mechanical strength, and clearly leads to a very high standard deviation of the resulting values (Figure 4.55). This again can be due to the contaminant (re)adsorption, that was mentioned to take place on high energy surfaces, and also found by tensiometry.

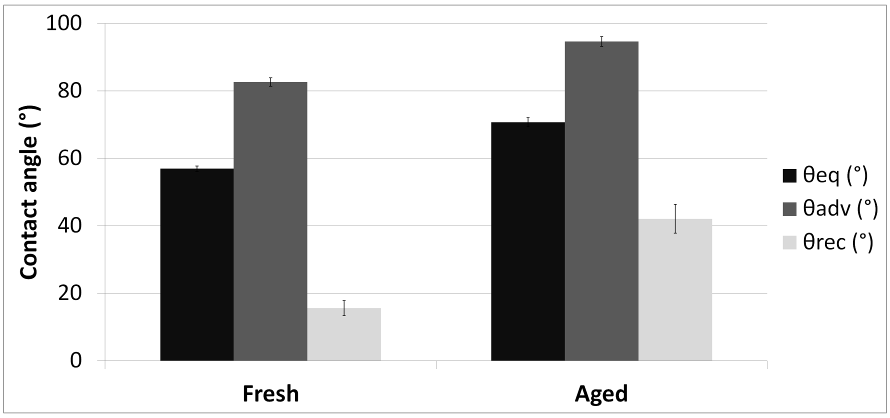

Figure 4.54: Influence of ageing (16 days) after oven treatment of the APS layer on the equilibrium, advancing and receding contact angle of a SST substrate after deposition (from a 2/90/10 APS/H_2O/EtOH solution).

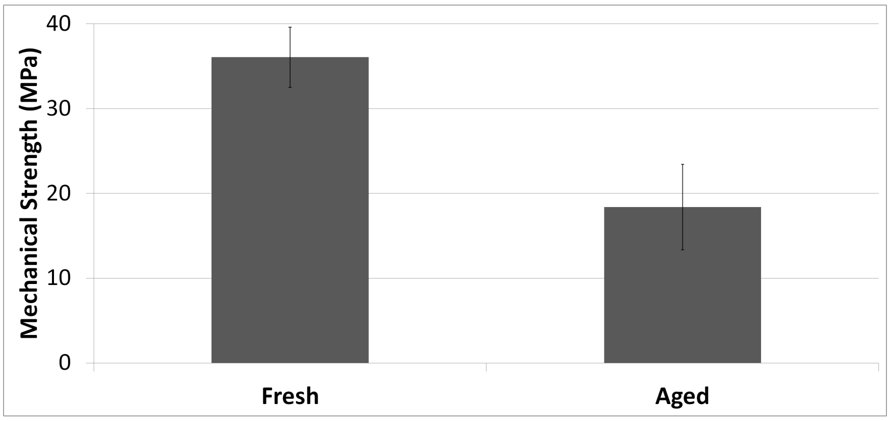

Figure 4.55: Mechanical strength as determined from dolly testing of SST-epoxy samples coated with an oven treated APS layer deposited under the same conditions but with a different ageing time (0 and 16 days) before epoxy application.

4.5 Comparison with a Benchmark Solution

Oxsilan, a commercially available silane mixture containing a.o. APS and BTSE is often used as an adhesion and corrosion resistance promotor. Here it is tested to benchmark the final properties of the optimized silane film. The manufacturer prescribes deposition from a 5 *v*% solution, without rinsing, but as earlier experience pointed out a positive influence of rinsing, this handling was also applied on the benchmark species. Compared to the optimized APS film (2 *v*%, rinsed), the benchmark solution obviously has a higher receding angle both in the presence and absence of rinsing (Figure 4.56), which points at a lower fraction of polar species, presumably at least partially due to the presence of BTSE.

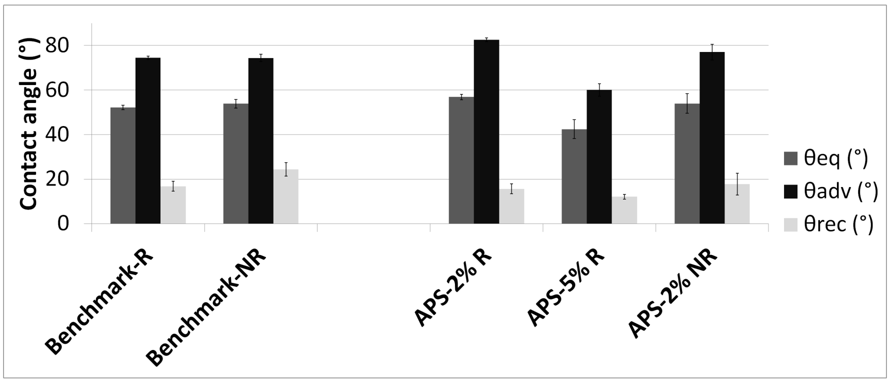

Figure 4.56: Comparison of the equilibrium, advancing and receding contact angle of a SST substrate after deposition from a 2/90/10 and 5/90/10 APS/H_2O/EtOH solution or deposition from a 5/100/0 Oxsilan/H_2O/EtOH solution (followed by oven treatment). R means rinsed after dipping, whereas NR means no rinsing.

The advancing angle of the tested benchmark samples remains constant disregarding the rinsing procedure, pointing at a rather constant low energy component of the upper surface of those samples, mainly due to the apolar BTSE. More polar species are exposed after rinsing, as seen by the relatively lower receding angle, mainly caused by the polar nature of the APS. The advancing angle of the rinsed Oxsilan is in between that of the optimized and the 5 *v*% APS sample, pointing at an intermediate low energy component.

When treated according to the manufacturer prescriptions (without rinsing), Oxsilan SST-epoxy joints lead to inferior mechanical strength (Figure 4.57), comparable to the strength of the blanc, uncoated sample.

Rinsing of this sample for 60 s in ethanol increases the performance, although only to an extent comparable to that of the higher concentrated APS series and it is still inferior to the best strength found during this work. The benchmark solution concerns a mixture of different silanes, amongst which APS and BTSE, causing a thicker layer that explains the lower performance (see Figure 4.23 and Section 4.1.1.1). Moreover this benchmark, aiming at improved adhesion in combination with an increase in corrosion resistance should be used in a more concentrated solution with at least 5-10 *v*% of silane in the mixture. This reinforces the thickening of the silane layer and probably decreases ordering, lowering the mechanical strength.

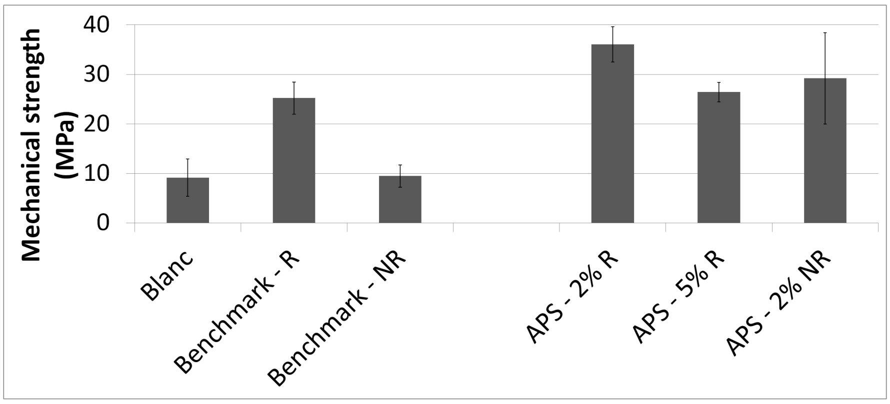

Figure 4.57: Mechanical strength as determined from dolly testing of SST-epoxy samples coated with an oven treated APS layer and an oven treated Oxsilan layer. R means rinsed after dipping, whereas NR means no rinsing after dipping.

4.6 Transfer to Other Systems

4.6.1 Change of Dolly Material

During the optimization of the silane coating process, the dolly testing setup was optimized by the University of Gent, Gent, Belgium and Vrije Universiteit Brussel, Belgium by combining experimental work with simulations. Experimental work resulted in the setup used in previous mechanical testing, simulations suggested the replacement of the aluminum dollies with stainless steel dollies (Section 2.3.7.1 for

Experimental details). This results in similar trends but higher values for the resulting strength, due to a better match between properties of the testing sample and the setup itself. Comparison of Figure 4.57 and Figure 4.58 clearly illustrates this trend of increased mechanical strength and compares an uncoated sample, a benchmark coated sample (rinsed) and an APS coated sample (both coated according to the optimized procedure). The resulting strength of more than 60 MPa by far exceeds values currently found in literature and approaches the epoxy fracture strength by which the original adhesive failure mode in the absence of an (optimized) silane coupling layer converts into a more cohesive. This points at an optimized APS layer, that no longer constitutes the weak part in the hybrid. Rather the epoxy itself becomes the weak part in the hybrid and in a next step the epoxy characteristics should be optimized.

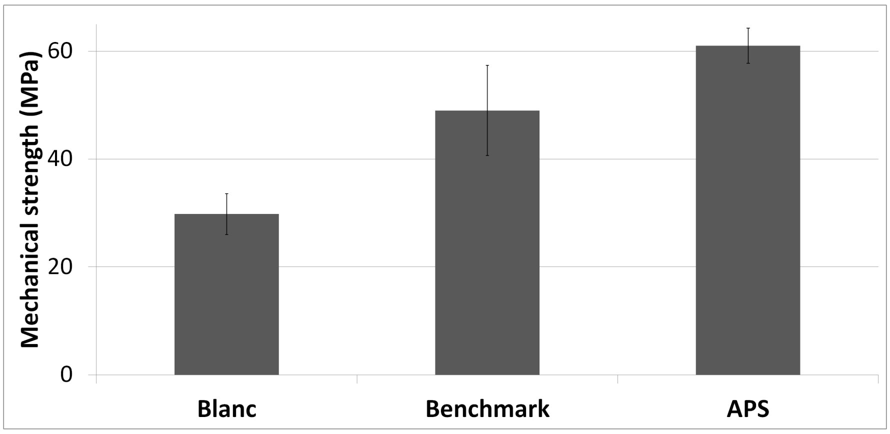

Figure 4.58: Mechanical strength as determined from dolly testing of SST-epoxy samples using SST dollies. The blanc sample has no silane coating, the benchmark is coated with an Oxsilan layer, while the APS sample is coated with APS.

4.6.2 Polyamide Matrix

As not only SST-epoxy interfaces suffer from lower strength, but polymer-steel interfaces in general lack adhesion, this work tried to transfer the optimized APS treatment to different systems. Here it has to be kept in mind that the organofunctional group of the silane has to be compatible with the matrix. Polyamide 6 (PA6) represents one of the most important commercial thermoplastics, and due to its functional groups it will also be able to interact with APS. Direct application of the polyamide matrix onto the substrates results in a strength of only 22 MPa, while application of an APS coupling layer according to the optimized coating procedure, increases this strength up to 40 MPa (Figure 4.59). This confirms interactions between the matrix and the APS layer that increase adhesion, and points at the transferability of the concepts found in this work based on epoxy resin systems.

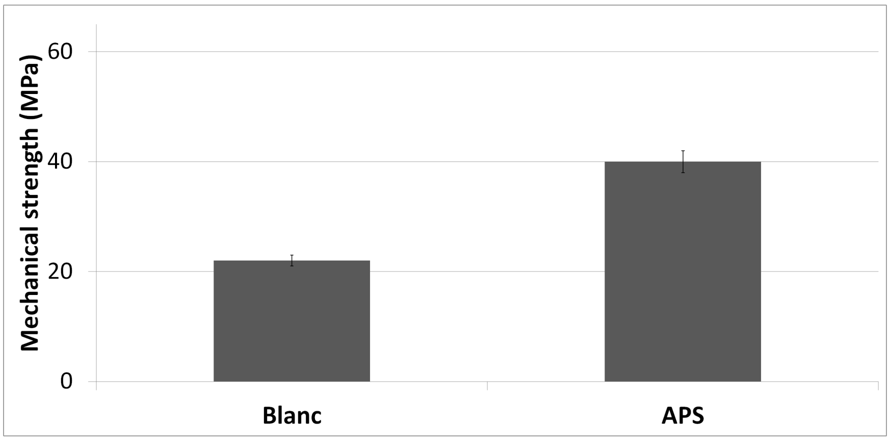

Figure 4.59: Mechanical strength as determined from dolly testing of SST-PA6 samples using SST dollies. The blanc sample has no silane coating, the APS sample is coated with an optimized APS layer.

4.6.3 Steel Fiber Substrate

The aim of this work is to increase SST-polymer adhesion in general and stainless steel plated enabled optimization work. However, results should be transferred to composites with steel fibers, as they offer the advantage of a higher strain-to-failure compared to classical fibers (Chapter 1, Section 1.2.1 and 1.2.3). Bekaert provided ultrathin SST 316 fibers to be embedded in a polymer matrix. The department of Materials Engineering, KU Leuven, Leuven Belgium, tested different hybrids containing silane coated SST fibers in a polymer matrix using a 3-point bending test, as shown in Figure 4.60. Moreover they also did a more in depth study of the use of those fibers in hybrids and composites [211].

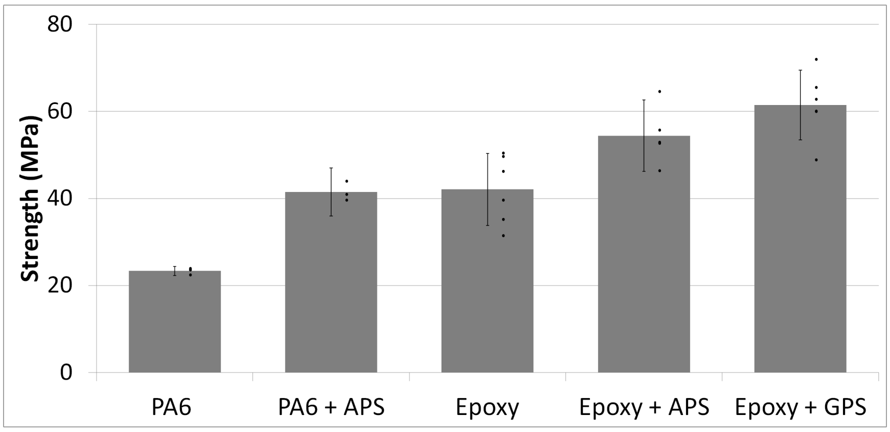

Figure 4.60: Mechanical strength as determined from 3-point bending tests of SST fibers embedded in respectively a PA6 and an epoxy matrix, in the absence (PA6 and epoxy) and presence (PA6 + APS, epoxy + APS and epoxy + GPS) of a silane coupling layer.

First of all APS deposited according to the optimized coating procedure, is applied on SST fibers, followed by application of the epoxy matrix and testing of the resulting hybrid. Compared to epoxy application in the absence of a coupling agent, this results in an increase in strength of about 30%, confirming that this treatment also works if the substrate appears in a different form. Also GPS was tested as a coupling agent, and this resulted in an even larger increase in strength of more than 45%. On plate-like substrates APS displayed higher performance compared to GPS. The reason for this is still unclear, but the slightly different composition of the fibers, being SST 316 (plates are type 304) may be the cause. The former contain 2-3 % of molybdenum and may have a slightly lower (2%) of chromium and a slightly higher (2%) nickel content. Due to a lack of time, the reason for this difference was not investigated any further.

Also application of a polyamide matrix was tested in combination with an APS coupling agent on SST fibers. After application of the same coating procedure used many times before, a PA6 matrix was applied. This results in an increase in strength of more than 77% compared to the blanc sample, again confirming that the optimized conditions can be transferred to other systems.

4.7 Conclusion

When working with silane coupling agents, a lot of parameters have to be taken into account, each having their own influence. This Chapter used a combination between physical, chemical and mechanical characterization techniques to find the optimal coating procedure.

Firstly the silane solution has to be controlled to give maximal hydrolysis of the molecules, meanwhile limiting self-condensation. APS mixtures at their natural pH are easily handled, resulting in a sufficiently broad working window due to the autocatalytic effect of the amine group. GPS on the contrary requires the addition of acid to speed up hydrolysis, while BTSE not only needs acid but also at least 50 $v\%$ of alcohol to maintain a stable solution. Addition of an alcohol decreases the hydrolysis rates, but enables spreading of the solution on the substrate in the next step. This leads to working solutions with a water/alcohol ratio of 90/10 ($v\%/v\%$) for APS and GPS. Higher silane concentrations increase hydrolysis and self-condensation kinetics, and lead to a higher amount of adsorption and a thicker layer deposited on the steel substrate. The optimal silane concentration causes complete substrate coverage, and omits the formation of clusters. In this way it causes a higher degree of ordering and condensation after oven treatment.

Secondly the deposition conditions influence the silane film appearance. During the dipping process silane species are adsorbed on the substrate. Shorter dipping times cause insufficient and possibly also wrongly oriented adsorption, while longer dipping times induce the adsorption of thicker layers. The former leads to insufficient coupling, while the second suffers mainly from a weak silane layer. Although especially the layer next to the substrate is strongly bound, longer dipping times cause strong sorption of a higher amount of species. During the rinsing treatment the excess of weaker bound silane can be removed. In this way a thin, more perfectly ordered and oriented APS layer is left behind, improving joint performance after matrix application.

Figure 4.61 briefly summarizes the influence of the previous parameters on the appearance of a silane layer. Moreover also their relation with the contact angle is summarized.

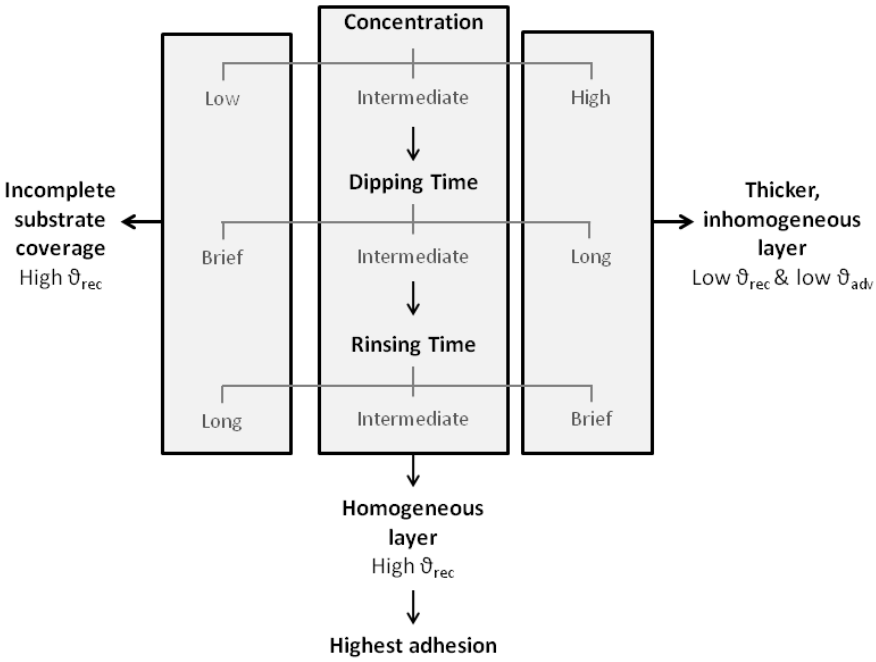

Figure 4.61: Influence of the silane concentration, dipping and rinsing time on the characteristic contact angles and the appearance of an APS layer.

Finally the oven conditions have to be optimized in order to obtain sufficient (but not too much) crosslinking while molecules have sufficient time to rearrange themselves in an optimal way. Use of vacuum seems to enhance the mechanical properties of the silane layer, as it removes water and residues that may interfere with the polymer matrix or inhibit formation of the desired APS layer. The optimal temperature-time settings ensure a certain degree of self-condensation, while avoiding over-crosslinking. Regarding the oven residence time, reactions require a certain amount of time to reach a certain degree of self-condensation, but longer times destroy the ideal properties. Mechanical and tensiometric testing indicate that, as in the case of freshly cleaned samples, coated samples should be used without delay in order to avoid contaminant adsorption, having a detrimental effect on adhesion performance.

In conclusion the optimized coupling layer starts from a 2/90/10 APS/H_2O/EtOH solution. After dipping the US cleaned sample in this solution for 30 s and rinsing it for 1 min in ethanol, samples should be placed in an oven at 70°C for 1.5 h under vacuum.

Comparison of the optimized APS layer with a benchmark coupling layer results in higher strengths for the former, pointing at the importance of tuning the coating process (although the benchmark silane is intended to improve both adhesion and corrosion resistance). Moreover, this optimized process can be applied to other systems, where it also proves to be fairly efficient. Before this transfer, first the dolly setup was optimized by changing the aluminum to SST dollies, in this way increasing compatibility with the other components. When using a SST fiber substrate instead of a plate-like substrate, APS also increases performance. Also when changing the matrix from epoxy to PA6 a silane coupling agent increases mechanical performance, both for SST plates and fibers.

Chapter 5

Interphase Adaptations: Hyperbranched Polylysine

As literature suggests that the amount of anchoring points relates to the degree of interfacial adhesion, hyperbranched polylysine (PL) was added to the interphase [167]. In this way a combination of a silane coupling agent and the hyperbranched polymer acts as a chemical bridge between the steel substrate and the polymer (epoxy) matrix.

Ideally the GPS silanol groups form a covalent link to the substrate or react with each other, creating siloxane linkages (after maximum hydrolysis). Meanwhile intact GPS epoxy groups link to the polylysine that still contains many unreacted amine functional groups (Figure 5.1). The latter then can react with the epoxy matrix in a next stage.

Experimental details and sample preparation again can be found in the Materials and Methods Chapter, Section 2.4.

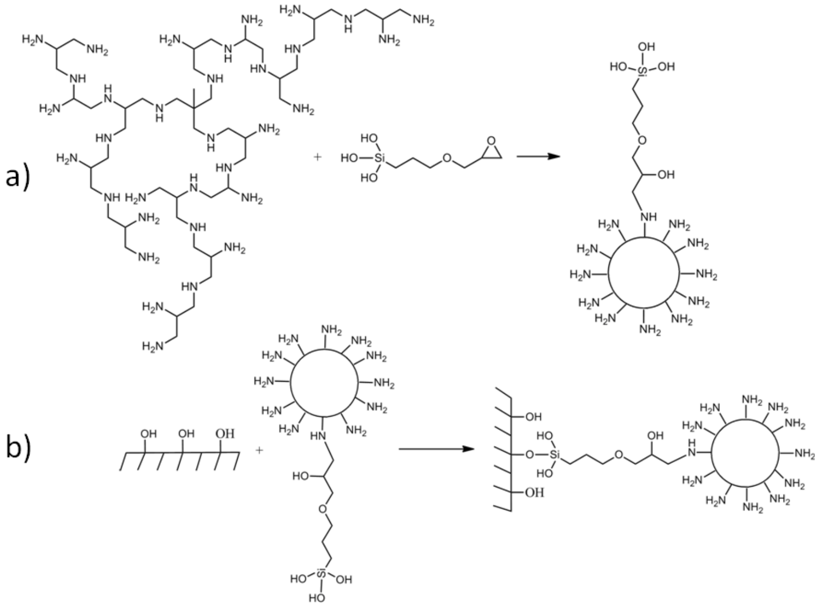

Figure 5.1: Reaction of PL with hydrolyzed GPS (a) and coupling of PL to a metal substrate by GPS (b).

5.1 Layer by Layer Deposition

First of all the layer by layer deposition technique was applied, starting with the deposition of a GPS coupling layer from a 2/1.3/90/10 GPS/acac/H_2O/EtOH solution, aged for 5 minutes. The US cleaned SST substrate was dipped for 30 s, ethanol rinsed for 1 min and placed in an oven for 15 min at 70°C under vacuum. In this way the silane layer already can partially condense, without fully being crosslinked. Next this sample was dipped for 30 s in a 90/10 H_2O solution containing 1 $w\%$ of the hyperbranched polylysine, and oven treated for 75 min to complete the silane condensation as well as the reaction between the GPS epoxy and polylysine amine groups.

Figure 5.2 depicts a SEM micrograph of the so obtained GPS-polylysine layer, clearly demonstrating an inhomogeneous substrate coverage after deposition. Because of this it was decided not to continue with the layer by layer deposition technique.

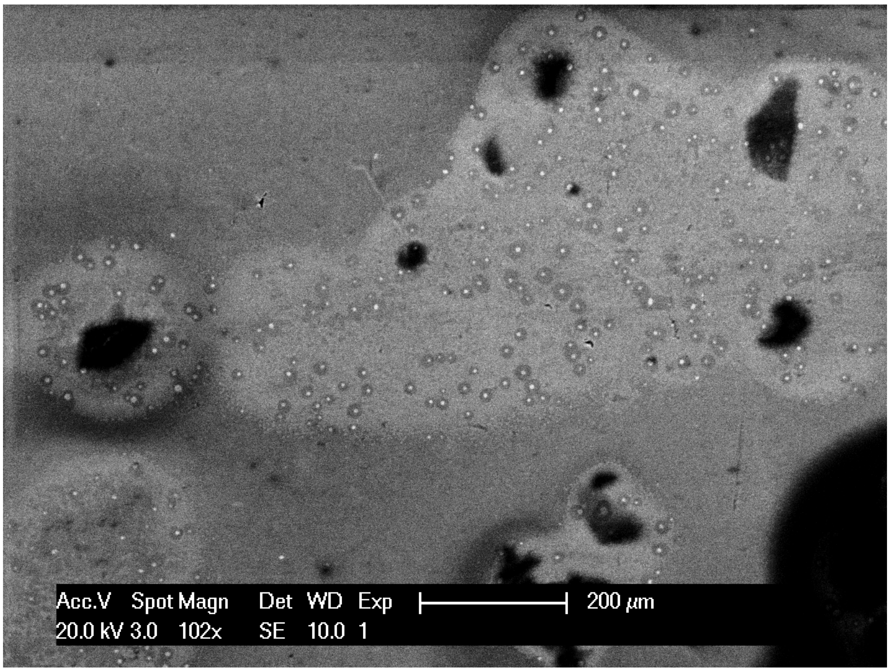

Figure 5.2: SEM micrograph of a SST substrate layer by layer coated with GPS and a polylysine layer, clearly demonstrating inhomogeneous coverage of the substrate.

5.2 Mixed Layer Deposition

As a layer by layer deposition did not result in homogeneous coverage of the substrate, a mixed layer was deposited starting from a solution that contains GPS as well as the hyperbranched polylysine. Application of this mixed coupling layer is similar to silane coating: after solution preparation and maximum hydrolysis, the steel substrate is dipped for 30 s and ethanol rinsed for 1 min. Next oven curing takes place at 70°C for 1.5 h under vacuum.

5.2.1 Solution Stability

Figure 5.3: 20 mL of a 90/10 H_2O/EtOH solution after addition of 2 *v*% of GPS and 95 mg polylysine (0.95 mmol of NH_2) (left) and after addition of only 95 mg polylysine (and no GPS) (right). The former clearly demonstrates solubility issues.

Figure 5.4: 20 mL of a 90/10 H_2O/EtOH solution after addition of 2 *v*% of GPS and 95 mg polylysine (0.95 mmol of NH_2) (left), a similar mixture with a changed solvent ratio (50/50 H_2O/EtOH) (mid) and a similar mixture with a decreased pH of 6 (using acetic acid) (right).

Figure 5.3 demonstrates that polylysine as such dissolves rather well in water and ethanol (mixtures)(right), but after the addition of GPS solubility problems show up (left). Increasing the percentage of ethanol or acidifying this solution increases solubility as seen respectively in the mid and right vessel in Figure 5.4.

5.2.2 NMR

Chapter 4 already described the importance of hydrolysis of the silane before applying it on the substrate. The ^{1}H NMR spectra in Figure 5.5 and 5.6 demonstrate the hydrolysis kinetics of the (at first sight) stable GPS-PL solutions. As described in Section 2.3.2 upon GPS hydrolysis methoxy groups convert into hydroxyl groups, thereby releasing methanol. Polylysine does increase the hydrolysis rates by alkaline catalysis of 2/50/50 GPS/D_2O/EtOD solution and maximum hydrolysis takes 4 days (Figure 5.5), which is fast compared to the hydrolysis kinetics of a neutral GPS/D_2O/EtOD solution (Chapter 4.1.1.2, Figure 4.10).

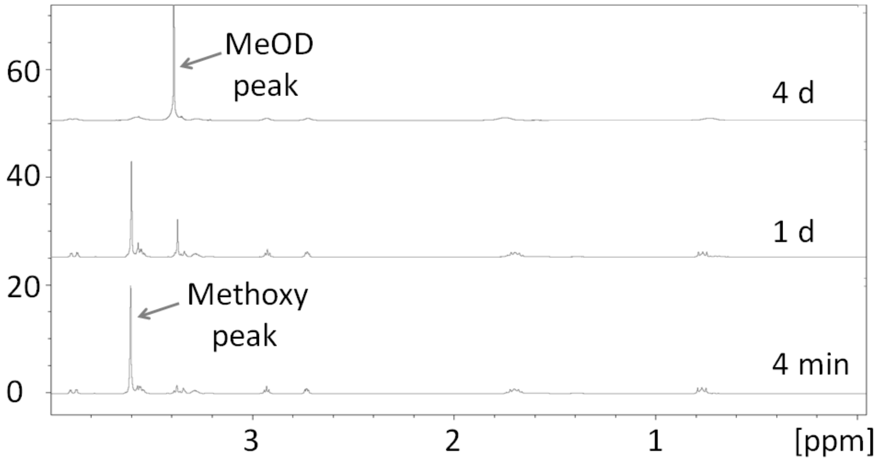

Figure 5.5: Hydrolysis kinetics of a 2/50/50 GPS/H_2O/EtOH solution after addition of 95 mg PL (0.95 mmol of NH_2) as determined by ^{1}H NMR, demonstrating the catalytic effect of the PL.

When acidifying the solution to a pH of 6 maximum hydrolysis takes 17 min (Figure 5.6), which is slightly longer compared to the same solution without PL (Chapter 4.1.1.4, Table 4.2). The epoxy groups of the silane are expected to react with the amine groups of the polylysine.

Monitoring of this reaction by ^{13}C NMR seemed rather difficult, and in the future some model compounds should be used to obtain more information about this reaction.

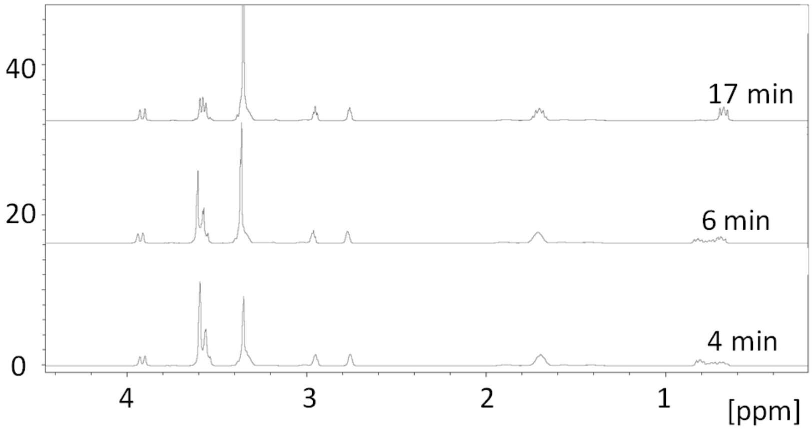

Figure 5.6: Hydrolysis kinetics of a 2/0.4/90/10 GPS/acac/H_2O/EtOH solution after addition of 95 mg PL (0.95 mmol of NH_2). PL slightly lowers the hydrolysis kinetics.

5.2.3 Mechanical Characterization

Figure 5.7 depicts the mechanical performance of SST-epoxy joints coupled by a GPS-PL layer in comparison to an uncoated, a GPS and an APS coupled joint. GPS-PL 1, 2 and 3 start from the same 2 *v*% GPS solution containing a different amount of polylysine, and a high nitrogen signal found during XPS points at deposition of these polymers (data not shown). The PL amine/GPS epoxy ratio is 1/100, 1/1 and 2/1 for respectively GPS-PL 1, 2 and 3. It is clear that for all 3 polylysine concentrations used, the resulting strength is below the strength of the uncoated sample, although it goes through a maximum with increasing concentration.

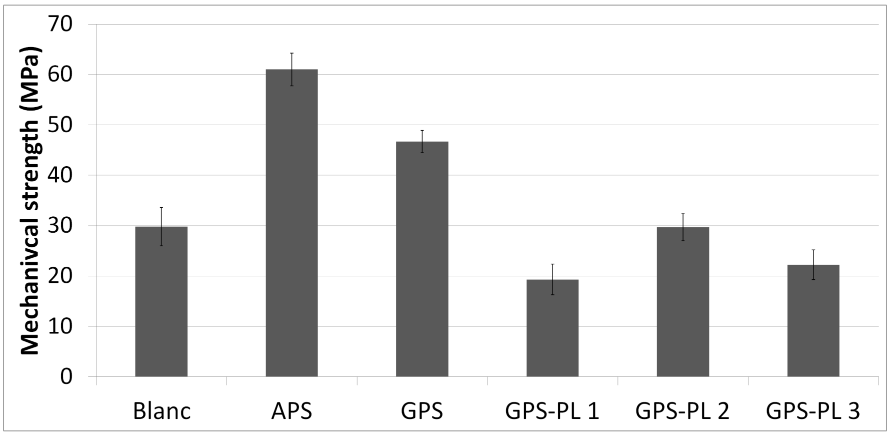

Figure 5.7: Mechanical strength as determined from Dolly testing (using SST dollies) of SST-epoxy samples coupled by a GPS-PL layer. PL 1, 2 and 3 represent deposition from a solution containing respectively a amine/epoxy ratio of 1/100, 1/1 and 2/1. Addition of PL decreases the mechanical strength.

For low PL concentrations (first sample) no amine anchoring points remain as they are consumed by reaction with GPS. Moreover, compared to an identical solution without PL less epoxy groups remain intact. In this way the probability for coupling decreases, decreasing interfacial strength. Moreover, the excess GPS may be unable to react with the epoxy matrix due to steric constraints, or may give rise to a highly unordered layer. Theoretically all epoxy and amine groups within the second solution can be consumed. If this takes place, not all GPS molecules will be able to react with the steel substrate due to steric constrains, and silanol groups may remain available for interaction with the epoxy matrix. In practice probably not all epoxy and amine functionalities are coupled, leaving (epoxy and amine) groups for interaction with the matrix. For the last sample there is an excess of amine groups. However, only one GPS molecule is needed to couple a PL molecule (with many amine functionalities) to the steel surface, in this way leaving the remaining amine groups for reaction with the epoxy matrix. Here insufficient GPS may cause the presence of uncoupled PL on the substrate, and the excess PL may induce higher stress concentrations.

Figure 5.8 and 5.9 depict SEM images and the associated elemental mapping of the substrate after mechanical testing of a GPS-PL coupled SST-epoxy joint (GPS-PL 2 in Figure 5.7).

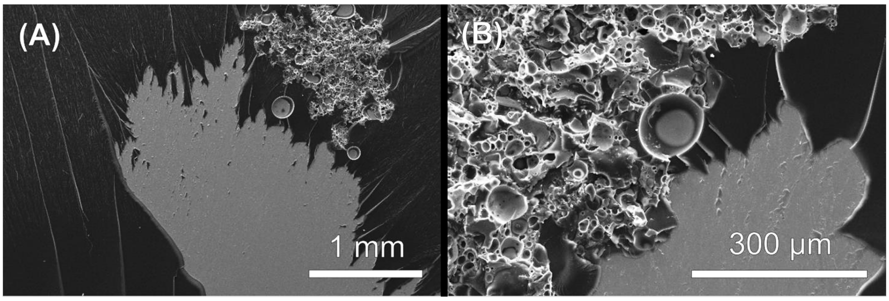

Figure 5.8: SEM images of a substrate after mechanical testing of a GPS-PL 2 coupled SST-epoxy joint, revealing a porous structure.

It clearly reveals a porous structure. Appearance of an iron signal shows that the epoxy layer is not the weak point in those joints. The oxygen and silicon map clearly show unwanted features in the coupling layer with bubble defects appearing, and a rather high silicon signal can be seen. This points at failure in the coupling layer. It is suggested that in PL-GPS solutions cluster formation takes place, causing inhomogeneous deposition on the substrate. This layer then forms the weak point in the joint, leaving silane and polylysine on both sides of the testing setup after failure.

Moreover, although the hygroscopic polylysine was dried prior to use this material again takes up water during deposition. If this water is not released during oven treatment, or if water take up happens again after oven treatment (before epoxy application) it interferes with the epoxy matrix, decreasing its performance.

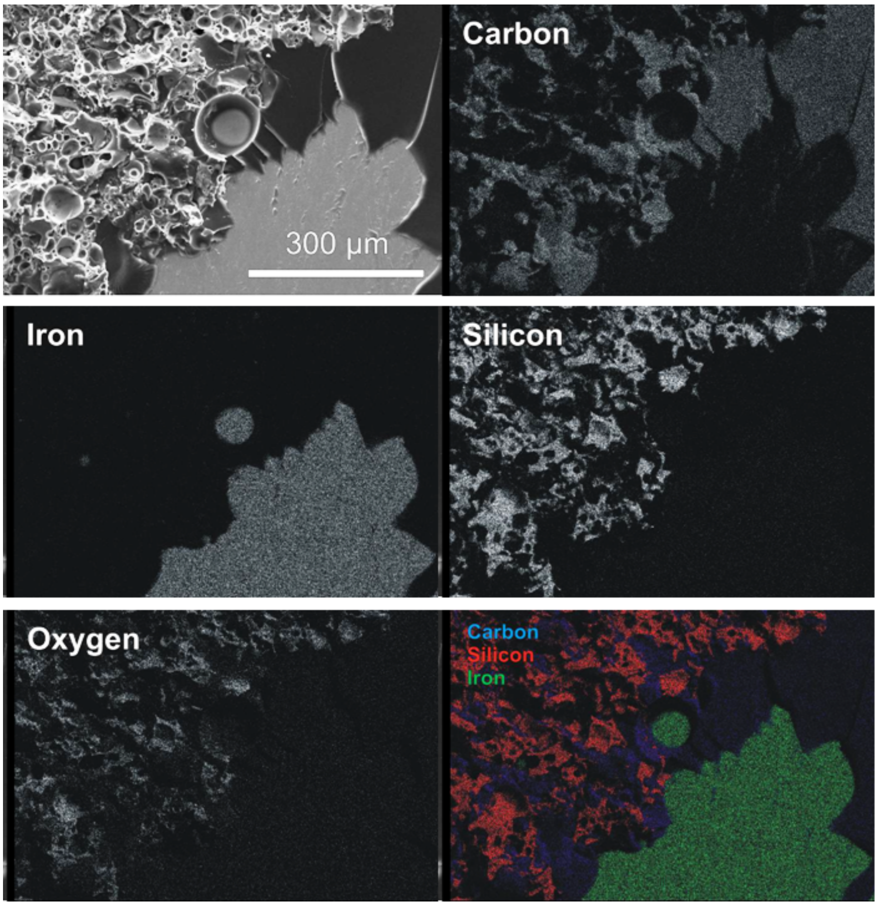

Figure 5.9: Elemental maps for the SEM image of a substrate after mechanical testing on a GPS-PL coupled SST-epoxy joint.

5.3 Conclusion

Contrary to what was expected, the modification of the interphase by adding hyperbranched polylysine does not improve SST-epoxy joint properties, neither when depositing a GPS and a polylysine layer consecutively, neither when depositing them in a mixed way. NMR indicated maximal hydrolysis of the GPS, and XPS showed the presence of polylysine, but combination of both lacks efficiency when applied to improve adhesion. Depending on the PL/GPS ratio this may be due to a decrease in the amount of anchoring points or an increase in steric constraints. Moreover SEM images point at a very inhomogeneous coupling layer containing quite some (bubble) defects. The polylysine as such was not used in any further experimental work, but future work may study again layer by layer deposition, or the use of an intermediate excess of PL amine groups compared to the GPS epoxy groups.

Chapter 6

Interphase Adaptations: Carbon Nanotubes

As found in Chapter 1, the reason for premature polymer-steel composite failure is twofold: a lack of adhesion on one side, a stiffness mismatch between both components on the other side. One of the proposals during this project was the dispersion of nanofillers (in)to the APS sizing layer to solve the second problem. Carbon nanotubes (CNT) can fulfill the role of nanofiller [160, 161].

To fully exploit CNT properties, they first should be brought into solution before further processing. Depositing nanotubes at the interphase starts from a stable nanotube dispersion, requiring addition of surfactants in the case of aqueous solutions. Hyperbranched polyglycerol (PG) nanoparticles with triphenylmethyl (trityl) end-group functionalization (Figure 6.1) synthesized during this work can act as a surfactant. Variation of the PG molar mass and of the degree of end-group functionalization allows optimization of the surfactant efficiency. Optimization work takes into account environmental considerations, and uses only aqueous solutions. However during deposition at the interphase, the solution should wet the substrate sufficiently, and ethanol is added to decrease the surface tension and to improve spreading behavior.

This hyperbranched surfactant is easily synthesized compared to hyperbranched molecules with aromatic backbones and does not rely on a covalent modification of the CNTs. The trityl groups are expected to interact with the nanotube surface, while the hyperbranched polyglycerol

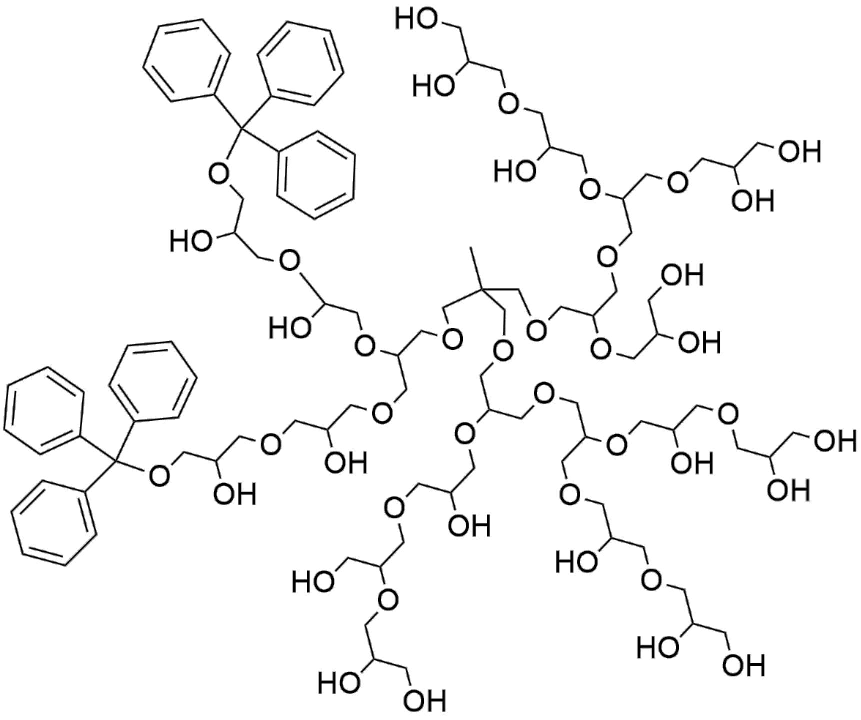

Figure 6.1: Schematic representation of a triphenylmethyl end-group functionalized hyperbranched polyglycerol molecule.

or polylysine mainly should account for water solubility and steric repulsion to prevent individualized nanotubes or small bundles from reapproaching [250]. The efficiency of a single phenyl group was confirmed by different authors by comparing SDS and DDBS [182, 189, 202, 251], even though the phenyl group of the latter is positioned at the hydrophilic end of the molecule [191]. Meanwhile the flexibility of this (trityl functionalized) hyperbranched molecule can enable interaction with the CNT surface without compromising steric repulsion properties.

Experimental and preparation details can be found in the Chapter Materials and Methods, Section 2.5. Part of this work was published by Bertels et al. [252].

6.1 Nanotubes in Solution

6.1.1 Surfactant Synthesis and Characterization

Synthesis of trityl functionalized PG was done by the group of Prof. M. Smet, Polymer Chemistry & Materials, KU Leuven, Leuven, Belgium and started from a PG core, further referred to as PG2000, PG5000 or PG10000 (specifications in Table 6.1), followed by reaction with triphenylmethyl chloride via a nucleophilic substitution as shown in Figure 6.2. A mass of 0.2 g of the desired PG was mixed with triphenylmethyl chloride in pyridine (10 mL), and stirred at room temperature for 48 h under argon atmosphere, followed by slow addition of the polymer mixture to a stirred solution of ethyl acetate (100 mL), resulting in a polymer suspension. Centrifugation of this suspension at 4000 g for 5 min yielded a pellet of functionalized PG that was dissolved in methanol (10 mL) and once again added dropwise to ethyl acetate (100 mL). The produced suspension was centrifuged, leading to the final pellet of functionalized PG that was dried in a vacuum oven for a minimum of 12 h at 40°C. Different degrees of functionalization i.e. a different percentage of available hydroxyl groups of the starting PG being functionalized with trityl groups, have been synthesized by varying the amount of trityl chloride (see Table 6.1 for a complete list of fabricated products). Products synthesized in this work starting from PG with molar mass y an with x% of the hydroxyl end-groups functionalized are further referred to as x% PGy.

Table 6.1: Surfactant specifications: Number average molar mass (M_n), polydispersity index (PDI) and number of hydroxyl groups (N) in the PG core prior to functionalization and the degree of trityl end-group functionalization (DG) after the reaction.

Name	**M_n** [g/mol]	**PDI**	**N** [#]	**DG** [%]
PG2000	1779	1.23	25	0, 2.9, 9
PG5000	5456	1.57	74	0, 5.6, 7.8, 13.1, 22.6
PG10000	9446	1.41	126	0, 0.6 , 2.7, 3.7, 11.2

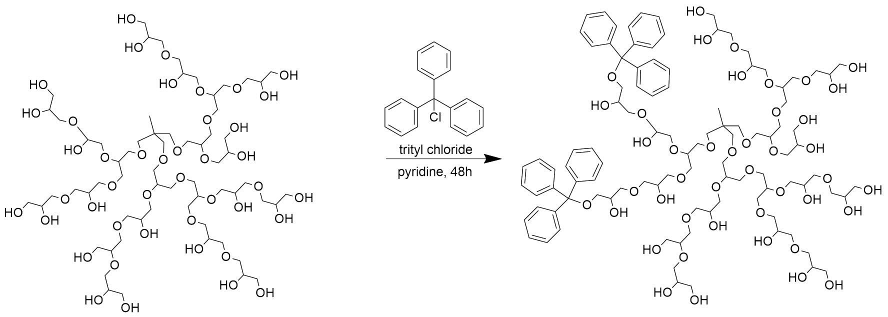

Figure 6.2: Synthesis the CNT surfactant used in this work: trityl end-group functionalized hyperbranched polyglycerol.

A ^{13}C NMR spectrum of purified material in DMSO-d$_6$ (Figure 6.3) provides evidence for successful functionalization (compare with the spectrum of unfunctionalized material Figure 6.4), with the quaternary carbon adjacent to the trityl phenyl groups giving rise to a signal at 85.7 ppm. The peak at 143.9 ppm originates from the quaternary carbon from the phenyl groups, whereas the other 5 phenyl carbons produce peaks at 128.3 ppm, 127.8 ppm and 126.9 ppm. The signals from the hyperbranched PG structure can be found between 81 and 60 ppm. DEPT-135 spectra (Figure 6.5 and 6.6) confirm this analysis.

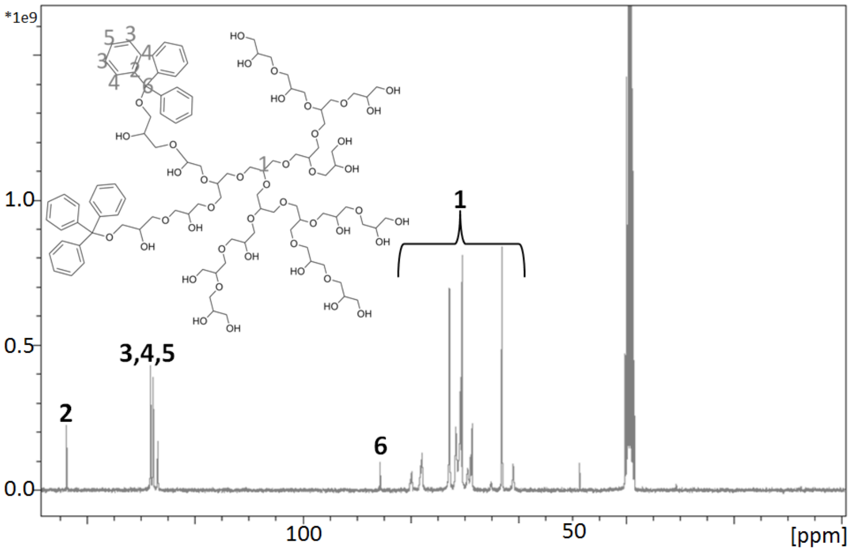

Figure 6.3: ^{13}C NMR spectrum of 3.7% PG10000, providing evidence for successful functionalization.

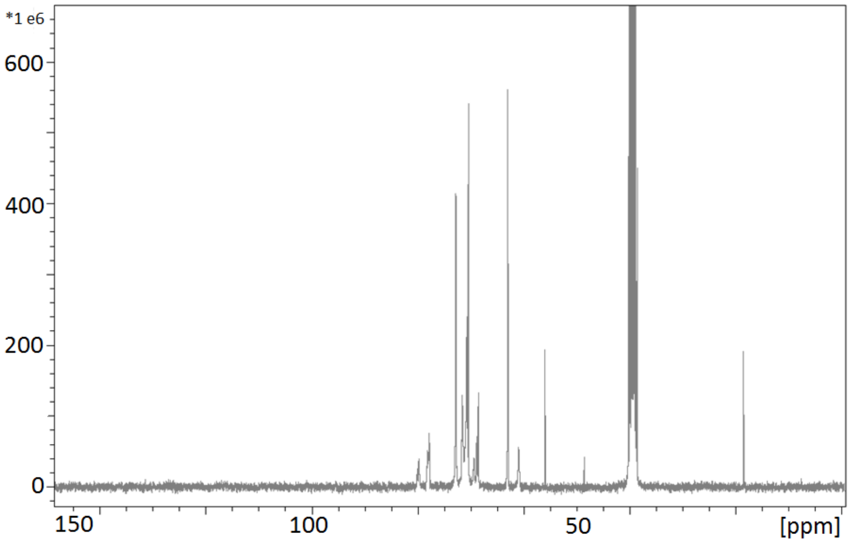

Figure 6.4: ^{13}C NMR spectrum for unfunctionalized PG10000.

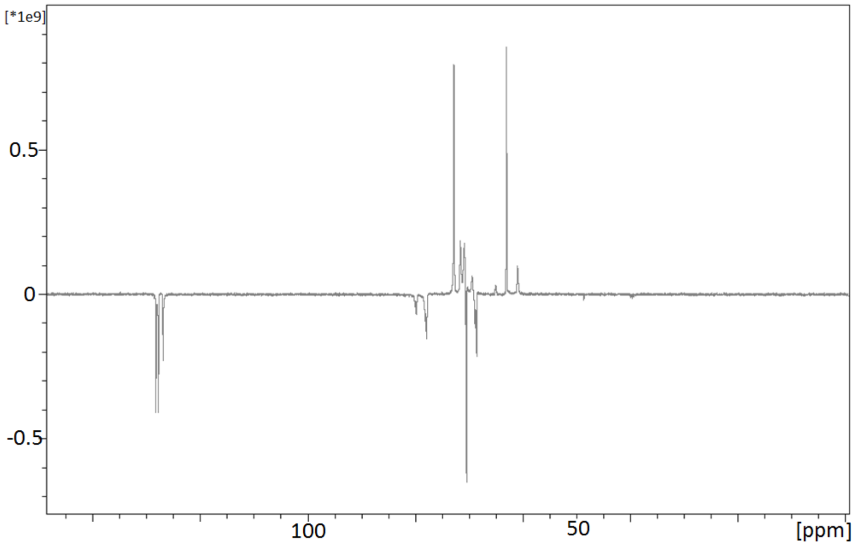

Figure 6.5: ^{13}C DEPT-135 NMR spectrum for 3.7% PG10000, confirming successful functionalization.

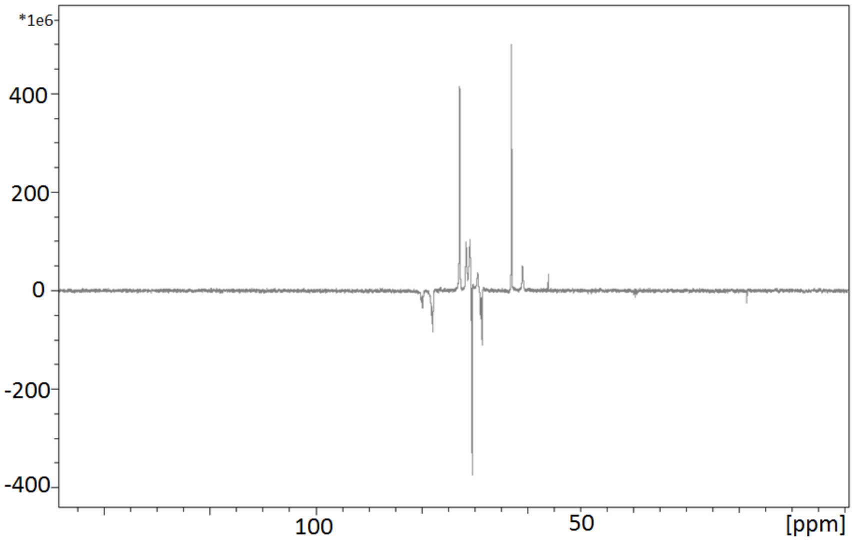

Figure 6.6: ^{13}C DEPT-135 NMR spectrum for unfunctionalized PG10000.

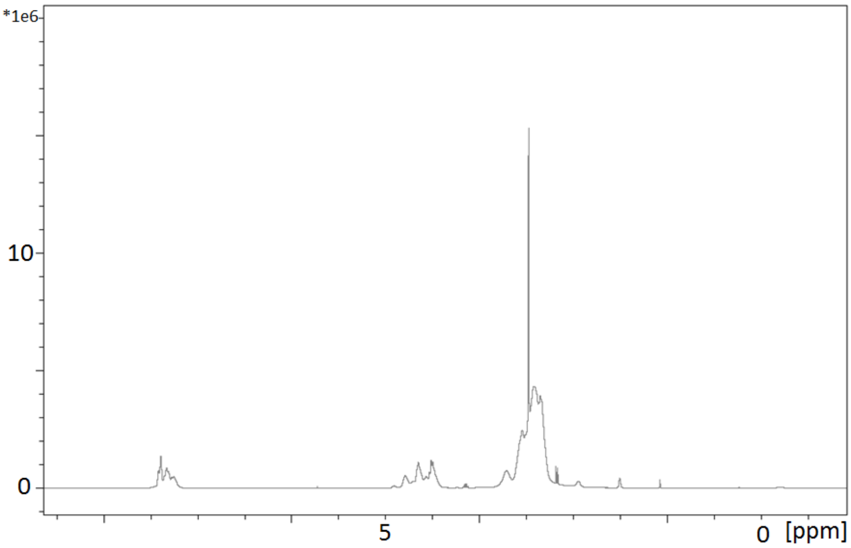

Figure 6.7: ^{1}H NMR spectrum for 3.7% PG10000, used to calculate the degree of PG end-group functionalization.

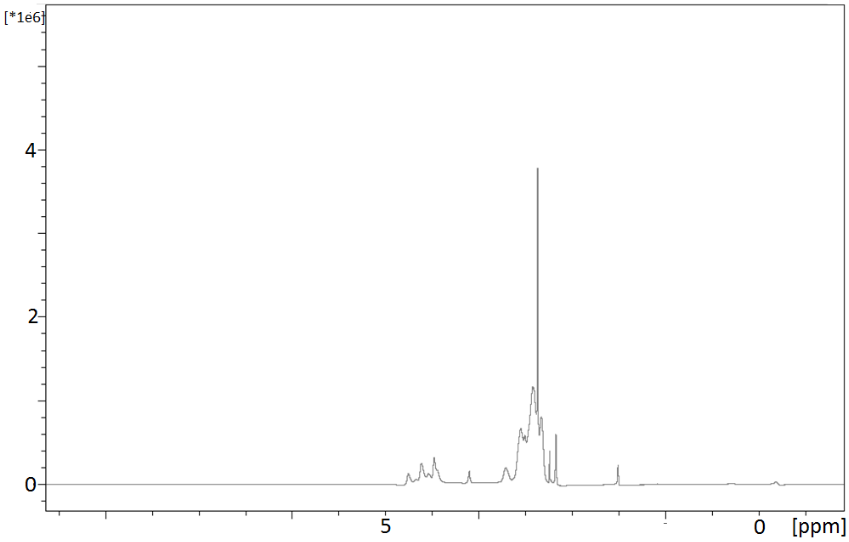

Figure 6.8: ^{1}H NMR spectrum for unfunctionalized PG10000.

^{1}H NMR in DMSO-d_6 (Figure 6.7) reveals the degree of functionalization (compare with the unfunctionalized molecule in Figure 6.8). By taking the integrated area between 3.9 and 2.8 ppm (-CH- and -CH_2- from the PG core) as a reference, the functionalization can be calculated from the integrated area in between 7.8 and 6.8 ppm (-C_6H_5 from trityl). The signal in between 4.9 and 4.3 is caused by the hydroxyl groups of the PG core.

6.1.2 Surfactant CMC and Solubility

In the absence of surfactant no individual tubes can be brought into dispersion in water. At the other extreme of excessively high surfactant concentrations and low surfactant/MWCNT (multi-walled CNT) ratios depletion aggregation may interfere and reduce the solubilizing capacity. Above the surfactant critical micelle concentration (CMC), micelles formed do not fit in between nanotubes, creating lower micelle concentrations at these locations. This leads to a concentration and consequential osmotic pressure difference in the solution, pushing nanotubes together and causing reagglomeration [192, 193]. Depletion interaction received quite some attention in research, but disagreement among authors exists as whether to work above [171, 182, 191] or below [194, 195] the CMC of surfactants. In any case, even in the absence of depletion interaction needlessly high surfactant amounts should be avoided for economic reasons and to avoid performance losses when used at a later stage in e.g. composites.

The presence of a CMC was studied with Dynamic Light Scattering (DLS), as upon reaching the CMC the slope of the intensity of the scattered light as a function of the concentration suddenly increases [212, 253]. Figure 6.9 reveals the absence of a CMC for 5.6% PG5000 in water as the slope of the graph (surfactant concentration vs. intensity) remains constant over a rather broad range of concentrations, up to 5 g/L. This concentration by far exceeds the CMC of commercially available surfactants such as Brij and Triton [254], which might be due to the inability of the synthesized molecules to form micelles. Precipitation due to solubility issues takes place rather than the formation of micelles (see further below). Given that the nanotubes consume surfactant during their dispersion and thus leave less free surfactant in solution for potential micelle formation, it is conceivable that CNT loaded systems do not contain any micelles [183]. Depletion interactions in the present cases therefore can be excluded.

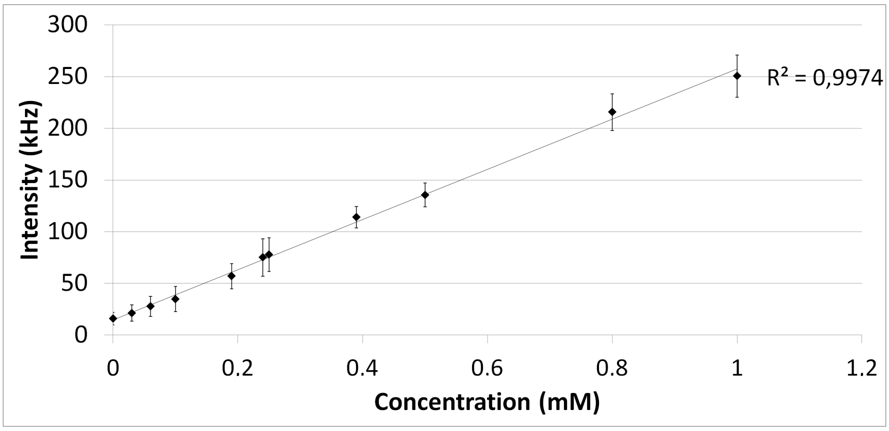

Figure 6.9: DLS intensity (in kHz) as a function of the surfactant (5.6% PG5000) concentration in pure water. The constant slope points at the absence of a CMC.

Highly functionalized species visually demonstrate solubility issues in aqueous solutions. 25% PG5000 does not dissolve at all, whereas 2.7% PG10000 (and higher degrees of functionalization for PG10000) as well as 22.6% PG5000 start to flocculate upon standing a few days. This illustrates the poor solubility for certain surfactants in the concentration range used.

6.1.3 Dispersion: Critical Ratio and Absorbance

UV-Vis measurements provide information on the carbon nanotube dispersion as bundled tubes are hardly active in the region measured, whereas individual tubes result in a clear absorption spectrum. The absorbance is linearly related to the amount of individual CNTs as described by the Lambert-Beer law [182, 190]. Combination of UV-Vis and TEM on fully dispersed solutions (Section 6.1.6), reveals an absorbance of 0.244 and 0.238 for every mg of pristine and acid functionalized CNTs brought into dispersion respectively.

Figure 6.10 depicts the absorbance at 500 nm during sonication of different masses (a mg) of acid functionalized multi-walled carbon nanotubes (COOH-MWCNT) for a constant mass (b mg) of surfactant (22.6% PG5000) in 20 mL of water, referred to as a/b 22.6% PG5000. The linear relation between the nanotube concentration and the ultimate absorbance (resulting in an absorbance of 0.24 per mg of nanotubes) suggests maximal dispersion, which is realized irrespective of the COOH-MWCNT/surfactant proportion, at least up to a ratio of 1/1 [180].

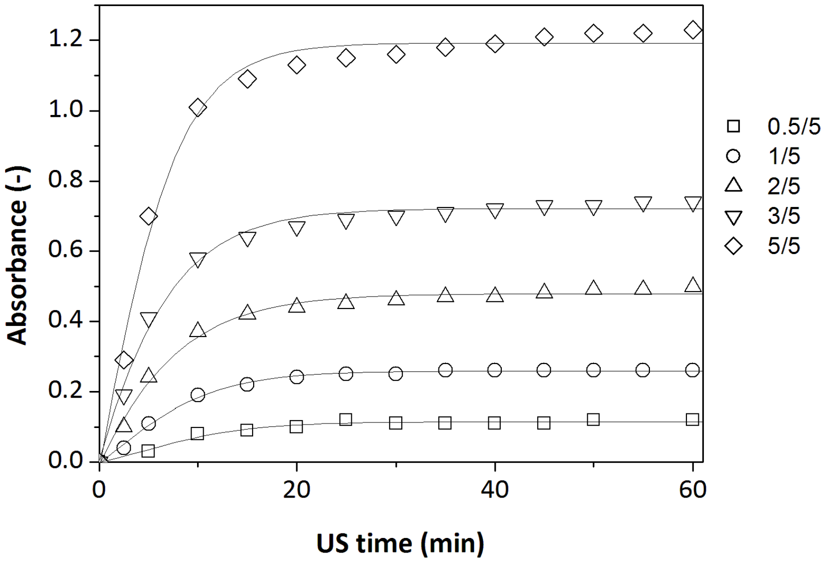

Figure 6.10: Absorbance of different COOH-MWCNT concentrations as a function of the ultrasonication time (US time) below the critical ratio for different COOH-MWCNT/22.6% PG5000 ratios. Here the absorbance per mg of CNTs dispersed remains constant.

Studies on pristine MWCNT/surfactant ratios above a certain value (see Figure 6.11) demonstrate that a critical ratio exists above which insufficient surfactant molecules are present to stabilize all individual tubes peeled off during ultrasonication [255]. This holds also for acid-functionalized MWCNTs.

Figure 6.11 shows for MWCNT/22.6% PG5000 systems that the 2/1 ratio has an absorbance slightly lower than twice the value of its 1/1

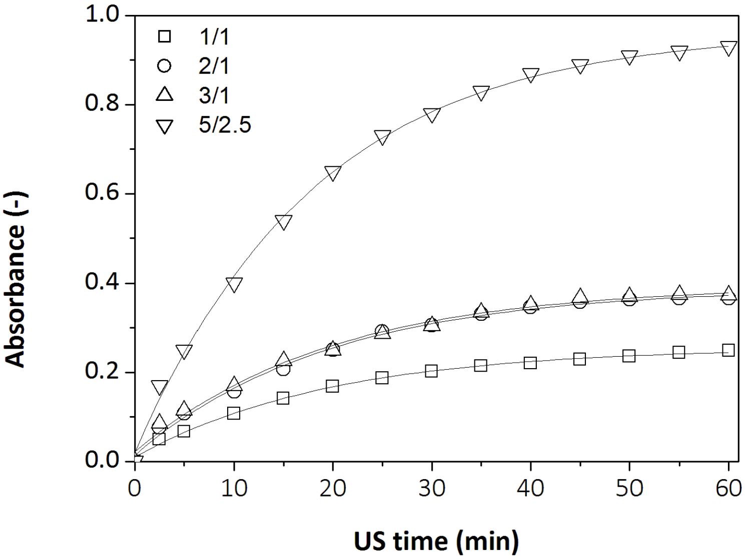

Figure 6.11: Absorbance around and above the critical ratio as a function of the ultrasonication time (US time) for different MWCNT/22.6% PG5000 ratios. Below the critical ratio the absorbance per mg of CNTs dispersed remains constant.

counterpart and that the absorbance of a 3/1 sample levels off around the same value as the 2/1 ratio does. The 1/1 proportion seems to be below the critical ratio for this surfactant given the absorbance of 0.24 per mg of nanotubes added. Moreover this solution remains stable for at least 2 months, as seen by the absorbance remaining constant.

The 2/1 and 3/1 ratio exceed the critical ratio as deduced from their absorbance being lower than 0.24 per mg of MWCNT added. Although both the 2/1 and 5/2.5 slightly exceed the critical ratio and thus contain some remaining bundles, their comparison demonstrates that higher surfactant concentrations can disperse more nanotubes. The absorbance of the latter is exactly 2.5 times that of the 2/1 ratio, confirming the existence of a critical ratio rather than a critical absolute surfactant concentration in the concentration range studied. Because the maximum dispersed nanotube concentration depends on the available amount of surfactant, knowledge of the critical ratio is of major importance: higher dispersed nanotube concentrations can only be realized by increasing the surfactant concentration such that the ratio tumbles below the critical one [202]. Moreover, it was also observed that when working at or below the critical ratio, absorbance remained constant for at least 2 months, pointing at the stability of these dispersions. However, when working above the critical ratio, a decrease in the absorbance can be observed after a few days.

Most authors agree that higher surfactant concentrations result in the potential of dispersing larger amounts of nanotubes [182, 183, 192]. Some on the contrary mention that the nanotube/surfactant ratio is of minor importance compared to the absolute surfactant concentration [191, 256]. Blanch et al. suggested that the increase of CNT dispersion with surfactant concentration is caused by an associated increase of the viscosity [191]. In the present work however the absolute surfactant concentration and the associated viscosity effect seem to be irrelevant and the nanotube/surfactant ratio to be dominant.

Figure 6.10 and 6.11 demonstrate that the absorbance of 0.24 per mg (COOH-)MWCNT added in case of maximum dispersion can already be found for a ratio of at least 1/1 for the entire PG5000 series, irrespective of the degree of functionalization. Also the other molar mass series demonstrate maximum dispersion for this ratio, with dispersions remaining stable for at least 2 months, except for the 11.2% PG10000 sample. This renders these species extremely efficient compared to other surfactants. Literature generally reports values from 1/5 to 1/10 by weight [182, 251], and extreme ratios from 1/2 [190, 194] down to 1/350 [257] occur more exceptionally. Hyperbranched dispersants with PPO-PPE copolymer arms require a CNT/surfactant ratio of 1/3 to disperse nanotubes, whereas a ratio of at most 1/30 is needed to keep these dispersions stable [183].

6.1.4 Influence of PG Molar Mass and End-Group Functionalization

Figure 6.12 depicts the maximum MWCNT mass (mg) dispersed per 1 mg of surfactant in 20 mL of water, a quantity further referred to as the surfactant efficiency. These efficiencies are numerically equivalent to the critical ratio and thus dimensionless (mass MWCNT/mass surfactant). Calculation of the amount of dispersed MWCNT based on the final absorbance after 60 min of sonication, assumed again that an absorbance increment of 0.24 corresponds to 1 mg of dispersed MWCNT. The efficiencies are grouped according to the core PG molar mass and represented as a function of the hydroxyl group percentage replaced with trityl functionalities. The model based trendlines will be explained in detail in Section 6.1.5. Note that 22.6% PG5000, 3.7% and 11.2% PG10000 are not used in analysis towards the trendlines as aqueous solutions of this surfactant appear hazy, pointing at solubility issues thereby potentially changing the active surfactant concentration.

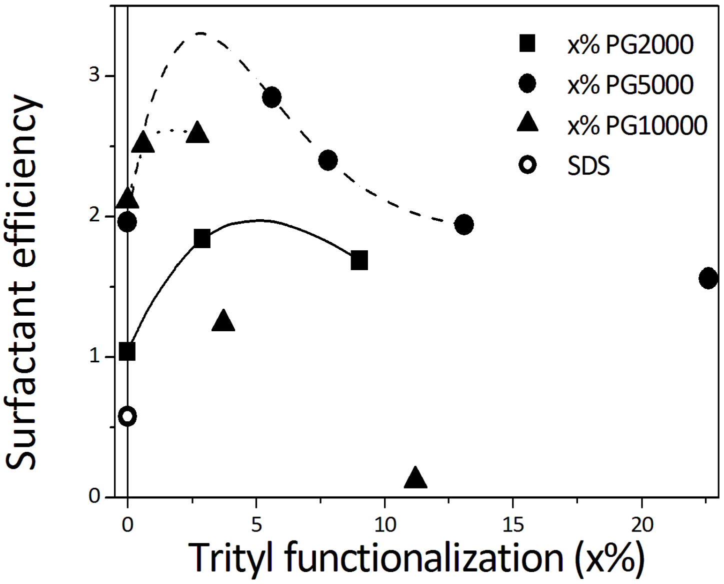

Figure 6.12: Surfactant efficiency as a function of the degree of PG trityl end-group functionalization (x%) for PG2000, PG5000 and PG10000. Trendlines are fits through the selected data points, leading to the molecular efficiencies displayed in Figure 6.17. The data points not being connected by the lines are excluded from the analysis because of surfactant solubility problems. Also SDS is added to further illustrate the high surfactant efficiency.

PG2000 has a lower efficiency compared to PG5000 and PG10000, probably because PG2000 is too small to cause a steric stabilization as large as that of its larger counterparts. An increased steric stabilization seems to outweigh the fact that a lower effective number of molecules per unit of mass is introduced when larger molar masses are used, which in principle may lead to a poorer nanotube stabilization. The surfactant efficiency as a function of the degree of functionalization appears to go through a maximum. Model calculations (Section 6.1.5) will help to explain this trend [189].

Most literature mentions a higher efficiency with an increase in molar mass for non-ionic surfactants such as the Pluronic, Brij, Tween and Triton series, due to an increase in steric stabilization and consequently in repulsive forces between individualized tubes [205, 258, 259]. Vaisman and Xin state that shorter (Pluronic) systems are inefficient in nanotube dispersion not only due to lower molar mass and poor steric hindrance but also due to shorter terminal hydrophilic groups and lower solubility [183, 189]. Nonetheless Vaisman added that enlarging the surfactant hydrophilic part decreases adsorption ratios onto the nanotubes [189, 250]. The mentioned trends are partially confirmed in Figure 6.12 where increasing the polyglycerol molar mass from 2000 up to 5000 g/mol at lower degrees of functionalization improves the nanotube dispersion efficiency. At a molar mass of 10000 g/mol the trend inverts, likely because of the surfactant solubility issues.

Figure 6.12 also includes the three unfunctionalized PG species, which clearly are already fairly efficient when compared to e.g. the commercially available SDS (also included), confirming interactions between the nanotubes and the PG core. This can be due to charge transfer interactions between the PG oxygen electron lone pairs and the carbon nanotube surface and perhaps also partially to small hydrophobic effects [183, 260]. However, highest efficiency is obtained after adding trityl groups, indicating their (π-π stacking) interaction with the CNTs.

The aromatic part of the ^{1}H NMR spectrum of an aqueous surfactant solution (3 mg 2.7% PG10000 in 1 mL of D_2O, Figure 6.13 A) and of this solution after addition of pristine MWCNTs and ultrasonication (Figure 6.13 B) are shown in Figure 6.13, both with chemical shifts referenced to the water peak. As shown in this figure, the signals assigned to the aromatic trityl groups (6.63-7.59 ppm) in the aqueous solution shift downfield after the addition of nanotubes and ultrasonication (6.79-7.67 ppm), similar to what was found by Chen et al. [198]. This confirms (the suggested π-π stacking) interactions between the trityl groups and the carbon nanotubes.

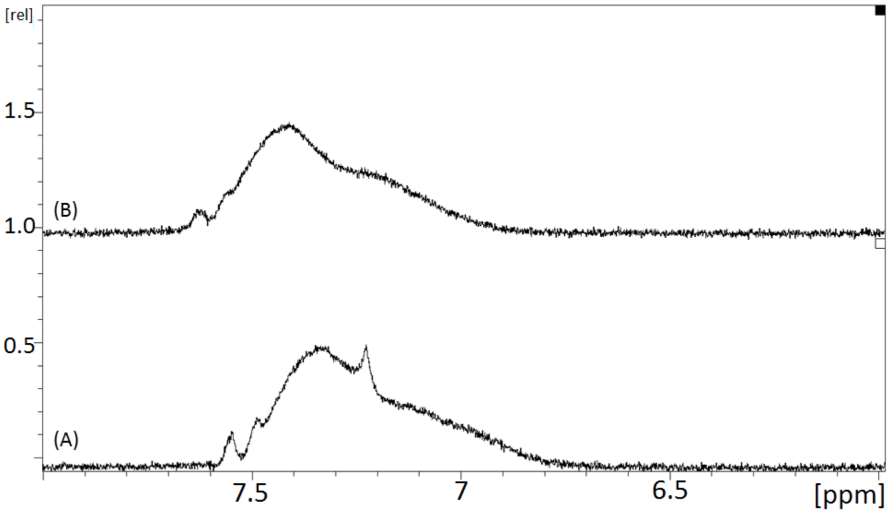

Figure 6.13: Aromatic part of the ^{1}H NMR spectrum of a 2.7% PG10000/MWCNT aqueous solution before (A) and after addition of MWCNT and ultrasonication (B). The shift observed confirms trityl-CNT interactions.

Visual inspection reveals solubility issues and lower efficiency for certain species, especially at higher degrees of functionalization. This can be attributed to the low hydrophilic-lyophilic balance and (intramolecular) interactions between trityl groups (see also Section 6.1.5). Pure 25% PG10000 has a powder like appearance, 20% PG5000 is a highly viscous liquid. The decrease in viscosity with a decrease in the degree of functionalization already indicates a change in the amount of interactions. The aromatic region of the ^{1}H NMR spectrum of PG5000 surfactants with a different degree of functionalization in DMSO-d_6, referenced to the DMSO peak (Figure 6.14) confirms those interactions.

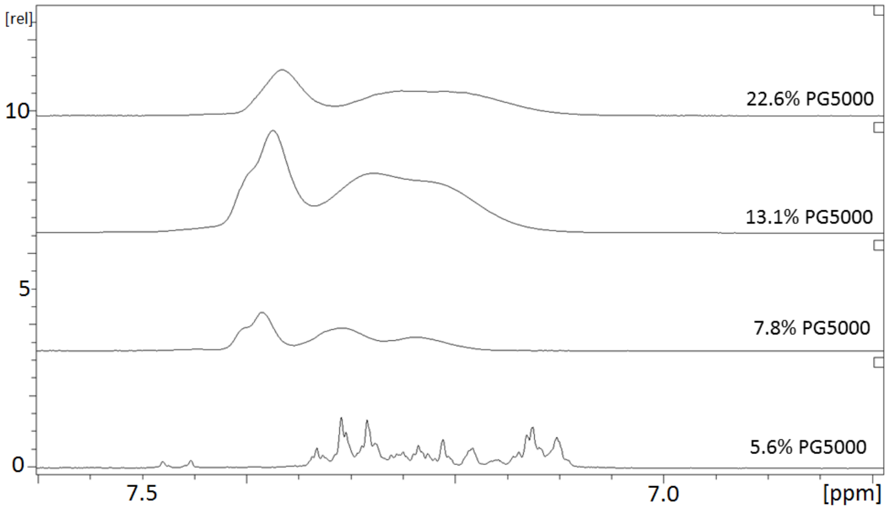

Figure 6.14: Aromatic part of the ^{1}H NMR spectrum of the PG5000 series dissolved in DMSO-d_6,demonstrating trityl interactions.

For the lowest degree of functionalization a more detailed fine structure can be seen. Higher degrees of functionalization cause a downfield shift, as well as the disappearance of the fine structure. This confirms trityl group interactions, and supports the hypothesis of intramolecular interactions between trityl groups at higher degrees of functionalization. However, it must be kept in mind that Figure 6.14 concerns DMSO as a solvent, rather than water. As DMSO is a better solvent for the trityl (functionalized) molecules compared to water, mutual trityl interactions probably will even further increase when using water. Similar phenomena can be seen for the PG2000 (Figure 6.15) and PG10000 (Figure 6.16) series.

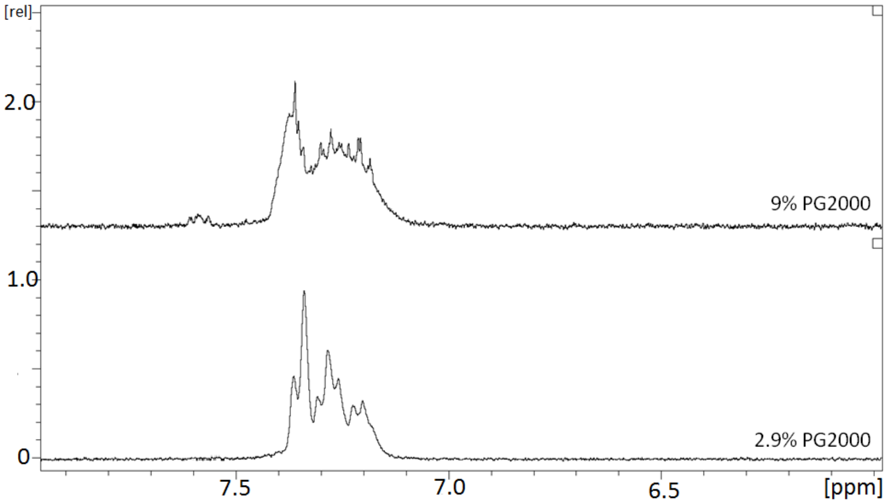

Figure 6.15: Aromatic part of the ^{1}H NMR spectrum of the PG2000 series dissolved in DMSO-d_6, demonstrating trityl interactions.

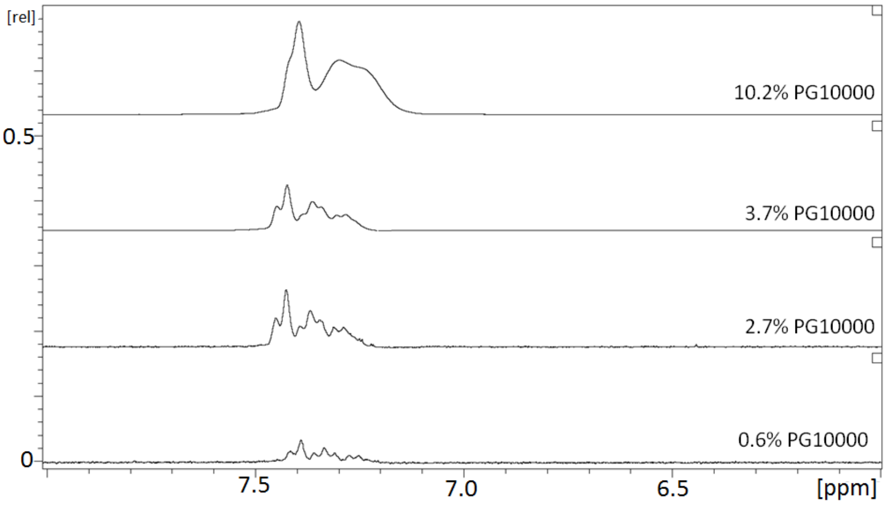

Figure 6.16: Aromatic part of the ^{1}H NMR spectrum of the PG10000 series dissolved in DMSO-d_6, demonstrating trityl interactions.

6.1.5 Model Calculations

The present surfactants differ from most others as they are complex mixtures of molecules with different molar masses and degrees of trityl functionalization per molecule. The introduced interpretation scheme attempts to grasp some of these aspects, based on the assumption that the global surfactant efficiency is the average of the molecule specific efficiencies. Furthermore the treatment focuses on the distribution in trityl functionalization and neglects the molar mass polydispersity as well as topological differences between molecules with an identical amount of trityl functionalizations. This assumes e.g. all molecules in PG2000 to be equally large, carrying 25 hydroxyl groups available for functionalization (see also Table 6.1). In addition, molecules with e.g. 2 functionalizations are considered equally efficient, irrespective of the attachment of the functionalizations: at the periphery, the core of the molecule or in each other′s proximity or on opposite sides of the PG molecule. Alternatively a single average efficiency represents all molecules with an identical number of functionalizations. Assuming that the probability of trityl functionalization does not depend on earlier trityl attachments nor on whether a primary or secondary alcohol is being replaced, one can compute the probability (p_i) that a molecule will carry i functionalizations as follows

$$p_i = \varphi^i \, (1 - \varphi)^{N-i} \, \frac{N!}{(N-i)!i!} \tag{6.1}$$

With φ the average fraction of functionalizations and N the number of hydroxyl groups available for functionalization in each molecule. With the assumptions listed above, φ and N for 5% PG2000 equal 0.05 and 25 respectively.

Figure 6.17 illustrates the result of such calculations for all samples studied, with p_i (expressed as % molecules, i.e. 100 p_i) in function of i, the number of trityl functionalizations per molecule. Very clearly, at a low (global) degree of functionalization (x%) and low PG molar mass, a significant percentage of the molecules remains unfunctionalized (up to about 50% in 2.9% PG2000). This unfunctionalized share vanishes at higher PG molar masses and larger x% values. Moreover, the trityl functionalization distributions for a given x% broaden with increasing PG molar mass.

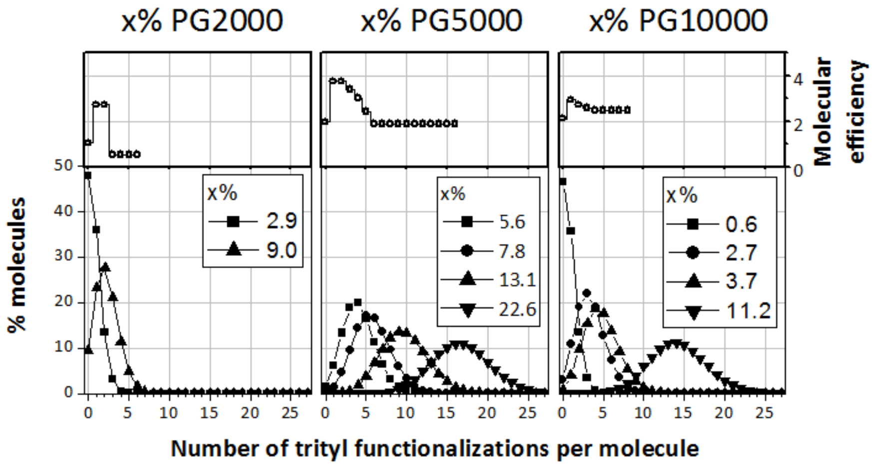

Figure 6.17: Trityl functionalization distribution for an average functionalization $x\%$ (with $x\% = \varphi$), as indicated in the legends (Bottom panels). The molecular efficiency, i.e. the efficiency to disperse MWCNTs for molecules with a given number of trityl functionalizations and PG core (Top panels). $x\%$ PG2000 species are depicted left, $x\%$ PG5000 in the middle and $x\%$ PG10000 at the right hand side.

Each of the molecules within the distributions is expected to display its specific molecular efficiency to disperse MWCNTs (top panel Figure 6.17). These molecular efficiencies were obtained by fitting the experimental global surfactant efficiencies depicted in Figure 6.12 to the p_i weighted sum of the molecular efficiencies using a least squares error minimization procedure varying the molecular efficiencies. The minimization procedure was executed combining all $x\%$ species of a given PG molar mass in a single run (but excluding the surfactants that display solubility problems, as mentioned before). Given the low number of experimental data points and to avoid spurious oscillations, the efficiency of molecules with i functionalizations was restricted to be smaller or equal to the efficiency of molecules with $i-1$ functionalizations, except for molecules with $i = 1$, having no constraint. All calculations were done using the Microsoft Excel solver. The molecular efficiencies for which p_i for all $x\%$ is less than 1% are not included in Figure 6.17 as these partitions do not significantly contribute. Interpolations based on the earlier obtained molecular efficiencies and the $x\%$ specific functionalization distribution (Equation 6.1) lead to the trendlines linking the symbols in Figure 6.12. Clearly, this procedure allows describing the experimental data rather well and with the aid of Figure 6.17, aspects related to the PG molar mass and degree of trityl functionalization can be discussed.

The molecular efficiencies for $x\%$ PG2000, $x\%$ PG5000 and $x\%$ PG10000 display a similar trend: at low degrees of functionalization, the efficiency is larger compared to unfunctionalized PG. Beyond a given number of trityl functionalizations however, the molecular efficiency tumbles down to another (fairly constant) value which for the PG2000 and PG5000 series occurs below that of the parent unfunctionalized PG. This fall back saturates at a trityl functionalization of 3, 6 and 4 for respectively the PG2000, PG5000 and PG10000 series (Figure 6.17 top panels).

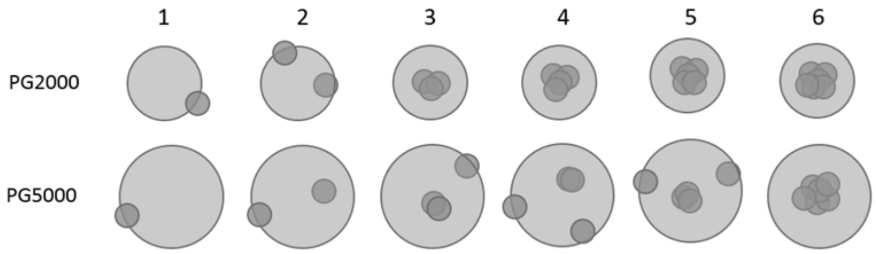

Figure 6.18: Figures representing the PG core (with a size proportional to the PG radius of gyration in water) [3] and trityl functionalizations for PG2000 (Top row) and PG5000 (Bottom row) based species. Beyond a threshold of 2-3 functionalizations the trityl groups tend to mutually interact and do so completely on the average at 3 and 6 functionalizations for respectively PG2000 and PG5000. Mutually interacting trityl groups are suggested to be shielded from the aqueous environment by the PG moieties.

The higher molecular efficiency for low trityl functionalizations seems natural and to be related to the anticipated π-π-stacking interactions between the trityl phenyl groups and the CNT surface, often found in literature and confirmed using ^{1}H NMR [198, 209]. As the functionalized species have a higher stability in time, trityl-CNT interactions can be considered superior to hydrophobic effects and charge transfer interactions between the surfactant lone pairs and carbon nanotubes. However, the phenyl rings may also interact mutually, both inter- and intramolecularly. The probability for intramolecular, mutual interactions increases with decreasing positioning distance between trityl groups, which in turn depends on the number of functionalizations and the size (molar mass) of the parent PG molecule. This effect, starting to take place at 2-3 functionalizations and becoming more probable with increasing degree of functionalization, is illustrated in Figure 6.18. This figure furthermore suggests that mutually interacting trityl groups may represent a rather hydrophobic entity with a tendency to be shielded from the aqueous environment by the PG moieties. With this shielding effect, no big differences between the efficiencies for functionalizations higher than the mentioned thresholds are expected, as observed in Figure 6.17.

It is conceivable that part of the charge transfer interactions between the PG oxygen electron lone pairs are taking place with the trityl groups rather than with the MWCNTs, and that this effect is adding to the reduction of the surfactant efficiency below that of pure PG. When the number of trityl functionalizations increases, the hydrophilic-lyophilic balance lowers, which influences the surfactant solubility. For the PG10000 series, haziness already starts to set in at a functionalization degree of 3.7%, for the PG5000 series the 22.6% species suffer from solubility issues. The higher efficiency for lower functionalizations thus agrees with what has been found for linear surfactants, i.e. a higher hydrophilic-lyophilic balance (HLB) and water solubility increase the surfactant efficiency in aqueous solutions [189].

The lower molar mass for PG2000 may account for the saturated fall back at 3 compared to at 6 trityl functionalizations for the larger PG5000. It can be verified that the efficiency fall back for these two systems saturates once the total mass corresponding to the trityl functionalizations exceeds about one third of the PG molar mass.

Following the above mentioned rule of thumb one expects the efficiency fall back for the PG10000 series to saturate at 16 functionalizations. In contrast, according to Figure 6.17 this already takes place at 4 functionalizations. The analysis of the PG10000 series should however, be considered with some care. Figure 6.12 demonstrates that the 3.7% and 11.2% PG10000 perform very poorly. This can obviously be explained by the low water solubility of the higher functionalized PG10000 species, by which the effective concentration and thus also the surfactant efficiency in solution decreases. This effect inflates with increasing degrees of functionalization. The 3.7% PG10000 sample in water was clearly hazy and was therefore excluded from the analysis. Although the 0.6 and 2.7% PG10000 samples did not show a visible lack of solubility, it cannot be excluded that a fraction of the latter (less likely for the 0.6% sample) cannot be dissolved either. If so, the entire analysis for the PG10000 series might be inaccurate. Finally, the model curves in Figure 6.12 predict a maximal surfactant efficiency for PG5000 with an average functionalization degree of about 2.5%. Therefore, this material deserves further consideration in the future.

6.1.6 Visual Solution Characterization

Visual inspection provides an indication of the surfactant efficiency. Figure 6.19 displays different systems with a 2/1 MWCNT/surfactant ratio using respectively 5.6% PG5000 (A), 2.9% PG2000 (B), and 3.7% PG10000 (C). Only in Figure 6.19 (A) the MWCNT/surfactant ratio lays below the critical one. Consequently the system appears very homogeneous and suggests a complete dispersion. In contrast, the system in Figure 6.19 (B) contains some fine dust and that in Figure 6.19 (C) clearly suffers from strong flocculation as its CNT/surfactant ratio lies far above the critical one.

A more detailed investigation using electron microscopy confirms the existence of individual, exfoliated nanotubes in optimized systems as well as the high surfactant efficiency. The TEM image in Figure 6.20 (left), collected from a CNT/5.6% PG5000 dispersion at its critical ratio displays individualized MWCNTs one day after US treatment. Figure 6.20 (right) (HR-TEM) confirms that the US conditions used do not destroy the nanotubes, as individual tubes with rather straight borders and intact graphene layers can be seen, with an interplanar spacing of 0.34 nm, the typical graphene interlayer distance in graphite. The objects at the nanotube wall do not necessarily originate from adsorbed surfactants, but can also be due to damage because of the electron beam as well as to contaminants.

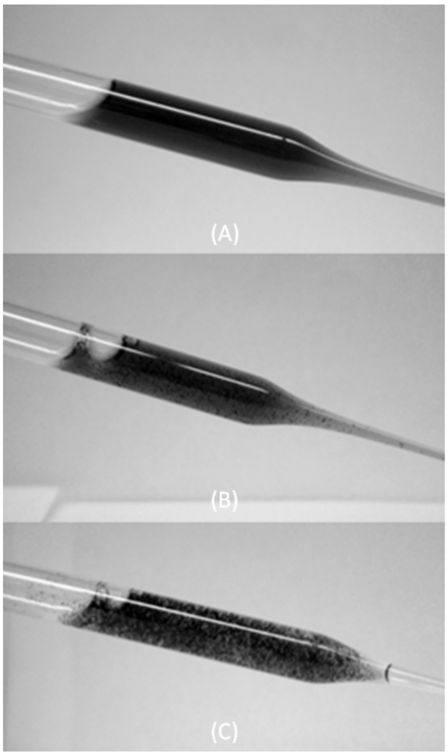

Figure 6.19: Visual inspection of dispersions with (A) 5.6% PG5000, (B) 2.9% PG2000 and (C) 3.7% PG10000. For all samples 2 mg and 1 mg of respectively MWCNT and the surfactant were brought into 20 mL of water and sonicated for 60 min.

Figure 6.21 (left) displays a TEM image of a drop of a CNT solution with 5 mg of MWCNT dispersed with 2.5 mg of PG5000, one day after the sonication treatment. Some dangling and loose nanotubes can be found, but the majority of the nanotube forms a cluster, although tubes are probably rather entangled than tightly stacked. This illustrates the lower stability in time of the unfunctionalized PG, despite its high initial efficiency. Also here the US treatment does not seem to damage nanotubes, as seen in Figure 6.21 (right).

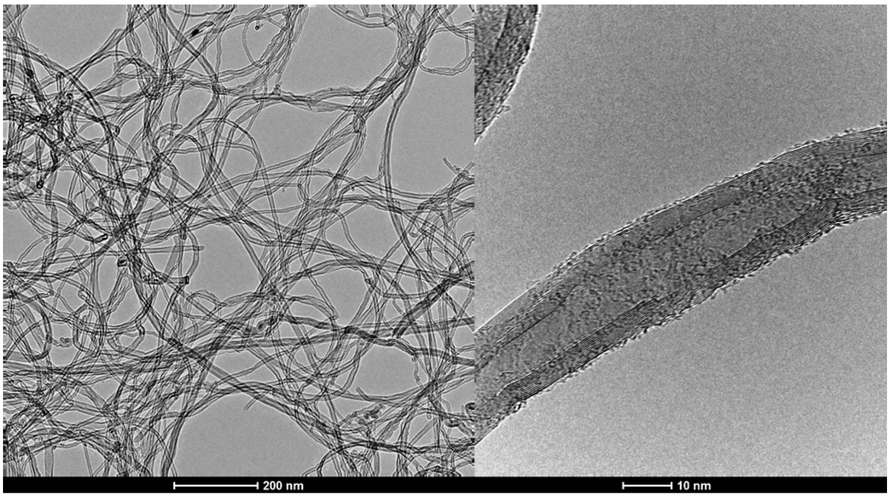

Figure 6.20: TEM image collected from a 5/2.5 CNT/5.6% PG5000 solution (left) and HR-TEM image of an individual tube in this solution (right), demonstrating full dispersion.

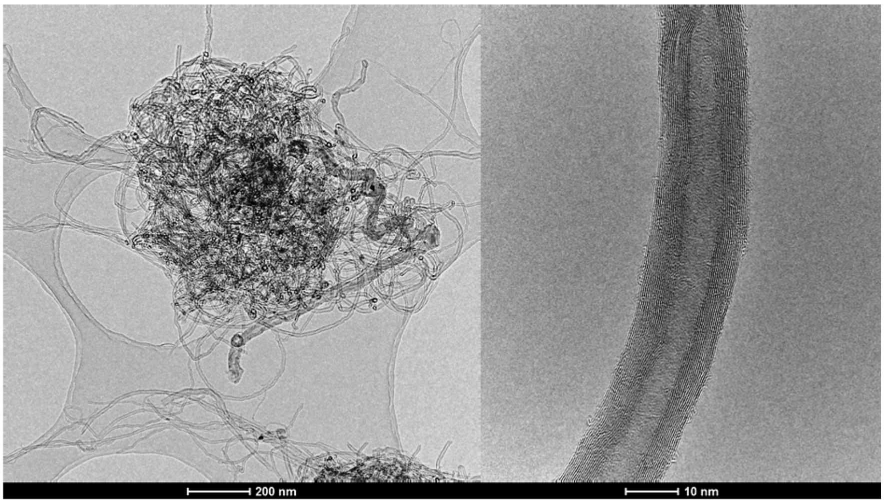

Figure 6.21: TEM image collected from a 5/2.5 CNT/ PG5000 solution (left) and HR-TEM image of an individual tube in this solution (right) that is not dispersed to the fullest.

6.1.7 Influence of CNT Functionalization

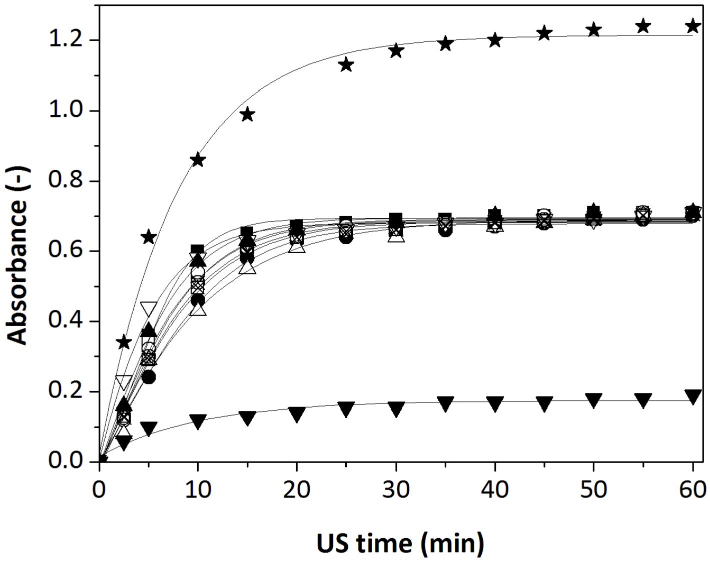

Figure 6.22: Absorbance of COOH-MWCNT dispersions as a function of the ultrasonication time (US time) for 3/1 MWCNT/2.9% PG2000 (■), 3/1 MWCNT/9% PG2000 (•), 3/1 MWCNT/5.6% PG5000 (□), 3/1 MWCNT/7.88% PG5000 (○), 3/1 MWCNT/13.1% PG5000 (△), 3/1 MWCNT/22.6% PG5000 (▽), 3/1 MWCNT/0.6% PG10000 (⊠), 3/1 MWCNT/2.7% PG10000 (⨂), 3/1 MWCNT/3.7% PG10000 (▲), 3/1 MWCNT/11.2% PG10000 (▼) and 5/1 MWCNT/5.6% PG5000 (★).

Although functionalized carbon nanotubes have inferior mechanical, electrical and thermal properties, they offer advantages. Firstly these species have the ability to react with certain functionalities of the matrix or substrate, resulting in a stronger anchorage. Secondly they are easier to disperse. Except for Bystrzejewski who claims that the acid oxidation of nanotubes does not influence the dispersed concentration [182], literature agrees that chemical CNT functionalization results in higher populations of individual tubes [171], even at very low levels of covalent functionalization (1-2 *at*%) [178]. Chemical treatment disrupts the CNT structure, decreases π-π-stacking and increases interactions with the solvent, consequently enabling dispersion.

The higher efficiency after CNT functionalization is confirmed in Figure 6.22, demonstrating that a ratio at least as high as 3/1 leads to most efficient dispersion for COOH-MWCNT when using the PG2000 and PG5000 series. Whereas 11.2% PG10000 clearly disperses less nanotubes (as seen by the lower absorbance), 1 mg of the most efficient surfactant (5.6% PG5000) can disperse more than 5 mg of COOH-MWCNTs. It must be noted that the highest possible absolute (COOH-)MWCNT loading was not studied, as this leads to absorbances too high to be measured. Therefore earlier solution characterization focused on MWCNT systems, as MWCNT dispersions display saturations in dispersing capabilities already at lower CNT/surfactant ratios compared to COOH-MWCNT systems, facilitating dispersion studies.

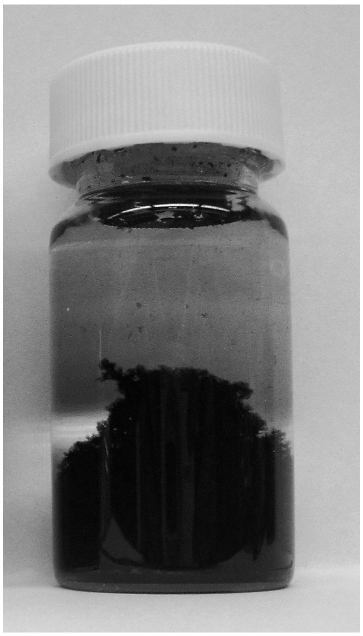

Figure 6.23: Photograph of a 1/10 NH_2-MWCNT/22.6% PG5000 aqueous solution 1 h after ultrasonication, demonstrating the instability of the solution.

Dispersions of NH_2-MWCNTs using the surfactants synthesized during this work are not stable. Figure 6.23 displays such a solution 1 h after sonication. The precipitation can be attributed to a lack of charge transfer interactions, pointing at the importance of the PG core to stabilize these dispersions [187, 206]. Literature often refers to pristine nanotubes as slightly p-doped due to oxygen adsorption [261–263] and also the acid functionalized nanotubes are p-doped. The free electron pairs in the hyperbranched polymer can interact with the excess of holes in these tubes, leading to so-called charge transfer interactions [260]. Amino functionalized nanotubes on the contrary belong to the n-type species, inhibiting the charge transfer interactions and decreasing the surfactant efficiency. For this reason, this work focuses on pristine and acid functionalized MWCNTs.

6.1.8 Influence of Ethanol in the Solvent

As the CNT solution should wet the APS coated substrate in the next stage, ethanol is added to the solvent to decrease the surface tension and enable spreading. First a MWNCT/8% PG5000 solution in a 90/10 H_2O/EtOH ratio is studied. Table 6.2 demonstrates that addition of a small amount of ethanol increases the efficiency of the surfactant.

Table 6.2: Efficiency of different surfactants to disperse MWCNTs in a solvent with a H_2O/EtOH ratio of x/y. Addition of ethanol increases the efficiency.

Surfactant	**100/0**	**90/10**	**50/50**
7.8% PG5000	2.40	2.49	-
13.1% PG5000	1.94	-	2.8
11.2% PG10000	0.12	-	2.71

As the higher functionalized species suffer visibly from lower solubility in pure water, the reason for the improved efficiency might be found in the solubility of the surfactant, which increases after the addition of ethanol. Testing of 2 less efficient surfactants further confirms this statement. Especially the -in water poorly performing- 11.2% PG10000 performs impressively good after the addition of 50% of ethanol to the solvent. This supports the theory that ethanol increases the solubility of the (higher functionalized) surfactants, increasing the effective active concentration and thus efficiency. Further work uses water/ethanol mixtures, although at the critical CNT/surfactant ratio determined for the pure aqueous solutions. Working at this ratio requires only a small amount of surfactant and for sure lies below the critical ratio for the ethanol containing solutions.

6.1.9 Polylysine-Based Surfactants

When deposited at the SST-epoxy interface, synthesized surfactants preferably interact with (both the substrate and) the polymeric matrix, thereby improving the mechanical properties of CNT/polymer composites. If not, they act as the weak point in the hybrid. Ideally the hyperbranched part should react with the (polar) polymer through hydrogen bonding or by a covalent reaction, making it act as a coupling agent [202, 208, 264]. Replacing the PG core with a polylysine (PL) core (Chapter 5, Figure 1.17) brings in amine instead of hydroxyl functionalities and may increase the interaction with an epoxy matrix. The so-obtained surfactants have similar synthesis and testing methods, but due to the amine groups of the PL core, it may have an improved reactivity with the epoxy. Naming conventions are the same as for the polyglycerol counterparts.

Table 6.3 displays the surfactant efficiency of the 2 types of surfactant with a similar degree of end-group functionalization and core molar mass, but with respectively a PG and a PL core. This table reveals the lower efficiency of the PL based surfactant, with an efficiency decrease of about 40% for MWCNT in pure water. Whereas for the acid functionalized CNTs most PG surfactants displayed full dispersion when using a CNT/PG ratio of 3/1, the PL surfactant is not able to fully disperse this amount of nanotubes, nor in pure water, nor after the addition of ethanol. However, Table 6.3 confirms the trend of increased efficiency after the addition of ethanol (Section 6.1.8) for the polylysine species. This work did not study into detail the reason for the lower efficiency of PL based surfactants. It might be due to solubility issues (although not visually seen), as well as due to a decreased interaction between the hyperbranched core and the carbon nanotube. Nonetheless experiments performed reveal the critical ratio used for further work.

Table 6.3: Efficiency of different surfactants to disperse (COOH-)MWCNTs in a solvent with H_2O/EtOH ratio of x/y.

	H_2O/EtOH	**7.8% PG**5000	**8% PL**5000
MWCNT	100/0	2.4	0.97
COOH-MWCNT	100/0	> 3	2.12
COOH-MWCNT	90/10	>3	2.51

6.1.10 Summary

End-group functionalized hyperbranched polymers can act as a CNT surfactant in aqueous solutions. Variation of the percentage of triphenylmethyl (trityl) functionalization and of the molar mass of the hyperbranched PG core, results in the highest measured surfactant efficiency for a 5000 g/mol PG with 5.6% of the available hydroxyl end-groups replaced by trityl functions, as shown by UV-Vis measurements. Semi-empirical model calculations suggest an even higher efficiency for PG5000 with 2.5% functionalization and maximal molecule specific efficiency in general at low degrees of functionalization. Addition of trityl groups increases the surfactant-nanotube interactions in comparison to unfunctionalized PG because of π-π stacking interactions. However, at higher functionalization degrees mutual interactions between trityl groups come into play, decreasing the surfactant efficiency, while lack of water solubility becomes an issue at very high functionalization degrees. Low molar mass surfactants are less efficient compared to higher molar mass species most likely because the higher bulkiness of the latter allows for a better CNT separation and stabilization. The most efficient surfactant studied allowed dispersing 2.85 mg CNT in 20 mL of pure water with as little as 1 mg of surfactant. These dispersions, remaining stable for at least 2 months, were mainly composed of individual CNTs as revealed by electron microscopy.

Varying different parameters reveals easier dispersion when changing pristine by acid functionalized CNTs, (at least partially) due to the lower intermolecular stacking interactions of the latter and a better interaction with the solvent. Exchanging the PG surfactant core for a PL core may increase interactions with an epoxy matrix, but decreases efficiency. The addition of ethanol increases the efficiency for both PL and PG based surfactants. This probably relates to the higher solubility of the surfactant after the addition of ethanol, as the in water poorly performing 11.2% PG10000 (with visible solubility issues) increases its efficiency by a factor 20 after adding ethanol.

6.2 Nanotubes at the Interface

In the next phase the carbon nanotubes can be deposited at the interface. Literature already mentioned high affinity between APS coated substrates and CNTs [179, 265]. To start with samples are coated according to the optimized APS deposition process (2/90/10 APS/H_2O/EtOH, 30 s of dipping, 60 s of EtOH rinsing) which can be followed by an (brief) oven treatment. Next CNT deposition takes place from a sonicated 90/10 H_2O/EtOH solution prior to oven treatment for 1.5 h at 70°C under vacuum. Also here different parameters can be varied, such as the concentration and type of CNT, the solvent composition and the deposition and curing protocol. Acid functionalized nanotubes are preferred because of their improved ability to interact with both the substrate and the matrix, and again preference goes to high water/ethanol solutions. The standard CNT deposition procedure starts from a CNT solution (20 mL, 90/10 H_2O/EtOH), in which the (APS coated) substrate is dipped for 1 h. Next the edges of the sample are gently touched with tissue to remove excess solution, followed by an oven treatment for 1.5 h at 70° under vacuum.

This work focuses on CNT deposition at the interface to improve mechanical properties [266]. However, the surfactant developed can also serve different purpose, such as in electronic and thermal applications, as well as for matrix reinforcements [173–175].

6.2.1 Morphological Characterization: SEM

During CNT deposition on a (coated) substrate, different parameters can be varied, both in the APS coating process and the CNT coating process. SEM allows visual inspection of the influence of different parameters.

6.2.1.1 Influence of APS coating parameters

During APS deposition different parameters can be varied. Nonetheless earlier experiments pointed out the optimal coating process resulting in highest adhesion strength. Hence the only parameters checked are the presence and absence of APS as well as the effect of partial APS condensation after APS and before CNT deposition.

Figure 6.24 verifies the need for APS on SST substrates to allow for CNT attachment as it clearly shows barely any nanotubes for a substrate without APS. This image reveals no individual tubes at all, but does show some clusters (indicated by the arrow). From this it can be concluded that individual nanotube deposition requires APS. Moreover, it suggests interaction between the CNTs and APS. Usrey et al. already noted interaction between APS molecules and carbon nanotubes, with the CNT adsorption strongly depending on the amount of APS on the surface [178].

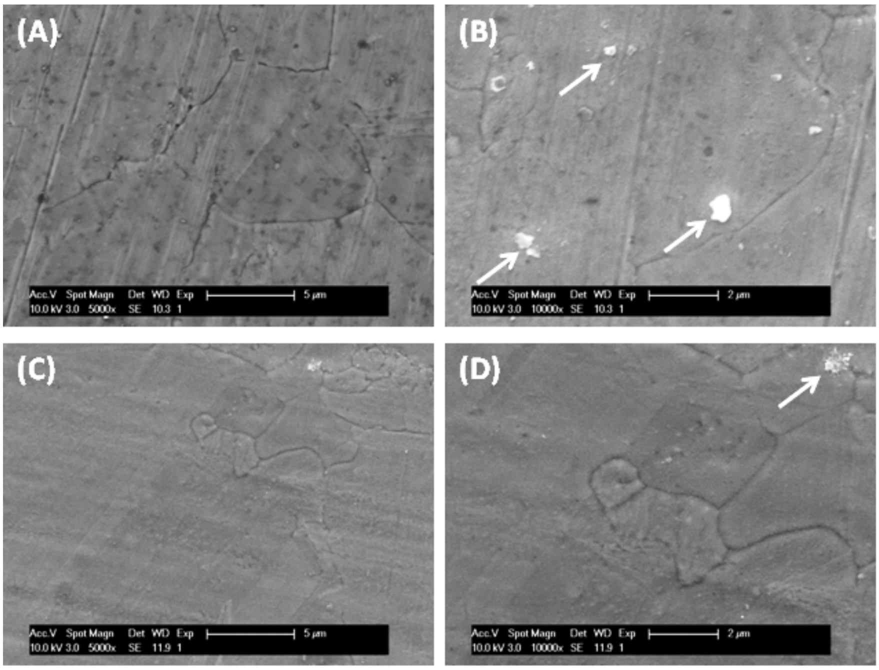

Figure 6.24: SEM image of SST surfaces without APS, but coated with CNT according to the standard procedure from a 2/20 (A and B) and a 0.5/10 (C and D) COOH-MWCNT/22.6% PG5000 solution. No individual CNTs can be seen.

A brief (15 min) oven treatment after APS deposition increases the amount of CNT deposited (when compared to a not oven treated sample) (Figure 6.25). This probably can be attributed to the anchorage of the APS during oven treatment. In the absence of this procedure the silane might partially redissolve in the CNT solution, leaving less 'anchoring' points for the nanotubes.

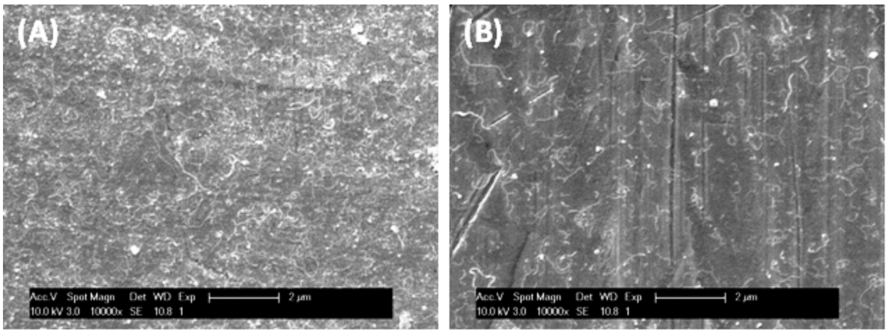

Figure 6.25: SEM image of an APS coated SST surface, coated with CNT according to the standard procedure (from a 1/10 COOH-MWCNT/22.6% PG5000 solution) for samples oven treated after APS deposition (A) and samples not treated after APS deposition (B), the former showing a larger amount of (individual) tubes.

6.2.1.2 Influence of CNT coating parameters

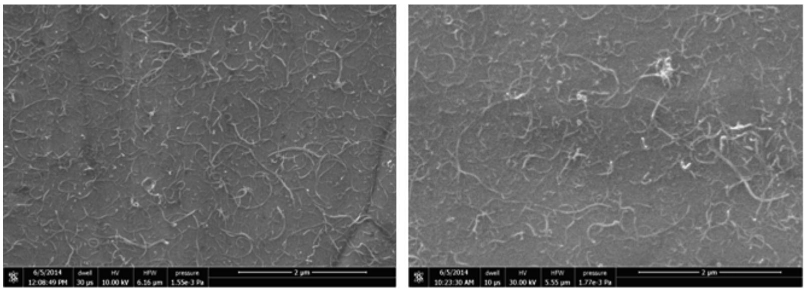

Figure 6.26: SEM image of an APS coated SST surface, coated with CNT according to the standard procedure, but from a different CNT concentration. The left and right images concern respectively a 2/0.7 and 5/1.8 MWCNT/5.6% PG5000 solution.

After oven treatment of an APS covered substrate carbon nanotubes can be applied on this substrate. During CNT coating parameters can be varied: the concentration and type of nanotubes and the type of surfactant, the dipping time and the rinsing procedure after dipping. This part however focuses on acid CNTs as they have a higher affinity for the APS coated substrate and can interact with the matrix in the next step, which is expected to enhance the mechanical properties compared to non-interacting nanotubes [178].

The CNT solution concentration influences the amount of nanotubes deposited, with an increased amount of CNT deposition with increasing concentration (Figure 6.26), as was also found by Usrey et al. [178]. Also longer dipping times cause more CNTs to be adsorbed (Figure 6.27). However, after a dipping time of about 45 min adsorption saturates, as was already found in literature [178].

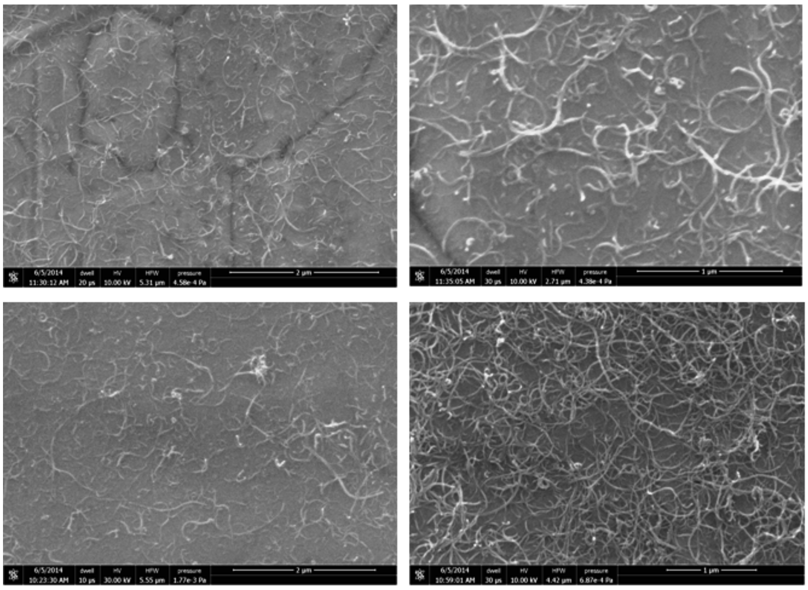

Figure 6.27: SEM image of an APS coated SST surface, coated with CNT with a dipping time of 15 min (Top images) and of 60 min (Bottom images). Longer dipping times cause a higher amount of nanotubes adsorbed. Samples concern deposition from a 5.6% PG5000 solution with a MWCNT/surfactant ratio of 5/1.8.

Figure 6.28 shows the influence of water rinsing in between silane dipping and oven treatment and reveals that rinsing removes carbon nanotubes to a large extent. This points at weak interactions between the nanotubes(/surfactant species) and the APS coated substrate, easily being disturbed by water rinsing. However, after oven treatment, nanotubes are more strongly anchored, as rinsing after this treatment does not remove any nanotubes.

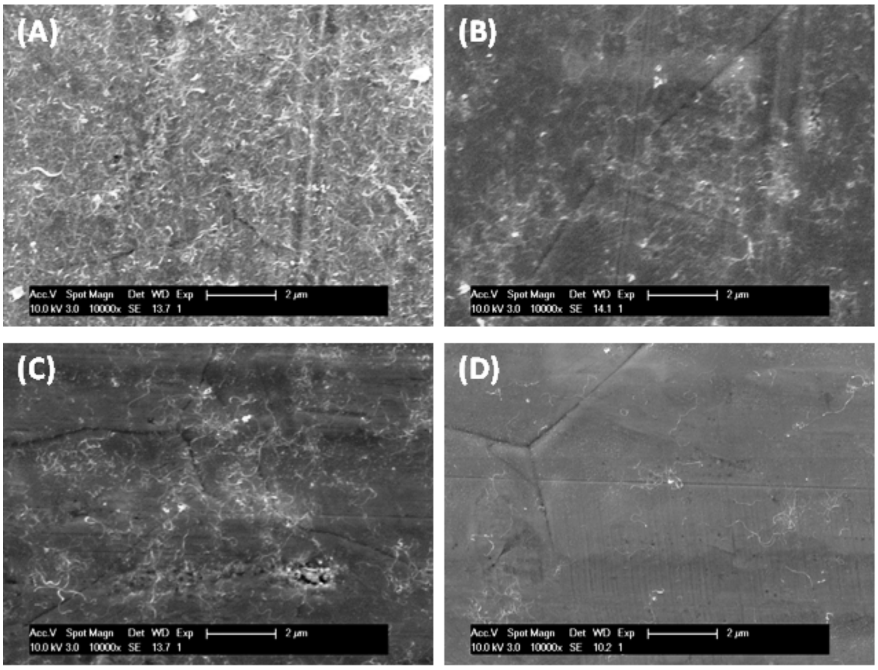

Figure 6.28: SEM image of an APS coated SST surface, coated with CNT according to the standard procedure (A and B) and rinsed for 15 s after CNT deposition (before oven treatment) (C en D). Left and right images concern deposition from respectively a 8% PL5000 and a 7.88% PG5000 solution with a COOH-MWCNT/surfactant ratio of 2/1. After oven treatment no nanotubes are rinsed away.

The exact degree of functionalization of the PG does not cause visual differences in the CNT population on a coated substrate. However, when using unfunctionalized PG5000 as a surfactant (Figure 6.29) clearly a lower amount of individual nanotubes is deposited, although one larger cluster can be seen. Previous experiments already illustrated the rather high dispersion efficiency, but lower stability in time of the unfunctionalized surfactant, pointing at a different type of interactions between the surfactant and the nanotube after functionalization. This surfactant seems to impede individual nanotube adsorption during deposition.

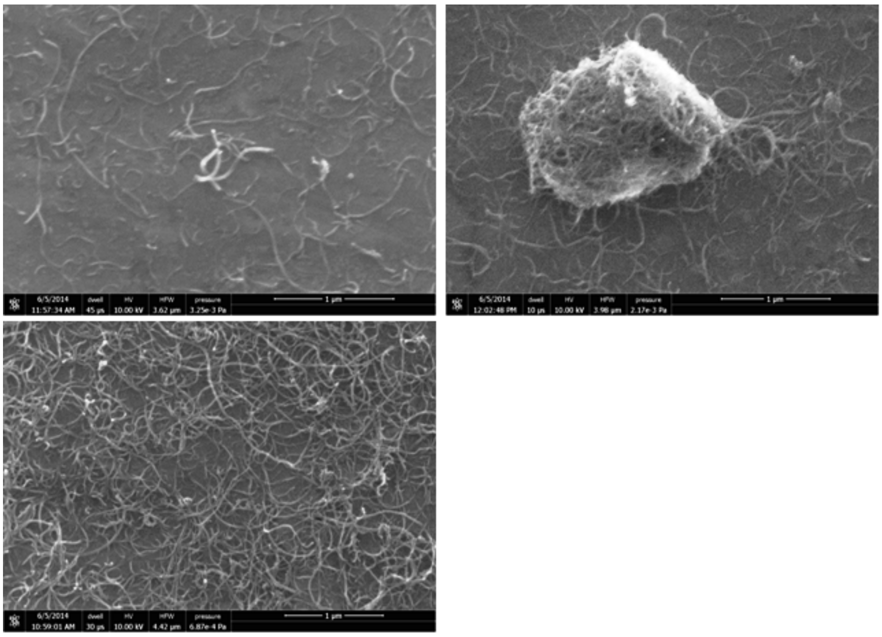

Figure 6.29: SEM image of an APS coated SST surface, coated with CNT according to the standard procedure. The top images use PG5000 as a surfactant, whereas the bottom image uses 5.6% PG5000 and clearly shows a higher amount of (individual) nanotubes.

Figure 6.30 shows that despite the lower efficiency of polylysine based surfactants, they result in a higher amount of deposition. This cannot be due to an increased CNT-surfactant interaction, but probably can be attributed to a higher interaction between the substrate and the surfactant, which still is bound to the nanotubes during and after deposition.

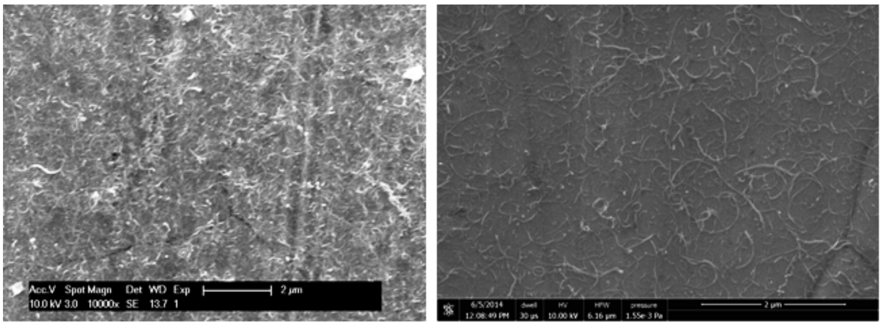

Figure 6.30: SEM image of an APS coated SST surface, coated with CNT according to the standard procedure. The left image started from a 8% PL5000 solution, the right from a 5.6% PG5000 solution. The PL based surfactant leads to a higher amount of CNTs deposited.

6.2.2 Mechanical Characterization

Dolly tests reveal that deposition of acid carbon nanotubes at the interphase does not increase the mechanical performance of APS coupled SST-epoxy joints (Figure 6.31). Use of functionalized surfactants however, does lead to an increase in strength compared to the blanc sample. It is conceivable that the deposition of a too high amount of nanotubes disrupts the bridging ability of the APS, by covering amine groups that should interact with the epoxy matrix. Moreover it may put steric constraints on the matrix close to the interphase.

Figure 6.31 clearly shows that lowering the amount of nanotubes increases performance (CNT C) (compared to a higher amount, CNT B) supporting this theory. Use of the unfunctionalized PG5000 (CNT D) results in the lowest strength, probably due to the deposition of clusters as seen with SEM.

Changing the hyperbranched core from PG to PL does not drastically influence the mechanical strength, despite the increased interaction between the matrix and the surfactant. This points at the weak interface at the nanotube surface, being the weak point in these joints (See also Figure 6.32). However, this does not put aside the theory of a gradient leading to increased mechanical properties. Moreover, it may be interesting to add some nanomodifications in the matrix itself, close to the interface. Research at Materials and Chemistry Department (MACH), Vrije Universiteit Brussel, Brussels, Belgium as well as in other universities already pointed out higher performance when modifying the matrix properties as a whole, e.g. by adding clay or nanotubes. The developed surfactant still can assist in the dispersion of these tubes in the matrix.

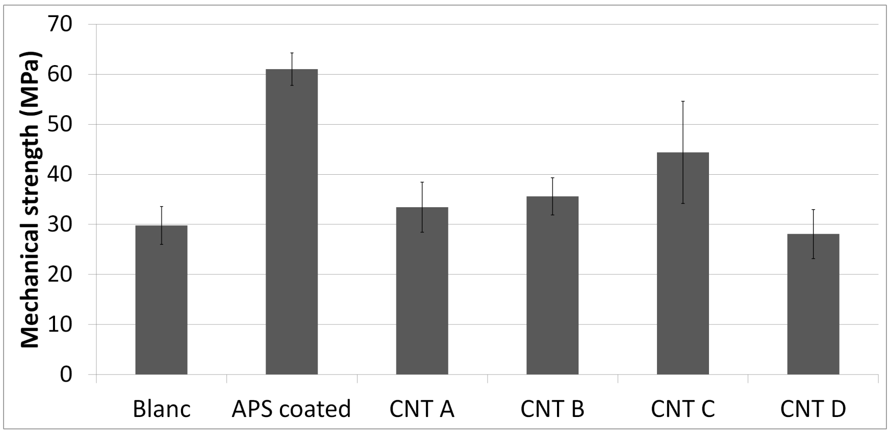

Figure 6.31: Mechanical strength as determined from Dolly testing of SST-epoxy samples using SST dollies. The blanc sample lacks a coupling layer, the APS sample is coated with APS layer, the CNT samples contain an APS layer with a CNT layer on top. This layer is deposited from 1.0/0.4 COOH-MWCNT/8% PL5000 (A), 1.0/0.4 COOH-MWCNT/5.6% PG5000 (B), 0.5/0.2 COOH-MWCNT/5.6% PG5000 (C) and 1.0/0.5 COOH-MWCNT/PG5000 (D).

Figure 6.32 depicts SEM images of the epoxy covered Dolly after mechanical testing of a SST-epoxy joint, coupled by a standard APS and CNT layer from a 1.0/0.4 COOH-MWCNT/5.6% PG5000 solution. Because of the removal of most of the nanotubes from the steel surface during mechanical testing, the epoxy layer remaining on the Dolly is visualized. This again supports the idea of the nanotube disrupting the bridging behavior of the APS. Moreover, the CNTs remaining in the matrix after testing, indicates that their tight enclosure in the epoxy matrix overcomes their interaction with the APS coated substrate.

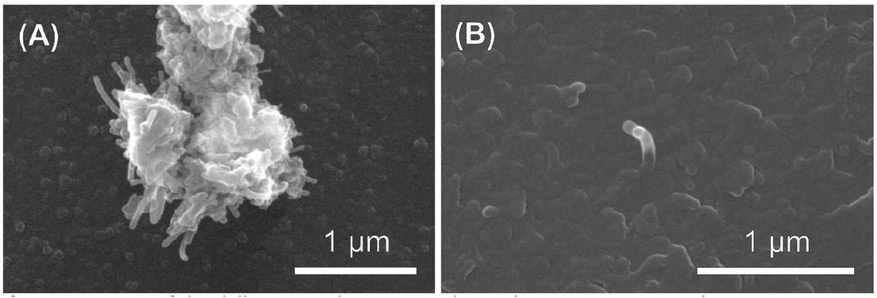

Figure 6.32: SEM image of a Dolly sample after mechanical testing of sample CNT B from Figure 6.31.

6.3 Conclusion

In order to create a gradient interphase between the polymer matrix and the steel substrate, carbon nanotubes can be deposited from an aqueous solution. To do so, first a new trityl end-group functionalized hyperbranched polymer was developed. This results in a highly efficient functionalized polyglycerol surfactant, requiring only 1 mg of surfactant to disperse as much as 2.85 mg of pristine MWCNTs. The hyperbranched core takes into account water solubility and has charge transfer interactions with the nanotubes, whereas the trityl end-groups interact with the nanotube by π-π stacking. A higher core molar mass results in an increased steric hindrance and thus efficiency, although it also induces a faster onset of solubility issues upon an increase of the degree of functionalization.

Despite the possibility to use the so-obtained solutions for multiple purposes, the influence of slight changes to the system are studied keeping in mind the goal of deposition at the interface. Acid-functionalization of nanotubes increases efficiency, as it is expected to increase interaction with both the matrix and the substrate. Also the addition of (a small amount of) ethanol leads to a higher efficiency, probably due to solubility reasons. Hyperbranched polylysine based surfactant, designed for a higher interaction with the polymer matrix, has a lower efficiency.

SEM based characterization reveals the influence of different deposition parameters. CNTs remaining on the substrate after deposition require the presence of an APS layer. Partial curing of the latter before CNT deposition increases the amount of tubes on the surface, probably to the higher amount of APS remaining after dipping in the CNT solution. Water rinsing after oven treatment of the APS-CNT layer does not visually influence the amount of CNTs, so the latter are assumed to interact with the substrate. Longer dipping times and higher concentrations as well as the absence of a rinsing procedure after dipping increase the CNT concentration on the substrate. Unfortunately mechanical testing points out that application of nanotubes at the interface deteriorates mechanical strength, although performance is still better than in the absence of any coating. A decrease in the coupling performance of APS, and possibly also steric constraints due to the nanotubes can explain this lower performance. An even lower CNT concentration may further increase the mechanical strength as this decreases the steric constraints. Nonetheless it must be kept in mind that a highly efficient surfactant was developed, useful for a lot of other applications, including matrix reinforcement by CNTs.

General Conclusion

This work focused on the mechanical improvement of polymer-steel hybrids. To do so two problems can and have to be faced. On one side a lack of adhesion at the interface deteriorates mechanical performance of polymer-steel joints, while on the other side a mismatch between the properties of both constituents has a negative influence on the hybrid properties. Silane coupling agents deal with the first issue, while introduction of interphasial adaptations mainly should handle the second one.

First of all different stainless steel substrate cleaning methods were evaluated (Chapter 3), from which ultrasonic cleaning appeared to be the most efficient. This treatment generated the highest hydrophilicity, mainly due to the removal of contaminants in combination with the appearance and generation of oxides and hydroxides. The latter enable reaction with the silane coupling agent in the next step. Also alkaline cleaning influenced the contact angles drastically, but appeared unsuitable for these substrates as it removes the oxide layer necessary for coupling.

As during silane coating small variations in solution, deposition or oven parameters (largely) influence the resulting coupling layer, every system should be characterized separately in the ideal case. To do so different parameters were varied systematically to find the optimized silane coupling layer, resulting in highest mechanical strength for SST 304-epoxy joints (Chapter 4). Layers resulting in highest adhesion strengths started from a 90/10 ($v\%/v\%$) H_2O/ethanol solution with 2 $v\%$ of 3-aminopropyltriethoxysilane (APS), used after minimum 22 min of stirring. This time ensures maximum hydrolysis. Despite a low degree of self-condensation, solutions were used at most 4 h after preparation, to ensure optimal reproducibility of all results. The ethanol improves spreading of the solution on the substrate although it decreases hydrolysis kinetics. Solutions with a lower silane concentration cause incomplete substrate coverage and less anchoring to both the substrate and the matrix, while higher silane concentrations increase self-condensation kinetics and silane adsorption in the next step. Moreover the latter cause the appearance of APS patches after deposition, being the weak point in the resulting hybrid.

Investigation of the deposition step, consisting of a dipping and rinsing procedure, resulted in optimal performance after 30 s of dipping followed by 60 s of ethanol rinsing. During the deposition step the APS species adsorb on the substrate, either chemically or physically. Shorter dipping times cause insufficient adsorption and thus insufficient coupling opportunities. Longer dipping times induce the adsorption of thicker layers, even when a rinsing procedure is applied afterwards. These layers suffer from less ordering which decreases their adhesion performance. The rinsing step should remove the excess of physically bound species. However, it is seen that at short rinsing times not all of this excess species can be removed. Longer dipping times probably remove some of the stronger anchored species and deteriorate the ordering of the silane layer, again decreasing adhesion performance.

Finally the adsorbed silane layer has to be oven treated, in order to covalently link the APS to the substrate and increase crosslinking. Use of a vacuum improves mechanical properties of the silane layer, as it removes water and residues that may interfere with the polymer matrix or inhibit formation of the desired APS layer. The optimal temperature-time settings ensure a certain degree of self-condensation, but avoid over-crosslinking. An oven treatment under vacuum for 1.5 h at 70°C resulted in the highest adhesion performance.

Mechanical and tensiometric testing demonstrated that, as in the case of freshly cleaned samples, coated samples should be used as soon as possible after cleaning. This avoids contaminant adsorption, which has a detrimental effect on adhesion performance as it interrupts the matrix-silane interactions.

Thin, ordered, fully substrate covering APS layers provided best results when self-condensed to a certain degree. This optimization, resulted in strengths 4 times higher compared to the blanc joints, causing the epoxy matrix to be the weak point in the hybrid. Benchmarking with a commercial coupling agent revealed higher strengths for the optimized APS layer. Moreover, the optimized APS coating procedure can be successfully transferred to other polymer-steel systems, provided that the interaction between the polymer and the silane organofunctional group is suited. Exchanging the epoxy for a polyamide matrix and the plate-like for fibrous substrates still results in improved adhesion after coupling with APS.

Contrary to what was expected the addition of nanomodifications to the interphase, in addition to a silane coupling layer, failed in improving hybrid properties (Chapter 5). Combination of a GPS coupling layer (coated according to the optimized APS procedure) with hyperbranched polylysine aimed at a higher degree of anchoring points to the matrix, but lacks efficiency and decreases performance. Depending on the polylysine/silane ratio this may be due to a decrease in the amount of available anchoring points or an increase in steric constraints. Moreover, polylysine is very hygroscopic and resulting water uptake can deteriorate silane and matrix properties. SEM images show a very inhomogeneous coupling layer, containing quite some defects, in this way decreasing performance.

As disrupting the structure of the silane layer decreases the mechanical properties of the hybrid, nanomodifications were added on top of the APS. Addition of functionalized carbon nanotubes at the interphase to create a gradient, disrupted the bonding between the silane and the matrix, and deteriorated adhesion (Chapter 6). The tubes were deposited from an aqueous solution, starting with the development of a new trityl end-group functionalized hyperbranched surfactant. This resulted in a highly efficient functionalized polyglycerol surfactant, requiring only 1 mg of surfactant to disperse as much as 2.85 mg of pristine MWCNTs. The hyperbranched core takes care of the water solubility and charge transfer interactions with the nanotubes, whereas the trityl end-groups interact with the nanotubes by π-π stacking. A higher core molar mass resulted in increased steric hindrance and thus efficiency, although it also induced a faster onset of solubility issues upon an increase of the degree of functionalization.

Future work, focusing on further improvement of polymer-steel hybrids, can start from an optimized silane-modified adhesion, although the gradient concept still deserves some attention. However, also matrix modifications as such are an option to decrease the stiffness mismatch, despite the fact that this requires a higher amount of nano-modifier. Computational simulations of surfactant behavior in water or water/ethanol mixtures as a function of the degree of surfactant functionalization may provide extra support for the suggested interactions, and explain trends seen.

From an application point of view, the surfactants developed can be used for multiple applications using both acid and pristine nanotubes in aqueous solutions, being attractive because of their high efficiency and stability. Moreover these surfactants may enable the dispersion of CNT in polymeric matrices, thereby improving the mechanical properties of composites. Here the hydrophobic trityl moieties interact with the tube, while the hyperbranched part can interact with the (polar) polymer through hydrogen bonding or covalent reaction, making it act as a coupling agent. Change of the polyglycerol to a polylysine core may improve interaction with e.g. an epoxy matrix.

Also the hybridization of the fiber containing composites should be further investigated. Firstly characterization of the silane layer on the fibers has to confirm the complete transferability of the statements made in this work. Secondly further hybridization e.g. by introducing a second type of fibers in the matrix, can further improve the mechanical properties of the composite.

Bibliography

[1] G. Pan. Morphology and properties of anti-corrosion organosilane films. Master's thesis, University of Cincinnati, 2006.

[2] X.H. Gu, G. Xue, and B.C. Jiang. Effect of deposition conditions for gamma-aminopropyltriethoxy silane on adhesion between copper and epoxy resins. *Appl. Surf. Sci.*, 115(1):66–73, 1997.

[3] V.M. Garamus, T.V. Maksimova, H. Kautz, E. Barriau, H. Frey, U. Schlotterbeck, S. Mecking, and W. Richtering. Hyperbranched polymers: Structure of hyperbranched polyglycerol and amphiphilic poly(glycerol ester)s in dilute aqueous and nonaqueous solution. *Macromolecules*, 37(22):8394–8399, 2004.

[4] A. Baldan. Adhesively-bonded joints and repairs in metallic alloys, polymers and composite materials: Adhesives, adhesion theories and surface pretreatment. *J. Mater. Sci.*, 39(1):1–49, 2004.

[5] B.O. Bateup. Surface chemistry and adhesion. *Int. J. Adhes. Adhes.*, 1:233, 1981.

[6] M. Honkanen, M. Hoikkanen, M. Vippola, J. Vuorinen, and T. Lepisto. Metal-plastic adhesion in injection-molded hybrids. *J. Adhes. Sci. Technol.*, 23(13-14):1747–1761, 2009.

[7] L.H. Sharpe. Interphase in adhesion. *J. Adhes.*, 4(1):51–52, 1972.

[8] F. Awaja, M.l Gilbert, . Kelly, B. Fox, and P.J. Pigram. Adhesion of polymers. *Prog. Polym. Sci.*, 34(9):948–968, 2009.

[9] S.J. Shaw. Adhesives in demanding applications. *Polym. Int.l*, 41(2):193–207, 1996.

[10] D. E. Packham. Some contributions of surface analysis to the development of adhesion theories. *J. Adhes.*, 84(3):240–255, 2008.

[11] M.C.M. Vanloosdrecht, W. Norde, J. Lyklema, and A.J.B. Zehnder. Hydrophobic and electrostatic parameters in bacterial adhesion. *Aquat. Sci.*, 52(1):103–114, 1990.

[12] J.F. Watts, A. Rattana, and M.L. Abel. ToF-SIMS studies of the adsorption of epoxy resin molecules on organosilane-treated aluminium: adsorption kinetics and adsorption isotherms. *Int. J. Adhes. Adhes.*, 26:28–39, 2006.

[13] P. Puomi and H.M. Fagerholm. Characterization of hot-dip galvanized (HDG) steel treated with gamma-UPS, VS, and tetrasulfide. *J. Adhes. Sci. Technol.*, 15(5):509–533, 2001.

[14] M.N. Sathyanarayana and M. Yaseen. Role of promoters in improving adhesion of organic coatings to a substrate. *Prog. Org. Coat.*, 26(2-4):275–313, 1995.

[15] J.D. Venables. Adhesion and durability of metal polymer bonds. *J. Mater. Sci.*, 19(8):2431–2453, 1984.

[16] A.N. Rider, C.L. Olsson-Jacques, and D.R. Arnott. Influence of adherend surface preparation on bond durability. *Surf. Interface Anal.*, 27(12):1055–1063, 1999.

[17] V.E. Basin. Advances in understanding the adhesion between solid substrates and organic coatings. *Prog. Org. Coat.*, 12(3):213–250, 1984.

[18] T. Long. Designing adhesives using the polymer parameters: Structure property relationships. Adhesion Society, 2013.

[19] P. Jussila, K. Lahtonen, M. Lampimaki, M. Hirsimaki, and M. Valden. Influence of minor alloying elements on the initial stages of oxidation of austenitic stainless steel materials. *Surf. Interface Anal.*, 40(8):1149–1156, 2008.

[20] P. Jussila, H. Ali-Loytty, K. Lahtonen, M. Hirsimaki, and M. Vaden. Effect of surface hydroxyl concentration on the bonding and morphology of aminopropylsilane thin films on austenitic stainless steel. *Surf. Interface Anal.*, 42(3):157–164, 2010.

[21] P. Karjalaine and S. Hertzman. In *Proceedings of the 6th European stainless steel conference*, 2008.

[22] M. Honkanen, M. Vippola, and T. Lepisto. Characterisation of stainless steel surfaces - modified in air at 350 C. *Surf. Eng.*, 27(5):325–331, 2011.

[23] C.O.A. Olsson and D. Landolt. Passive films on stainless steels - chemistry, structure and growth. *Electrochim. Acta*, 48(9):1093–1104, 2003.

[24] E. McCafferty and J.P. Wightman. Determination of the concentration of surface hydroxyl groups on metal oxide films by a quantitative XPS method. *Surf. Interface Anal.*, 26(8):549–564.

[25] J. Wielant, R. Posner, G. Grundmeier, and H. Terryn. Interface dipoles observed after adsorption of model compounds on iron oxide films: Effect of organic functionality and oxide surface chemistry. *J. Phys. Chem. C*, 112(33):12951–12957, 2008.

[26] F. Sinapi, A. Naji, J. Delhalle, and Z. Mekhalif. Assessment by XPS and electrochemical techniques of two molecular organosilane films prepared on stainless steel surfaces. *Surf. Interface Anal.*, 36(11):1484–1490, 2004.

[27] R.A. Hayes, G.W. Watson, and D.J. Willock. Simulation of the structure of organosilane film coatings. *Mol. Simul.*, 32(12-13):1095–1101, 2006.

[28] J. Cognard. Some recent progress in adhesion technology and science. *C. R. Chim.*, 9(1):13–24, 2006.

[29] J. Chung. Nanoscale characterization of epoxy interphase on copper microstructures. Master's thesis, Bundesanstalt fur Materialforschung and -prufung, Prozesswissenschaften der Technischen Universitat Berlin, 2006.

[30] A.M. Ikaev, P.G. Mingalyov, and G.V. Lisichkin. Chemical modification of iron oxide surface with organosilicon and organophosphorous compounds. *Colloid J.*, 69(6):741–746, 2007.

[31] P.R. Underhill, G. Goring, and D.L. DuQuesnay. A study of the curing of 3-glycidoxypropyltrimethoxy silane films on aluminum. *Int. J. Adhes. Adhes.*, 18(5):313–317, 1998.

[32] T. Sinmazcelik, E. Avcu, M.O. Bora, and O. Coban. A review: Fibre metal laminates, background, bonding types and applied test methods. *Mater. Des.*, 32(7):3671–3685, 2011.

[33] V. Subramanian and W.J. van Ooij. Silane based metal pretreatments as alternatives to chromating. *Surf. Eng.*, 15(2):168–172, 1999.

[34] S.X. Zheng and J.H. Li. Inorganic-organic sol gel hybrid coatings for corrosion protection of metals. *J. Sol-Gel Sci. Technol.*, 54(2):174–187, 2010.

[35] A. Franquet, H. Terryn, and J. Vereecken. Study of the effect of different aluminium surface pretreatments on the deposition of thin non-functional silane coatings. *Surf. Interface Anal.*, 36(8):681–684, 2004.

[36] S. Maeda. Surface chemistry of galvanized steel sheets relevant to adhesion performance. *Prog. Org. Coat.*, 28(4):227–238, 1996.

[37] M. Grujicic, V. Sellappan, M. A. Omar, N. Seyr, A. Obieglo, M. Erdmann, and J. Holzleitner. An overview of the polymer-to-metal direct-adhesion hybrid technologies for load-bearing automotive components. *J. Mater. Process. Technol.*, 197(1-3):363–373, 2008.

[38] S.Y. Park, W.J. Choi, H.S. Choi, H. Kwon, and S.H. Kim. Recent trends in surface treatment technologies for airframe adhesive bonding processing: A review (1995-2008). *J. Adhes.*, 86(2):192–221, 2010.

[39] J. Liu, M.K. Chaudhury, D.H. Berry, J.E. Seebergh, J.H. Osborne, and K.Y. Blohowiak. Fracture behavior of an epoxy/aluminum interface reinforced by sol-gel coatings. *J. Adhes. Sci. Technol.*, 20:277–305, 2006.

[40] R.G. Dillingham and B.R. Oakley. Surface energy and adhesion in composite-composite adhesive bonds. *J. Adhes.*, 82(4):407–426, 2006.

[41] Xie, Y. and Hill, C.A.S. and Zefang, X. and Militz, H. and Mai, C. Silane coupling agents used for natural fiber/polymer composites: A review. *Composites Part A*, 41:806–19, 2010.

[42] M. Honkanen, M. Hoikkanen, M. Vippola, J. Vuorinen, T. Lepisto, P. Jussila, H. Ali-Loytty, M. Lampimaki, and M. Valden. Characterization of silane layers on modified stainless steel surfaces and related stainless steel-plastic hybrids. *Appl. Surf. Sci.*, 257(22):9335–9346, 2011.

[43] C. Ochoa-Putman and U.K. Vaidya. Mechanisms of interfacial adhesion in metal-polymer composites - Effect of chemical treatment. *Compos. Pt. A-Appl. Sci. Manuf.*, 42(8):906–915, 2011.

[44] M.M.D. Ramos and J.P.P. Almeida. Atomistic modelling of interfacial bonding at metal/polymer interface. *J. Mater. Process. Technol.*, 93:147–150, 1999.

[45] .F Yang and R. Pitchumani. Effects of interphase formation on the modulus and stress concentration factor of fiber-reinforced thermosetting-matrix composites. *Compos. Sci. Technol.*, 64(10-11):1437–1452, 2004.

[46] J. Jancar. Review of the role of the interphase in the control of composite performance on micro- and nano-length scales. *J. Mater. Sci.*, 43(20):6747–6757, 2008.

[47] E.P. Plueddemann. *Silane coupling agents*. Springer, 1982.

[48] F. de Buyl and A. Kretschmer. Understanding hydrolysis and condensation kinetics of gamma-glycidoxypropyltrimethoxysilane. *J. Adhes.*, 84(2):125–142, 2008.

[49] L. Yang, J. Feng, W. Zhang, and J. Qu. Experimental and computational study on hydrolysis and condensation kinetics of gamma-glycidoxypropyltrimethoxysilane. *Appl. Surf. Sci.*, 257:990–6, 2010.

[50] F. Beari, M. Brand, P. Jenkner, R. Lehnert, H.J. Metternich, J. Monkiewicz, and H.W. Siesler. Organofunctional alkoxysilanes in dilute aqueous solution: new accounts on the dynamic structural mutability. *J. Organomet. Chem.*, 625(2):208–216, 2001.

[51] M.C.B. Salon, M. Abdelmouleh, S. Boufi, M.N. Belgacem, and A. Gandini. Silane adsorption onto cellulose fibers: Hydrolysis and condensation reactions. *J. Colloid Interface Sci.*, 289(1):249–261, 2005.

[52] Li A.J. and Wang X.M. Low carbon steel surface pretreated by silane coupling agents for preparing PE coatings. In *Multi-functional Materials and Structures II Pts 1 and 2*, volume 79-82 of *Advanced Materials Research*, pages 643–646, 2009.

[53] A. Najari, P. Lang, P. C. Lacaze, and D. Mauer. A new organofunctional methoxysilane bilayer system for promoting adhesion of epoxidized rubber to zinc Part 1: Optimization of practical adhesion. *Prog. Org. Coat.*, 64(4):392–404, 2009.

[54] S.A. Torry, A. Campbell, A. Cunliffe, and D.A. Tod. Kinetic analysis of organosilane hydrolysis and condensation. *Int. J. Adhes. Adhes.*, 26(1-2, SI):40–49, 2006.

[55] S. Flink, F. van Veggel, and D.N. Reinhoudt. Functionalization of self-assembled monolayers on glass and oxidized silicon wafers by surface reactions. *J. Phys. Org. Chem.*, 14(7):407–415, 2001.

[56] D. Blaudez, M. Bonnier, B. Desbat, and F. Rondelez. Two-dimensional polymerization in Langmuir films: A PM-IRRAS study of octadecyltrimethoxysilane monolayers. *Langmuir*, 18(24):9158–9163, 2002.

[57] W.J. van Ooij, D.Q. Zhu, G. Prasad, S. Jayaseelan, Y. Fu, and N. Teredesai. Silane based chromate replacements for corrosion control, paint adhesion, and rubber bonding. *Surf. Eng.*, 16(5):386–396, 2000.

[58] M.L. Abel, J.F. Watts, and R.P. Digby. The influence of process parameters on the interfacial chemistry of gamma-GPS on aluminium: A review. *J. Adhes.*, 80(4):291–312, 2004.

[59] R. Pena-Alonso, F. Rubio, J. Rubio, and J. L. Oteo. Study of the hydrolysis and condensation of gamma-aminopropyltriethoxysilane by FT-IR spectroscopy. *J. Mater. Sci.*, 42(2):595–603, 2007.

[60] J.F. Watts and J.E. Castle. The determination of adsorption isotherms by XPS and ToF-SIMS: their role in adhesion science. *Int. J. Adhes. Adhes.*, 19(6):435–443, 1999.

[61] W.S. Kim and J.J. Lee. Adhesion strength and fatigue life improvement of co-cured composite/metal lap joints by silane-based interphase formation. *J. Adhes. Sci. Technol.*, 21(2):125–140, 2007.

[62] M. Tanoglu, S.H. McKnight, G.R. Palmese, and J.W. Gillespie. Use of silane coupling agents to enhance the performance of adhesively bonded alumina to resin hybrid composites. *Int. J. Adhes. Adhes.*, 18(6):431–434, 1998.

[63] W.J. van Ooij, D. Zhu, M. Stacy, A. Seth, T. Mugada, J. Gandhi, and P. Puomi. Corrosion protection properties of organofunctional silanes - an overview. *Tsinghua Science and Technology*, 10:639–64, 2005.

[64] N.A. Smith, G.G. Antoun, A.B. Ellis, and W.C. Crone. Improved adhesion between nickel-titanium shape memory alloy and a polymer matrix via silane coupling agents. *Compos. Pt. A-Appl. Sci. Manuf.*, 35(11):1307–1312, 2004.

[65] M. Mohseni, M. Mirabedini, M. Hashemi, and G. E. Thompson. Adhesion performance of an epoxy clear coat on aluminum alloy in the presence of vinyl and amino-silane primers. *Prog. Org. Coat.*, 57(4):307–313, 2006.

[66] M.L. Jenkins, R.H. Dauskardt, and J.C. Bravman. Important factors for silane adhesion promoter efficacy: surface coverage, functionality and chain length. *J. Adhes. Sci. Technol.*, 18(13):1497–1516, 2004.

[67] M.K. Harun, S.B. Lyon, and J. Marsh. A surface analytical study of functionalised mild steel for adhesion promotion of organic coatings. *Prog. Org. Coat.*, 46(1):21–27, 2003.

[68] K.C. Vrancken, K. Possemiers, P. Vandervoort, and E.F. Vansant. Surface modification of silica-gels with aminoorganosilanes. *Colloid Surf. A-Physicochem. Eng. Asp.*, 98(3):235–241, 1995.

[69] K. Wen, R. Maoz, H. Cohen, J. Sagiv, A. Gibaud, A. Desert, and B.M. Ocko. Postassembly chemical modification of a highly ordered organosilane multilayer: new insights into the structure, bonding, and dynamics of self-assembling silane monolayers. *ACS Nano*, 2:579, 2008.

[70] T.J. Horr and P.S. Arora. Determination of the acid-base properties for 3-amino, 3-chloro and 3-mercaptopropyltrimethoxysilane coatings on silica surfaces by XPS. *Colloid Surf. A-Physicochem. Eng. Asp.*, 126(2-3):113–121, 1997.

[71] E. Asenath-Smith and W. Chen. How to prevent the loss of surface functionality derived from aminosilanes. *Langmuir*, 24(21):12405–12409, 2008.

[72] M.L. Abel, A. Rattana, and J.F. Watts. Interaction of epoxy analogue molecules with organosilane-treated aluminum: A study by XPS and ToF-SIMS. *Langmuir*, 16(16):6510–6518, 2000.

[73] B.B. Johnsen, K. Olafsen, and A. Stori. Reflection-absorption FT-IR studies of the specific interaction of amines and an epoxy adhesive with GPS treated aluminium surfaces. *Int. J. Adhes. Adhes.*, 23(2):155–163, 2003.

[74] J. C. Suarez, S. Miguel, P. Pinilla, and F. Lopez. Molecular dynamics simulation of polymer-metal bonds. *J. Adhes. Sci. Technol.*, 22(13):1387–1400, 2008.

[75] M.L. Abel, R. Joannic, M. Fayos, E. Lafontaine, S.J. Shaw, and J.F. Watts. Effect of solvent nature on the interaction of gamma-glycidoxy propyl trimethoxy silane on oxidised aluminium surface: A study by solution chemistry and surface analysis. *Int. J. Adhes. Adhes.*, 26(1-2):16–27, 2006.

[76] S.K. Jayaseelan and W.J. Van Ooij. Rubber-to-metal bonding by silanes. *J. Adhes. Sci. Technol.*, 15(8):967–991, 2001.

[77] R.E. Jensen, G.R. Palmese, and S.H. McKnight. Viscoelastic properties of alkoxy silane-epoxy interpenetrating networks. *Int. J. Adhes. Adhes.*, 26(1-2):103–115, 2006.

[78] G.L. Witucki. A silane primer - chemistry and applications of alkoxy silanes. *J. Coat. Technol.*, 65(822):57–60, 1993.

[79] M. Hughes, J. Carpenter, and C. Hill. Deformation and fracture behaviour of flax fibre reinforced thermosetting polymer matrix composites. *J. Mater. Sci.*, 42(7):2499–2511, 2007.

[80] J. C. Del Real, M. Cano de Santayana, J. Abenojar, M. Pantoja, and M. A. Martinez. Influence of silanisation parameters with gamma-methacryloxypropyltrimethoxysilane on durability of aluminium/acrylic adhesive joints. *J. Adhes. Sci. Technol.*, 22(13):1461–1475, 2008.

[81] M.C.B. Salon and M.N. Belgacem. Competition between hydrolysis and condensation reactions of trialkoxysilanes, as a function of the amount of water and the nature of the organic group. *Colloid Surf. A-Physicochem. Eng. Asp.*, 366(1-3):147–154, 2010.

[82] A. F. Scott, J. E. Gray-Munro, and J. L. Shepherd. Influence of coating bath chemistry on the deposition of 3-mercaptopropyl trimethoxysilane films deposited on magnesium alloy. *J. Colloid Interface Sci.*, 343(2):474–483, 2010.

[83] F.D. Osterholtz and E.R. Pohl. Kinetics of the hydrolysis and condensation of organofunctional akoxysilanes - a review. *J. Adhes. Sci. Technol.*, 6(1):127–149, 1992.

[84] V. Roche, F. X. Perrin, D. Gigmes, F. Vacandio, F. Ziarelli, and D. Bertin. Tracking the fate of gamma-aminopropyltriethoxysilane from the sol state to the dried film state. *Thin Solid Films*, 518(14):3640–3645, 2010.

[85] P. Puomi and H.M. Fagerholm. Characterization of hot-dip galvanized (HDG) steel treated with bis-1,2-(triethoxysilyl)ethane and gamma-aminopropyltriethoxysilane. *J. Adhes. Sci. Technol.*, 15(8):869–888, 2001.

[86] E.T. Vandenberg, L. Bertilsson, B. Liederberg, K. Uvdal, R. Erlandsson, H. Elwing, and I. Lundstrom. Structure of 3-aminopropyl triethoxy silane on silicon-oxide. *J. Colloid Interface Sci.*, 147(1):103–118, 1991.

[87] M.L. Abel, J.F. Watts, and P.P. Digby. The adsorption of alkoxysilanes on oxidised aluminium substrates. *Int. J. Adhes. Adhes.*, 18(3):179–192, 1998.

[88] L. Houssiau and P. Bertrand. TOF-SIMS study of organosilane adsorption on model hydroxyl terminated surfaces. *Appl. Surf. Sci.*, 203:580–585, 2003.

[89] M.L. Abel and J.F. Watts. Influence of temperature on aminosilane thin films deposited on aluminium substrates: A study by surface analysis. *J. Adhes.*, 84(10):849–873, 2008.

[90] French, S.A. and Sokol, A.A. and Catlow, C.R.A. and Kornherr, A. and Nauer, G.E. and Zifferer, G. A computational investigation of the different intermediates during organoalkoxysilane hydrolysis. *J. Phys. Chem. B*, 110(48):24311–24317, 2006.

[91] W.J. van Ooij, D. Zhu, V. Palanivel, J.A. Lamar, and M. Stacy. Potential of silanes for chromate replacement in metal finishing industries. *Silicon Chemistry*, 2006.

[92] A.V. Cunliffe, S. Evans, D.A. Tod, S.A. Torry, and P. Wylie. Optimum preparation of silanes for steel pre-treatment. 21(4):287–296, 2001.

[93] M.W. Daniels, J. Sefcik, L.F. Francis, and A.V. McCormick. Reactions of a trifunctional silane coupling agent in the presence of colloidal silica sets in polar media. *J. Colloid Interface Sci.*, 219(2):351–356, 1999.

[94] T.M. Alam, R.A. Assink, and D.A. Loy. Hydrolysis and esterification in organically modified alkoxysilanes: A Si-29 NMR investigation of methyltrimethoxysilane. *Chem. Mat.*, 8(9):2366–2374, 1996.

[95] Y. Castro, A. Duran, J. J. Damborenea, and A. Conde. Electrochemical behaviour of silica basic hybrid coatings deposited on stainless steel by dipping and EPD. *Electrochim. Acta*, 53(20):6008–6017, 2008.

[96] F. Deflorian, S. Rossi, L. Fedrizzi, and M. Fedel. Integrated electrochemical approach for the investigation of silane pre-treatments for painting copper. *Prog. Org. Coat.*, 63(3, SI):338–344, 2008.

[97] A. Franquet, C. Le Pen, H. Terryn, and J. Vereecken. Effect of bath concentration and curing time on the structure of nonfunctional thin organosilane layers on aluminium. *Electrochim. Acta*, 48(9):1245–1255, 2003.

[98] G. Li, X. Wang, A. Li, W. Wang, and L. Zheng. Fabrication and adhesive properties of thin organosilane films coated on low carbon steel substrates. *Surf. Coat. Technol.*, 201(24):9571–9578, 2007.

[99] M.L. Abel, R.D. Allington, R.P. Digby, N. Porritt, S.J. Shaw, and J.F. Watts. Understanding the relationship between silane application conditions, bond durability and locus of failure. *Int. J. Adhes. Adhes.*, 26(1-2):2–15, 2006.

[100] M.F. Tsai, Y.D. Lee, and K.N. Chen. NMR spectroscopic studies of dimethyldiethoxy silane hydrolysis and polysiloxane conversion. *J. Appl. Polym. Sci.*, 86(2):468–477, 2002.

[101] D.J. Oostendorp, G.L. Bertrand, and J.O. Stoffer. Kinetics and mechanism of the hydrolysis and alcoholysis of alkoxysilanes. *J. Adhes. Sci. Technol.*, 6(1):171–191, 1992.

[102] J.S. Gandhi, S. Singh, W.J. Van Ooij, and P. Puomi. Evidence for formation of metallo-siloxane bonds by comparison of dip-coated and electrodeposited silane films. *J. Adhes. Sci. Technol.*, 20(15):1741–1768, 2006.

[103] P.R. Underhill, G. Goring, and D.L. DuQuesnay. The effect of humidity on the curing of 3-glycidoxypropyltrimethoxy silane. *Int. J. Adhes. Adhes.*, 20(3):195–199, 2000.

[104] Z. Demjen, B. Pukanszky, E. Foldes, and J. Nagy. Interaction of silane coupling agents with $CaCO_3$. *J. Colloid Interface Sci.*, 190(2):427–436, 1997.

[105] C. Le Pen, B. Vuillemin, S. Van Gils, H. Terryn, and R. Oltra. In-situ characterisation of organosilane film formation on aluminium alloys by electrochemical quartz crystal microbalance and in-situ ellipsometry. *Thin Solid Films*, 483(1-2):66–73, 2005.

[106] J.S. Quinton and P.C. Dastoor. Conformational dynamics of gamma-APS on the iron oxide surface: an adsorption kinetic study using XPS and ToF-SIMS. *Surf. Interface Anal.*, 30(1):21–24, 2000.

[107] N.G. Cave and Kinloch A.J. The effect of the silane deposition donditions on the durability of aluminum joints pretreated using 3-aminopropyltrimethoxysilane . *J. Adhes.*, 34(1-4):175–187, 1991.

[108] J. Song and W.J. Van Ooij. Bonding and corrosion protection mechanisms of gamma-APS and BTSE silane films on aluminum substrates. *J. Adhes. Sci. Technol.*, 17(16):2191–2221, 2003.

[109] X. Wang, G.i Li, A.u Li, and Z. Zhang. Influence of thermal curing on the fabrication and properties of thin organosilane films coated on low carbon steel substrates. *J. Mater. Process. Technol.*, 186(1-3):259–264, 2007.

[110] J. Bouchet, G. M. Pax, Y. Leterrier, V. Michaud, and J. A. E. Manson. Formation of aminosilane-oxide interphases. *Compos. Interfaces*, 13(7):573–588, 2006.

[111] I. De Graeve, J. Vereecken, A. Franquet, T. Van Schaftinghen, and H. Terryn. Silane coating of metal substrates: Complementary use of electrochemical, optical and thermal analysis for the evaluation of film properties. *Prog. Org. Coat.*, 59(3):224–229, 2007.

[112] D. Zhu. *Corrosion protection of metals by silane surface treatment.* PhD thesis, University of Cincinnati, Ohio, US, 2005.

[113] C. Le Pen and J. Vereecken. Effect of curing on the corrosion protective properties of thin organosilane films on aluminium. *J. Appl. Electrochem.*, 35(12):1303–1309, 2005.

[114] B. Riegel, S. Blittersdorf, W. Kiefer, S. Hofacker, M. Muller, and G/ Schottner. Kinetic investigations of hydrolysis and condensation of the glycidoxypropyltrimethoxysilane/aminopropyltriethoxy-silane system by means of FT-Raman spectroscopy I. *J. Non-Cryst. Solids*, 226(1-2):76–84, 1998.

[115] B. Chico, J. C. Galvan, D. de la Fuente, and M. Morcillo. Electrochemical impedance spectroscopy study of the effect of curing time on the early barrier properties of silane systems applied on steel substrates. *Prog. Org. Coat.*, 60(1):45–53, 2007.

[116] T. Gunji, Y. Makabe, N. Takamura, and Y. Abe. Preparation and characterization of organic-inorganic hybrids and coating films from 3-methacryloxypropylpolysilsesquioxane. *Appl. Organomet. Chem.*, 15(8):683–692, 2001.

[117] S.H. Lee. Elucidation of the structure of silane coupling agent films formed on metal surface. Master's thesis, Massachusetts Institute of Technology, 1979.

[118] A. Kuznetsova, E.A. Wovchko, and J.T. Yates. FTIR study of the adsorption and thermal behavior of vinyltriethoxysilane chemisorbed on gamma-Al2O3. *Langmuir*, 13(20):5322–5328, 1997.

[119] Gelest. Silane coupling agents: Connecting across boundaries. http://www.gelest.com/goods/pdf/couplingagents.pdf, 2014. [Online; accessed 29-July-2014].

[120] T. Van Schaftinghen, C. Le Pen, H. Terryn, and F. Horzenberger. Investigation of the barrier properties of silanes on cold rolled steel. *Electrochim. Acta*, 49(17-18):2997–3004, 2004.

[121] A. Franquet, H. Terryn, P. Bertrand, and J. Vereecken. Use of optical methods to characterize thin silane films coated on aluminium. *Surf. Interface Anal.*, 34(1):25–29, 2002.

[122] A.N. Rider. Factors influencing the durability of epoxy adhesion to silane pretreated aluminium. *Int. J. Adhes. Adhes.*, 26(1-2):67–78, 2006.

[123] F. Deflorian, S. Rossi, and L. Fedrizzi. Silane pre-treatments on copper and aluminium. *Electrochim. Acta*, 51(27):6097–6103, 2006.

[124] C.M. Bertelsen and F.J. Boerio. Linking mechanical properties of silanes to their chemical structure: an analytical study of gamma-GPS solutions and films. *Prog. Org. Coat.*, 41(4):239–246, 2001.

[125] R.A. Gledhill, S.J. Shaw, and D.A. Tod. Durability of adhesive-bonded joints employing organosilane coupling agents. *Int. J. Adhes. Adhes.s*, 10(3):192–198, 1990.

[126] F.M. Francisca, V.A. Rinaldi, and J.C. Santamarina. Instability of hydrocarbon films over mineral surfaces: Microscale experimental studies. *J. Environ. Eng.*, 129(12):1120–1128, 2003.

[127] C.A. Fuentes Rojas. *Interfacial adhesion in natural and synthetic fibre composites: A physical-chemmical-mechanical approach.* PhD thesis, KU Leuven, Belgium, 2014.

[128] G. Barnes and I. Gentle. *Interfcial science: An introduction.* Oxford University Press, 2011.

[129] Nuttha Thongyai. Study of stainless steel surface cleanability. Master's thesis, King Mongkut's Institute of Technology North Bangkok, 2005.

[130] H.Y. Erbil. *Surface chemistry of solid and liquid interfaces.* Wiley-Blackwell, 2006.

[131] C. Della Volpe and S. Siboni. A 'conveyor belt' model for the dynamic contact angle. *Eur. J. Phys.*, 32(4):1019–1032, 2011.

[132] L. Gao and T.J. McCarthy. Wetting 101 °. *Langmuir*, 25(24):14105–14115, 2009.

[133] T. Young.

[134] A.W. Adamson. *Physical chemistry of surfaces*, volume 4. Wiley New York, 1990.

[135] J.D. Bernardin, I. Mudawar, C.B. Walsh, and E.I. Franses. Contact angle temperature dependence for water droplets on practical aluminum surfaces. *Int. J. Heat Mass Transf.*, 40(5):1017–1033, 1997.

[136] R.J. Good. Contact angle, wetting and adhesion - A critical review. *J. Adhes. Sci. Technol.*, 6(12):1269–1302, 1992.

[137] C. Della Volpe, D. Maniglio, S. Siboni, and M. Morra. An experimental procedure to obtain the equilibrium contact angle from the Wilhelmy method. *Oil Gas Sci. Technol.*, 56(1):9–22, 2001.

[138] K. Sefiane, L. Tadrist, and M. Douglas. Experimental study of evaporating water-ethanol mixture sessile drop: influence of concentration. *Int. J. Heat Mass Transf.*, 46(23):4527–4534, 2003.

[139] M. Strobel and C.S. Lyons. Thoughts on contact angles and wettability. In *2013 Annual Meeting Abstracts*, 2013.

[140] M. Strobel and C.S. Lyons. An essay on contact angle measurements. *Plasma Process. Polym.*, 8(1):8–13, 2011.

[141] L. Gao and T.J. McCarthy. Contact angle hysteresis explained. *Langmuir*, 22(14):6234–6237, 2006.

[142] C. Della Volpe, A. Penati, R. Peruzzi, S. Siboni, L. Toniolo, and C. Colombo. The combined effect of roughness and heterogeneity on contact angles: the case of polymer coating for stone protection. *J. Adhes. Sci. Technol.*, 14(2):273–299, 2000.

[143] L. Wang, J. Wei, and Z.i Su. Defects and topography: which one is more important for contact angle hysteresis?

[144] D.Y. Kwok and A.W. Neumann. Contact angle measurement and contact angle interpretation. *Adv. Colloid Interface Sci.*, 81(3):167–249, 1999.

[145] C. Della Volpe, D. Maniglio, M. Morra, and S. Siboni. The determination of a 'stable-equilibrium' contact angle on heterogeneous and rough surfaces. In *Colloids and Surfaces A (Physicochemical and Engineering Aspects)*, volume 206, pages 47–67. Elsevier, 2002.

[146] J. Long and P. Chen. On the role of energy barriers in determining contact angle hysteresis. *Adv. Colloid Interface Sci.*, 127(2):55–66, 2006.

[147] A.W. neumann and R.J. Good. Thermodynamics of contact angles. 1. Heterogeneous solid surfaces. *J. Colloid Interface Sci.*, 38(2):341, 1972.

[148] D.L. Schmidt, R.F. Brady, K. Lam, D.C. Schmidt, and M.K. Chaudhury. Contact angle hysteresis, adhesion, and marine biofouling. *Langmuir*, 20(7):2830–2836, 2004.

[149] J. D. Andrade. *Surface and interfacial aspects of biomedical polymers*, volume 1. Springer US, 1985.

[150] G. Dillingham, C. Frazier, and B. Oakly. What do contact angle measurements tell us about surface preparation? Adhesion Society, Annual Meeting of the Adhesion Society, 2013.

[151] J.P. Youngblood and T.J. McCarthy. Ultrahydrophobic polymer surfaces prepared by simultaneous ablation of polypropylene and sputtering of poly(tetrafluoroethylene) using radio frequency plasma. *Macromolecules*, 32(20):6800–6806, 1999.

[152] K. Stoev, .E Rame, and S. Garoff. Effects of inertia on the hydrodynamics near moving contact lines. *Phys. Fluids*, 11(11):3209–3216, 1999.

[153] F.M. Fowkes. Attractive forces at interfaces. *Ind. and Eng. Chem.*, 56(12):40, 1964.

[154] C.A. Ward and A.W. Neumann. Surface thermodynamics of a 2-component liquid-vapor ideal solid system. *J. Colloid Interface Sci.*, 49(2):286–290, 1974.

[155] A.W. Neumann, R.J. Good, C.J. Hope, and M. Sejpal. Equation-of-state approach to determine surface tensions of low-energy solids from contact angles. *J. Colloid Interface Sci.*, 49(2):291–304, 1974.

[156] D. Berthelot. Sur le melange des gaz. *Compt. Rendus*, 126:1857–1858, 1898.

[157] D.K. Owens and R.C. Wendt. Estimation of surface free energy of polymers. *J. Appl. Polym. Sci.*, 13(8):1741, 1969.

[158] C.J. Van Oss, M.K. Chaudhurry, and R.J. Good. Interfacial lifshitz-van der waals and polar interactions in macroscopic systems. *Chem. Rev.*, 6:927–941, 1988.

[159] B.Y. Wen, G. Wu, and J/ Yu. A flat polymeric gradient material: preparation, structure and property. *Polymer*, 45(10):3359–3365, 2004.

[160] S. Zhang, B. You, G. Gu, and L. Wu. A simple approach to fabricate morphological gradient on polymer surfaces. *Polymer*, 50(26):6235–6244, 2009.

[161] R.C. Zhuang, T. Burghardt, R. Plonka, J.W. Liu, and E. Maeder. Affecting glass fibre surfaces and composite properties by two stage sizing application. *Express Polym. Lett.*, 4(12):798–808, 2010.

[162] N.J. Lee, J. Jang, M. Park, and C.R. Choe. Characterization of functionally gradient epoxy/carbon fibre composite prepared under centrifugal force. *J. Mater. Sci.*, 32(8):2013–2020, 1997.

[163] E.P. Plueddemann and G.L. Stark. Catalytic and electrokinetic effects in bonding through silanes. *Mod. Plast.*, 51(3):74, 1974.

[164] L.M. Bronstein, A. Ivanovskaya, T. Mates, N. Holten-Andersen, and G.D. Stucky. Bioinspired gradient materials via blending of polymer electrolytes and applying electric forces. *J. Phys. Chem. B*, 113(3):647–655, 2009.

[165] M.T. Tilbrook, L. Rutgers, R J. Moon, and M. Hoffman. Fatigue crack propagation resistance in homogeneous and graded alumina-epoxy composites. *Int. J. Fatigue*, 29(1):158–167, 2007.

[166] L. Mei, X. He, Y. Li, Q. Peng, R. Wang, and J. Xu. Enhancement of composite-metal interfacial adhesion strength by dendrimer. *Surf. Interface Anal.*, 43(3):726–733, 2011.

[167] J. P. Matinlinna, L. V. J. Lassila, and P. K. Vallittu. The effect of a novel silane blend system on resin bond strength to silica-coated Ti substrate. *J. Dent.*, 34(7):436–443, 2006.

[168] T.L. Menz and T.M. Chapman. Synthesis and characterization of hyperbranched polylysine. *Abstr. Pap. Am. Chem. Soc.*, 226(2), 2003.

[169] H. Chen, O. Jacobs, W. Wu, G. Ruediger, and B. Schaedel. Effect of dispersion method on tribological properties of carbon nanotube reinforced epoxy resin composites. *Polym. Test.*, 26(3):351–360, 2007.

[170] S. Iijima. Helical microtubules of graphitic carbon. *Nature*, 354(6348):56–58, 1991.

[171] J.N. Coleman. Liquid-phase exfoliation of nanotubes and graphene. *Adv. Funct. Mater.*, 19(23):3680–3695, 2009.

[172] F.H. Gojny, M.H.G. Wichmann, B. Fiedler, and K. Schulte. Influence of different carbon nanotubes on the mechanical properties of epoxy matrix composites - A comparative study. *Compos. Sci. Technol.*, 65(15-16):2300–2313, 2005.

[173] F.H. Gojny, M.H.G. Wichmann, B. Fiedler, I.A. Kinloch, W. Bauhofer, A.H. Windle, and K. Schulte. Evaluation and identification of electrical and thermal conduction mechanisms in carbon nanotube/epoxy composites. *Polymer*, 47(6):2036–2045, 2006.

[174] T.X. Liu, I.Y. Phang, L. Shen, S.Y. Chow, and W.D. Zhang. Morphology and mechanical properties of multiwalled carbon nanotubes reinforced nylon-6 composites. *Macromolecules*, 37(19):7214–7222, 2004.

[175] C.T. White and T.N. Todorov. Carbon nanotubes as long ballistic conductors. *Nature*, 393(6682):240–242, 1998.

[176] J.N. Coleman, U. Khan, W.J. Blau, and Y.K. Gun'ko. Small but strong: A review of the mechanical properties of carbon nanotube-polymer composites. *Carbon*, 44(9):1624–1652, 2006.

[177] B. Safadi, R. Andrews, and E.A. Grulke. Multiwalled carbon nanotube polymer composites: Synthesis and characterization of thin films. *J. Appl. Polym. Sci.*, 84(14):2660–2669, 2002.

[178] M.L. Usrey and M.S. Strano. Adsorption of single walled carbon nanotubes onto silicon oxide surface gradients of 3-aminopropyltri(ethoxysilane) described by polymer Adsorption Theory. *Langmuir*, 25(17):9922–9930, 2009.

[179] J. Liu, M.J. Casavant, M. Cox, D.A. Walters, P. Boul, W. Lu, A.J. Rimberg, K.A. Smith, D.T. Colbert, and R.E. Smalley. Controlled deposition of individual single-walled carbon nanotubes on chemically functionalized templates. *Chem. Phys. Lett.*, 303(1-2):125–129, 1999.

[180] J.H. Rouse. Polymer-assisted dispersion of single-walled carbon nanotubes in alcohols and applicability toward carbon Nanotube/Sol-Gel composite formation. *Langmuir*, 21(3):1055–1061, 2005.

[181] V. Sa and K.G. Kornev. Analysis of stability of nanotube dispersions using surface tension isotherms.

[182] M. Bystrzejewski, A. Huczko, H. Lange, T. Gemming, B. Buechner, and M. H. Ruemmeli. Dispersion and diameter separation of multi-wall carbon nanotubes in aqueous solutions. *J. Colloid Interface Sci.*, 345(2):138–142, 2010.

[183] X. Xin, G. Xu, T. Zhao, Y. Zhu, X. Shi, H. Gong, and Z. Zhang. Dispersing carbon nanotubes in aqueous solutions by a starlike block copolymer. *J. Phys. Chem. C*, 112(42):16377–16384, 2008.

[184] J.L. Bahr, E.T. Mickelson, M.J. Bronikowski, R.E. Smalley, and J.M. Tour. Dissolution of small diameter single-wall carbon nanotubes in organic solvents? *Chem. Comm.*, (2):193–194, 2001.

[185] C.X. Liu and J.W. Choi. Improved dispersion of carbon nanotubes in polymers at high concentrations.

[186] C.J. Brinker and G.W. Schere. *Sol-gel science: The physics and chemistry of sol-gel processing.* Academic Press: New York, 1990.

[187] S.W. Kim, T. Kim, Y.S. Kim, H.S. Choi, H.J. Lim, S.J. Yang, and C.R. Park. Surface modifications for the effective dispersion of carbon nanotubes in solvents and polymers. *Carbon*, 50(1):3–33, 2012.

[188] A. Skender, A. Hadj-Ziane-Zafour, and E. Flahaut. Chemical functionalization of Xanthan gum for the dispersion of double-walled carbon nanotubes in water. *Carbon*, 62:149–156, 2013.

[189] L. Vaisman, H.D. Wagner, and G. Marom. The role of surfactants in dispersion of carbon nanotubes. *Adv. Colloid Interface Sci.*, 128:37–46, 2006.

[190] J. Yu, N. Grossiord, C.E. Koning, and J. Loos. Controlling the dispersion of multi-wall carbon nanotubes in aqueous surfactant solution. *Carbon*, 45(3):618–623, 2007.

[191] A.J. Blanch, C.E. Lenehan, and J.S. Quinton. Optimizing surfactant concentrations for dispersion of single-walled carbon nanotubes in aqueous solution. *J. Phys. Chem. B*, 114(30):9805–9811, 2010.

[192] H. Wang, W. Zhou, D.L. Ho, K.I. Winey, J.E. Fischer, C.J. Glinka, and E.K. Hobbie. Dispersing single-walled carbon nanotubes with surfactants: A small angle neutron scattering study. *Nano Lett.*, 4(9):1789–1793, 2004.

[193] B. Vigolo, A. Penicaud, C. Coulon, C. Sauder, R. Pailler, C. Journet, P. Bernier, and P. Poulin. Macroscopic fibers and ribbons of oriented carbon nanotubes. *Science*, 290(5495):1331–1334, 2000.

[194] L.Q. Jiang, L. Gao, and J. Sun. Production of aqueous colloidal dispersions of carbon nanotubes. *J. Colloid Interface Sci.*, 260(1):89–94, 2003.

[195] Z. Shen and G.T. Wang. *Colloids and surfaces chemistry.* Chemical Industry Press, Peking, 1991.

[196] D. Chattopadhyay, L. Galeska, and F. Papadimitrakopoulos. A route for bulk separation of semiconducting from metallic single-wall carbon nanotubes. *J. Am. Chem. Soc.*, 125(11):3370–3375, 2003.

[197] J.C. Lewenstein, T.P. Burgin, A. Ribayrol, L.A. Nagahara, and R.K. Tsui. High-yield selective placement of carbon nanotubes on pre-patterned electrodes. *Nano Lett.*, 2(5):443–446, 2002.

[198] S. Chen, Y. Jiang, Z. Wang, X. Zhang, L. Dai, and M. Smet. Light-controlled single-walled carbon nanotube dispersions in aqueous solution. *Langmuir*, 24(17):9233–9236, 2008.

[199] Y. Ding, S. Chen, H. Xu, Z. Wang, X. Zhang, T..H. Ngo, and M. Smet. Reversible dispersion of single-walled carbon nanotubes based on a CO2-responsive dispersant. *Langmuir*, 26(22):16667–16671, 2010.

[200] W. Zhong and J.P. Claverie. Probing the carbon nanotube-surfactant interaction for the preparation of composites. *Carbon*, 51:72–84, 2013.

[201] E. Camponeschi, B. Florkowski, R. Vance, G. Garrett, H. Garmestani, and R. Tannenbaum. Uniform directional alignment of single-walled carbon nanotubes in. viscous polymer flow. *Langmuir*, 22(4):1858–1862, 2006.

[202] O. Matarredona, H. Rhoads, Z.R.R Li, J.H. Harwell, L. Balzano, and D.E. Resasco. Dispersion of single-walled carbon nanotubes in aqueous solutions of the anionic surfactant NaDDBS. *J. Phys. Chem. B*, 107(48):13357–13367, 2003.

[203] K.A.S. Fernando, Y. Lin, W. Wang, S. Kumar, B. Zhou, S.Y. Xie, L.T. Cureton, and Y.P. Sun. Diminished band-gap transitions of single-walled carbon nanotubes in complexation with aromatic molecules. *J. Am. Chem. Soc.*, 126(33):10234–10235, 2004.

[204] J. Zhang, J.K. Lee, Y. Wu, and R.W. Murray. Photoluminescence and electronic interaction of anthracene derivatives adsorbed on sidewalls of single-walled carbon nanotubes. *Nano Lett.*, 3(3):403–407, 2003.

[205] V.C. Moore, M.S. Strano, E.H. Haroz, R.H. Hauge, R.E. Smalley, J. Schmidt, and Y/ Talmon. Individually suspended single-walled carbon nanotubes in various surfactants. *Nano Lett.*, 3(10):1379–1382, 2003.

[206] X. Xin, G. Xu, Z. Zhang, Y. Chen, and F. Wang. Aggregation behavior of star-like PEO-PPO-PEO block copolymer in aqueous solution. *Eur. Polym. J., Journal-ISO = Eur. Polym. J.,*, 43(7):3106–3111, 2007.

[207] Z.Q. Zhang, G.Y. Xu, W. Fang, S.L. Dong, and Y.J. Chen. Demulsification by amphiphilic dendrimer copolymers. *J. Colloid Interface Sci.*, 282(1):1–4, 2005.

[208] Y. Dror, W. Pyckhout-Hintzen, and Y. Cohen. Conformation of polymers dispersing single-walled carbon nanotubes in water: A small-angle neutron scattering study. *Macromolecules*, 38(18):7828–7836, 2005.

[209] J.T. Sun, C.Y. Hong, and C.Y. Pan. Surface modification of carbon nanotubes with dendrimers or hyperbranched polymers. *Polym. Chem.*, 2(5):998–1007, 2011.

[210] M F. Montemor and M.G.S. Ferreira. Analytical characterisation and corrosion behaviour of bis-aminosilane coatings modified with carbon nanotubes activated with rare-earth salts applied on AZ31 Magnesium alloy. *Surf. Coat. Technol.*, 202(19):4766–4774, 2008.

[211] M.G. Callens. *Development of ductile stainless steel fibre composites*. PhD thesis, KU Leuven, Belgium, 2014.

[212] O. Topel, B.A. Cakir, L. Budama, and N. Hoda. Determination of critical micelle concentration of polybutadiene-block-poly(ethyleneoxide) diblock copolymer by fluorescence spectroscopy and dynamic light scattering. *J. Mol. Liq.*, 177:40–43, 2013.

[213] R.L. Crane and G. Dillingham. Composite bond inspection. *J. Mater. Sci.*, 43(20):6682–6694, 2008.

[214] J. Dillard. Interfacial energy and adhesion. In *2013 Annual Meeting Short Course*, 2013.

[215] L. Boulange-Petermann and B. Gabet, .and Baroux. Relation between the cleanability of bare or polysiloxane-coated stainless steels and their water contact angle hysteresis. *J. Adhes. Sci. Technol.*, 20(13):1463–1474, 2006.

[216] C. Vittoz, M. Mantel, and J.C. Joud. Wettability of metallic oxides - Application to stainless steel acid-base properties. *J. Adhes.*, 67(1-4):347–358, 1998.

[217] D. Susac, X. Sun, and K.A.R. Mitchell. Adsorption of BTSE and gamma-APS organosilanes on different microstructural regions of 2024-T3 aluminum alloy. *Appl. Surf. Sci.*, 207(1-4):40–50, 2003.

[218] C.M. Stafford, A.Y. Fadeev, T.P. Russell, and T.J. McCarthy. Controlled adsorption of end-functionalized polystyrene to silicon-supported tris(trimethylsiloxy)silyl monolayers. *Langmuir*, 17(21):6547–6552, 2001.

[219] J.A. Howarter and J.P. Youngblood. Optimization of silica silanization by 3-aminopropyltriethoxysilane. *Langmuir*, 22(26):11142–11147, 2006.

[220] J. Ambati and S.E. Rankin. Reaction-induced phase separation of bis(triethoxysilyl)ethane upon sot-gel polymerization in acidic conditions. *J. Colloid Interface Sci.*, 362(2):345–353, 2011.

[221] C.J. Lund and P.D. Murphy. Oligomerization of an aminosilane coupling agent and its effects on the adhesion of thin polimide films to silica. *J. Adhes. Sci. Technol.*, 6(1):33–47, 1992.

[222] R. Knowles. Kinetic isotope effects in organic chemistry. Technical report, MacMillan Group, 2005.

[223] D.Q. Zhu and W.J. van Ooij. Corrosion protection of metals by water-based silane mixtures of bis-[trimethoxysilylpropyl]amine and vinyltriacetoxysilane. *Prog. Org. Coat.*, 49(1):42–53, 2004.

[224] D. Zhu and W.J. Van Ooij. Structural characterization of bis-[triethoxysilylpropyl]tetrasulfide and bis-[trimethoxysilylpropyl]amine silanes by Fourier-transform infrared spectroscopy and electrochemical impedance spectroscopy. *J. Adh. Sci. Tech.*, 16:1235–60, 2002.

[225] S. Naviroj, S.R. Culler, J.L. Koenig, and H. Ishida. Structure and adsoprtion characteristics of silane coupling agents on silica and E-glass fiber - dependence on pH. *J. Colloid Interface Sci.*, 97(2):308–317, 1984.

[226] M.P. Besland, C. Guizard, N. Hovnanian, A. Larbo, L. Cot, J Sanz, I. Sobrados, and M. Gregorkiewitz. Silicon and carbon solid-state mass and liquid state nmr study of the polycondensation of heteropolysiloxanes. *J. Am. Chem. Soc.*, 113(6):1982–1987, 1991.

[227] R.J. Hook. A Si-29 NMR study of the sol-gel polymerisation rates of substituted ethoxysilanes. *J. Non-Cryst. Solids*, 195(1-2):1–15, 1996.

[228] F. Biscay, A. Ghoufi, and P. Malfreyt. Surface tension of water-alcohol mixtures from Monte Carlo simulations. *J. Chem. Phys.*, 134(4), 2011.

[229] J.M. Chovelon, L.E. Aarch, M. Charbonnier, and M. Romand. Silanization of stainless steel surfaces: Influence of application parameters. *J. Adhes.*, 50(1):43–58, 1995. 17th Annual Meeting of the Adhesion-Society-Inc, Orlando.

[230] M.C.B. Salon, P.A. Bayle, M. Abdelmouleh, S. Boufi, and M.N. Belgacem. Kinetics of hydrolysis and self condensation reactions of silanes by NMR spectroscopy. *Colloid Surf. A-Physicochem. Eng. Asp.*, 312(2-3):83–91, 2008.

[231] M. Lundgren, N.L. Allan, and T. Cosgrove. Wetting of water and water/ethanol droplets on a non-polar surface: A molecular dynamics study. *Langmuir*, 18(26):10462–10466, 2002.

[232] T.R.E. Simpson, J.F. Watts, P.A. Zhdan, J.E. Castle, and R.P. Digby. A combined atomic force microscopy (AFM)/X-ray photoelectron spectroscopy (XPS) study of organosilane molecules adsorbed on the aluminium alloy L157-T6. *J. Mater. Chem.*, 9(11):2935–2941, 1999.

[233] C.Y.K. Lung and J.P. Matinlinna. Aspects of silane coupling agents and surface conditioning in dentistry: An overview. *Dent. Mater.*, 28(5):467–477, 2012.

[234] B.M. Zhang and S.H. Choi. Suppress polystyrene thin film dewetting by modifying substrate surface with aminopropyltriethoxysilane. *Surf. Sci.*, 600, 2006.

[235] J.K. Kim, D.S. Shin, W.J. Chung, K.H. Jang, K.N. Lee, Y.K. Kim, and Y.S. Lee. Effects of polymer grafting on a glass surface for protein chip applications. *Colloid Surf. B-Biointerfaces*, 33(2):67–75, 2004.

[236] L.. F. M. da Silva, R.J.C. Carbas, G.W. Critchlow, M.A V. Figueiredo, and K. Brown. Effect of material, geometry, surface treatment and environment on the shear strength of single lap joints. *Int. J. Adhes. Adhes.*, 29(6):621–632, 2009.

[237] R.D. Adams and N.A. Peppiatt. Stress analysis of adhesive-bonded lap joints. *J. Strain. Anal.*

[238] L.F.M. da Silva, T.N.S.S. Rodrigues, M.A.V. Figueiredo, M.F.S.F. de Moura, and J.A.G. Chousal. Effect of adhesive type and thickness on the lap shear strength. *J. Adhes.*, 82(11):1091–1115, 2006.

[239] D.M. Gleich, M.J.L. Van Tooren, and A. Beukers. Analysis and evaluation of bondline thickness effects on failure load in adhesively bonded structures. *J. Adhes. Sci. Technol.*, 15(9):1091–1101, 2001.

[240] S. Savard, L.P. Blanchard, J. Leonard, and R.E. Prudhomme. Hydrolysis and condensation of silanes in aqueous solutions. *Polym. Compos.*, 5(4):242–249, 1984.

[241] A. Franquet, J. De Laet, T. Schram, H. Terryn, V. Subramanian, W.J. van Ooij, and J. Vereecken. Determination of the thickness of thin silane films on aluminium surfaces by means of spectroscopic ellipsometry. *Thin Solid Films*, 384(1):37–45, 2001.

[242] F. Zucchi, V. Grassi, A. Frignani, and G. Trabanelli. Inhibition of copper corrosion by silane coatings. *Corrosion Sci.*, 46(11):2853–2865, 2004.

[243] X. Zeng, G. Xu, Y. Gao, and Y. An. Surface wettability of (3-aminopropyl)triethoxysilane self-assembled monolayers. *J. Phys. Chem. B*, 115(3):450–454, 2011.

[244] J. Kim, K. C. Wong, P. C. Wong, S. A. Kulinich, J. B. Metson, and K. A. R. Mitchell. Characterization of AZ91 magnesium alloy and organosilane adsorption on its surface. *Appl. Surf. Sci.*, 253(9):4197–4207, 2007.

[245] R.G. Dillingham and F.J. Beorio. Interphase composition in aluminium epoxy adhesive joints. *J. Adhes.*, 24(2-4):315–335, 1987.

[246] W.X. Que, Y. Zhou, Y.L. Lam, Y.C. Chan, and C.H. Kam. Preparation and characterizations of TiO2/organically modified silane composite materials produced by the sol-gel method. *J. Sol-Gel Sci. Technol.*, 20(2):187–195, 2001.

[247] S. Choi, A.P. Janisse, C. Liu, and E. P. Douglas. Effect of water addition on the cure kinetics of an epoxy-amine thermoset. *J. Polym. Sci. Pol. Chem.*, 49(21):4650–4659, 2011.

[248] L.X. Wu, S.V. Hoa, and M.T. Ton-That. Effects of water on the curing and properties of epoxy adhesive used for bonding FRP composite sheet to concrete. *J. Appl. Polym. Sci.*, 92(4):2261–2268, 2004.

[249] S.R. Culler, H. Ishida, and J.L. Koenig. FT-IR characterization of the reaction at the silane matrix resin interphase of composite materials. *J. Colloid Interface Sci.*, 109(1):1–10, 1986.

[250] L. Vaisman, G. Marom, and H.D. Wagner. Dispersions of surface-modified carbon nanotubes in water-soluble and water-insoluble polymers. *Adv. Funct. Mater.*, 16(3):357–363, 2006.

[251] M.F. Islam, E. Rojas, D.M. Bergey, A.T. Johnson, and A.G. Yodh. High weight fraction surfactant solubilization of single-wall carbon nanotubes in water. *Nano Lett.*, 3(2):269–273, 2003.

[252] E. Bertels, K. Bruyninckx, M. Kurttepeli, M. Smet, S. Bals, and B. Goderis. Highly efficient hyperbranched CNT surfactants: Influence of molar mass and functionalization. *Langmuir*, 30(41):12200–12209, 2014.

[253] Y. Wang, A.M. Alb, and S.M. He, J.and Grayson. Neutral linear amphiphilic homopolymers prepared by atom transfer radical polymerization. *Polym. Chem.*, 5(2):622–629, 2014.

[254] Catalog sigma-aldrich, 2014.

[255] N. Grossiord, P. van der Schoot, J. Meuldijk, and C.E. Koning. Determination of the surface coverage of exfoliated carbon nanotubes by surfactant molecules in aqueous solution. *Langmuir*, 23(7):3646–3653, 2007.

[256] Z. Sun, V. Nicolosi, D. Rickard, S. D. Bergin, D. Aherne, and J.N. Coleman. Quantitative evaluation of surfactant-stabilized single-walled carbon nanotubes: Dispersion quality and its correlation with zeta potential. *J. Phys. Chem. C*, 112(29):10692–10699, 2008.

[257] R. Rastogi, R.l Kaushal, S K. Tripathi, A.L. Sharma, I. Kaur, and L.M. Bharadwaj. Comparative study of carbon nanotube dispersion using surfactants. *J. Colloid Interface Sci.*, 328(2):421–428, 2008.

[258] R. Haggenmueller, S.S. Rahatekar, J.A. Fagan, J. Chun, M.L. Becker, R.R. Naik, T. Krauss, L. Carlson, J.F. Kadla, P.C. Trulove, D.F. Fox,

H. C. DeLong, Z. Fang, S.O. Kelley, and J.W. Gilman. Comparison of the quality of aqueous dispersions of single wall carbon nanotubes using surfactants and biomolecules. *Langmuir*, 24(9):5070–5078, 2008.

[259] D.H. Napper. *Polymeric Stabilization of Colloidal Dispersion.* Academic Press, London, 1983.

[260] G. Jayamurugan, K. S. Vasu, Y. B. R. D. Rajesh, S. Kumar, V. Vasumathi, P. K. Maiti, A. K. Sood, and N. Jayaraman. Interaction of single-walled carbon nanotubes with poly(propyl ether imine) dendrimers. *J. Chem. Phys.*, 134(10), 2011.

[261] D. Kang, N. Park, J.H. Ko, E. Bae, and W. Park. Oxygen-induced p-type doping of a long individual single-walled carbon nanotube. *Nanotechnology*, 16(8):1048–1052, 2005.

[262] P.L. McEuen, M.S. Fuhrer, and H.K. Park. Single-walled carbon nanotube electronics. *IEEE Trans. Nanotechnol.*, 1(1):78–85, 2002.

[263] Y. Nonoguchi, K. Ohashi, R. Kanazawa, K. Ashiba, K.i Hata, T. Nakagawa, C. Adachi, T. Tanase, and T. Kawai. Systematic conversion of SWNT into n-type thermoelectric materials by molecular dopants. *Sci. Rep.*, 3, 2013.

[264] X.Y. Gong, J. Liu, S. Baskaran, R.D. Voise, and J.S. Young. Surfactant-assisted processing of carbon nanotube/polymer composites. *Chem. Mat.*, 12(4):1049–1052, 2000.

[265] T.P. Burgin, J.C. Lewenstein, and D. Werho. Investigations into the mechanism of adsorption of carbon nanotubes onto aminopropylsiloxane functionalized surfaces. 21(14):6596–6602, 2005.

[266] M.G. Callens, N. De Greef, J.W. Seo, L. Gorbatikh, and I. Verpoest. *Ductile steel fibre composites with carbon nanotubes grafted on the fibres.* Proceedings of the CompositeWeek@Leuven, Leuven, Belgium, 2013.

List of Publications

International Peer-Reviewed Journal Papers

- E. Bertels, K. Bruyninckx, M. Kurttepeli, M. Smet, S. Bals and B. Goderis. Highly efficient hyperbranched cnt surfactants: Influence of molar mass and functionalization. *Langmuir*, 30(41):12200–12209, 2014.
- E. Bertels, A.K. Ghosh, B. Goderis, M. Smet, D. Van Hemelrijck and B. Van Mele . Optimization of wet chemical silane deposition to improve the interfacial strength of stainless steel/epoxy. *Applied Surface Science*, 324:134–142, 2015.
- M.G. Callens, E. Bertels, M. Smet, B. Goderis, L. Gorbatikh and I. Verpoest. Tensile behavior of steel fibre/epoxy composites with modified adhesion. *Composites Part A: Applied Science and Manufacturing*, 69:208–218, 2015.
- M.G. Callens, E. Bertels, B. Goderis, M. Smet I. Verpoest and L. Gorbatikh. Influence of matrix and interphase properties on the tensile behaviour of steel fibre/PA-6 composites. *Composites Part A: Applied Science and Manufacturing*, in preparation.

Conferences

- E. Bertels, M.G. Callens, N. De Roo, D. Poelman, I. Verpoest, M. Smet and B. Goderis. Improving the properties of polymer-steel composites by using silane coupling agents. In *Annual Meeting of the Adhesion Society, Florida, USA*, March 2013.
- E. Bertels B. Goderis M. Smet M.G. Callens, L. Gorbatikh and I. Verpoest. Ductile steel fiber/epoxy composites with modified adhesion. In *19th International Conference on Composite Materials. ICCM, Montreal, Canada*, July-August 2013.

- E. Bertels and E. Nies. Study of P3HT in solution: Phase diagram. In *BPG, Houffalize, Belgium*, May 2011.
- E. Bertels, M. Smet and B. Goderis. Improving polymer-steel adhesion: On the chemistry of silane coupling agents. In *BPG, Blankenberge, Belgium*, May 2012.
- E. Bertels, M.G. Callens, N. De Roo, D. Poelman, I. Verpoest, M. Smet and B. Goderis. Silane based sizings for steel fibers/plates in steel-polymer hybrids. In *SIM User Forum, Antwerp, Belgium*, December 2012.
- E. Bertels, N. De Roo, A.K. Ghosh, D. Poelman, B. Van Mele, M. Smet and B. Goderis. Towards better polymer-steel hybrids: Optimizing silane deposition conditions. In *BPG, Houffalize, Belgium*, May 2013.
- E. Bertels, A.K. Ghosh, B. Van Mele, M. Smet and B. Goderis. Optimizing silane deposition conditions: Tensiometry and mechanical testing. In *SIM User Forum, Antwerp, Belgium*, October 2013.
- E. Bertels, A.K. Ghosh and G. Da Ponte. Optimizing interfacial strength between steel and polymer through plasma and wet chemistry treatments. In *SIM User Forum, Antwerp, Belgium*, October 2013.
- E. Bertels, K. Bruyninckx, M. Smet and B. Goderis. Highly efficient hyperbranched cnt surfactants: Influence of functionalization and molar mass. In *BPG, Gent, Belgium*, May 2014.
- A.K. Ghosh, D. Van Hemelrijck, E. Bertels, B. Goderis, G. Da Ponte, B. Verheyde and B. Van Mele. Optimizing interfacial strength between steel and epoxy resin through atmospheric plasma and wet chemistry treatments. In *BPG, Gent, Belgium*, May 2014.

Curriculum Vitae

Personal Data

Ellen Bertels
Address: Dr. Van de Perrestraat 46, 2440 Geel
Place and date of birth: Turnhout, April 7^{th} 1986
Nationality: Belgian

Education

- **2014-...** Project Manager Inkjet Ink Development, Agfa Gevaert N.V. (Mortsel, Belgium)

- **2010-2015:** PhD in Sciences, Chemistry (KU Leuven)
  PhD thesis: Nano-Engineered Polymer-Steel Hybrids - Chemical and Physical Compatibilization (SIM-SBO project)
  Promotor: Prof. B. Goderis
  Co-Promotor: Prof. M. Smet

- **2008-2010:** Master of Chemistry, Professional Option – Specialization Polymer and Nanomaterials (KU Leuven)
  Master's thesis: Towards High-Performance Solar Cells by Controlling the Active Layer Morphology
  Promotor: Prof. E. Nies

- **2006-2008:** Bachelor of Chemistry, Option Chemical Technology (KU Leuven)

FACULTY OF SCIENCE
DEPARTMENT OF CHEMISTRY
POLYMER CHEMISTRY AND MATERIALS
Celestijnenlaan 200F box 2404
B-3001 Heverlee
ellen.bertels@chem.kuleuven.be
http://www.dept.cs.kuleuven.be